

**BAINITE TRANSFORMATION
AND NOVEL BAINITIC RAIL STEELS**

by
Liou Chun Chang
Hughes Hall

Department of Materials Science and Metallurgy
Pembroke Street
Cambridge
CB2 3QZ

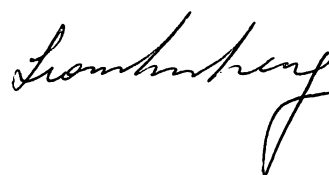
*A dissertation submitted for the degree of
Doctor of Philosophy
at the University of Cambridge*

March 1995

PREFACE

This dissertation is submitted for the degree of Doctor of Philosophy at the University of Cambridge. The investigation described in this report was carried out under the supervision of Dr. H.K.D.H. Bhadeshia at the Department of Materials Science and Metallurgy, Cambridge, between October 1991 and March 1995. Except where acknowledgement and reference to previous work is made, this work is, to the best of my knowledge, original and carried out without collaboration. Neither this, nor any substantially similar dissertation has been or is being submitted for any degree, diploma or other qualification at any other university. This dissertation contains less than 60,000 words.

The contents of Chapters 4 and 6 have been accepted for publication in *Materials Science and Technology*. Chapter 7 has been submitted to *Journal of Materials Science* for publication.



ACKNOWLEDGEMENTS

I would like to express my sincere gratitude to my supervisor, Dr. Harry Bhadeshia, for his constant encouragement and, especially, optimism during the course of this work. I am grateful to all the members of the PT group for their kindness and for providing amusing environment. Thanks are especially due to Mr. Akihiro Matsuzaki, Dr. Gethin Rees, Dr. Rachel Thomson and Dr. Tong-Shung Chou for their help during the course of my study.

I wish to thank Professor C. Humphreys for the provision of laboratory facilities in the Department of Materials Science and Metallurgy at the University of Cambridge.

Thanks are also due to the Ministry of Education, Taiwan, Republic of China, for financial support, and Dr. V. Jerath, of British Steel, for providing the alloys.

Finally, it is with considerate pleasure that I acknowledge the support of my family, in particular my wife, Hung-Mei, and daughter, Jen. I dedicate this thesis to my parent Kao-Chin Chang and Wu Hsiung.

ABSTRACT

This thesis deals with the mechanism of the bainite transformation in steels, with emphasis on a special class of carbide-free bainitic steels. Their microstructure is designed to consist of a mixture of bainitic ferrite, retained austenite and martensite. The steels are destined for applications in the railway industry, and generally wherever resistance to mechanical wear is an important selection criterion.

For commercial production it is necessary for any steel or thermomechanical treatment to be cheap and practicable. It is particularly important for the kinetics of transformation to be such that the alloys can be manufactured on a large scale using continuous cooling transformation. The work reported in the thesis therefore establishes the mechanism and kinetics of transformation, and then continues to apply the concepts to the successful development of rail steels.

The thesis begins with a survey of the literature about solid-state transformations in steels, together with a detailed assessment of bainite. This is followed by a description of the experimental techniques used. Chapter 3 contains measurements of the isothermal transformation kinetics of a variety of silicon-rich steels, and the data are demonstrated to be reasonably consistent with a mechanism in which bainitic ferrite grows without diffusion. This conclusion is reinforced with the results presented in Chapter 4, which for the first time identify quantitatively, the factors responsible for the thickness of austenite films found in bainitic microstructures. Such films have in the past been shown to be of the utmost importance in controlling toughness.

Some new information of fundamental importance was revealed during the course of routine metallographic investigations (Chapter 5). Firstly, it was found that when the driving force for transformation is large, it is possible for separately nucleated platelets of bainite to coalesce into coarse plates. Chapter 6 contains observations which prove that the bainitic ferrite/austenite interface behaves like that of martensite, in that it bows between obstacles. In addition, there is clear evidence that the shear associated with bainite growth can be accommodated by mechanical twinning when differently oriented plates collide.

Chapter 7 establishes for the first time that the number of carbide variants that form in lower bainite can be influenced by the application of an external stress. It reinforces a published hypothesis that the frequently observed single variant of carbide in lower bainite is a consequence of stress-affected precipitation.

Chapters 8 and 9 deal with the wear properties of the bainitic alloys and include extensive data on microstructures generated by continuous cooling transformation. There is also

an outcome from difficulties encountered during the manufacture of thick section, that the embrittlement caused by phosphorus can be overcome by the addition of a controlled amount of molybdenum to the steels.

The thesis finishes with a brief chapter summarizing the key conclusions and proposing some ideas for future work.

CONTENTS

Preface	i
Acknowledgements	ii
Abstract	iii
Nomenclature List	ix

CHAPTER 1 Introduction

1.1 The Decomposition of Austenite to Ferrite	1
1.1.1 Equilibrium	1
1.1.2 Metastable Phase Transformations	1
1.1.3 Allotriomorphic Ferrite	2
1.1.4 Widmanstätten Ferrite	4
1.1.5 Bainite	4
1.1.5.1 Growth of Bainite	5
1.1.5.2 Bainite-Start Temperature	6
1.1.5.3 Incomplete Reaction Phenomenon	6
1.1.5.4 Surface Relief	7
1.1.5.5 Transition From Upper to Lower Bainite	7
1.1.5.6 Carbides in Bainite	7
1.1.6 Martensite Formation	8
1.2 Microstructure and Properties (Bainite)	9
1.2.1 The Role of Austenite	9
1.2.1.1 Strength	9
1.2.1.2 Ductility	10
1.2.1.3 Toughness	10
1.2.2 Temper Embrittlement	11
1.2.2.1 Impurity Induced Embrittlement	11
1.2.2.2 Embrittlement by a Grain Boundary Phase	11
1.2.2.3 Precipitation at Sub-Grain Boundaries	12
1.2.3 Wear Performance	12

CHAPTER 2: General Experimental Techniques

2.1 Alloys	25
2.2 Sample Preparation and Heat Treatment	26
2.3 Dilatometry	26

2.4 Expansivity Measurements	28
2.5 Calculation of B_S and M_S Temperatures	29
2.6 Metallography	29
2.6.1 Transmission Electron Microscopy	29
2.6.2 Scanning Electron Microscopy	29
2.6.3 Optical Microscopy	29
2.7 Mechanical Tests	30
2.7.1 Tensile Test	30
2.7.2 Charpy Impact Test	30
2.7.3 Hardness Test	30

CHAPTER 3: Microstructures and Kinetics of the Bainite Transformation in Si-Rich Steels

3.1 Introduction	33
3.2 Experimental	33
3.3 Metallography	34
3.4 Kinetics	35
3.5 Time-Temperature-Transformation Diagrams	38
3.6 Conclusions	39

CHAPTER 4: Austenite Films in Bainitic Microstructures

4.1 Introduction	54
4.2 Experimental	54
4.2.1 Materials	54
4.2.2 Stereological Measurements	54
4.3 Results	55
4.3.1 General Microstructure	55
4.3.2 Mechanism of Transformation	56
4.3.3 Calculation of the Thickness of Austenite Films	58
4.3.3.1 Finite Difference Analysis	60
4.4 Conclusions	61

CHAPTER 5: The Microstructure of Lower Bainite Formed at A Large Undercoolings Below the Bainite-Start Temperature

5.1 Introduction	80
5.2 Experimental Methods	80

5.3 Results and Discussion	80
5.3.1 Transformation Temperatures	80
5.3.2 New Metallographic Observations	82
5.4 Conclusions	85

CHAPTER 6: Two Metallographic Observations on the Mechanism of the Bainite Transformation

6.1 Introduction	95
6.2 Experimental Materials	95
6.3 Thermoelastic Equilibrium	96
6.4 Accommodation Twinning	97
6.5 Conclusions	98

CHAPTER 7: Stress Affected Transformation to Lower Bainite

7.1 Introduction	105
7.2 Experimental Procedures	106
7.3 Results and Discussion	107
7.3.1 Aligned Microstructure	107
7.3.2 Carbide Precipitation	107
7.4 Conclusions	108

CHAPTER 8: The Rolling/Sliding Wear Performance on High Silicon Carbide-Free Bainitic Ferrite

8.1 Introduction	113
8.2 Experimental Materials	114
8.3 Experimental Procedures	114
8.3.1 Wear Tests	114
8.3.2 X-ray Determination of Retained Austenite	115
8.3.3 Microhardness Tests	116
8.4 Results and Discussion	116
8.4.1 Microstructural Characterisation	116
8.4.2 Tensile Properties and Hardness	117
8.4.3 Impact Properties	118
8.4.4 Wear Tests	118
8.4.5 Retained Austenite Content	121
8.5 Further Discussion	123

8.6 Conclusions	124
CHAPTER 9: Impurity-Induced Temper Embrittlement in Carbide-Free Bainitic Steels Containing Austenite and Martensite	
9.1 Introduction	145
9.2 Experimental Materials	146
9.3 Results and Discussion	146
9.3.1 Microstructural Characterisation	146
9.3.2 Impact Energy	148
9.3.3 Ductility	149
9.3.4 Regression Analysis	150
9.4 Conclusions	151
CHAPTER 10: Conclusions and Future Work	170
REFERENCES	172

NOMENCLATURE

α	Ferrite (body-centered cubic iron or steel)
α_1	Parabolic thickening rate constant for allotriomorphic ferrite growth
β	Autocatalysis constant in the bainite kinetics model
δ	Uniaxial dilatation normal to the habit plane
γ	Austenite (face-centered cubic iron)
θ	The maximum extent of bainite that can form at a given temperature
$\lambda_1 \lambda_2$	Empirical constants arising in the bainite transformation kinetics model
ξ	Normalised volume fraction of bainite, <i>i.e.</i> v/θ
ν	Poisson's ratio of austenite
μ	Shear modulus of austenite
Ae'_3	Paraequilibrium phase boundaries separating the $(\gamma+\alpha)$ and γ phase fields
a	Bainite plate thickness
c	Bainite plate width
$c_1^{\gamma\alpha}$	Concentration of carbon in austenite at ferrite/austenite phase boundary in a ternary alloy
$c_1^{\alpha\gamma}$	Concentration of carbon in ferrite at ferrite/austenite phase boundary in a ternary alloy
$c_2^{\gamma\alpha}$	Concentration of substitutional solute in austenite at ferrite/austenite phase boundary in a ternary alloy
$c_2^{\alpha\gamma}$	Concentration of substitutional solute in ferrite at ferrite/austenite phase boundary in a ternary alloy
D_{11}	Diffusion coefficient of carbon in austenite
D_{22}	Diffusion coefficient of substitutional solute in austenite in a ternary alloy
\bar{D}	Weighted average diffusivity of carbon in austenite
D^γ	Diffusivity of carbon in austenite
E	Young's modulus for austenite
$G^{\gamma\alpha}$	Free energy change for transformation of austenite to ferrite of identical composition
ΔG_m^0	Maximum free energy change per mole of ferrite at the onset of the bainite transformation
ΔG_m	Maximum free energy change per mole of precipitate phase

G_N	The critical value of ΔG_m^0 required for nucleation of displacive transformation product
G_S	Strain energy associated with phase transformation
H_b	Hardness of bainitic ferrite
H'_α	Hardness of virgin martensite
H_γ	Hardness of austenite
I	Nucleation rate of bainite per unit volume
I_0	Nucleation rate of bainite at the W_S temperature, independent of the effects of autocatalysis
I_{WS}	Nucleation rate of bainite at the W_S temperature
$K'_1 K_2$	Empirical constants arising in bainite transformation kinetics model
\bar{L}	Mean linear intercept of a series of random test lines on to random two-dimensional section of a square plate of thickness t and sides $a \times t$
\bar{L}_T	Mean linear intercept of a series of test lines normal to random two-dimensional section of a square plates of thickness t and sides $a \times t$
P_A	Perimeter per unit area
n	Number of slices divided for the purpose of finite difference analysis
Q	Dependence of martensite hardness on carbon content
r	Grid number for finite difference analysis
R	Universal gas constant
s	Shear component of the IPS shape deformation or amount of carbon trapped in bainitic ferrite in solid solution
S_v	Grain boundary surface area pre unit volume
t	Reaction time or time interval between successive calculations in finite analysis
t_d	Time required to decarburise a plate of bainite
T	Temperature
T_0	Temperature at which γ and α of the same composition have the same free energy
T'_0	As T_0 but accounting for the stored energy of ferrite
v	Volume fraction of bainite or velocity of α/γ interface
V_m	Molar volume of austenite
V_α	Volume fraction of bainitic ferrite
V_γ	Volume fraction of austenite
V'_α	Volume fraction of martensite

x	Carbon concentration
x'_γ	Normalized carbon concentration defined as x_γ/\bar{x}
X	General representation of the substitutional solute in a ternary alloy steel
\bar{x}	Mean carbon concentration in an alloy
x_γ	Carbon concentration in austenite
$x^{\gamma\alpha}$	Carbon concentration in austenite which is in paraequilibrium with ferrite
$x^{\alpha\gamma}$	Carbon concentration in ferrite which is in paraequilibrium with austenite
$x_{T'_o}$	Carbon concentration corresponding to the T'_o curve for the temperature concerned
w_γ z_γ	Thickness of the austenite film
w_α	Thickness of the ferrite plate
w_γ^s	Thickness of slice of austenite for the finite difference analysis
z	Coordinate normal to the α/γ interface plane
Z	Thickness of allotriomorphic ferrite

CHAPTER 1

INTRODUCTION

The aim of this chapter is to provide a concise summary of the phase transformations from austenite to ferrite, of which the bainite transformation, the central part of this research, will be especially emphasized. The other topic addressed is the microstructure-properties relationships for bainitic steels. This latter discussion is confined to the influence of retained austenite on some essential mechanical properties, and some considerations of wear performance and temper embrittlement. These topics are particularly relevant to the use of bainitic steels in rail applications.

1.1 THE DECOMPOSITION OF AUSTENITE TO FERRITE

1.1.1 Equilibrium

Phase diagrams define the regions of phase stability, as illustrated for the Fe-C system shown in Fig. 1.1. The diagram is an equilibrium phase diagram in the sense that the observations have been made at a stage where the samples show no perceptible change over reasonably long periods of time. Nevertheless, metastable equilibrium cannot be ruled out. For example, graphite is in fact more stable than cementite, but does not form in the vast majority of steels during service. The state of true equilibrium is therefore a notion rather than a particularity. This does not pose any major difficulties since metastable equilibria follows the same laws of the equilibrium thermodynamics. The phase diagram is therefore an important and useful for indicating the probable phases as a function of parameters such as the chemical compositions or temperature.

1.1.2 Metastable Phases Transformations

When the formation of an equilibrium phase is prevented by a large activation energy of nucleation, or a slow growth process, a metastable phase can form instead provided that there is sufficient thermodynamic driving force. This is why there are so many kinds of ferrite transformation products. It is widely accepted that the different forms of ferrite can be categorised into those which are reconstructive and others which grow by displacive transformations.

Reconstructive transformation involves the uncoordinated transfer of atoms across the interface leading to the change of crystal structure. The random movement of atoms is thermally activated; all elements diffuse during the process in a way which minimises the strain energy. The relative positions of atoms in the product phase do not correspond with the original

locations in the parent phase, so that “atomic correspondence” is said to have been destroyed. The process is illustrated in Fig. 1.2.

The atomic mobility necessary for reconstructive transformation becomes increasingly difficult to achieve as the transformation temperature is reduced. The driving force for transformation, nevertheless increases so that eventually a situation is reached in which transformation can proceed by a deformation of the parent structure. This is called displacive transformation. The atoms move less than an interatomic distance and maintain their relative positions with respect to neighbouring atoms. The transformation proceeds by the motion of a glissile interface (coherent or semi-coherent) which sweeps across the parent phase.

The deformation can in the case of steels be described as an invariant-plane strain with a large shear component. The process is illustrated in Fig. 1.2. The strain energy due to the displacive transformation is, therefore, much higher than is the case for reconstructive transformation. It is therefore understandable that the displacive transformation needs a higher driving force, *i.e.*, a lower formation temperature.

The major transformation products can be categorised, in order of decreasing transformation temperature as follows:

Allotriomorphic ferrite

Widmanstätten ferrite

Bainite

Martensite

1.1.3 Allotriomorphic Ferrite

Allotriomorphic ferrite nucleates at austenite grain boundaries. It is sometimes also called proeutectoid ferrite, grain boundary ferrite or polygonal ferrite, but these terms are ambiguous. The growth of allotriomorphic ferrite is not hindered by the presence of austenite grains, which can therefore be destroyed completely during transformation.

In Fe-C alloys, the growth of allotriomorphic ferrite usually occurs at a rate controlled by the diffusion of carbon in the austenite ahead of the moving α/γ interface [Bhadeshia, 1985b]. Local equilibrium is then assumed to exist in the phases in contact at the interface as illustrated in Fig. 1.3. Since the solubility of carbon in ferrite is small compared with austenite, an excess concentration of carbon builds up in the austenite ahead of the interface. The extent of the carbon diffusion field increases with the amount of ferrite that has formed, so that the growth rate of ferrite must decrease as transformation progresses. It has been demonstrated that the thickness Z of the layer of allotriomorphic ferrite is related to time t

during isothermal transformation as follows [Christian, 1975]:

$$Z = \alpha_1 t^{0.5} \quad (1.1)$$

where $Z = 0$ at $t = 0$ and Z defines the position of the interface along the co-ordinate z which is normal to the interface. α_1 is called the one-dimensional parabolic thickening rate constant and can be deduced using diffusion theory.

In the case of Fe-C-X alloys (where X represents a substitutional solute), the situation is complicated by the fact that the diffusivity of X is generally much smaller than that of interstitial carbon atoms [Purdy *et al.*, 1964; Coates, 1973]. It is generally impossible to simultaneously satisfy the conditions for the conservation of mass at the moving interface for both X and C, for the tie-line which passes through the alloy composition. After neglecting the interdiffusion coefficients, the equations for the conservation of mass at the interface become:

$$(c_1^{\gamma\alpha} - c_1^{\alpha\gamma})v = -D_{11}\nabla c_1|_{z=Z} \quad (1.2)$$

$$(c_2^{\gamma\alpha} - c_2^{\alpha\gamma})v = -D_{22}\nabla c_2|_{z=Z} \quad (1.3)$$

where $c_1^{\gamma\alpha}$ and $c_2^{\gamma\alpha}$ represent the respective concentrations of carbon and substitutional element in austenite at the interface, and D_{11} and D_{22} are the respective diffusion coefficients. v is the velocity of the interface. To match the interstitial and substitutional fluxes, it is necessary to select tie lines which compensate for the disparity in diffusion coefficients by affecting the concentration gradients, ∇c_1 and ∇c_2 . At low undercoolings the gradient of carbon, ∇c_1 can be made very small by selecting a tie line which allows $c_1^{\gamma\alpha} \simeq \bar{c}_1$, where \bar{c}_1 is the average carbon concentration in the alloy. The driving force for carbon diffusion is in effect reduced, allowing its flux to be consistent with that of X. This is the “Partitioning, Local Equilibrium” (PLE) mechanism which involves the long-range diffusion of X in austenite [Purdy *et al.*, 1964; Coates, 1973].

Alternatively, at high undercoolings, the tie-line can be chosen to allow $c_2^{\alpha\gamma} \simeq \bar{c}_2$ so that the gradient of X can be drastically increased since only small amounts of X partition into the austenite. The diffusion of X can thus keep pace with that of carbon. This mode of ferrite transformation is called “Negligible Partitioning, Local Equilibrium” (NPLE) [Coates, 1973]. Both the PLE and NPLE mechanisms are equilibrium modes of transformation since the compositions of both species at the interface can be determined by a tie-line of the corresponding phase diagram.

The selection of tie-lines for the PLE and NPLE is illustrated in Fig. 1.4. The α/γ phase field can be divided into domains where either the PLE or NPLE mechanism can operate.

When the transformation conditions do not permit the partitioning of X, the Fe/X ratio remains uniform across the interface although carbon achieves its equilibrium with both phases. This is “Para-equilibrium” [Hultgren, 1951; Aaronson *et al.*, 1966a, b; Coates, 1973], in which the growth rate is controlled by the diffusivity of carbon. The interface compositions are given by the tie-line of the paraequilibrium phase diagram, calculated such that the Fe/X ratio is fixed for all locations.

1.1.4 Widmanstätten Ferrite

Widmanstätten ferrite can either grow from austenite grain boundaries (primary Widmanstätten ferrite) or from allotriomorphic ferrite (secondary Widmanstätten ferrite). It has a thin wedge-shape and usually a tent-like surface relief indicative of a displacive transformation mechanism [Watson and McDougall, 1973]. The doubly tilted surface relief arises because of the adjacent growth of two mutually accommodating variants, each of which has a slightly different habit plane with the austenite. This leads to a minimisation of strain energy [Bhadeshia, 1981a], a necessary feature since there is insufficient driving force to support the formation of a single plate on its own at the relatively high temperatures where the transformation occurs.

Widmanstätten ferrite is considered to grow under paraequilibrium conditions [Bhadeshia, 1981a, 1985a]. The growth rate is thus controlled by the diffusion of carbon in austenite ahead of the moving interface. Due to its plate shape, the lengthening rate of Widmanstätten ferrite is constant [Trivedi, 1970].

1.1.5 Bainite

The term bainite refers to the microstructural constituent formed in steels when austenite decomposes at temperatures above that for martensitic transformation, but below that at which pearlite occurs. Bainite is generally described as a nonlamellar ferrite-carbide aggregate [Hehemann, 1970]. Two major morphological variants are upper bainite and lower bainite [Mehl, 1939], both of which consist of aggregates of platelets or laths of ferrite separated by regions of residual phases. These latter phases consist of untransformed austenite, martensite or cementite. The aggregates of bainitic ferrite platelets are called sheaves [Aaronson and Wells, 1956], and the individual platelets are sometimes called sub-units, which are the basic growth units of bainitic ferrite. The platelets within a given sheaf may not be completely isolated from one another by the residual phases, in which case, low-misorientation grain boundaries are formed along the surface where the sub-units come in contact [Bhadeshia and Christian,

1990]. The nature of a bainite sheaf is shown schematically in Fig. 1.5.

In upper bainite, the bainitic ferrite is free of carbide precipitation, any carbide growing from the regions of the carbon enriched residual austenite which are trapped between the sub-units of ferrite. By contrast, lower bainitic ferrite contains, apart from inter-platelet carbide precipitates, a fine dispersion of plate-like carbides (*e.g.*, ϵ -carbide or cementite) within the ferrite platelets [Hehemann, 1970; Hehemann *et al.*, 1972].

Using two-surface analysis, which involves the simultaneous observation of the habit plane trace on two non-parallel surfaces, and other observations on specimens partially transformed to bainite, it has been able to show that the overall shape of a sheaf is that of a wedge shaped plate [Oblak *et al.*, 1964; Srinivasen and Wayman, 1968; Ohmori, 1971; Bhadeshia and Edmonds, 1980]. The thick end of the sheaf originates at an austenite grain boundary. A similar morphology is found for lower bainite [Oblak *et al.*, 1964].

Bainite is considered to grow by displacive transformation without diffusion, but with the carbon partitioning from the ferritic component into the surrounding austenite after the completion of growth.

1.1.5.1 Growth of Bainite

Sheaves of bainite normally nucleate at the austenite grain boundaries and then propagate towards the grain interior by the successive formation of individual sub-units, each of which grows to a limited size. New sub-units form mainly near the tips of existing platelets, a process known as sympathetic nucleation [Aaronson and Wells, 1956]. The width of each sub-unit is typically 0.2 μm and is found to decrease as the transformation temperature is lowered [Kunitake *et al.*, 1972]. The number of sub-units in an individual sheaf increases as the transformation temperature decreases [Sandvik, 1982a].

The growth of bainite has been investigated extensively using hot-stage light microscopy [Obalk and Hehemann, 1967; Speich and Cohen, 1960; Goodenow *et al.*, 1963; Rao and Winchell, 1967; Simonen *et al.*, 1973]. These observations, because of the low spatial resolution, related to sheaf growth rather than the growth of sub-units [Bhadeshia and Christian, 1990]. The observed lengthening rates of sheaves of bainite in alloy steels are far greater than expected from calculations based on carbon diffusion-controlled paraequilibrium transformation [Ali and Bhadeshia, 1989]. Nevertheless carbon diffusion has been shown to be closely related to the growth of bainite sheaves [Bhadeshia, 1992]. This is consistent with the assumption that the sheaf grows by the nucleation of sub-units near the tips of existing platelets, since sub-unit nucleation only becomes possible when the carbon enrichment at the nucleation sites

becomes sufficiently small.

1.1.5.2 Bainite-Start Temperature

The bainite transformation is represented by its own C-curve on a time-temperature-transformation (TTT) diagram. The upper limit of this is the bainite-start or B_S temperature. When diffusional transformation overlaps with bainite, a bay is formed in the TTT diagram. The B_S temperature is the highest temperature at which bainite can form [Hehemann, 1970; Hehemann *et al.*, 1972], and since the transformation is diffusionless, $B_S < T_0$. The T_0 concept was introduced by Zener [1946] and modified by Aaronson *et al.* [1966a]. A further calculation was carried out by Bhadeshia *et al.*, [1982] allowing for the effect of elastic strain due to transformation, giving strain energy of about 400 J mole⁻¹. An illustration of the T_0 and T'_0 curves is presented in Fig. 1.6. The experimental data show that the B_S temperatures for Fe-C and Fe-C-X systems are indeed lower than the T_0 curve [Ohmori *et al.*, 1991]. This is not the case for some hyper-eutectoid steels because carbide precipitation precedes that of bainite. The carbon concentration of austenite before the bainite transformation is, thus, reduced.

1.1.5.3 Incomplete Reaction Phenomenon

The partitioning of carbon that follows the growth of bainite enriches the austenite. When the composition of the austenite eventually reaches the T_0 curve, diffusionless transformation becomes impossible [Bhadeshia *et al.*, 1980]. The negative slope of the T_0 curve permits larger quantities of bainite to form at lower temperatures. The bainite transformation is never able to consume all the austenite parent phase, and in fact leaves a great deal more of the austenite untransformed than is expected from the phase diagram. This is the so-called *incomplete reaction phenomenon* [Hehemann, 1970; Hehemann *et al.*, 1972].

The actual measurement of carbon in retained austenite at the point where bainite transformation stops can be done in several ways. Two direct measurements [Bhadeshia *et al.*, 1982; Josefsson *et al.*, 1991] have been carried out using an atom-probe and the results show that the carbon concentration in austenite is slightly higher than the T'_0 , though far away from Ae'_3 ($\alpha/\alpha + \gamma$ paraequilibrium phase boundary). Fig. 1.7 illustrates the incomplete reaction phenomenon and its counterpart where the growth is limited by the Ae'_3 phase boundary.

Many other methods, such as dilatometry, x-ray analysis and magnetic frequencies have been used to verify the incomplete reaction phenomenon [Bhadeshia *et al.*, 1980; Tomita and Okawa, 1993; Ericsson *et al.*, 1976; Chang and Bhadeshia, 1994].

1.1.5.4 Surface Relief

The growth of bainite is always accompanied by an invariant-plane strain surface relief similar to that of martensite [Hehemann, 1970]. It should be noted that although both diffusional and diffusionless transformation can result in surface relief, the relief for diffusional transformations is irregular and due to volume change alone [Bhadeshia, 1981a].

1.1.5.5 Transition From Upper to Lower Bainite

The transition from upper to lower bainite has been considered to occur due to two competitive processes: the partitioning of carbon from supersaturated ferrite into surrounding austenite, and carbide precipitation from supersaturated bainitic ferrite [Matas and Hehemann, 1961; Pickering, 1967; Takahashi and Bhadeshia, 1990]. Upper bainite forms when almost all of the excess carbon is rejected into the residual austenite; with lower bainite, carbon precipitates relatively rapidly in the supersaturated ferrite. There are circumstances where both phases can grow simultaneously during isothermal transformation near the transition temperature [Pickering, 1967]. Upper bainite forms first, enriches the residual austenite, which then transforms to lower bainite. Also, lower bainite is likely to be absent in alloys containing low carbon, while higher carbon alloys may form only lower bainite but no upper bainite [Ohmori and Honeycombe, 1971; Oka and Okamoto, 1986].

The transition temperature from upper to lower bainite is not considered to be constant, although high carbon alloys seem to have an constant transition temperature at 350 °C [Matas *et al.*, 1961; Pickering, 1967]. A quantitative model of the transition from upper to lower bainite has been developed by comparing the time required to decarburise supersaturated ferrite against cementite precipitation kinetics for the Fe-C system [Takahashi and Bhadeshia, 1990]. The essential features of this model are illustrated in Fig. 1.8.

1.1.5.6 Carbides in Bainite

(a) Upper Bainite

The carbide phase associated with upper bainite is almost always cementite. As a consequence of transformation of bainitic ferrite, the films of austenite which are trapped between the bainitic platelets become richer in carbon due to the fact that carbon partitions from ferrite. If the carbon concentration in the austenite exceeds that given by the extrapolated $\gamma/\gamma+Fe_3C$ phase boundary, then cementite precipitation occurs from the enriched-austenite [Kriesement *et al.*, 1956]. With either increasing carbon content or decreasing transformation temperature, the width of the bainitic ferrite laths decrease, and consequently the carbides appear closer together [Honeycombe *et al.*, 1972].

(b) Lower Bainite

The difference between lower and upper bainite is that in the former case the carbides precipitate both in the bainitic ferrite and in the austenite between the sub-units of lower bainite.

The carbides within an individual sub-unit of lower bainitic ferrite usually occur in a single crystallographic orientation. When the carbide is cementite, examination of planar sections shows that the particles are aligned at some 60° to the long axis of the ferrite [Speich, 1962; Lai, 1975]. In some cases, several variants have been observed although the 60° variant still tends to dominate [Bhadeshia *et al.*, 1979a; Srinivasan *et al.*, 1968]. Another carbide, ϵ -carbide ($\text{Fe}_{2.4}\text{C}$), in lower bainite was first identified by Austin and Schwartz [1952]. Several investigators subsequently also found the same ϵ -carbide within bainitic ferrite in lower bainite [Huang *et al.*, 1977; Matas *et al.*, 1961; Oblak *et al.*, 1964; Sandvik, 1982b].

Since some of the carbon in the alloy is tied up in the form of carbide within the lower bainite ferrite, the reaction can proceed further, and thus the volume fraction of residual austenite trapped bainitic platelets is less for lower bainite [Hehemann *et al.*, 1972]. Hence, less carbide precipitation occurs from austenite.

1.1.6 Martensite Formation

Rapid quenching of austenite to room temperature often results in the formation of martensite, by diffusionless nucleation and growth. This involves the movement of a coherent, or at least semi-coherent, interface. The velocity of the advancing interface is limited by the speed of sound in the metal. The atoms in austenite retain an exact atomic correspondence with those in the product martensite. The elegant phenomenological theory reviewed by Christian [1965] has helped to rationalize the structural relationship between the austenite and martensite. The martensitic reaction is a combination of a homogeneous lattice deformation (Bain strain plus a rigid body rotation) and an inhomogeneous lattice-invariant deformation. The former produces the right crystal structure and orientation relationship and has the net effect of an invariant-line strain. The inhomogeneous deformation is either slip or twinning, and makes the invariant-line strain appear on a macroscopic scale to be an invariant-plane strain so that the overall strain energy is minimized. A schematic illustration of the above theory is shown in Fig. 1.9.

Tempering martensite, by holding it at high temperature, results in carbide precipitation. If the martensite-start temperature is high, tempering can occur during cooling, leading to auto-tempering.

Martensite is believed to nucleate at faults in the parent austenite. For a given degree of undercooling, only a certain size of faults can be activated as martensitic nuclei. A further undercooling is needed to activate the other faults which have larger activation energies, in order to increase the volume fraction of martensite. Therefore at a certain temperature, only a certain amount of martensite can be obtained, giving it an athermal characteristic.

The composition variations in the vicinity of the transformation interfaces for a variety of growth mechanisms are illustrated in Fig. 1.10. The possibilities range from the local equilibrium at the interface to paraequilibrium and martensitic conditions. Bainite is considered to form in a martensitic manner with the partitioning of carbon soon afterwards.

1.2 MICROSTRUCTURE AND PROPERTIES (BAINITE)

1.2.1 The Role of Austenite

There is often a considerable amount of retained austenite present in bainitic microstructures as a result of the nature of the transformation mechanism, especially when the steel contains elements which retard the precipitation of carbides. Bainite is considered to grow by the propagation of discrete, carbon supersaturated sub-units, with partitioning of extra carbon into the surrounding austenite occurring shortly after transformation. The austenite trapped between sub-units will not be able to transform due to its high carbon concentration, but is retained after cooling to ambient temperature. This entrapped film shaped austenite can contain a carbon concentration close the paraequilibrium concentration [Rees and Bhadeshia, 1993b]. However, blocky austenite can be retained between bainitic sheaves; this is enriched to a lesser extent than its film austenite counterpart. The formation of film and blocky austenite is illustrated in Fig. 1.11.

An appropriate silicon concentration prevents the precipitation of cementite and therefore enhances the ability to retained austenite. These silicon-steels are the subject of this thesis and hence are discussed in detail.

1.2.1.1 Strength

Austenite is relatively soft, ~ 240 HV [Bhadeshia and Edmonds, 1983a, b], compared to its low temperature products bainite and martensite. Its contribution to the overall strength of bainitic microstructure is therefore minor, but nevertheless, its influence is important. It has been found that the strength of the isothermally transformed bainite decreases as the amount of retained austenite increases [Kalish *et al.*, 1965; Sandvik and Nevalainen, 1981]. For ultimate tensile strength, a generally constant value was obtained for a variety of retained

austenite contents at a given transformation temperature [Sandvik and Nevalainen, 1981]. It has been suggested that the retained austenite can decompose by stress-induced martensitic transformation during the course of plastic deformation after yielding [Kalish *et al.*, 1965], so that less strong retained austenite is compensated for by the formation of martensite during tensile testing. The ratio of proof stress to ultimate tensile strength is generally increased as the retained austenite content decreases [Sandvik and Nevalainen, 1981].

1.2.1.2 Ductility

Soft austenite generally is beneficial to ductility. It has, nevertheless, been found that the maximum elongation is associated with the presence of film austenite, while the occurrence of isolated, blocky austenite leads to a deterioration in the ductility [Bhadeshia and Edmonds, 1983a, b]. The austenite content associated with the optimum ductility is larger when the transformation temperature decreases [Sandvik and Nevalainen, 1981]. Since film austenite is trapped between ferrite sub-units, its fraction increases with the amount of ferrite. A decrease of transformation temperature not only decreases the size the sub-units but also increases the maximum extent of bainite that can form, leading to more and finer austenite.

A monotonic increase of elongation with retained austenite content has been reported by Miihkinen and Edmonds [1987a, b]. The retained austenite content was varied by altering the transformation temperature, so that the strength increases when the austenite content decreases. The two sets of data are difficult to correlate, since the carbon concentrations and the ways of controlling the retained austenite are different, and more importantly, the variation of ultimate tensile strength with the retained austenite content is not the same.

1.2.1.3 Toughness

The mechanical stability of retained austenite, due to its importance in affecting toughness, has been the subject of many investigations [Thomas, 1978; Bhadeshia, and Edmonds, 1979b; Cheruvu *et al.*, 1982; Bhadeshia and Edmonds, 1983a, b; Tomita and Okawa, 1993]. For martensite, two mechanisms (by which retained austenite may affect toughness) have been proposed: (a) localized transformation-induced plasticity or TRIP, and (b) crack tip branching and blunting [Lai *et al.*, 1974]. The former occurs when energy can be absorbed by the stress-induced phase transformation of austenite into martensite. The second mechanism applies to stable austenite which diverts or blunts cracks. The blocky austenite in bainite tends to decompose into untempered brittle martensite, whereas the more stable film austenite can survive plastic deformation [Bhadeshia and Edmonds, 1983a, b; Tomita and Okawa, 1993], which corresponds to the above mechanisms respectively. Nevertheless, the presence of blocky austenite

deteriorates toughness implies the energy absorbed during the stress-induced transformation of austenite into untempered martensite due to the brittleness of the latter phase.

The above discussion suggests that one way of improving the toughness is to increase the amount of film austenite at the expense of blocky austenite. Two main methods have been proposed: (a) reduction of the overall carbon content of the alloy concerned; (b) modification of the substitutional alloying element content such that the T_0 curve is shifted to higher carbon concentrations. Both allow more bainitic ferrite to form so that the blocky austenite is reduced and refined [Bhadeshia and Edmonds, 1983b].

1.2.2 Temper Embrittlement

Temper embrittlement occurs after the steel is heat treated; it results in the loss of one or more properties such as ductility, impact strength or fracture toughness. The effect of this embrittlement is to shift the curve of fracture energy versus test temperature to higher temperatures. The fracture path is generally along the most incoherent boundaries present in the steel. These may be the austenite or prior austenite boundaries, or particle/matrix boundaries, which may be coincident with the austenite grain boundaries [Briant and Banerji, 1978]. Tempering of bainite and martensite can also lead to embrittlement, which is due to the precipitation of carbides along the lath boundaries.

1.2.2.1 Impurity Induced Embrittlement

This embrittlement occurs when the steel is heated for prolonged periods in the temperature range 350 °C to 550 °C, or cooled slowly through it. The reason for the embrittlement is well established; impurities segregate into grain boundaries and reduce their strength. The impurities responsible are P, Sn, Sb, and As [Briant and Banerji, 1978]. Some elements like Mn and Ni promote impurities segregation by co-segregation [Joshi *et al.*, 1975; Mulford *et al.*, 1977]. Chromium promotes the segregation but does not itself enrich significantly in the grain boundaries [Mulford *et al.*, 1977]. Silicon is either classified as a embrittling element [Briant and Banerji, 1978] or as a cosegregating element like Mn and Ni [Olefjord, 1978]. Other elements are scavengers which can bind the impurities; these include Mo, Ti, V and W [Power, 1956; Ohtani *et al.*, 1976]. A 0.5wt.% Mo addition is suggested to be the most effective in preventing this kind of embrittlement [Power, 1956]. The mechanism by which Mo and Ti work is that they reduce the diffusivity of P by atomic association [Gruzin *et al.*, 1969]. Vanadium is believed to enhance the beneficial effect of Mo [Power, 1957].

1.2.2.2 Embrittlement by a Grain Boundary Phase

This type of embrittlement is due to the precipitation of particles along grain boundaries

[Briant and Banerji, 1978], producing preferred sites for void nucleation during fracture. These voids link and cause the crack to proceed along the grain boundary.

Appropriate particles can be carbides, AlN or MnS [Briant and Banerji, 1978], all of which occur in low alloy or maraging steels. The only way to avoid this embrittlement is to dissolve the precipitates by reheating and subsequently quenching rapidly enough to avoid reprecipitation during cooling.

1.2.2.3 Precipitation at Sub-Grain Boundaries

Apart from the inter-granular fracture described above, several kinds of trans-granular fracture result from the temper embrittlement of martensite and bainite. Tempered martensite embrittlement is caused by the precipitation of carbides at lath boundaries, at about 350 °C [Thomas, 1978]. Failure is distinctively trans-granular with respect to the prior austenite grains. The carbides assist in the nucleation of cracks, which then propagate into the matrix [Bhadeshia and Edmonds, 1983b]. Tempering at higher temperatures does not cause such fracture because the steel softens.

Tempering of bainite can have somewhat different outcomes. The tempering behaviour of upper and lower bainite has been reported by Johnson and Becker [1993]; lower bainite exhibits a much higher impact energy than upper bainite, because the carbide particles in upper bainite are usually coarser.

Another kind of temper embrittlement involves tempering high Si steel with a microstructure bainitic structure consisting of only bainitic ferrite and residual austenite, but without carbide precipitates [Bhadeshia and Edmonds, 1983a, b]. Prolonged tempering causes the decomposition of the austenite into a mixture of carbides and ferrite. The carbide particles enhance the nucleation rate of voids during “ductile” fracture. This results in a large reduction in the work of fracture even though the failure mode is ductile. A similar situation also occurs in a high Si bainitic cast iron [Dubensky and Rundamn, 1985].

1.2.3 Wear Performance

Ordinary rail steel usually contains about 0.7 wt.% of carbon, and gives an almost fully pearlitic microstructures during continuous cooling heat treatment from the austenite phase field. Bainitic steels have recently been investigated as candidate materials for rail applications in demanding situations [Callender, 1983; Heller *et al.*, 1982; Ichinose *et al.*, 1982; Kalousek *et al.*, 1987; Garnham *et al.*, 1992; Devanathan and Clayton, 1991; Clayton and Devanathan, 1991]. The first successful application was that of low carbon bainitic steels as railway crossings [Callender, 1983]. Their resistance to impact erosion and fatigue is superior to pearlitic

rail steel, and their increased weldability facilitates the joining process. However, many investigations [Heller *et al.*, 1982; Ichinose *et al.*, 1982; Kalousek *et al.*, 1987; Garnham *et al.*, 1992] into the likely performance of bainitic steels as railroad materials all concluded that pearlitic steel has superior wear resistance.

Heller *et al.* [1982] conducted some service trials with bainitic rail and found that they wore faster than conventional pearlitic steel, when the comparison was made at the same hardness level. Other work [Ichinose *et al.*, 1982] has revealed that a low carbon bainitic steel wore about ten times faster than a pearlitic steel of the same hardness in a rolling-sliding test, and Kalousek *et al.* [1987] confirmed the general trend. Garnham and Beynon [1992] demonstrated that carbide-free bainitic microstructures tend to be less wear resistant than the pearlitic counterparts. Although carbide containing bainitic steel has been found to show reasonable wear resistance, this is often achieved at considerable expense to the counter-material in the wear couple. It has therefore generally been concluded that bainitic steel is not suitable for rail applications.

Some of the results [Heller *et al.*, 1982; Ichinose *et al.*, 1992; Kalousek *et al.*, 1987] on bainitic steel investigations are dubious, since the studies did not involve a systematic investigation of the test conditions, and the microstructural characterizations were not sufficiently detailed [Clayton *et al.*, 1987]. Devanathan and Clayton [1992] recently demonstrated good wear resistance for bainitic steels, particularly at high contact pressures in rolling-sliding tests. This showed that a low carbon bainitic steel performed as well as a fully pearlitic steel of greater hardness, while it outperformed pearlitic steel of the same hardness level. This was attributed to the ability of the bainitic steel to work harden to a greater degree and its greater ductility compared with pearlitic steel.

Despite these contradictory results, a novel approach towards higher wear resistance and tougher rail steels has been based on carbide-free medium carbon bainitic alloys containing austenite and martensite. The origin of this is in the early research of [Bhadeshia and Edmonds, 1983a, b] where it was demonstrated that very strong and tough steels containing a high silicon concentration can be designed using phase transformation theory. Work done on this concept will be reported later in this thesis.

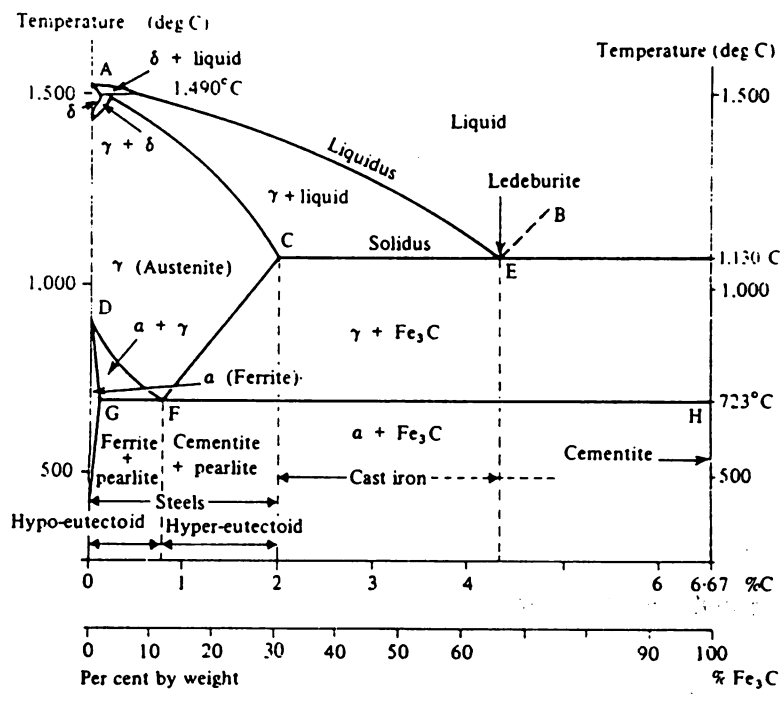


Fig. 1.1: The iron-carbon phase diagram (Anderson *et al.*, 1985).

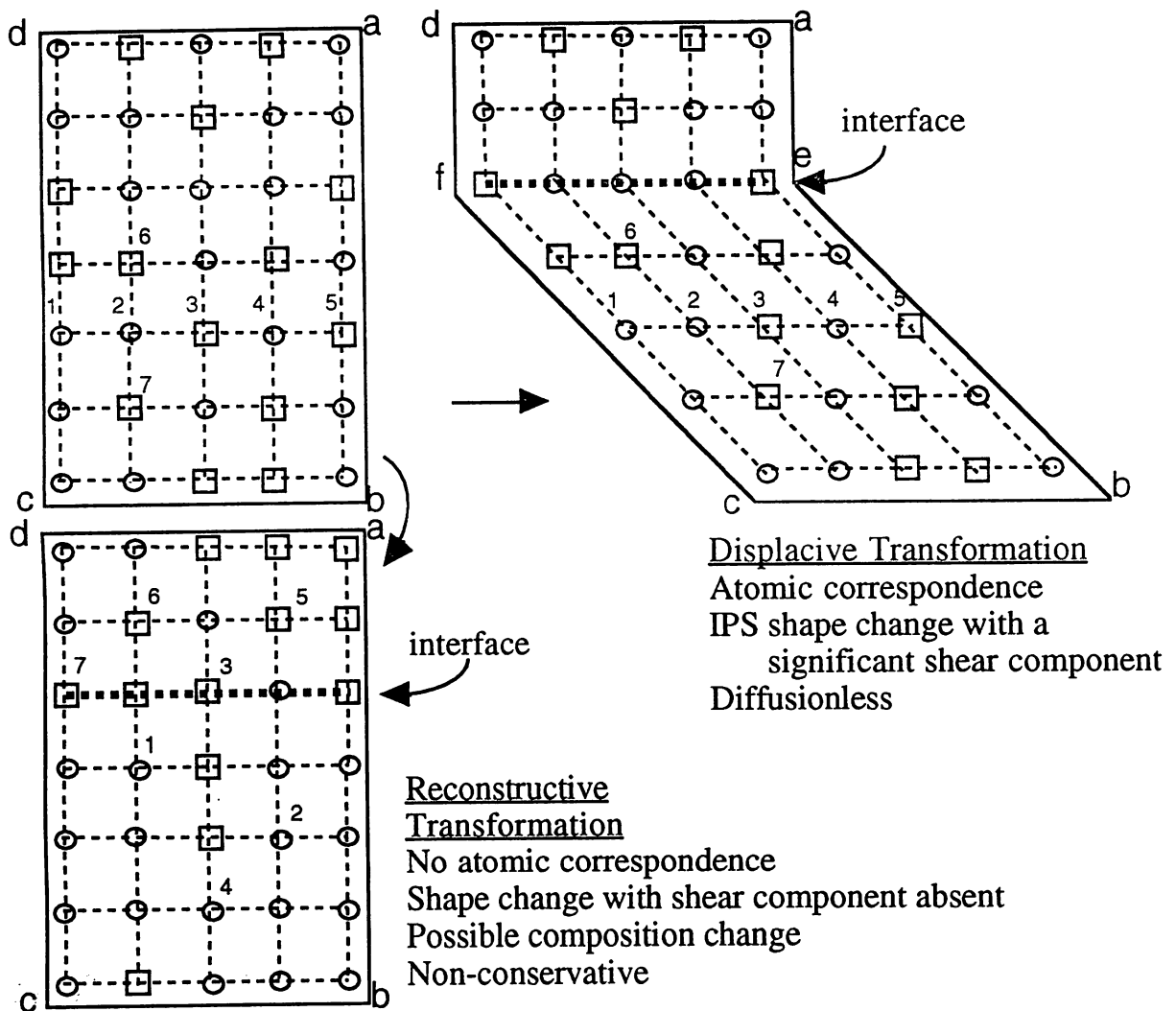


Fig. 1.2: Schematic illustration of the mechanisms of diffusional and shear transformations. The lines connect corresponding directions. (Bhadeshia, 1987).

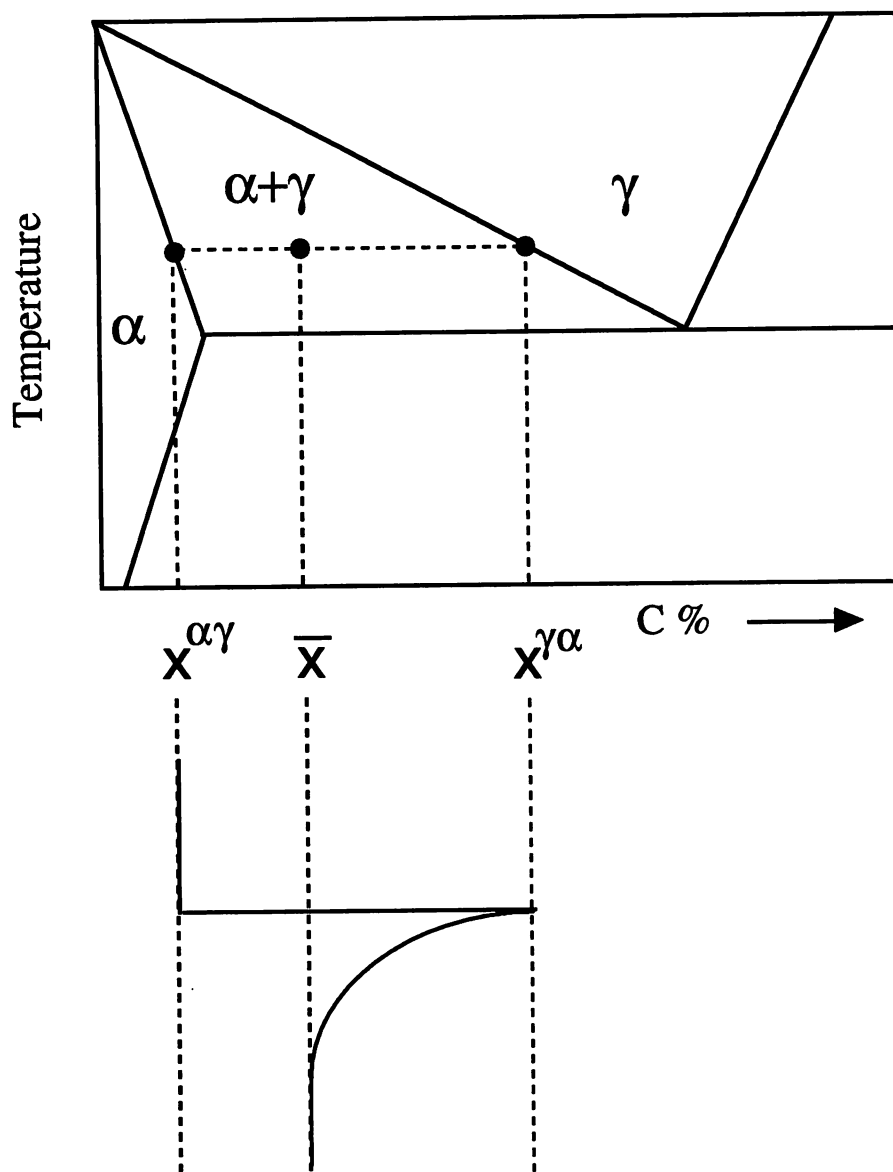
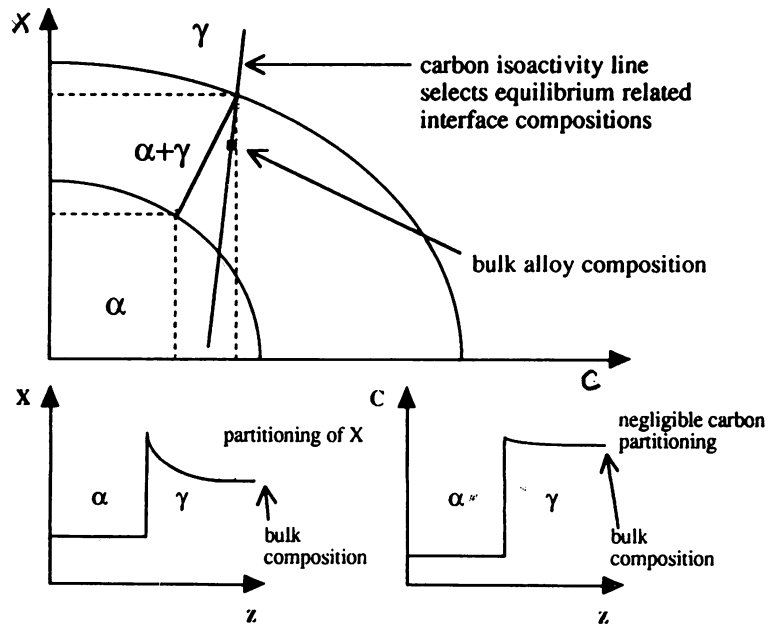


Fig. 1.3: Schematic illustration of the carbon profile expected in the vicinity of the interface for the allotriomorphic ferrite in the Fe-C system.

PLE



NPLE

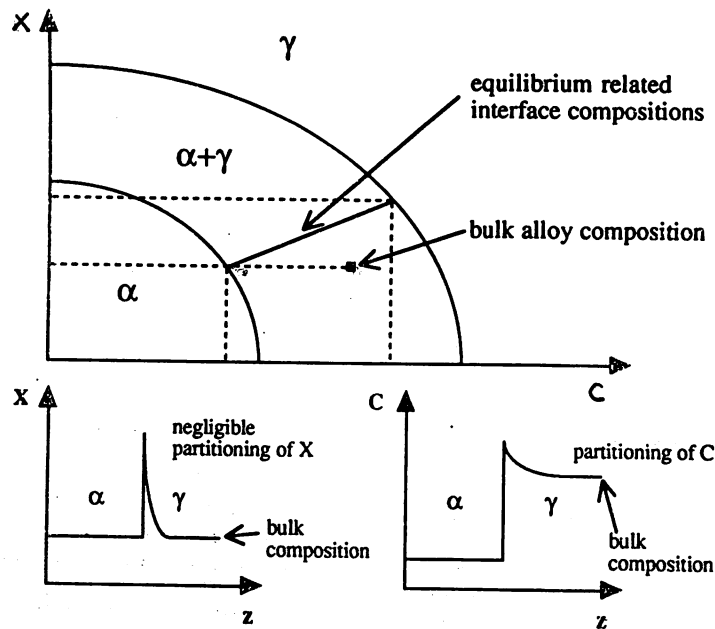


Fig. 1.4: Ternary Fe-C-X phase diagrams demonstrating the regimes in which PLE and NPLE transformations can occur, and the choice of interface compositions [Coates, 1973].

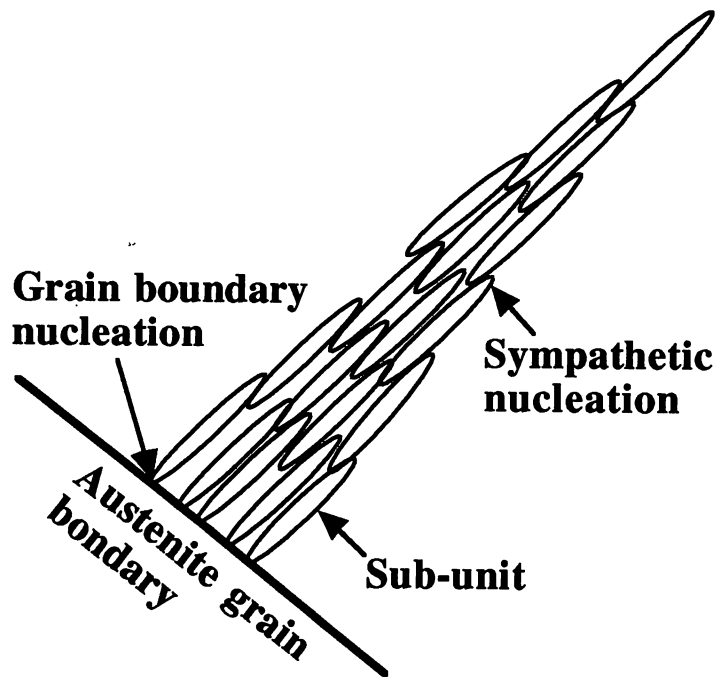


Fig. 1.5: Schematic illustration of a bainite sheaf.

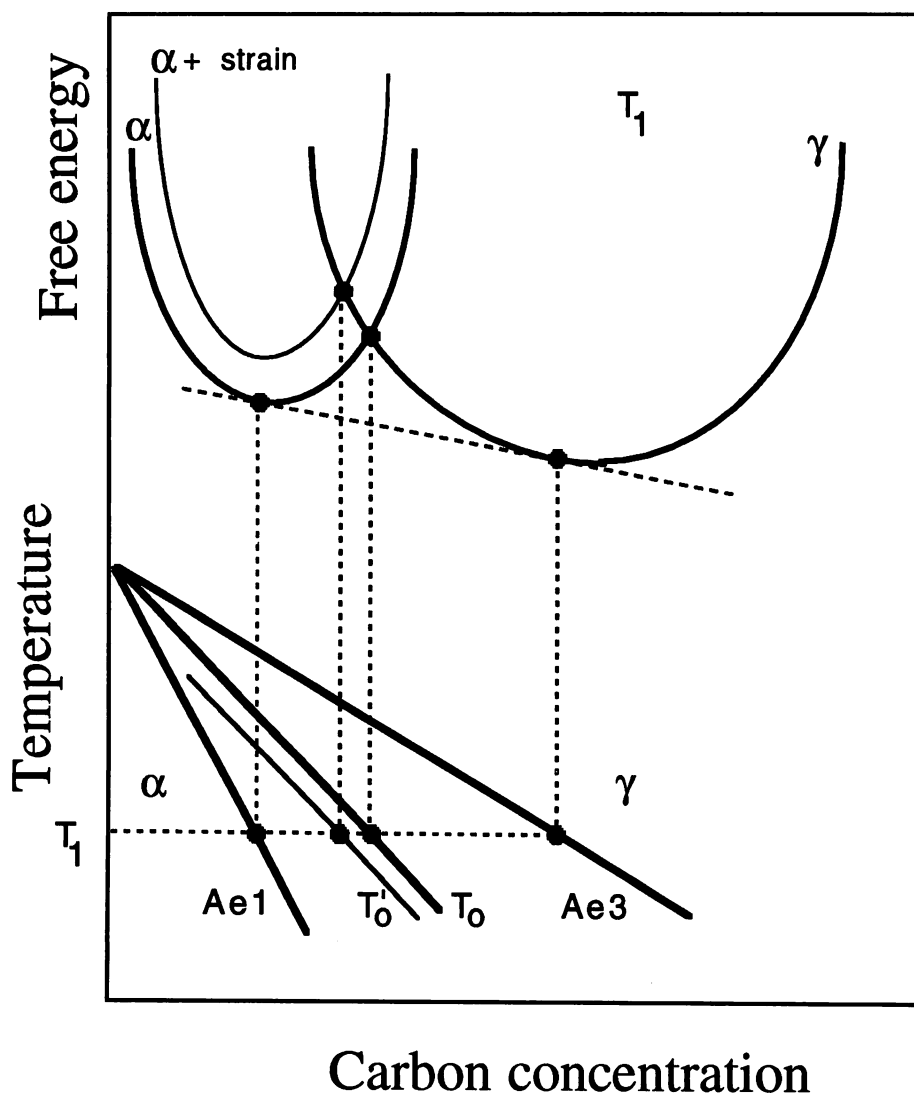


Fig. 1.6: Schematic illustration of the T_0 and T'_0 curves.

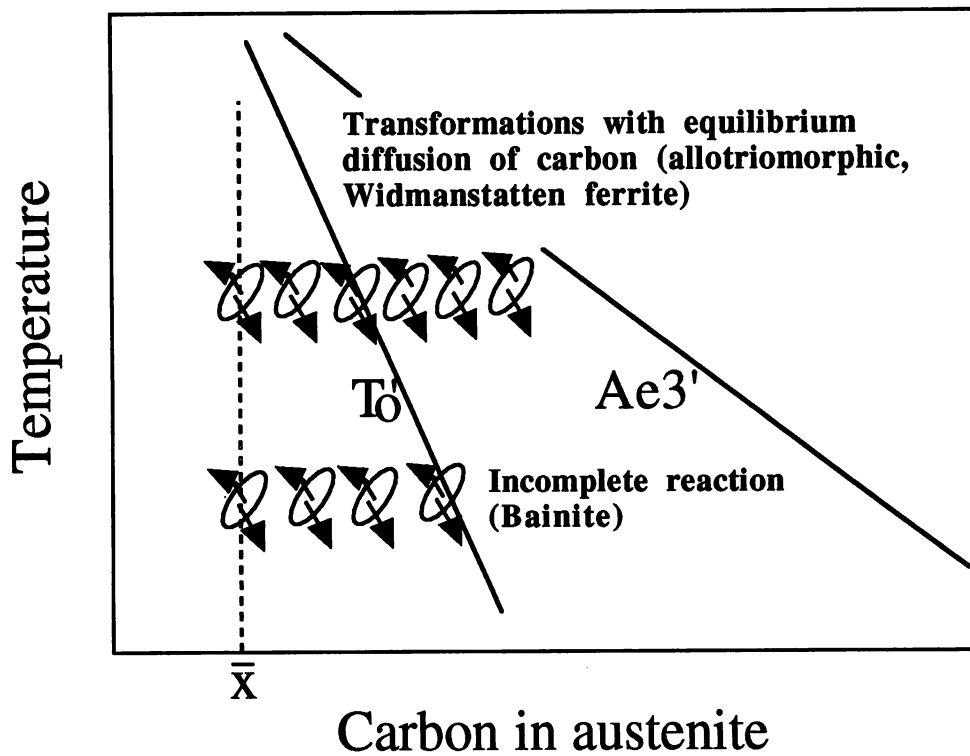


Fig. 1.7: Schematic illustration of the incomplete-reaction transformation (bainite) and transformation with equilibrium carbon partitioning ahead of the interface (allotriomorphic and Widmanstätten ferrite).

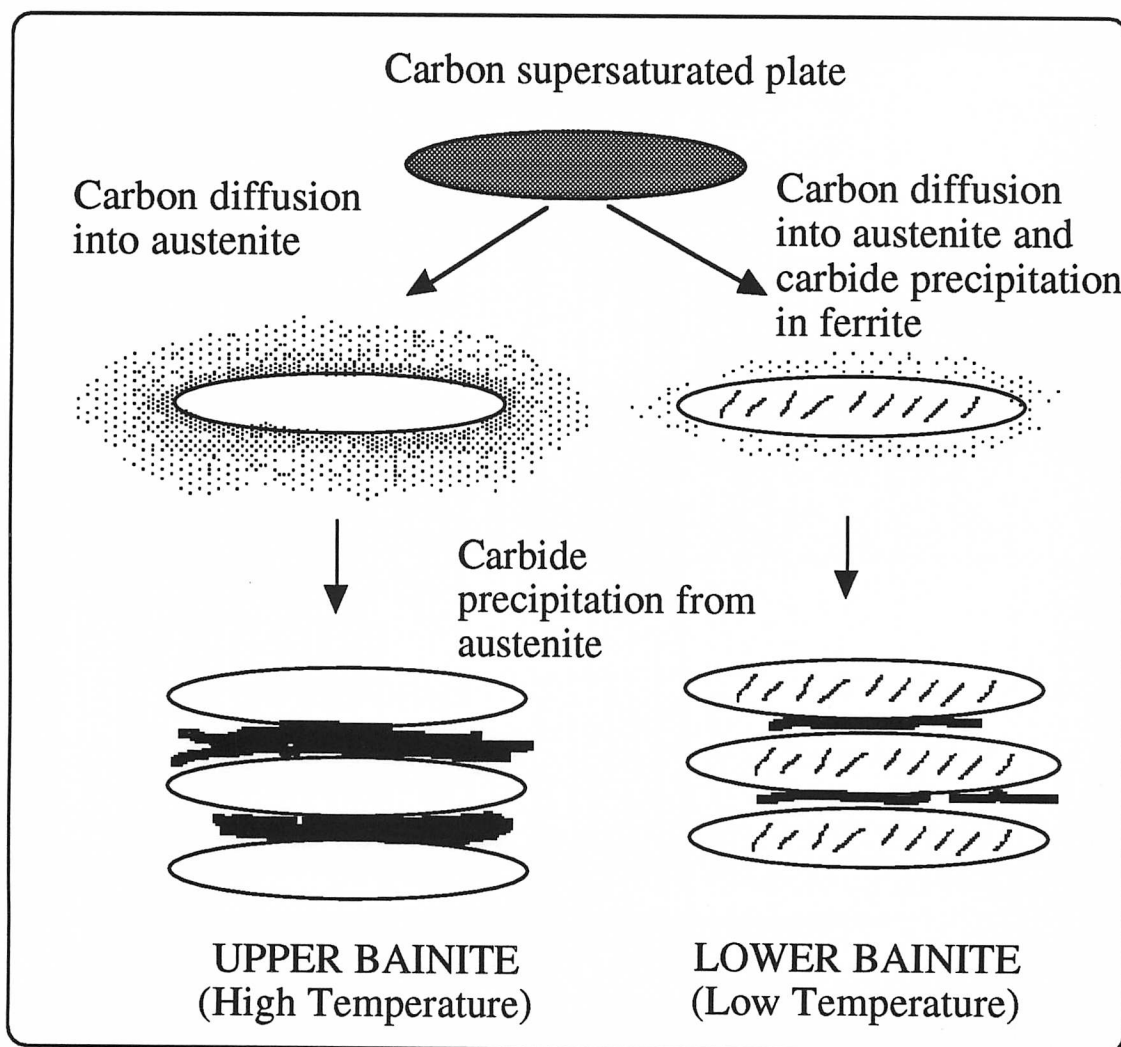


Fig. 1.8: Schematic illustration of the transition from upper to lower bainite (Takahashi and Bhadeshia, 1990).

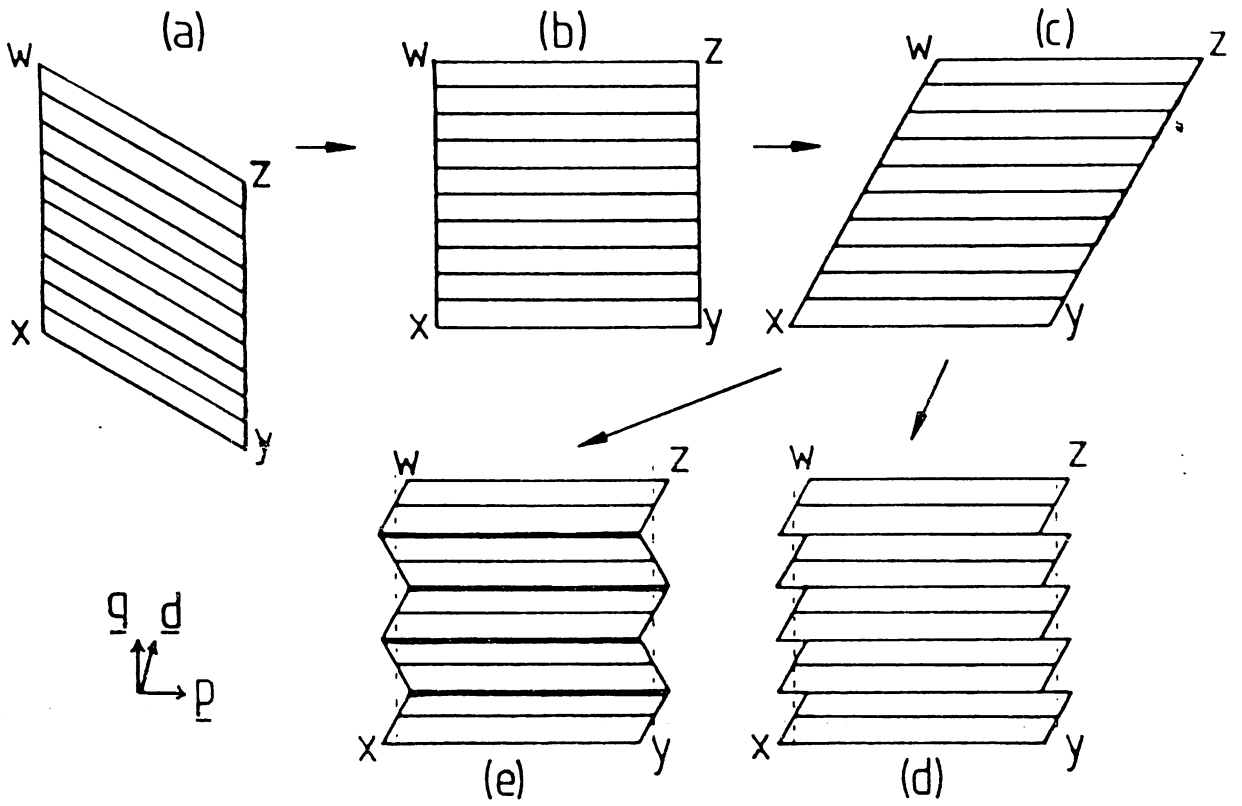
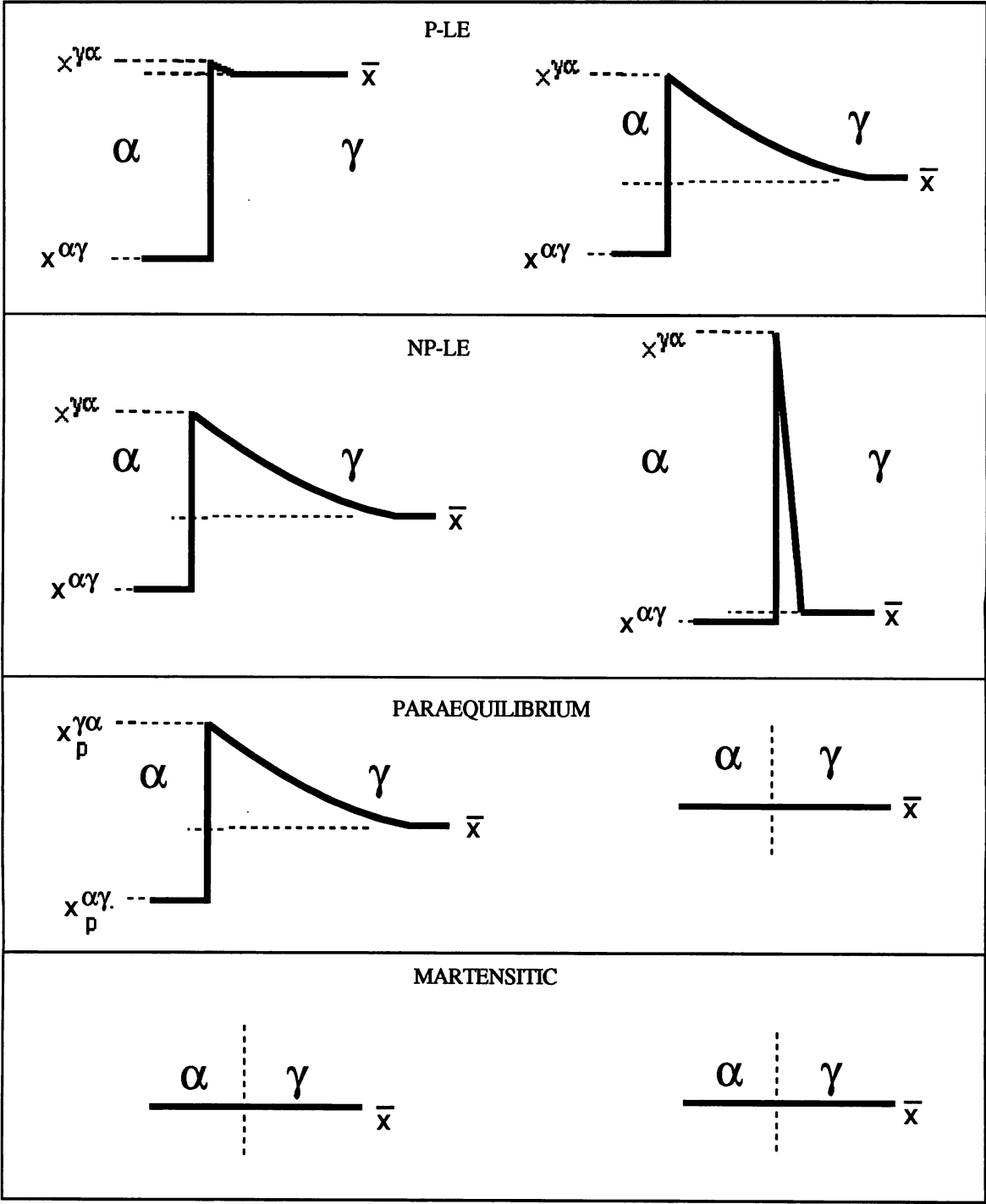


Fig. 1.9: Schematic illustration of the phenomenological theory of martensite. (a) represents the austenite crystal and (c), (d) and (e) all have a BCC structure. (b) has a structure between FCC and BCC, \underline{p} is the habit plane unit normal and \underline{q} is the unit normal to the plane on which the lattice-invariant shear occurs. The heavy horizontal lines in (e) are coherent twin boundaries [Bhadeshia, 1987].



CARBON

SUBSTITUTIONAL SOLUTE

Fig. 1.10: Schematic illustration of the composition variations expected in the vicinity of the transformation interface, for a variety of growth mechanisms (Bhadeshia, 1992).

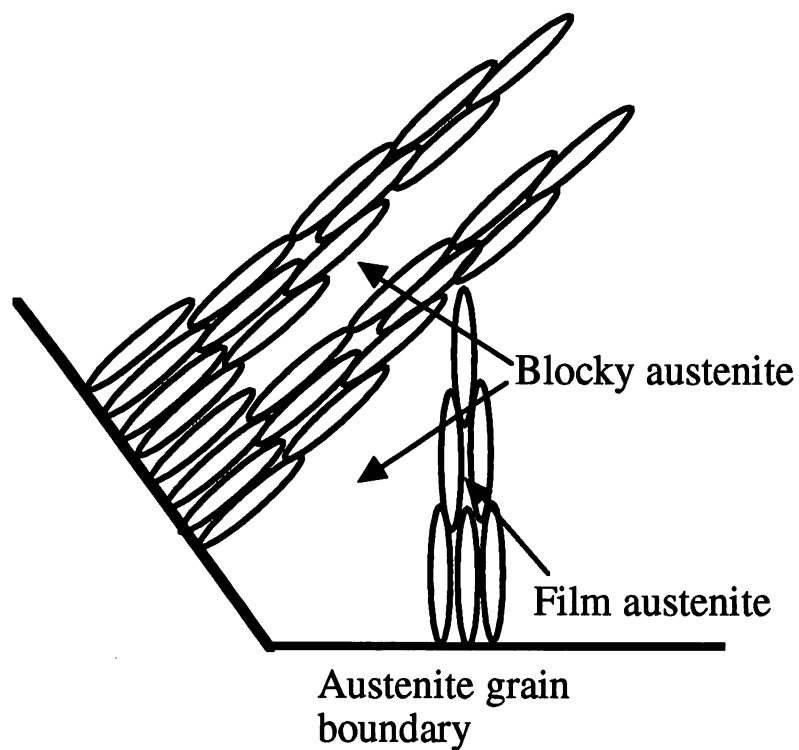


Fig. 1.11: Schematic illustration of the film austenite and blocky austenite. Film austenite occurs between ferrite sub-units while austenite remains untransformed between bainite sheaves is called blocky austenite.

CHAPTER 2

GENERAL EXPERIMENTAL TECHNIQUES

2.1 ALLOYS

The alloys used were rail steels designed in Cambridge and manufactured at British Steel. The alloys were made as 50 kg vacuum melted ingots, approximately 125×125 mm in cross-section, and forged into billet/slabs approximately 100×50 mm in cross-section. They were then reheated in a furnace set at a temperature of 1200°C and control-rolled down into approximately 15 mm thick plates in 8 or 10 passes. After the last pass, the plates were cooled down to 900°C before entering a water quenching unit.

The chemical compositions of eight of the main experimental alloys used in this study are listed in Table 2.1. Some further alloys were prepared for wear and temper embrittlement studies; their chemical compositions are presented in the appropriate chapter.

Table 2.1: Chemical compositions of the experimental alloys (wt.%).

Alloy	C	Si	Mn	Ni	Cr	P	S	N
A	0.27	1.98	2.18	0.02	1.9	0.015	0.012	0.0054
B	0.27	2.01	2.16	2.07	-	0.015	0.011	0.0049
C	0.46	2.10	2.15	0.02	-	0.014	0.013	0.0062
D	0.44	2.13	2.14	0.02	0.5	0.014	0.011	0.0079
E	0.10	1.77	2.12	2.0	0.02	0.013	0.012	0.0053
F	0.26	1.85	2.10	0.02	-	0.015	0.013	0.0086
G	0.26	1.93	2.04	0.02	1.02	0.015	0.010	0.0069
H	0.01	1.63	1.99	0.03	1.97	0.013	0.011	0.0080

All the alloys contain about 2 wt.% of silicon and manganese, with various carbon, nickel and chromium concentrations. The importance of silicon is that it inhibits the formation of cementite, which is detrimental to the mechanical properties. The addition of manganese helps to stabilize the untransformed austenite, and also to impart sufficient hardenability for heat treatment. Nickel has a similar effect as manganese but also improves toughness, while chromium and nickel are both added to increase the hardenability.

2.2 SAMPLE PREPARATION AND HEAT TREATMENT

The samples were first machined into 10 mm diameter rods, sealed in quartz tubes containing argon and then given a homogenisation heat-treatment at 1300 °C for three days, followed by furnace cooling to room temperature. Samples were machined from the homogenised specimens into cylindrical shapes, each of 8 mm diameter and 12 mm length. To ensure rapid cooling, each cylinder was drilled to give a 3 mm diameter longitudinal hole. The specimens were then nickel-plated using a two-stage procedure, striking and plating. The striking process used a solution consisting of 250 g nickel sulphate, 27 ml concentrated sulphuric acid in a litre of distilled water, at 50 °C for 3 min at a current density of 7.7 mA mm⁻². The plating was carried out at 50 °C for 15 min at a current density of 0.4 mA mm⁻² in an electrolyte containing 140 g nickel sulphate, 15 g ammonium chloride, 20 g boric acid in a litre of distilled water.

2.3 DILATOMETRY

Dilatometric studies can provide information on transformations as they happen. The studies were performed in a *Thermecmastor* thermo-mechanical simulator equipped to simultaneously monitor and record the diametrical and longitudinal length changes (strain), time, temperature and load data. The change in diameter is detected by laser interferometry, while the longitudinal dimensions are followed via the movement of the upper crosshead or with the help of a length transducer. This simulator is fully automatic and programmable. The specimen was heated using a radio-frequency coil and the temperature was measured with a Pt/Pt-10%Rh thermocouple spot welded to the sample. The temperature variation along the length of the sample was checked to be within 4-5 °C.

Both partial and fully transformed specimens were studied in order to reveal the early stages of transformation, and to establish the maximum extent of transformation possible at any temperature respectively.

The setup of the sample is illustrated schematically in Fig. 2.1. In a typical heat treatment cycle, the sample is first heated to 1000 °C for 10 minutes under vacuum for austenization, and then force-quenched with nitrogen or helium jets to a designated temperature below the bainite-start temperature (B_s) but above the martensite-start temperature (M_s). The volume change associated with a phase transformation can be obtained from the recorded dimensional changes, which over the temperature region of interest can provide information about the reaction kinetics. The following method is used for the calculation of the volume fraction of ferrite transformed as a function of time during isothermal transformation, when carbides do

not precipitate during the formation of ferrite [Bhadeshia, 1982a]:

$$\frac{\delta l}{l} = \frac{2Va_\alpha^3 + (1-V)a_{e\gamma}^3 - a_\gamma^3}{3a_\gamma^3} \quad (2.1)$$

where $\frac{\delta l}{l}$ is the relative length change due to transformation. V is the volume fraction of ferrite. a_α is the lattice parameter of ferrite given by,

$$a_\alpha = \bar{a}_\alpha[1 + e_\alpha(T - 298)] \quad (2.2)$$

where T is the absolute temperature, \bar{a}_α is the ferrite lattice parameter at ambient temperature (298 K), and e_α is the linear thermal expansivity of ferrite. The effect of alloying elements on the lattice parameter of pure iron was estimated as follows [Hume-Rothery *et al.*, 1942; Leslie, 1982; Bhadeshia *et al.*, 1991];

$$\begin{aligned} \bar{a}_\alpha = a_\alpha^o + (3a_\alpha^{o2})^{-1} \times [(x_c^\alpha - 0.0279x_c^\alpha)^2(x_c^\alpha + 0.2496x_c^\alpha) - (x_c^\alpha)^3] - 0.003x_{Si}^\alpha \\ + 0.006x_{Mn}^\alpha + 0.007x_{Ni}^\alpha + 0.031x_{Mo}^\alpha + 0.005x_{Cr}^\alpha + 0.0096x_V^\alpha \text{ nm} \end{aligned} \quad (2.3)$$

where x_i^α represents the mole fraction of the species i in phase α . Substitution of the appropriate concentrations (the amount of carbon in bainitic ferrite was assumed to be 0.03 wt.%, equivalent to $x_c^\alpha=0.00139$) and taking the lattice parameter of pure iron to be $a_\alpha^o=0.28664$ nm [X-ray Powder Data File, 1955] permits the estimation of \bar{a}_α .

a_γ is the lattice parameter of austenite before transformation, *i.e.*, when $V = 0$. It is given by,

$$a_\gamma = \bar{a}_\gamma[1 + e_\gamma(T - 298)] \quad (2.4)$$

where \bar{a}_γ is the lattice parameter of austenite at ambient temperature and e_γ is the thermal expansion coefficient of austenite. \bar{a}_γ (in nm) can be estimated using the following equation [Dyson and Holmes, 1970];

$$\begin{aligned} \bar{a}_\gamma = a_\gamma^o + 0.33x_c^\gamma + 0.0095x_{Mn}^\gamma - 0.002x_{Ni}^\gamma \\ + 0.006x_{Cr}^\gamma + 0.031x_{Mo}^\gamma + 0.018x_V^\gamma \text{ nm} \end{aligned} \quad (2.5)$$

where a_γ^o is the lattice parameter of unalloyed austenite, $a_\gamma^o=0.3537$ nm, the subscript i defines a solute element in the alloy and w_i is the weight fraction of component i in phase γ . The carbon content (x_c^γ) is equal to the mean carbon concentration of the alloy (\bar{x}_c).

$\bar{a}_{e\gamma}$ is the lattice parameter of austenite which is enriched in carbon as a consequence of ferrite formation. The expression for the $\bar{a}_{e\gamma}$ is identical to that of \bar{a}_γ described above, except for the carbon concentration. The carbon concentration for calculation of $\bar{a}_{e\gamma}$ is calculated using mass balance [Bhadeshia and Edmonds, 1980];

$$x_\gamma = \frac{\bar{x}_c - Vs}{1 - V} \quad (2.6)$$

where x_γ is the carbon concentration of the retained austenite and s is the content of carbon in the ferrite, taken to be 0.03 wt.%.

2.4 EXPANSIVITY MEASUREMENTS

The expansion coefficient data necessary for the interpretation of the dilatometric results were determined over the temperature range 250–600 °C for ferrite and 800–950 °C for austenite respectively, at a heating rate of 5 °C min⁻¹. To determine e_α , the specimens were first annealed at 600 °C for 2 hours before measuring, in order to induce the thermal decomposition of any austenite, and thus ensure an essentially ferritic microstructure. The expansion coefficients were found to be constant over the temperature ranges studied, as indicated by correlation coefficients greater than 0.99 when the length change versus temperature data were subjected to linear regression analysis. A typical set of data is illustrated in Fig. 2.2, and the data as measured for all the experimental alloys are listed in Table 2.2. The error terms represent the standard deviation from the best fit line.

Table 2.2: The measured linear thermal expansion coefficients (°C⁻¹).

Alloy	e_α	e_γ
A	$1.537 \times 10^{-5} \pm 8 \times 10^{-9}$	$2.467 \times 10^{-5} \pm 5 \times 10^{-8}$
B	$1.472 \times 10^{-5} \pm 6 \times 10^{-9}$	$2.801 \times 10^{-5} \pm 3 \times 10^{-8}$
C	$1.693 \times 10^{-5} \pm 1 \times 10^{-7}$	$2.466 \times 10^{-5} \pm 5 \times 10^{-8}$
D	$1.261 \times 10^{-5} \pm 3 \times 10^{-8}$	$2.064 \times 10^{-5} \pm 4 \times 10^{-8}$
E	$1.597 \times 10^{-5} \pm 8 \times 10^{-9}$	$1.923 \times 10^{-5} \pm 9 \times 10^{-8}$
F	$1.617 \times 10^{-5} \pm 2 \times 10^{-8}$	$2.164 \times 10^{-5} \pm 2 \times 10^{-7}$
G	$1.686 \times 10^{-5} \pm 4 \times 10^{-8}$	$2.493 \times 10^{-5} \pm 1 \times 10^{-7}$
H	$1.553 \times 10^{-5} \pm 2 \times 10^{-8}$	$1.922 \times 10^{-5} \pm 2 \times 10^{-7}$

2.5 CALCULATION OF M_S AND B_S TEMPERATURES

The transformation-start temperatures are important in the design of alloys and heat-treatments. They were calculated using a method due to Bhadeshia [1982b], and are listed in Table 2.3.

Table 2.3: Calculated M_S and B_S temperatures (°C).

Alloy	M_S	B_S
A	306	380
B	309	380
C	258	380
D	256	380
E	390	480
F	362	500
G	340	440
H	400	526

2.6 METALLOGRAPHY

2.6.1 Transmission Electron Microscopy

The procedure for thin foil sample preparation for transmission electron microscopy studies was as follows. After slicing 8 mm diameter rods into thin discs of 0.3 mm thickness, the discs were thinned down to 60-80 μm by abrasion using SiC coated grinding paper, and then eletropolished in a twin-jet polishing unit using an electrolyte consisting of a mixture of 5 % perchloric acid, 25 % glycerol and 70 % ethyl alcohol. The polishing potential was 55 V at a current of 20-30 mA, the electrolyte temperature range being -5 to -10 °C. The thin foils were examined using a Philips EM-400ST transmission electron microscope operated at 120 kV.

2.6.2 Scanning Electron Microscopy

Some metallographic investigation was carried out using scanning electron microscopy. The samples were ground, polished down to 1 μm and then etched in 2% nital, finally imaged in a Camscan 200 scanning electron microscope operated at 20 kV.

2.6.3 Optical Microscopy

The specimens were prepared for optical microscopy by mounting in conductive Bakelite and then grinding to 120 grit and polishing to 1 μm cloth. 2% nital (concentrated nitric acid in methanol) was used to etch the samples.

2.7 MECHANICAL TESTS

2.7.1 Tensile Tests

The tests were conducted at room temperature using a 200 kN Meyes tensile testing machine with specimen dimensions of 7.98 mm diameter and 40 mm gauge length. A strain rate of $2.08 \times 10^{-4} \text{ s}^{-1}$ (equivalent to a crosshead velocity of the tensile machine of 0.5 mm min^{-1}) was employed throughout the duration of the test. The 0.2% proof stress was measured by monitoring the strain using a 25 mm extensometer set at a magnification of 760:1.

2.7.2 Charpy Impact Tests

A number of standard Charpy V-notch impact specimens for the experimental alloys were tested at room temperature as well as other temperature.

2.7.3 Hardness tests

Hardness tests during the course of the current work were carried using a standard Vickers diamond pyramid hardness testing machine. A load of 30 kg was employed in each case and a mean of at least five suitably spaced hardness impressions was obtained.

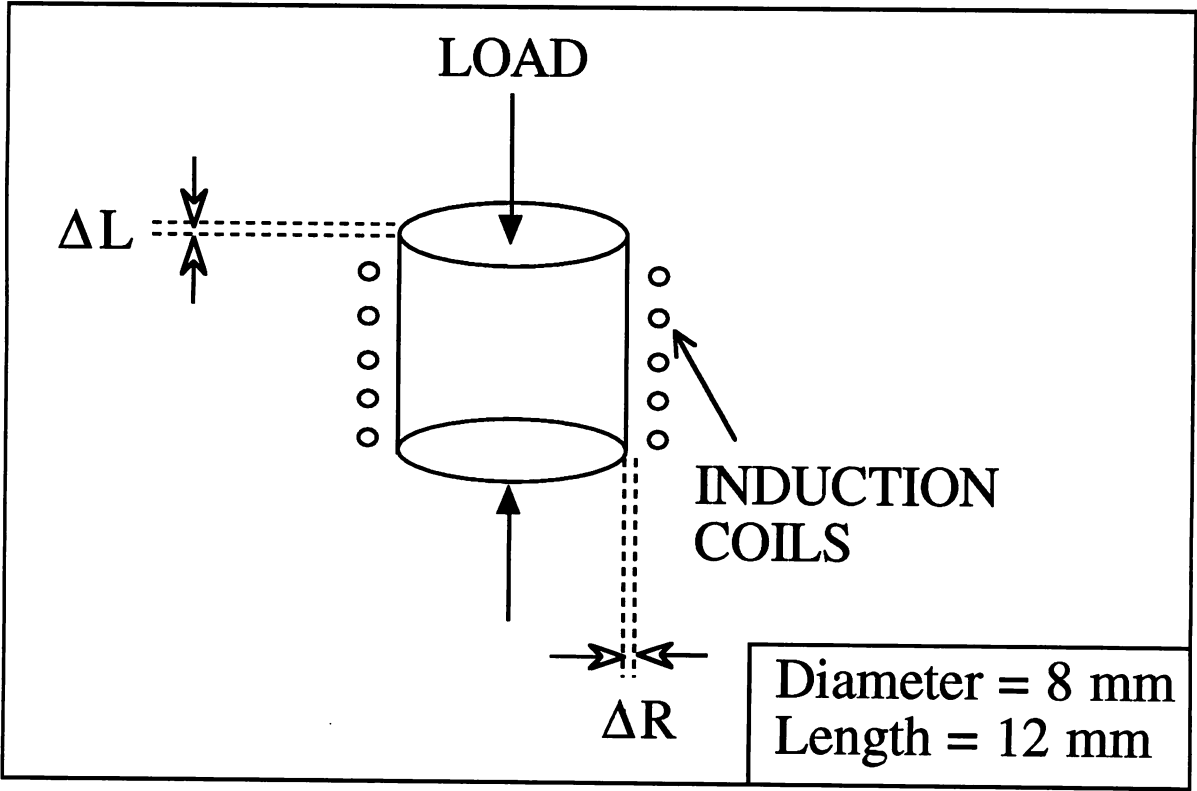
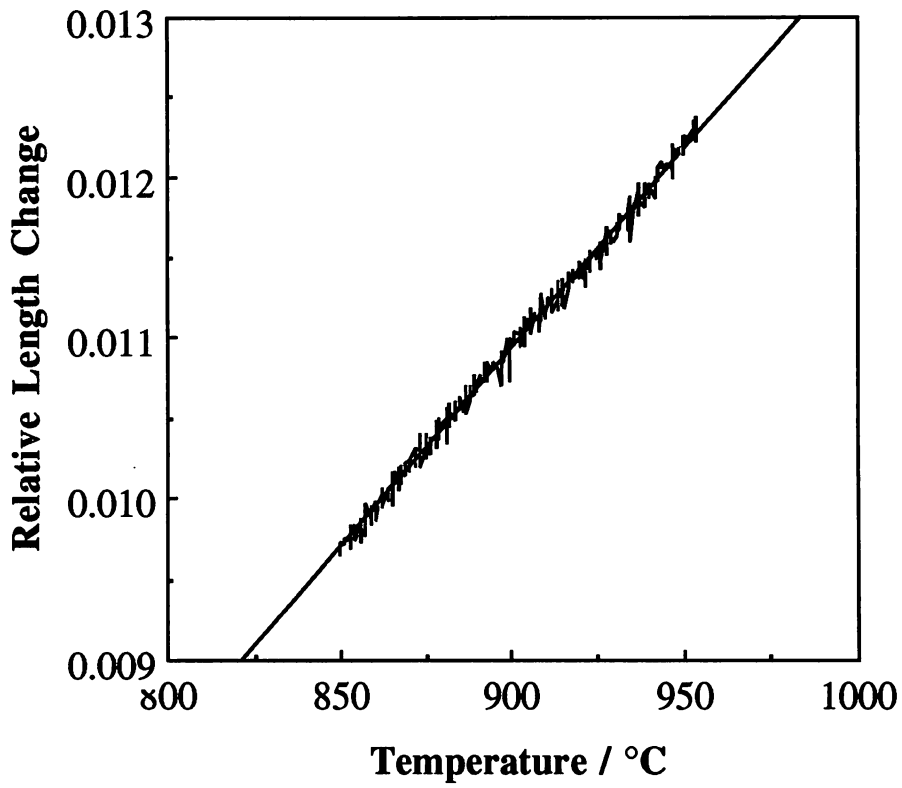
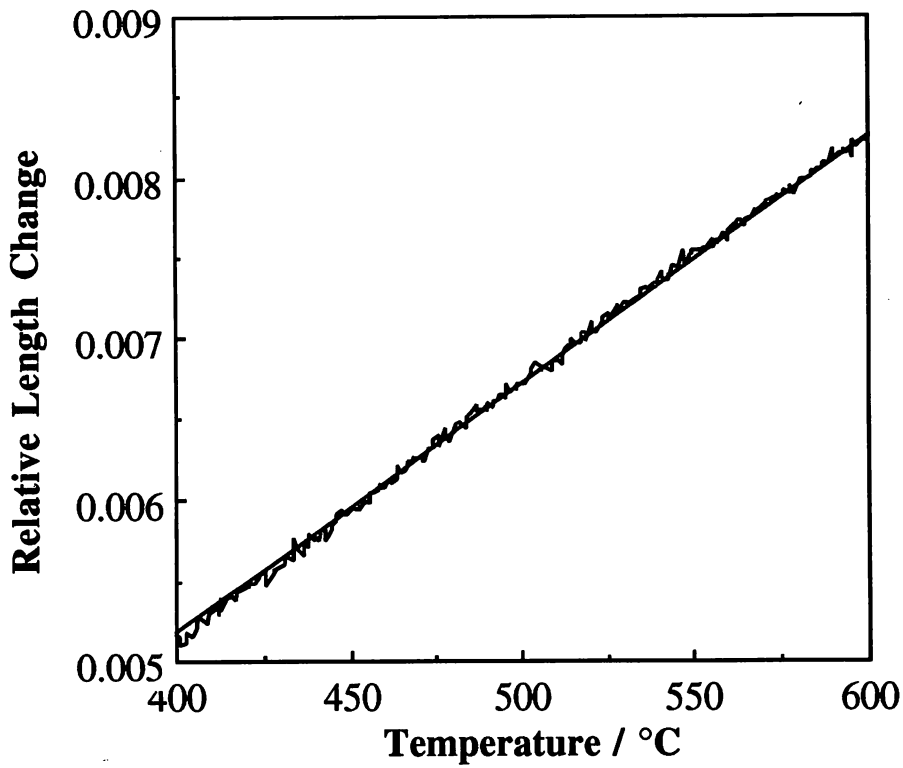


Fig. 2.1: Schematic illustration of the specimen arrangement in the *Thermecmaster* thermo-mechanical simulator.



(a)



(b)

Fig. 2.2: Typical data measured for (a) austenite (b) ferrite linear thermal expansion coefficients (Alloy A). The straight lines are best-fit lines.

CHAPTER 3

MICROSTRUCTURE AND KINETICS OF THE BAINITE TRANSFORMATION IN Si-RICH STEELS

3.1 INTRODUCTION

The literature review presented in Chapter 2 describes briefly what is known about the mechanism of the bainite transformation. It is likely that bainite grows without diffusion, but because of the relatively high transformation temperatures involved, the excess carbon is partitioned into the residual austenite [Bhadeshia and Edmonds, 1979a; Bhadeshia and Christian, 1990]. If the steel contains a sufficient quantity of silicon, then the carbon remains in, and stabilizes the austenite [Philip, 1983]. Consequently, large quantities of the austenite might be retained to ambient temperature, with some transforming to high-carbon martensite [Bhadeshia and Edmonds, 1983a; Sandvik, 1982a].

If the transformation temperature is such that the carbon cannot partition rapidly, then some of the excess carbon in the supersaturated ferrite might precipitate in the form of carbides, in which case a lower bainitic microstructure is obtained [Takahashi and Bhadeshia, 1990].

For both upper and lower bainite, the platelets (sub-units) of ferrite grow to a limited size before their growth becomes stifled by the plastic accommodation debris associated with the yielding of austenite at high temperatures (caused by the invariant-plane strain shape deformation as bainite grows) [Bhadeshia and Edmonds, 1980]. Thus, transformation propagates by the successive nucleation of sub-units, which grow in clusters called *sheaves*.

The purpose of the work presented here was to characterize the transformation behaviour of a series of experimental steels. This is to give confidence in what is believed to be the mechanism of bainitic transformation, but the characterisation was also necessary for the interpretation of properties presented in the remainder of the thesis.

3.2 EXPERIMENTAL

All the eight alloys, described in Chapter 2, contained sufficient silicon to suppress the precipitation of cementite from the carbon-enriched retained austenite. The steels were also designed to have a high hardenability; they all contained about 2 wt.% of manganese. Finally, there were systematic variations in the nickel and chromium concentrations as well.

3.3 METALLOGRAPHY

Fig. 3.1 shows the optical microstructures obtained following the isothermal transformation of Alloy C at a series of temperatures. As will be seen in the section dealing with kinetic analysis, the isothermal transformation time was always long enough for the formation of bainite to stop. At the highest transformation temperatures (480, 500 °C) there is some pearlite which forms at the austenite grain boundaries (dark-etching phase). The micrographs, which are in general representative of all alloys, show that the degree of bainitic transformation increases as the transformation temperature is reduced. This is expected because of the negative slope of the T'_0 boundary on the temperature versus carbon concentration plot. This means that the austenite can tolerate more carbon before diffusionless transformation becomes impossible and bainite growth ceases.

A typical transmission electron micrograph of an upper bainitic microstructure in Alloy C is illustrated in Fig. 3.2. It consists of sheaves in which the sub-units are separated by films of austenite. Lower bainite was found in Alloy C for transformation below 305 °C, and a typical transmission electron micrograph is shown in Fig. 3.3. It is interesting that the lower bainite sheaf also consists of sub-units, with the single-variant of cementite. However, consistent with previous work [Srinivasan and Wayman, 1968; Lai, 1975; Bhadeshia and Edmonds, 1979a], there were many occasions when several variants of cementite precipitation could be seen in the lower bainite (Fig. 3.4). The carbides precipitated in all the alloys examined are identified as cementite by using selected area diffraction (SAD); a typical SAD pattern is shown in Fig. 3.4. This aspect is addressed in detail in Chapter 7. An interesting micrograph of individual, isolated lower bainite sub-units in Alloy C is shown in Fig. 3.5 – carbide precipitation is visible within these sub-units.

As pointed out earlier, all of the features reported for Alloy C could also be found for the other alloys. However, the scale of the sub-units depended on the transformation temperature. This is illustrated in Fig. 3.6 where the measured sub-unit widths, corrected for stereological effects, are plotted as a function of the transformation temperature. The results are consistent with the general trends reported elsewhere. Fig. 3.7 shows a comparison against published data by Ohmori *et al.* [1971] and Sandvik *et al.* [1981]. There are obviously deviations between the different data, but it should be noted that the published data are not corrected for stereological effects, and the details of the way in which the measurements were carried out are not available. The general trend, that the sub-unit size increases as the transformation temperature increases is true for all the data.

It is unfortunate that the size of sub-units cannot as yet be predicted. The size must depend on the extent to which the shape deformation accompanying the growth of bainitic ferrite is plastically accommodated. This might be expected to increase with transformation temperature since the yield strength of the austenite and ferrite decreases with increasing temperature. Thus, contrary to the experimental observations, the sub-unit size should decrease as the transformation temperature is raised. Another possibility is that the rate of nucleation is large at low temperatures, so that adjacent sub-units are stifled in their thickness direction by impingement. This would be consistent with the observed trend. This model should introduce a significant alloying element effect as well the temperature effect, since the driving force for transformation (and hence the nucleation rate) can be influenced by alloying.

Finally, the very high grain boundary nucleation rates that might occur at large undercoolings below the bainite-start temperature have been proposed as an explanation for the occurrence of “grain boundary lower bainite” [Bhadeshia and Edmonds, 1979a]. This consists of numerous adjacently nucleated sub-units in tight clusters, growing at a common (serrated) front. Such bainite has indeed been observed in the present work as well, as illustrated in Fig. 3.8.

3.4 KINETICS

Fig. 3.9 shows the measured isothermal transformation curves for all the experimental alloys listed in Table 1. The volume fraction of bainite was obtained directly from the dilatometric data using a procedure described elsewhere [Bhadeshia, 1982a], as described in Chapter 2.

The isothermal transformation curves presented in Fig. 3.9 mostly show the expected behaviour, in that the degree of transformation increases with undercooling below the bainite-start temperature.

However, it is particularly noticeable that the curves for the lowest of transformation temperatures are not well-behaved, in the sense that they sometimes cross each other. This kind of behaviour might be attributed to the transition from upper to lower bainite, which is not accounted for in the conversion of the observed length change into volume fraction using the analysis of dilatometric data presented earlier. This is because the exact fraction of carbide precipitation in lower bainite is not known.

If the lower bainitic data are excluded, then it is possible to subject the kinetic measurements to further analysis using a recent theory due to Rees and Bhadeshia [1992a]. It can be explained as follows:

The expression for the nucleation rate of bainite is shown to be

$$I = K_1 \exp \left\{ -\frac{K_2}{RT} - \frac{K_2 \Delta G_m}{rRT} \right\} \quad (3.1)$$

where K_1 and K_2 are constants and ΔG_m is the maximum possible free energy change on nucleation. This expression is consistent with the activation energy for nucleation being directly proportional to ΔG_m [Bhadeshia, 1982c]. K_1 implicitly contains the number density of potential sites for nucleation as discussed later. According to Bhadeshia [1981a], bainite and Widmanstätten ferrite nucleate by the same mechanism, but it is the thermodynamic conditions which exist during growth which determine whether a nucleus develops into bainite or Widmanstätten ferrite. At the Widmanstätten-start temperature (W_s) the expression given in equation (3.1) becomes

$$I = K_1 \quad (3.2)$$

regardless of the alloy composition.

As transformation proceeds it becomes necessary to account for the decrease in driving force due to the carbon-enrichment of untransformed austenite. The effect of auto-catalysis also becomes important. As mentioned above, the formation of bainite can only occur when the thermodynamic criteria for both nucleation and growth are satisfied. At the onset of transformation the criterion for nucleation is that

$$\Delta G_m < G_N \quad (3.3)$$

and the growth criterion is that the driving force for transformation without a composition change exceeds the stored energy of bainite:

$$\Delta G^{\gamma\alpha} < -400 \text{ J mol}^{-1} \quad (3.4)$$

This last expression defines the T'_0 curve, but both the nucleation and growth criteria must be satisfied during transformation. As the austenite carbon concentration increases during transformation, the magnitude of both ΔG_m and $\Delta G^{\gamma\alpha}$ will decrease. Eventually the reaction will cease when one criterion is not satisfied. The value of θ , the maximum allowable volume fraction at the reaction temperature, is taken as the ferrite volume fraction when reaction ceases, regardless of whether termination is by a failure of the nucleation or the growth criterion.

Let x_{N_0} represents the austenite carbon concentration when the nucleation criterion fails and $x_{T'_0}$ when the growth criterion fails. If the driving force is assumed to vary linearly with

the extent of reaction, between its initial value ΔG_m^0 and its final value when the reaction terminates, then

$$\Delta G_m = \Delta G_m^0 - \xi(\Delta G_m^0 - G_N) \quad (3.5)$$

where ξ is the normalized volume fraction of bainite. ξ is defined as $\xi = v/\theta$, v is the actual volume fraction of bainitic ferrite. The equation (3.5) is inaccurate when $x_{N_0} > x_{T_0'}$, but this is not a significant problem since the model also includes a growth criterion in which reaction ceases when the fraction θ is achieved. The form of the equation has the additional advantage in that the linear function of ξ preserves the ability to integrate the final differential equation representing the overall transformation kinetics analytically.

Steels with a high carbon concentration eject more carbon from the newly transformed ferrite than lower carbon steels. The build up of carbon at the ferrite-austenite interfaces will cause a temporary local decrease in the driving force for diffusionless transformation. The process of further nucleation on the previously formed plates (*i.e.* autocatalysis) will be inhibited by this carbon build up. This suggests that the autocatalysis factor used in the kinetics model should in some way be dependent on the overall carbon concentration of the alloy. For simplicity the following assumption is used

$$\beta = \lambda_1 (1 - \lambda_2 \bar{x}) \quad (3.6)$$

where \bar{x} represents the mean carbon concentration of the alloy, and β is the autocatalysis factor with λ_1 and λ_2 are empirical constants. In this way, the effect of autocatalysis is less for high carbon steels than for those with lower carbon content. The additional nucleation sites introduced as transformation proceeds is denoted by

$$I_{W_s} = I_0 (1 + \beta \theta \xi) \quad (3.7)$$

where β is the empirical autocatalysis constant.

Since bainite always nucleates firstly from austenite grain boundaries, the nucleation rate of a grain boundary-nucleated transformation can be assumed to be proportional to the surface area of austenite grain boundaries per unit volume S_V . The reason for this is that the number of suitable sites for nucleation is expected to be directly proportional to the surface area of austenite/austenite grain boundaries within the sample.

Stereological theory relates S_V to the mean linear intercept \bar{L} of a series of random lines with the austenite grain boundaries, by the expression [Dehoff and Rhines, 1968]

$$S_V = 2/\bar{L}. \quad (3.8)$$

In the new expression for the nucleation rate of bainite the term K_1 will be a function of the austenite grain size, as expressed by the mean linear intercept

$$K_1 = (\bar{L}K'_1)^{-1} \quad (3.9)$$

where K'_1 is an empirical constant.

The factors discussed above can be incorporated into a model as follows. The volume fraction increment between times t and $t + dt$ is

$$\theta d\xi = (1 - \xi)uI dt \quad (3.10)$$

where u is the sub-unit volume and I is the nucleation rate of bainite per unit volume. The expression for the nucleation rate of bainite (equation 3.1) can be substituted into this equation giving a differential equation for the overall transformation rate of bainite

$$\frac{d\xi}{dt} = \frac{uK_1}{\theta}(1 - \xi)(1 + \beta\theta\xi) \exp \left\{ -\frac{K_2}{RT} \left(1 + \frac{\Delta G_m^0}{r} \right) + \gamma_2\xi \right\} \quad (3.11)$$

where γ_2 is given by

$$\gamma_2 = \frac{K_2(\Delta G_m^0 - G_N)}{rRT} \quad (3.12)$$

There are four unknown, K_1 , K_2 , λ_1 , and λ_2 in this equation, which is integrated numerically.

The unknowns were determined by optimising the theory using the same data as used by Bhadeshia [1982a].

The analysis shows that the kinetic equation is capable of representing each of the individual steels with remarkable accuracy (Fig. 3.10), although the results are less impressive when all the data are considered together (Fig. 3.11). The determined constants are tabulated in Table 3.1. The discrepancies seen are probably due to two factors. The first is that the volume per sub-unit is unknown; although the sub-unit widths have been measured, the sub-unit lengths are not known. The dimensions of the sub-units cannot at the moment be predicted either. A second factor is that whereas the nucleation theory has been shown to be successful in giving a reasonable transformation-start temperature, it has never been verified experimentally as far as the number density of nuclei is concerned. Bearing these difficulties in mind, the level of agreement achieved is perhaps reasonable.

3.5 TIME-TEMPERATURE-TRANSFORMATION DIAGRAMS

The kinetic data are presented differently in Fig. 3.12, in the form of isothermal transformation diagrams for the early stages of austenite decomposition. The form of the diagrams is

consistent with previous works reproduced in Fig. 3.13 [Babu *et al.*, 1976; Howard *et al.*, 1948]. The diagrams emphasize particularly that there is an acceleration of transformation to lower bainite as the martensite–start temperature is approached. It is believed that this is because the growth of bainite is actually simulated by the formation of martensite, via a stress effect [Smith *et al.*, 1959]. In fact, recent experiments by Shipway and Bhadeshia [1995] have verified that the application of an external stress can exaggerate this acceleration.

Table 3.1: Constants determined in kinetics data analysis. The steel compositions are given in Table 2.1.

Dataset	$K'_1/u(\text{m}^2\text{s})$	$K_2 \text{ (J mol}^{-1}\text{)}$	λ_1	λ_2
Combined data	127.69×10^6	0.0158	336	45.05
A	24.73×10^6	0.161×10^5	16.58	0.00
B	27.20×10^6	0.597×10^4	7.34	0.00
C	30.80×10^6	0.0221	46.58	0.00
D	164.0×10^6	0.103×10^5	71.07	0.00
E	1.974×10^6	0.273	2.58	0.00
F	3.953×10^6	0.642×10^3	4.13	0.00
G	15.76×10^6	0.745×10^5	21.55	0.00
H	5.908×10^6	0.817×10^5	48.42	0.00

3.6 CONCLUSIONS

It has been verified that the steels listed in Table 2.1, all of which are rich in silicon, transform to bainite in the manner expected from published data. Thus, upper bainite is free of carbides, and lower bainite only contains carbides precipitated from the bainitic ferrite. Both variants of bainite are clearly associated with substantial quantities of retained austenite.

Isothermal transformation experiments have been shown to be consistent with a published model on the kinetics of the bainite transformation, although it is clear that further theory is required to predict the alloy dependence with greater accuracy. The most important of these is probably a better understanding of the size of bainite sub-units.

Kinetic data in the lower bainite regime close to the martensite–start temperature are difficult to interpret because, consistent with published work, the transformation accelerates as the martensite–start temperature is approached. This has been suggested to be a consequence of the stimulation of martensite formation by the stresses caused by the growth of lower bainite.

480 °C. (i) 500 °C.

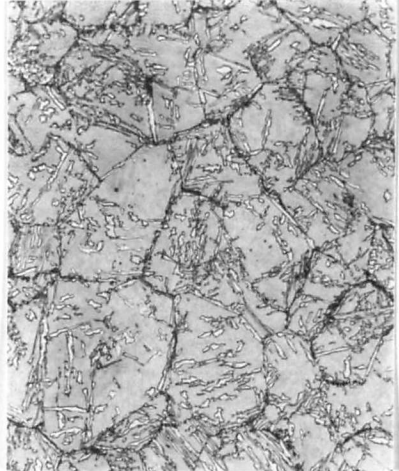
(a) 270 °C. (b) 290 °C. (c) 305 °C. (d) 345 °C. (e) 400 °C. (f) 430 °C. (g) 460 °C. (h)

Fig. 3.1: Optical micrographs for alloy C reacted across the bainite formation range.

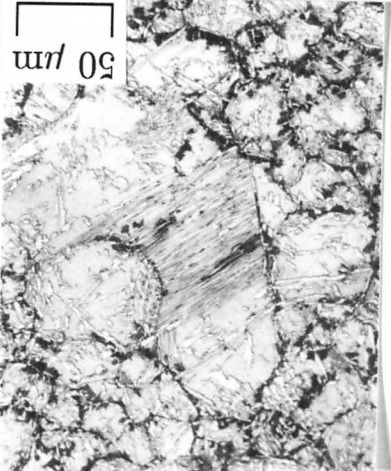
(g) 460 °C



(h) 480 °C



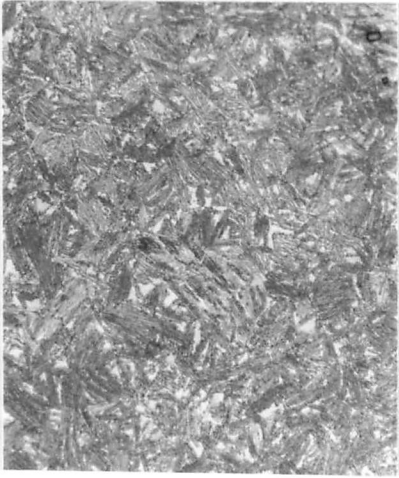
(i) 500 °C



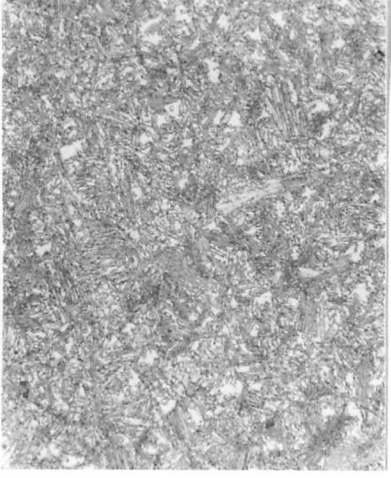
(d) 345 °C



(e) 400 °C



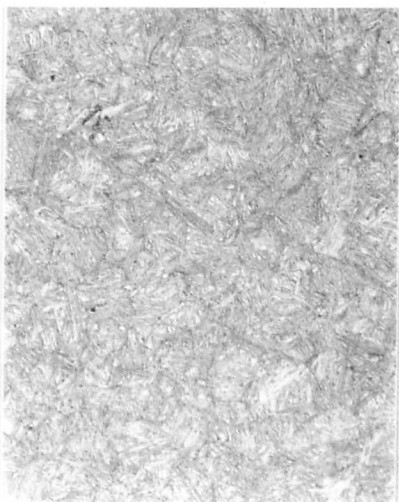
(f) 430 °C



(a) 270 °C

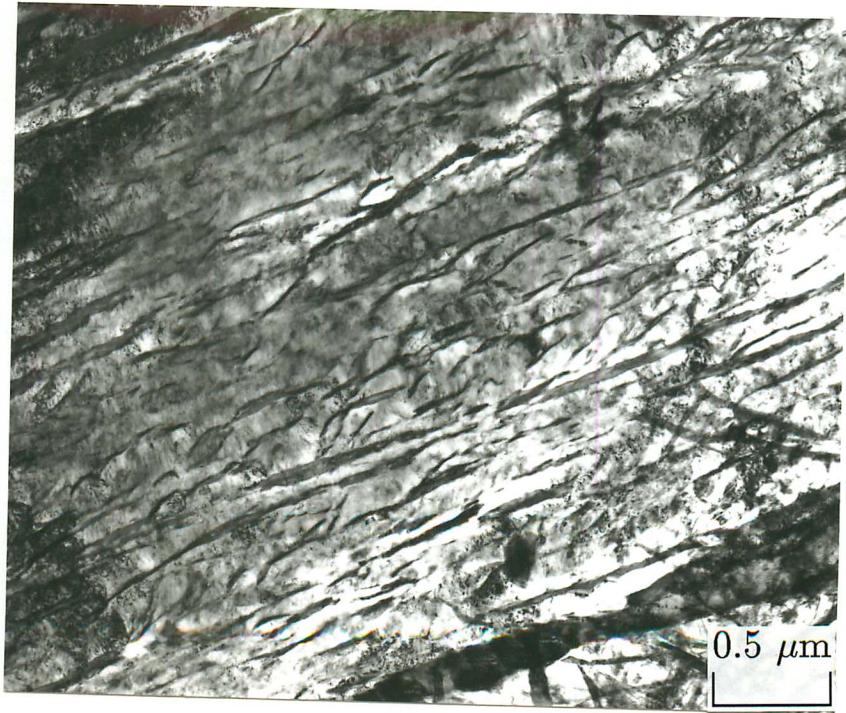


(b) 290 °C

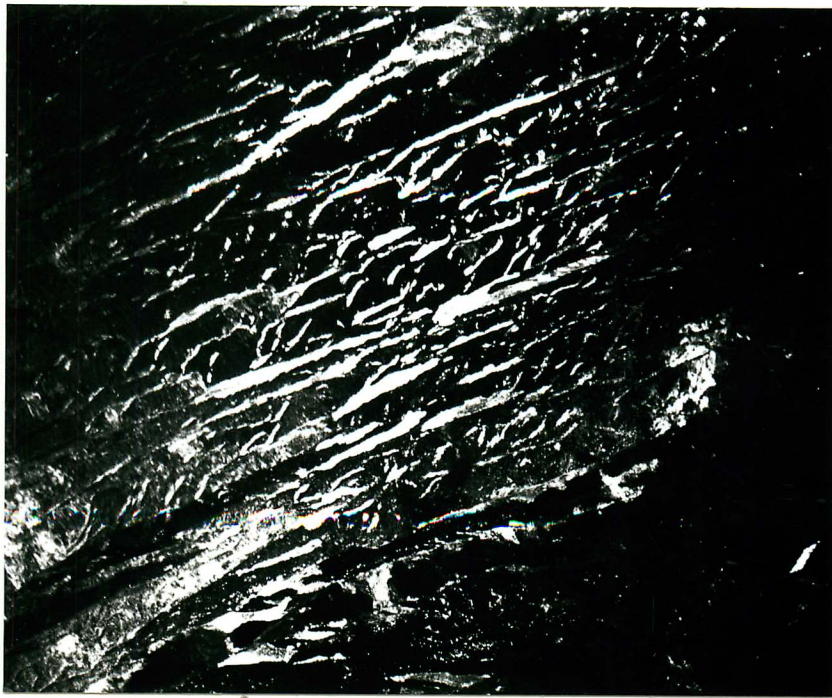


(c) 305 °C





(a)



(b)

Fig. 3.2: (a) TEM bright-field image of alloy C isothermally transformed at 320 °C, showing bainite sheaves, sub-units and retained austenite. (b) Corresponding austenite dark field image. 1000 °C @ 600 s → 320 °C @ 2000 s → gas quench.

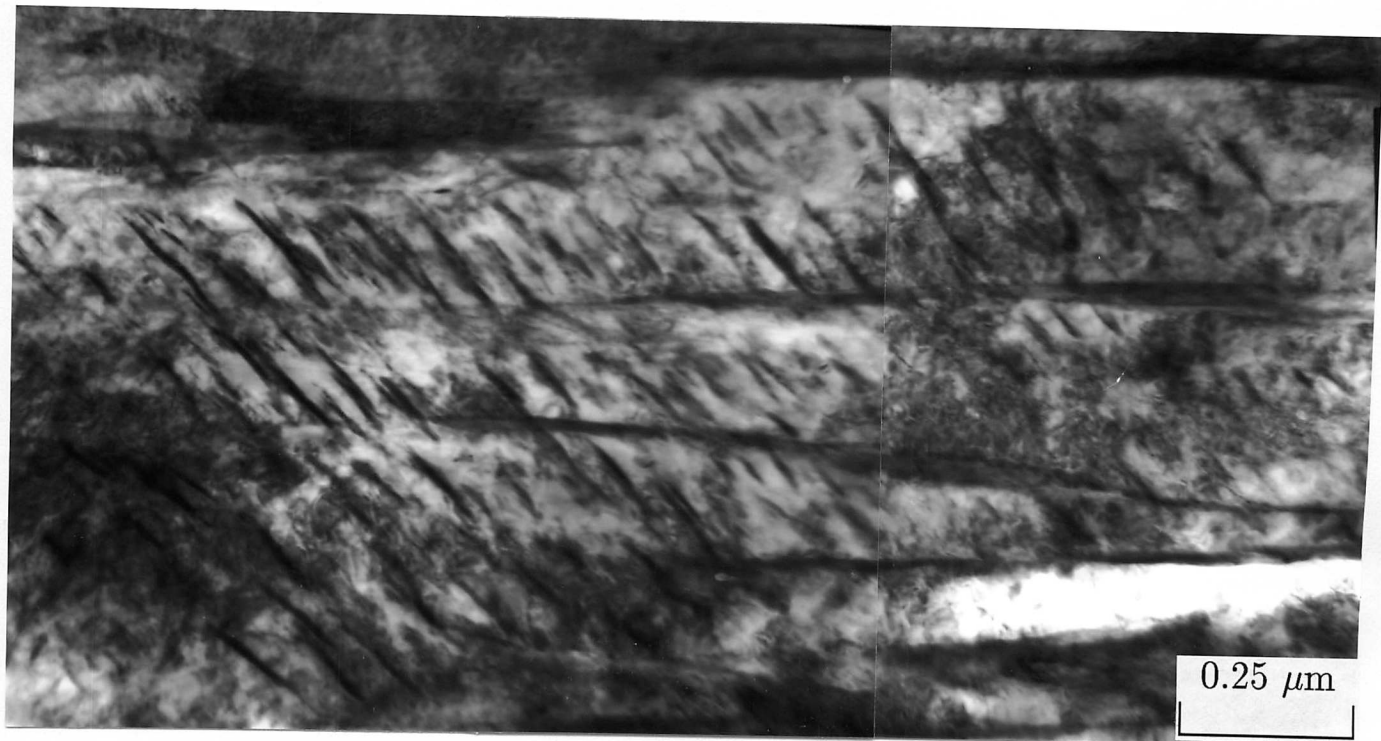
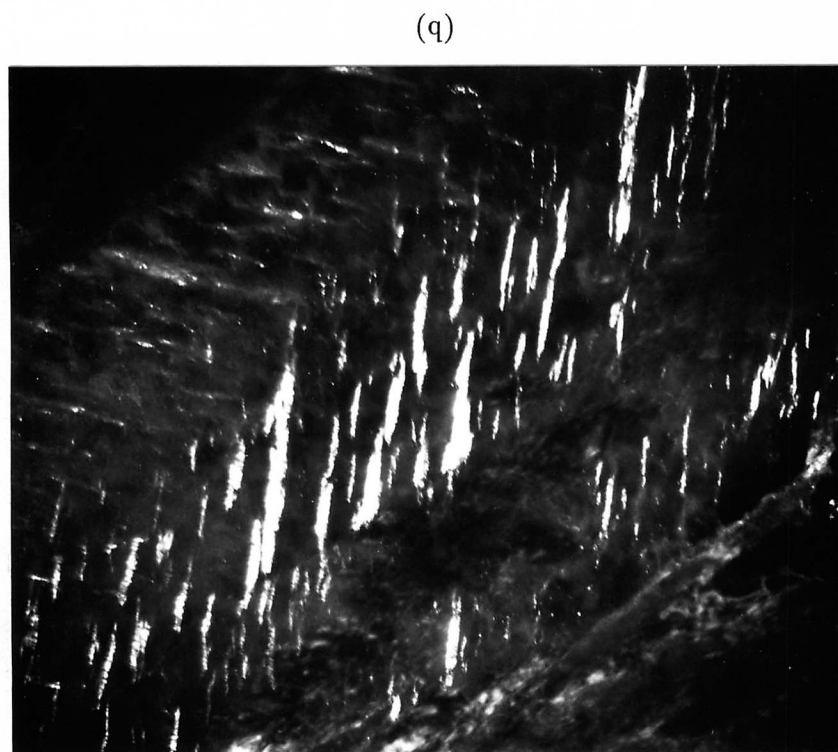


Fig. 3.3: TEM bright-field image of alloy C isothermally transformed at 270 °C, showing carbides precipitated along single variant in lower bainite sub-units. 1000 °C @ 600 s → 270 °C @ 2000 s → gas quench.

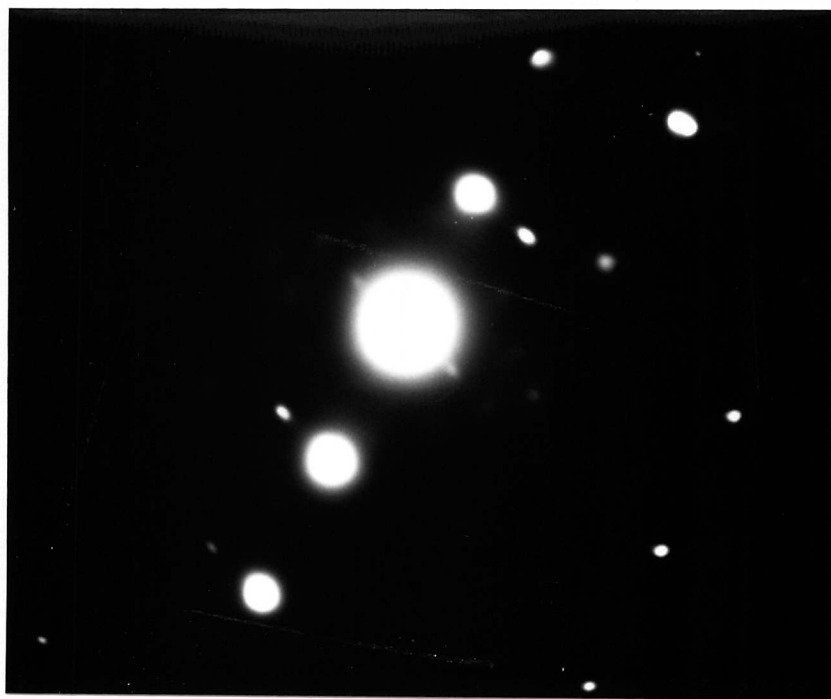
Fig. 3.4: TEM micrographs showing particles precipitated along two orthogonal variants in a lower bainite plate. (a) Bright-field image. (b) Carbide dark-field image. (c) Corresponding selected area diffraction (SAD) pattern of carbide. (d) Schematization of (c). The carbide is determined to be cementite. Alloy C, 1000 °C @ 600 s → 270 °C @ 2000 s → gas quench.



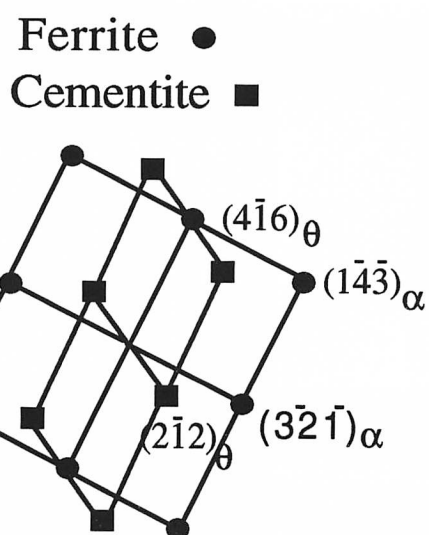
(b)



(a)



(c)



(d)

Fig. 3.4: TEM micrographs showing particles precipitated along two orthogonal variants in a lower bainite plate. (a) Bright-field image. (b) Carbide dark -field image. (c) Corresponding selected area diffraction (SAD) pattern of carbide. (d) Schematization of (c). The carbide is determined to be cementite. Alloy C, 1000 °C @ 600 s → 270 °C @ 2000 s → gas quench.

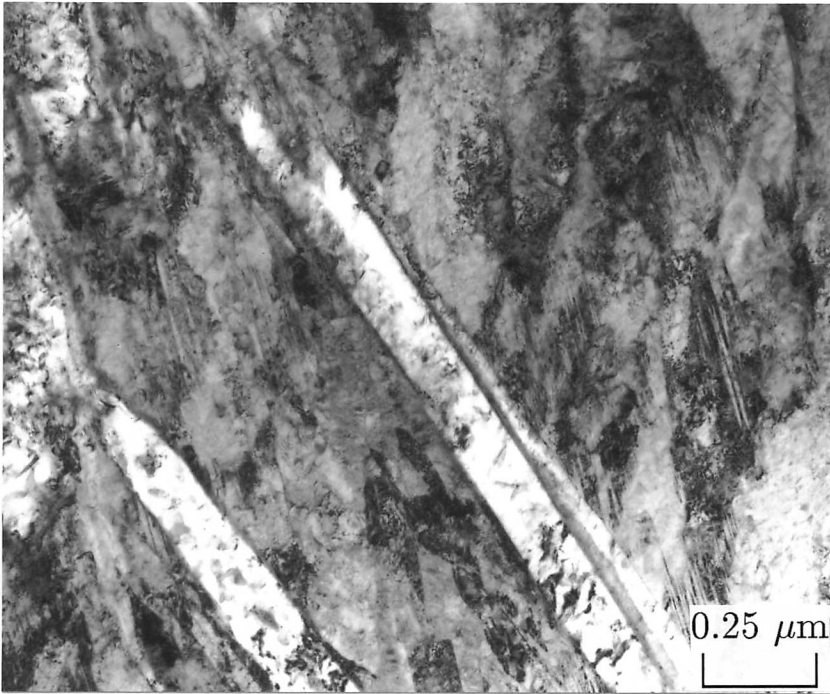
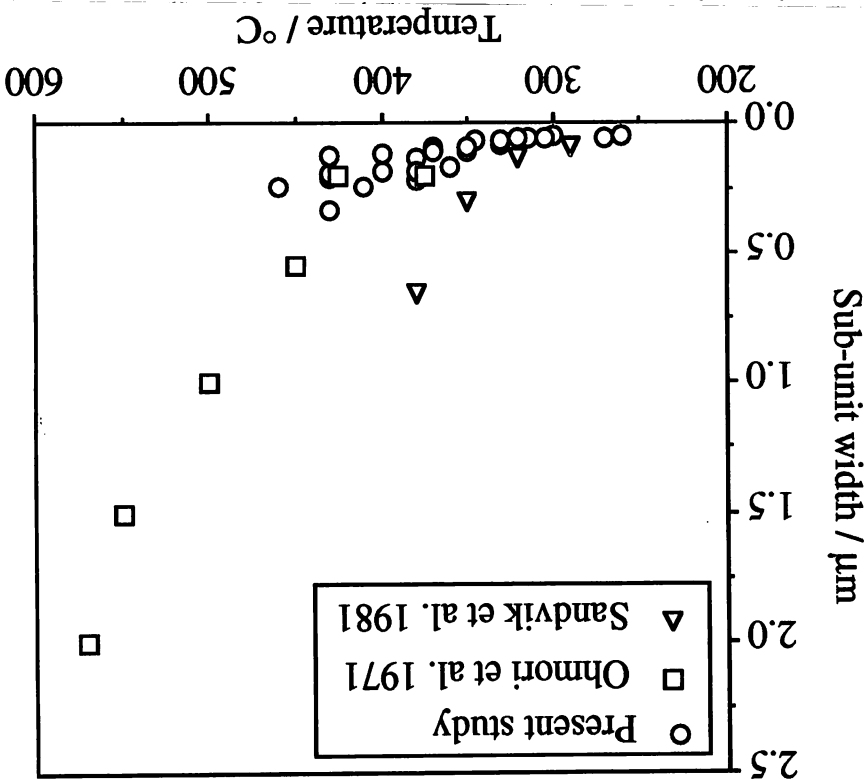


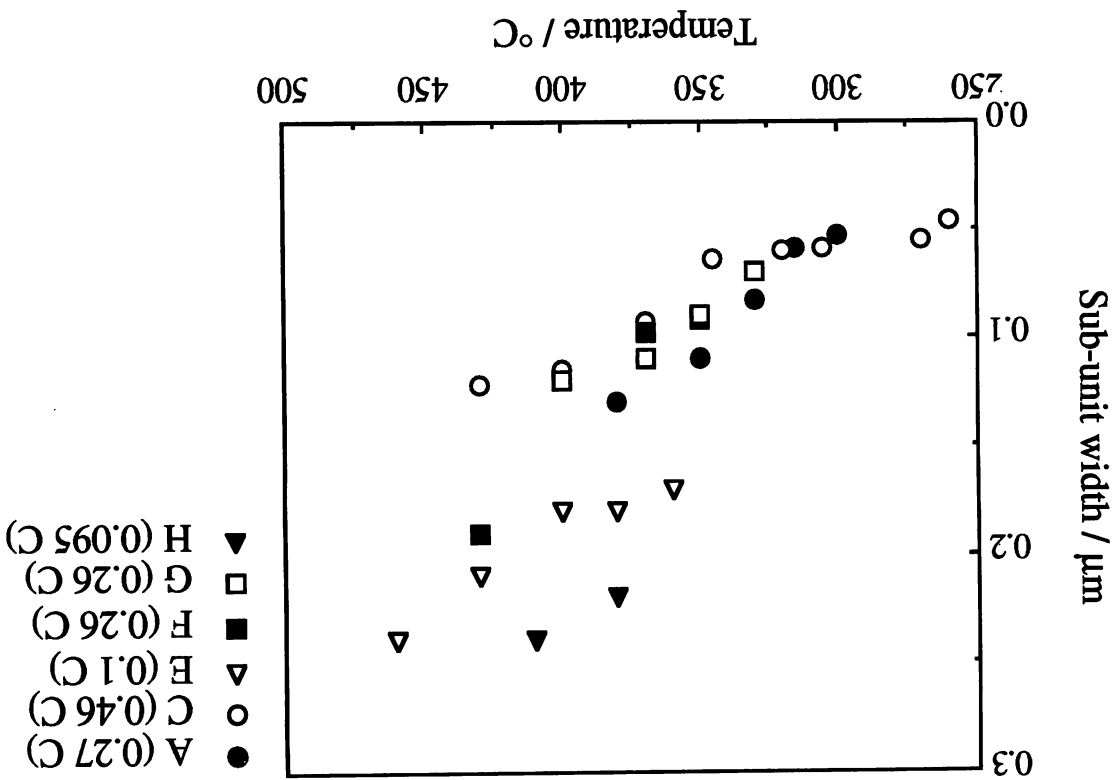
Fig. 3.5: TEM bright-field image of lower bainite sub-units with carbide precipitates.
Alloy C, 1000 °C @ 600 s → 305 °C @ 150 s → gas quench.

Fig. 3.7: Comparison of present data of sub-unit widths with those of some other sources. The obvious discrepancies increase as temperature increases.



reaction temperatures.

Fig. 3.6: Measured upper bainite sub-unit widths of the experimental alloys plotted against



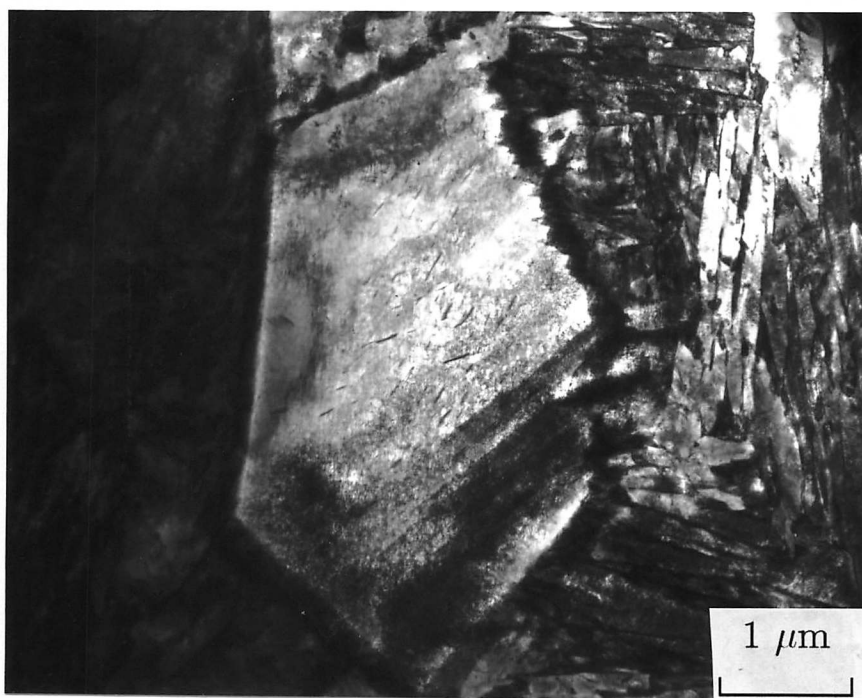
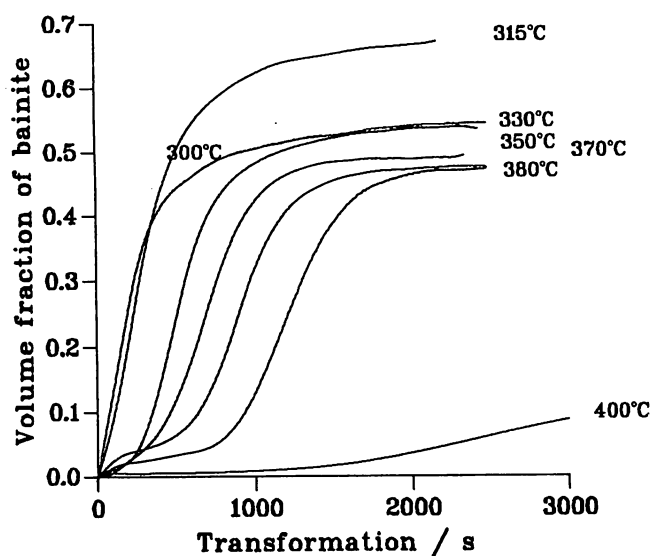
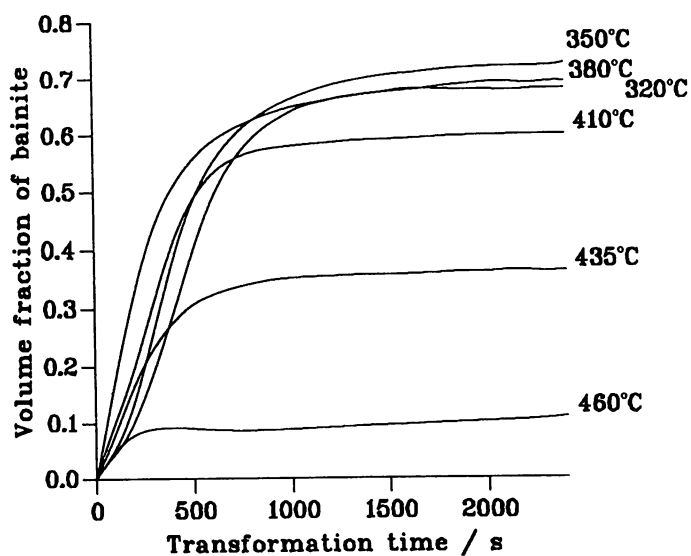


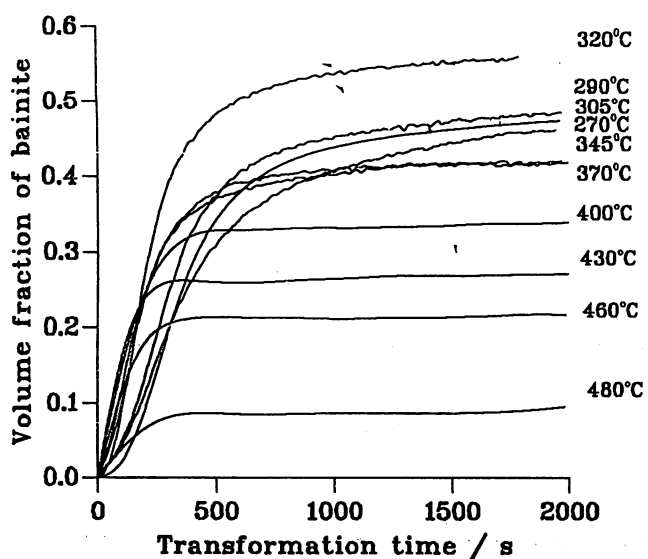
Fig. 3.8: TEM bright-field image of grain boundary lower bainite. Alloy H, 1000 °C @ 600 s \rightarrow 380 °C @ 50 s \rightarrow gas quench.



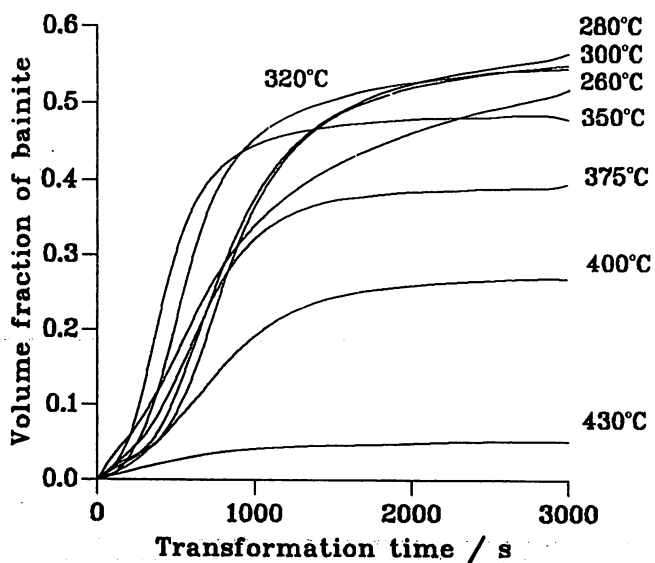
(a)



(b)

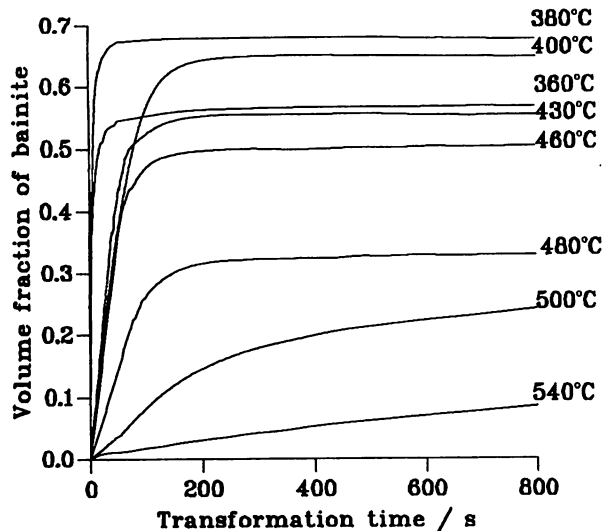


(c)

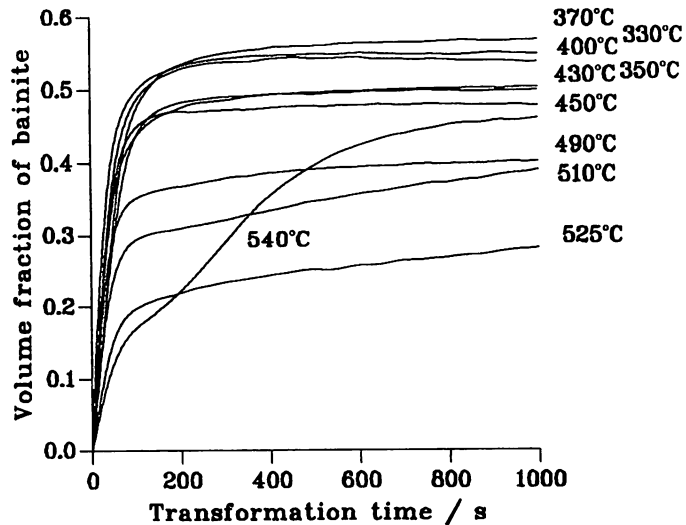


(d)

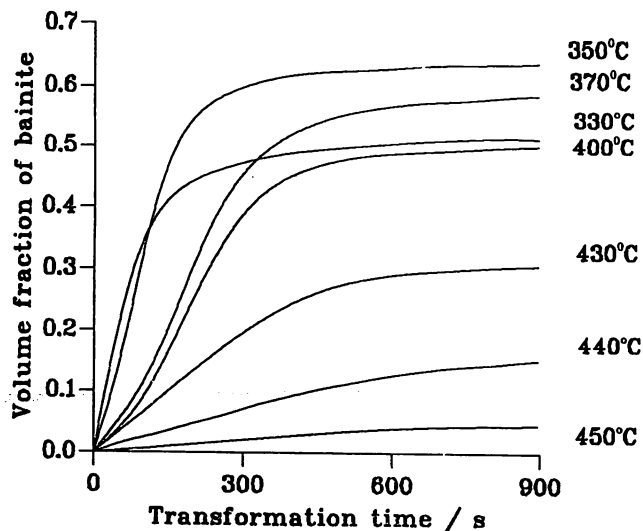
Fig. 3.9: Measured isothermal transformation curves of the experimental alloys. (a) Alloy A. (b) Alloy B. (c) Alloy C. (d) Alloy D. (e) Alloy E. (f) Alloy F. (g) Alloy G. (h) Alloy H.



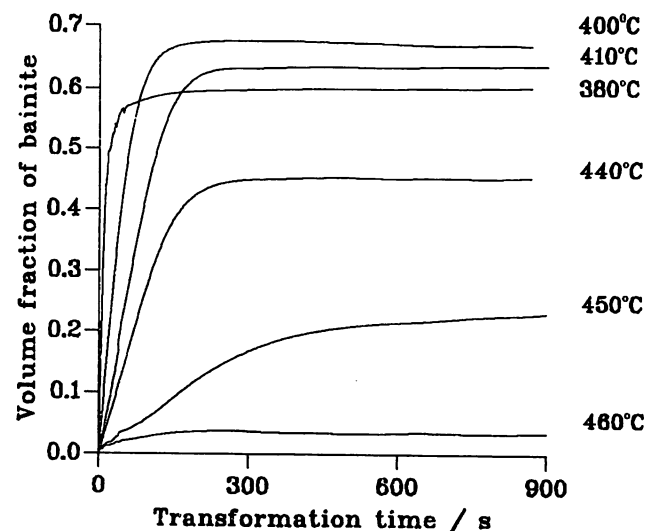
(e)



(f)



(g)



(h)

Fig. 3.9: Measured isothermal transformation curves of the experimental alloys. (a) Alloy A. (b) Alloy B. (c) Alloy C. (d) Alloy D. (e) Alloy E. (f) Alloy F. (g) Alloy G. (h) Alloy H.

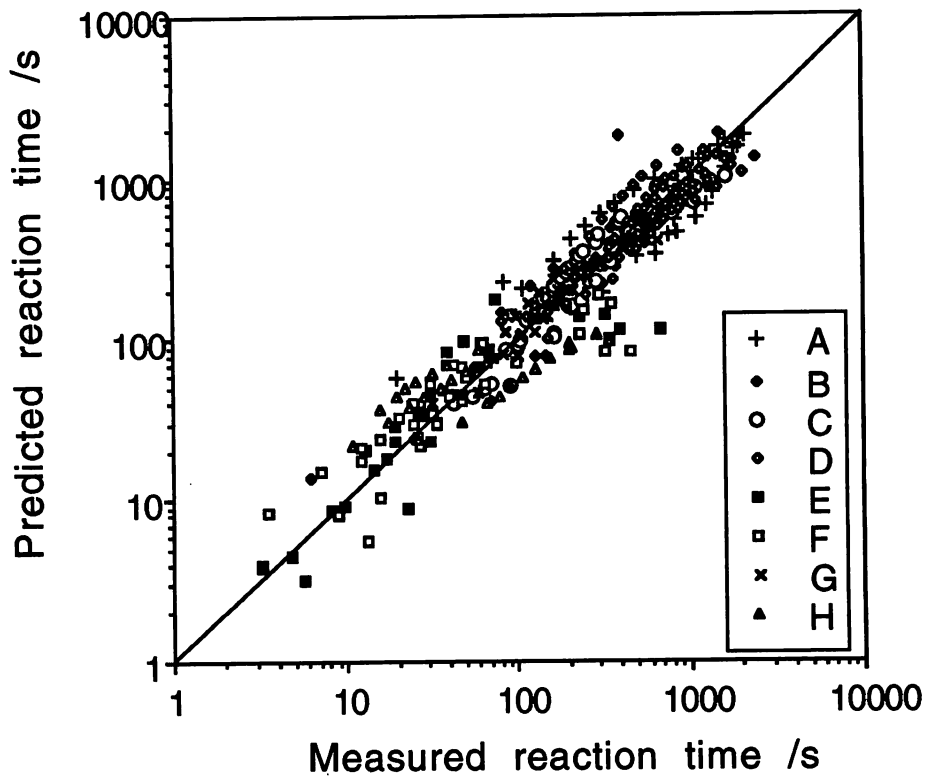


Fig. 3.10: Comparison of experimental kinetics data against predictions, different alloy was calculated separately.

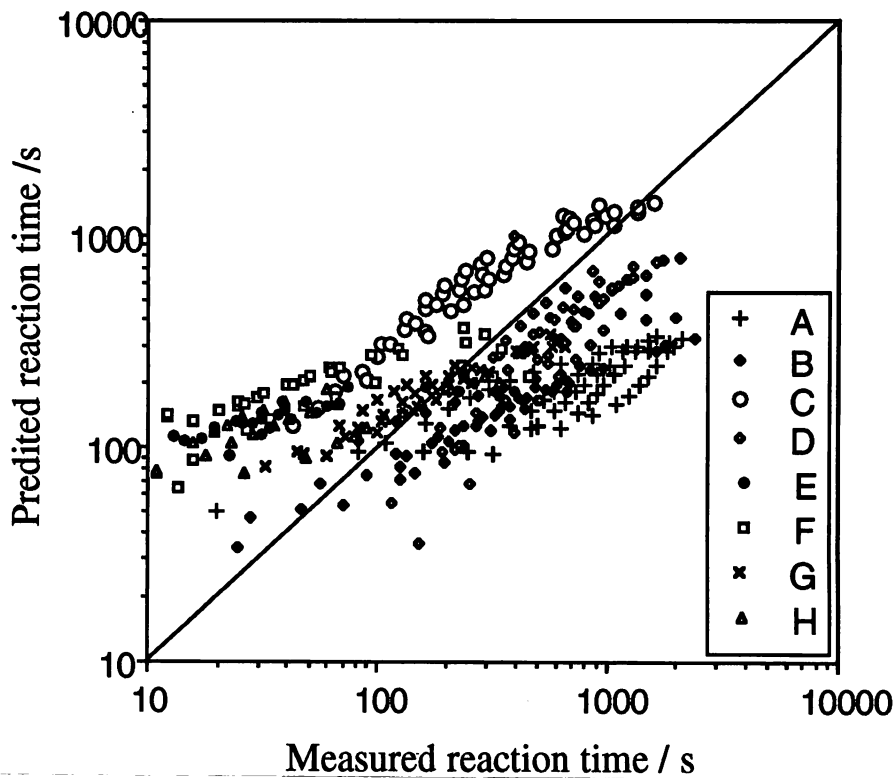
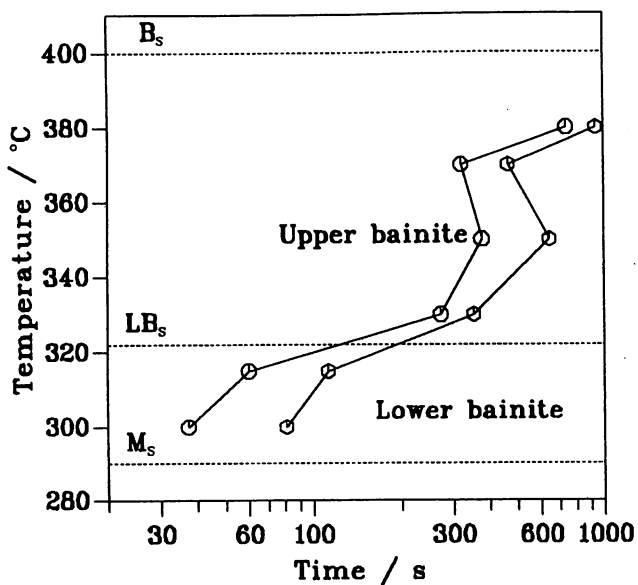
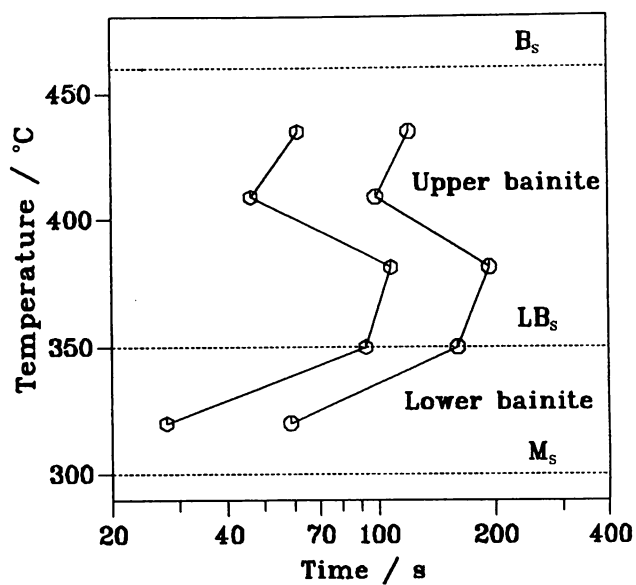


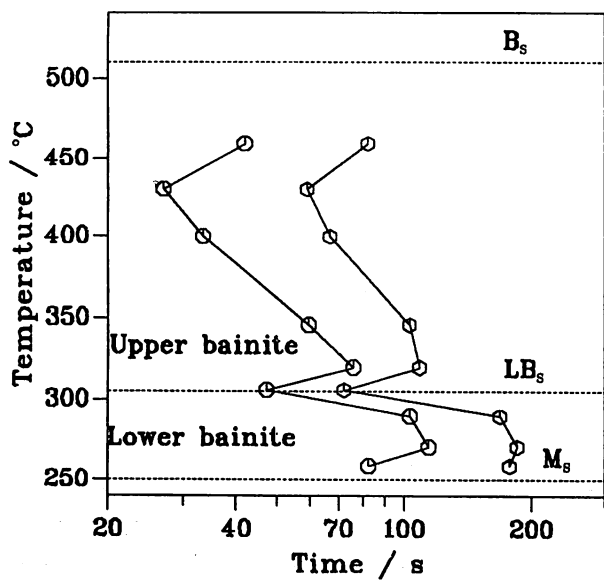
Fig. 3.11: Comparison of experimental kinetics data against predictions, all alloys were calculated together.



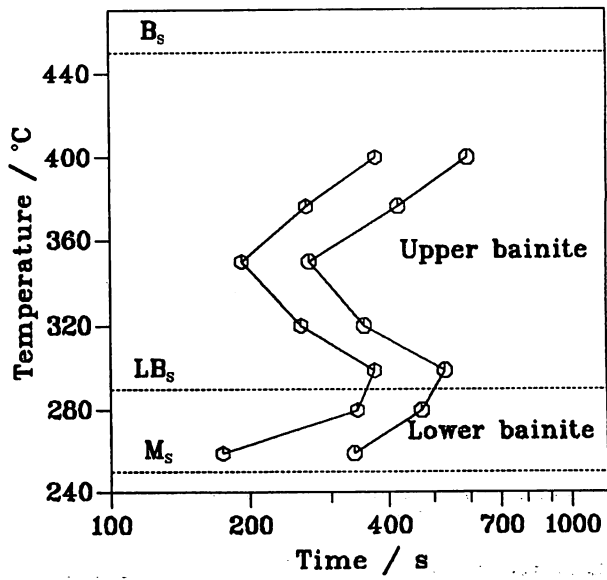
(a)



(b)

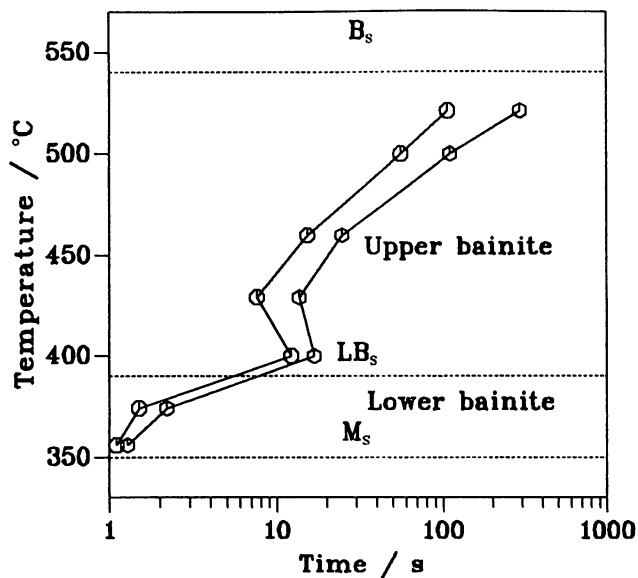


(c)

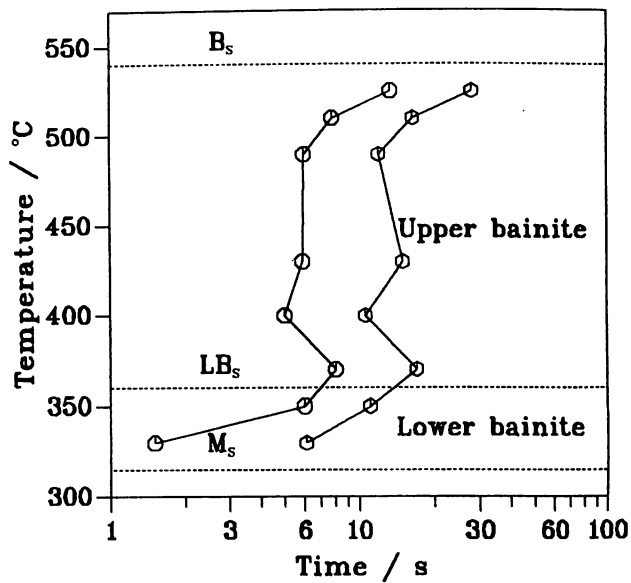


(d)

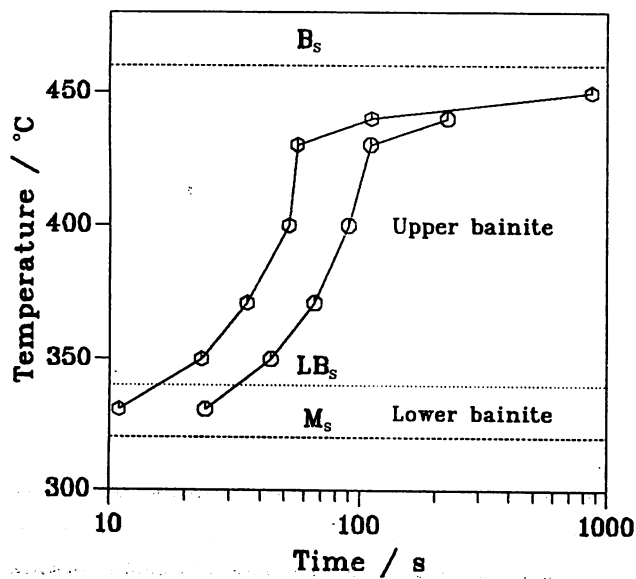
Fig. 3.12: Dilatometrically determined 5 and 10 pct transformation TTT curves for the experimental alloys. (a) Alloy A. (b) Alloy B. (c) Alloy C. (d) Alloy D. (e) Alloy E. (f) Alloy F. (g) Alloy G. (h) Alloy H.



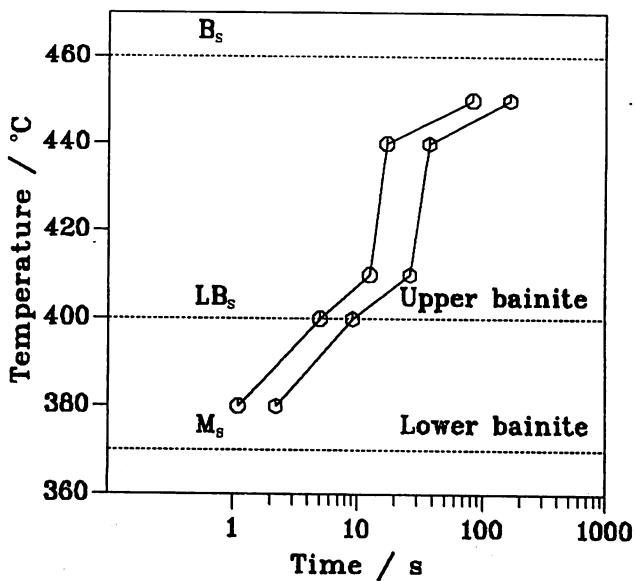
(e)



(f)

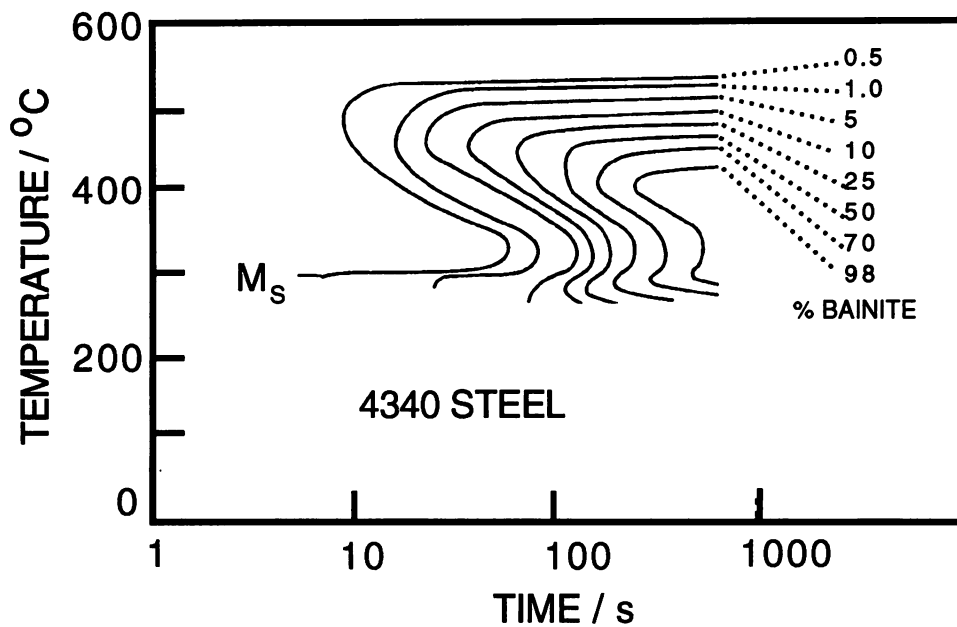


(g)

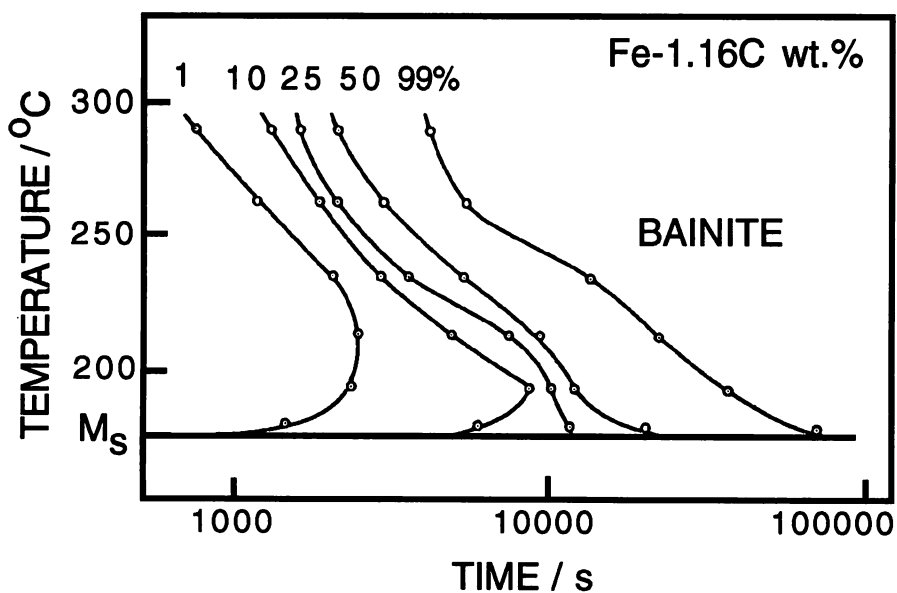


(h)

Fig. 3.12: Dilatometrically determined 5 and 10 pct transformation TTT curves for the experimental alloys. (a) Alloy A. (b) Alloy B. (c) Alloy C. (d) Alloy D. (e) Alloy E. (f) Alloy F. (g) Alloy G. (h) Alloy H.



(a)



(b)

Fig. 3.13: TTT diagram for a Fe-0.39C-0.70Mn-1.7Ni-0.76Ni-0.2Mo-0.28Si-0.22Cu wt.% alloy austenitized at 900 °C for 15 min. Note the acceleration in the rate of transformation as the M_S temperature is approached [Babu *et al.*, 1976]. (b) Similar data for a plain carbon steel [Howard *et al.*, 1948].

CHAPTER 4

AUSTENITE FILMS IN BAINITIC MICROSTRUCTURES

4.1 INTRODUCTION

It is now well established that substantial quantities of austenite can be retained in the microstructure when silicon-rich steels are transformed to bainite [Hehemann, 1970; Bhadeshia and Edmonds, 1979a; 1983a, b]. This is because the silicon and other elements such as aluminium, which have low solubility in cementite, retard its precipitation. The carbon that is partitioned into the austenite as a consequence of the formation of bainitic ferrite therefore remains in the austenite, stabilising it to ambient temperature.

A microstructure like this, in which fine plates of bainitic ferrite are separated by films of austenite, is in many respects ideal from the point of view of mechanical properties. The fine scale of the ferrite plates is conducive to good toughness, as is the absence of carbides (which have the potential of nucleating cleavage cracks or voids). The ductile austenite films which are mixed intimately with the ferrite are also believed to be beneficial to toughness.

Many features of bainitic microstructures in silicon-rich steels can be calculated theoretically. These include the volume fractions of bainitic ferrite and austenite as a function of steel composition and transformation temperature, and the chemical compositions of the austenite and bainitic ferrite. However, the factors controlling the thickness of the austenite films are not yet established, and indeed, the films themselves have never been characterized quantitatively. The purpose of the present work was to study a series of experimental silicon-rich steels in order to develop and verify a theory for the factors controlling the thickness of the austenite films.

4.2 EXPERIMENTAL

4.2.1 Materials

Six alloys (A, C, E, F, G and H) were used for the present study. Chemical compositions and heat treatment have been described in Chapter 2.

4.2.2 Stereological Measurements

The austenite film thicknesses were measured directly from TEM micrographs at magnifications ranging from $\times 17,000$ to $\times 36,000$. The shortest distance perpendicular to the longitudinal dimension of the austenite film was measured in each case. The same procedure

was used to measure the apparent thickness of the bainitic ferrite sub-units. Approximately 30–100 measurements were made for each heat-treatment.

Some stereological corrections are necessary since the measurements are made on random sections. For a square plate of thickness t and sides $a \times t$, the mean linear intercept obtained by projecting random test lines on to random two-dimensional sections is given by [Mack, 1956]:

$$\bar{L} = 2t \quad (4.1)$$

when $a \gg t$. However, for the present work, it was much more convenient to measure the mean intercept \bar{L}_T , which is obtained by orienting the test line in a direction normal to the longitudinal dimension of the film or plate. The effect of doing this is illustrated in Fig. 4.1; it is as if the plane of observation always contains a long edge of the plate, with the additional condition that the test line is normal to this long edge. The perimeter P_A per unit area (Fig. 4.1) is given by:

$$P_A = \frac{(t + a)}{at} \simeq \frac{1}{t} \quad (4.2)$$

We note that the perimeter is taken to be $t + a$ rather than $2(a + t)$ because the interface is shared between adjacent grains. Using the standard stereological relationship [Underwood, 1968]:

$$P_A = \frac{\pi}{2\bar{L}_T} \quad (4.3)$$

we get

$$\bar{L}_T = \frac{\pi}{2}t \quad (4.4)$$

Comparison with equation (4.1) shows, as might be expected, that the linear intercept as measured here is closer to the true thickness than would be the case if the test line were completely randomly oriented. All the ferrite and austenite thickness data reported here have therefore been corrected by the factor $\pi/2$.

4.3 RESULTS

4.3.1 General Microstructure

There are two essential morphologies of austenite in silicon-rich steels which are transformed to bainite. There are films of austenite between the individual platelets (sub-units) of bainitic ferrite, and the coarser, more equiaxed, blocks of austenite between nonparallel

sheaves of bainite [Bhadeshia and Edmonds, 1979a; 1983a, b]. The blocks of austenite are easily visible in the optical microstructure, as illustrated in Fig. 4.2a. The sample illustrated was isothermally transformed at 300 °C until the formation of bainite stopped, so that the fraction of bainite illustrated is a limiting fraction. Since the limiting fraction is smaller at higher temperatures (until it becomes zero at the bainite-start temperature), the blocks of austenite become larger when the isothermal transformation is at a higher temperature (Fig. 4.2b).

The film austenite can only be resolved using transmission electron microscopy, as shown in Fig. 4.3a. The films of austenite are dispersed between the sub-units of bainitic ferrite. Fig. 4.4 illustrates that the films of austenite clearly become finer as the transformation temperature is reduced, or as the carbon concentration is reduced.

Fig. 4.5a shows that the distinction between blocky austenite and film austenite becomes less clear when the blocks of austenite occur between *parallel* sheaves. However, the thickness of the blocks is clearly much larger than of the films, and they extend to greater lengths, so that there was usually no difficulty in distinguishing between inter-plate films of austenite and inter-sheaf blocks of austenite. However, the extent of transformation in the lowest carbon alloys can be so large as to make the individual sheaf indistinct. For example, Fig. 4.5b shows the low carbon Alloy E transformed at 380 °C, where there are no large regions of austenite between different sheaves, although there is obviously a bimodal distribution of austenite thickness. The measurements of austenite film thickness in those cases were confined to the fine films which truly represent the films between the ferrite sub-units.

4.3.2 Mechanism of Transformation

The analysis of experimental film thickness measurements requires a knowledge of the mechanism of transformation. There is evidence to suggest that although the plates of bainite grow by a displacive, diffusionless transformation mechanism, any excess carbon in the ferrite is soon afterwards partitioned into the residual austenite [Bhadeshia, 1992]. The austenite thus progressively enriches in carbon, until a point is reached where it becomes thermodynamically impossible for further transformation to occur via this mechanism.

It is useful to restate a number of thermodynamic concepts consistent with this mechanism of bainite growth. The T_0 curve represents the locus of all points on a plot of temperature versus carbon concentration, where austenite and ferrite of the same chemical composition also have identical free energies. Hence, austenite with a carbon concentration in excess of that defined by the T_0 curve cannot, even in principle, transform without diffusion. The growth of

bainite is accompanied by a change in shape which is characterized as an invariant-plane strain with a large shear component. The strains caused in the austenite as it accommodates this shape deformation are associated with an estimated 400 J mol^{-1} of strain energy [Bhadeshia *et al.*, 1982]. The T_0 curve, modified to account for this strain energy is called the T'_0 curve.

An alternative scenario is that the transformation mechanism is diffusionless only for the iron and substitutional solutes. Interstitial carbon may partition to such an extent that the bainitic ferrite is, at no stage of its existence, supersaturated with carbon. If strain energy is neglected, then the austenite can in these circumstances continue to transform until its carbon concentration reaches the Ae'_3 curve on the temperature/carbon-concentration plot. The Ae'_3 curve represents the paraequilibrium $\alpha + \gamma/\gamma$ phase boundary.

To summarize, a completely diffusionless transformation mechanism would be limited by the T'_0 curve, whereas one in which only carbon diffused during transformation would be expected to be limited by the Ae'_3 paraequilibrium phase boundary. As stated earlier, there is accumulated evidence [Bhadeshia, 1992; Bhadeshia and Edmonds, 1980; Chang and Bhadeshia, 1994] that the transformation to bainite stops when the carbon concentration of the residual austenite reaches the T'_0 boundary. Nevertheless, it was felt useful to verify these principles for the steels considered here, especially since the heat treatments were all carried out in a thermomechanical simulator so that there was no extra expense in collecting the necessary data.

Isothermal transformation experiments were carried out over a temperature range between B_S and M_S , the exact temperature depending on the alloy concerned. The transformation strain was monitored until reaction ceased. This strain can then be converted into a volume fraction of bainitic ferrite, and the fraction can in turn be used to calculate the carbon concentration of the residual austenite at the point where the reaction ceased. The detailed procedure has been described previously in Chapter 2 and elsewhere [Bhadeshia, 1982a; Bhadeshia and Edmonds, 1980]. Fig. 4.6 shows three diagrams, comparing the measured austenite carbon concentration against the concentrations expected if the formation of bainite ceases when the austenite carbon concentration reaches that given by the Ae'_3 , T_0 or T'_0 conditions described above. These latter concentrations can be calculated using well-established thermodynamic methods [Zener, 1946; Aaronson *et al.*, 1966; Bhadeshia and Edmonds, 1980; Bhadeshia *et al.*, 1982]. Fig. 4.6a is interesting in two respects. Firstly, it is obvious that the formation of bainitic ferrite ceases well before the austenite achieves the paraequilibrium carbon concentration. Secondly, the extent of the discrepancy increases as the transformation temperature is reduced (*i.e.* at larger austenite carbon levels). Both of these results are expected, the latter

because the T'_0 curve has a steeper slope on the phase diagram when compared with the Ae'_3 curve [Bhadeshia and Edmonds, 1980]. The agreement between the experimental data and the calculations improve considerably when the comparison is made against the T_0 concentrations (Fig. 4.6b), but there is nevertheless an overestimation of the experimental data. The best agreement is clearly when the comparison is against the T'_0 concentrations (Fig. 4.6c), which are based on diffusionless transformation including a strain energy term, as described above.

These results are useful in that they confirm that for the alloys of interest in the present work, it is reasonable to assume that the plates of bainitic ferrite form initially without diffusion, but that the excess carbon in the ferrite partitions soon afterwards into the residual austenite. Furthermore, the value of stored energy used in the T'_0 calculations, at 400 J mol^{-1} [Bhadeshia *et al.*, 1982] also seems reasonable.

Fig. 4.7 shows the measured austenite film thickness as a function of the measured bainite sub-unit thickness. It might be expected that a thicker ferrite plate would lead to a thicker austenite film since the amount of carbon partitioned is then larger. Whereas a trend of this kind can be seen in Fig. 4.7, the correlation is poor because (as discussed later) certain factors which depend on the alloy chemistry have not been taken into account. An earlier assumption [Bhadeshia and Edmonds, 1983a; b] that the ratio of the film to plate thickness should be approximately constant is clearly not justified.

Since the films of austenite are isolated by the adjacent platelets of ferrite, their thickness should not change as transformation progresses. Partial transformation experiments in which the samples were held at temperature for only 150 s, were conducted for Alloy C at 300, 350 and 400°C . The results are plotted alongside the data from the fully transformed samples in Fig. 4.8. The two sets of data are essentially identical, showing that the thickness of the film does not change during the course of the transformation.

4.3.3 Calculation of the Thickness of Austenite Films

The method used to calculate the thickness of the austenite films is based on the hypothesis that transformation to bainite can only occur in regions of austenite where $x_\gamma \leq x_{T'_0}$. The term x_γ is the carbon concentration in the austenite and $x_{T'_0}$ is the carbon concentration corresponding to the T'_0 curve for the temperature of interest. As a sub-unit of bainitic ferrite forms, it partitions its excess carbon into the residual austenite. This creates a carbon diffusion field around the sub-unit. Another parallel sub-unit (of the same sheaf) which forms subsequently, can only approach the original sub-unit to a point where $x_\gamma \leq x_{T'_0}$. This is illustrated schematically in Fig. 4.9. The method assumes that the interval between sub-unit

formation is larger than the time required to decarburise each sub-unit. The validity of this assumption can only be justified by testing the proposed model for the austenite thickness.

The problem therefore amounts to a calculation of the carbon concentration profile normal to the bainitic ferrite sub-unit habit plane, at the point where the sub-unit is decarburised to its paraequilibrium carbon concentration. This should in principle be done using a finite difference method [Mujahid and Bhadeshia, 1992], but an approximate analytical solution is used instead. This is because of the simplicity of the analytical method which also can give greater insight into the physical principles involved. The concentration profile when the excess carbon has all partitioned into the adjacent austenite is therefore given by [Mujahid and Bhadeshia, 1992]:

$$x_\gamma = \bar{x} + (x^{\gamma\alpha} - \bar{x})\text{erfc}\{z/2(\bar{D}t_d)^{0.5}\} \quad (4.5)$$

where z is a coordinate defined normal to the habit plane, $x^{\gamma\alpha}$ is the paraequilibrium carbon concentration in the austenite, t_d is the time to decarburise the ferrite plate and \bar{D} is the weighted average diffusivity of carbon in the austenite [McLellan *et al.*, 1965; Smith, 1953; Trivedi and Pound, 1967]:

$$\bar{D} = \int_{x^{\gamma\alpha}}^{\bar{x}} \frac{D^\gamma\{x, T\}}{(\bar{x} - x^{\gamma\alpha})} dx \quad (4.6)$$

The function $D^\gamma\{x, T\}$ adopted in this study is based on the theory of Siller and McLellan [1970] and Bhadeshia [1981b]. This relationship can be integrated to give:

$$t_d^{0.5} = \frac{w_\alpha(\bar{x} - x^{\alpha\gamma})\pi^{0.5}}{4\bar{D}^{0.5}(x^{\gamma\alpha} - \bar{x})} \quad (4.7)$$

where w_α is the thickness of the ferrite plate.

The carbon profiles for Alloy A, at the instant of completion of decarburisation are plotted in Fig. 4.10a, for five different temperatures with x_{T_0} marked in each case. It is clear that the austenite film thickness should increase with temperature. The effect of carbon is illustrated in Fig. 4.10b. An increase in the average carbon concentration, at constant temperature, also leads to an increase in film thickness.

The complete assessment of all measurements is presented in Fig. 4.11, which shows that the trends in the variation of austenite film thickness as a function of the transformation temperature and alloy chemistry are well predicted, although the experimental data are systematically underestimated. One possibility for the underestimation is the assumption that the carbon diffusion field of a sub-unit is that which is established immediately after the excess carbon has partitioned into the residual austenite. The austenite is clearly not homogeneous at this stage, and diffusion in the austenite will tend to level out the concentration gradients,

making the approach distance of the next sub-unit larger. This is investigated qualitatively in the next section. A fully quantitative study is not yet possible since that would require a knowledge of the time interval between the formation of adjacent sub-units.

4.3.3.1 Finite difference analysis

The homogenisation of carbon in the austenite can be studied using a standard finite difference method discussed by Crank [1975]. The diffusion process is normal to the α/γ interface, and is symmetrical about the centerline of the ferrite plate, so that only one side of the plate needs to be considered.

For the purpose of numerical analysis, the austenite region was divided into a number of slices n with

$$w_{\gamma}^s = \frac{w_{\gamma}}{n} \quad (4.8)$$

where w_{γ}^s is the thickness of slice of austenite. Larger values of n lead to greater accuracy at the expense of computing time, so n was chosen to be between 3000 and 10000. A check was made to ensure that there was no substantive change in the results when the value of n was increased. The initial concentration profile in the austenite (following the decarburisation of ferrite) was set using equation (4.5). The time interval t between successive calculations of the concentration distribution is given by:

$$t = r \frac{(w_{\gamma}^s)^2}{D} \quad (4.9)$$

where r is a grid parameter in the finite difference method, which can be set to a smaller value for higher accuracy; the value of r was fixed by ensuring that the results become insensitive to the choice.

The explicit finite difference formula is:

$$x'_{\gamma}(i, j+1) = x'_{\gamma}(i, j) + r[x'_{\gamma}(i-1, j) - 2x'_{\gamma}(i, j) + x'_{\gamma}(i+1, j)] \quad (4.10)$$

where the normalized concentration $x'_{\gamma} = x_{\gamma}/\bar{x}$, i is the slice number and j represents the successive time rows of the grid. The first and last slices of each time row follow the relations:

$$x'_{\gamma}(1, j) = x'_{\gamma}(1, j-1) + r[x'_{\gamma}(2, j-1) - x'_{\gamma}(1, j-1)] \quad (4.11)$$

$$x'_{\gamma}(i_l, j) = x'_{\gamma}(i_l, j-1) + r[x'_{\gamma}(i_l-1, j-1) - 2x'_{\gamma}(i_l, j-1) + x'_{\gamma}(i_l-1, j-1)] \quad (4.12)$$

where i_l is the number of the last slice. Precautions were taken to ensure that mass is conserved throughout the process.

The method can be used to analyse how the carbon homogenizes in the austenite after the plate of bainitic ferrite has decarburised. Fig. 4.12 shows the calculated profiles as a function of time for a number of transformation temperatures (Alloy A). The profiles obviously change faster at the higher temperatures, because of the correspondingly larger diffusion coefficients involved. Examination of the $x_{T'_0}$ condition shows that the calculated austenite film thickness should, as expected, increase. However, the change is not very large, for what are believed to be realistic time intervals, because in general, $x_{T'_0} \ll x^{\gamma\alpha}$.

4.4 CONCLUSIONS

It appears that the thickness of those austenite films which lie between parallel bainitic ferrite sub-units is controlled by the T'_0 condition. As a supersaturated bainite plate grows and partitions its excess carbon into the surrounding austenite, an adjacent carbon-enriched austenite layer is created in which the carbon concentration is greater than that which would permit diffusionless transformation. It is this layer which is retained as the thin film of austenite. The general trend in the thickness of the austenite films, as a function of the transformation temperature and alloy composition, can be predicted using a simple analytical model. The model, however, underestimates the thickness because it contains nothing about the time interval between the growth^{of} successive, adjacent sub-units.

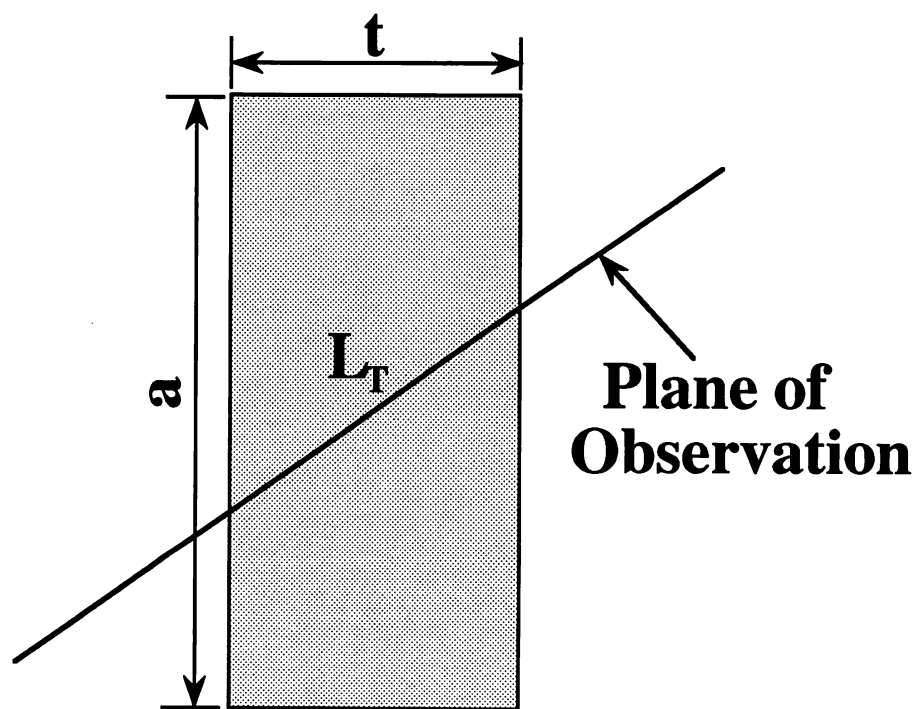


Fig. 4.1: The linear intercept L_T obtained when the test plane is restricted to rotation about one of the long edges of the plate, and the test line is restricted to an orientation normal to the longitudinal direction of the plate in the test plane.

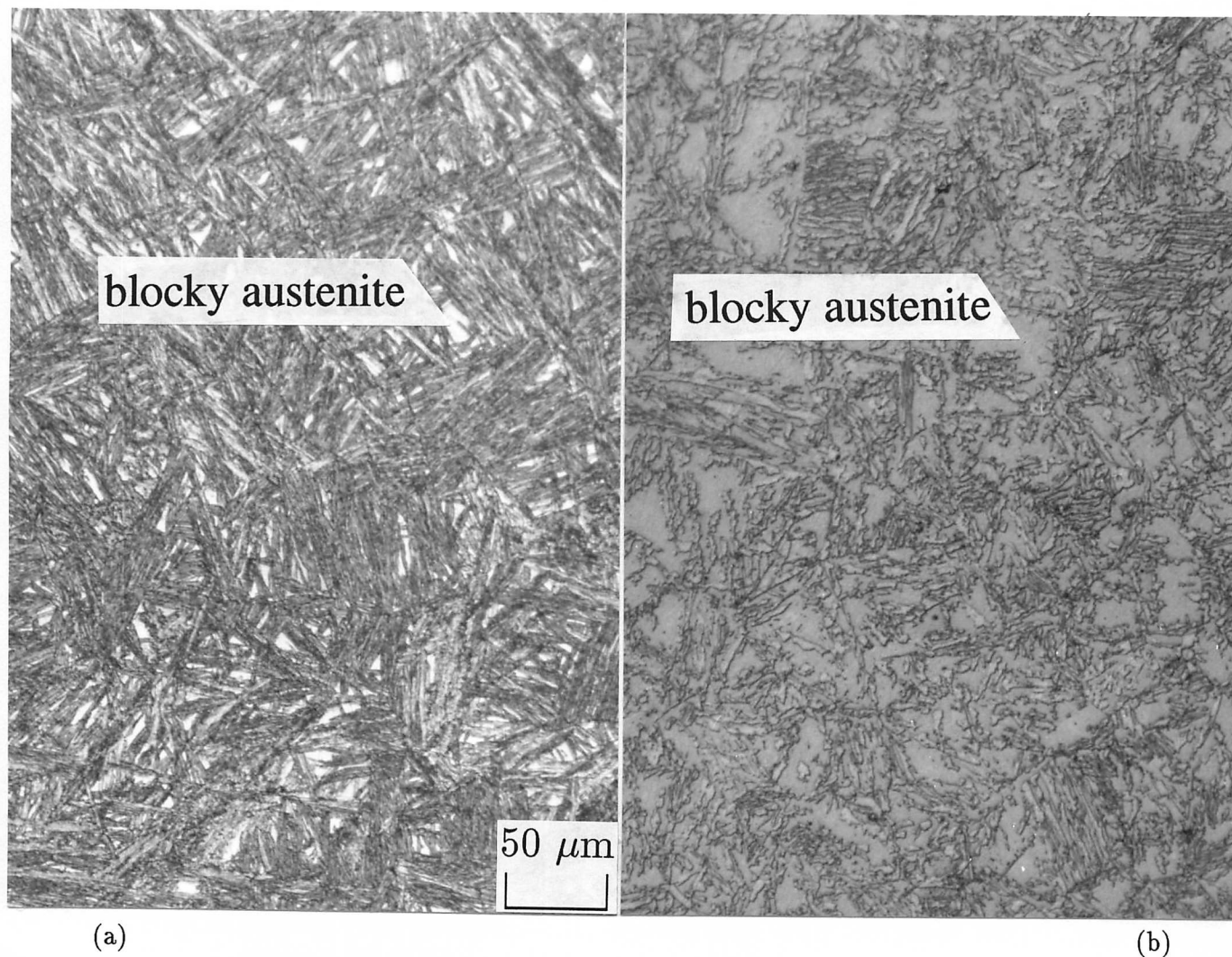


Fig. 4.2: Optical micrographs of Alloy C, showing a mixture of bainitic ferrite and austenite, which is the white-etching phase. The darker etching regions consist of a mixture of fine bainitic ferrite platelets separated by films of austenite, which cannot be resolved optically. (a) Heat treated as follows: 1000 °C for 600 s → 300 °C for 2000 s before gas quenching to room temperature. (b) As above, but isothermally transformed at 460 °C, showing coarser blocks of austenite.

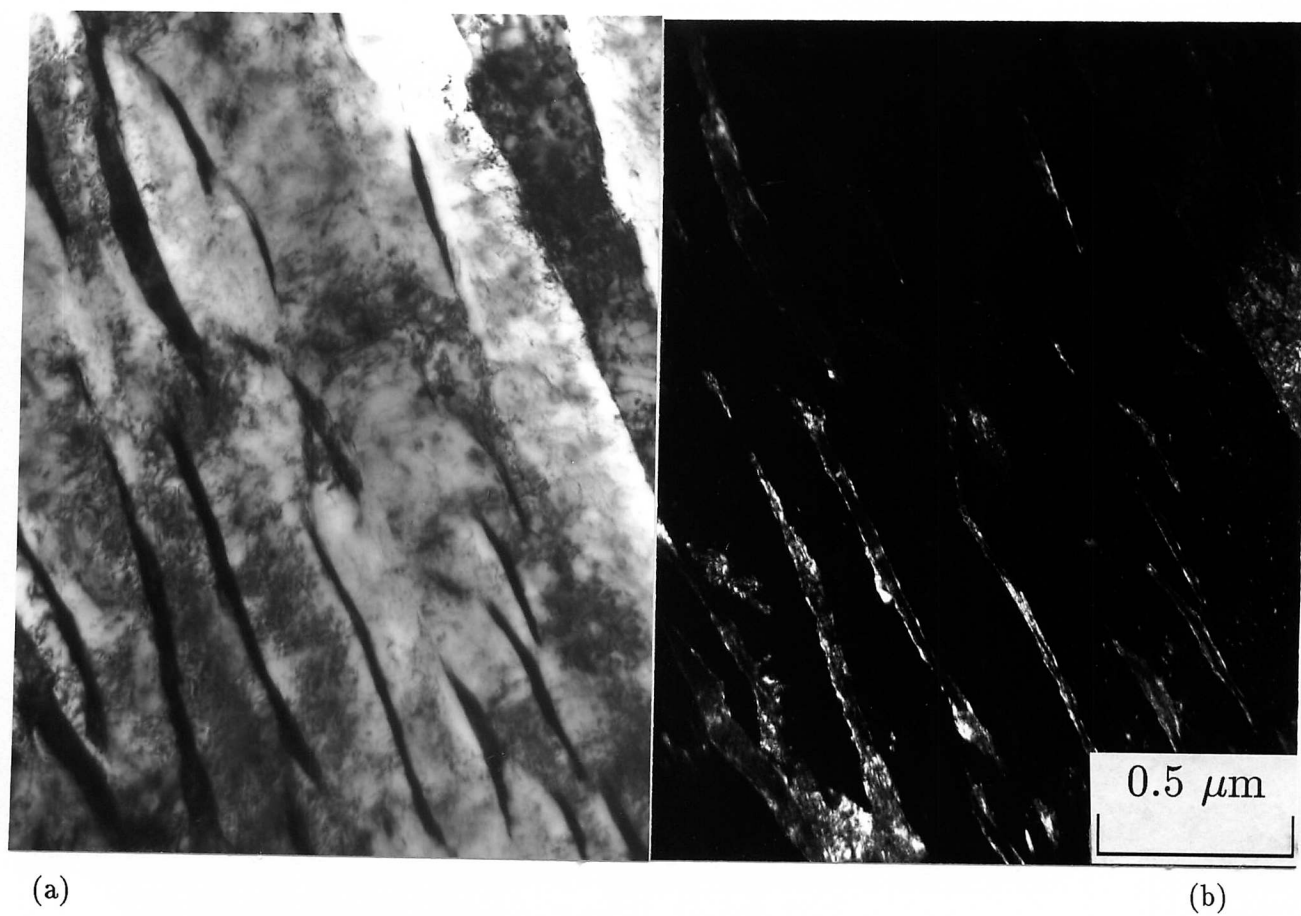


Fig. 4.3: (a) Alloy C isothermally transformed at 350 °C, showing the films of austenite. (b) Corresponding austenite dark field image.

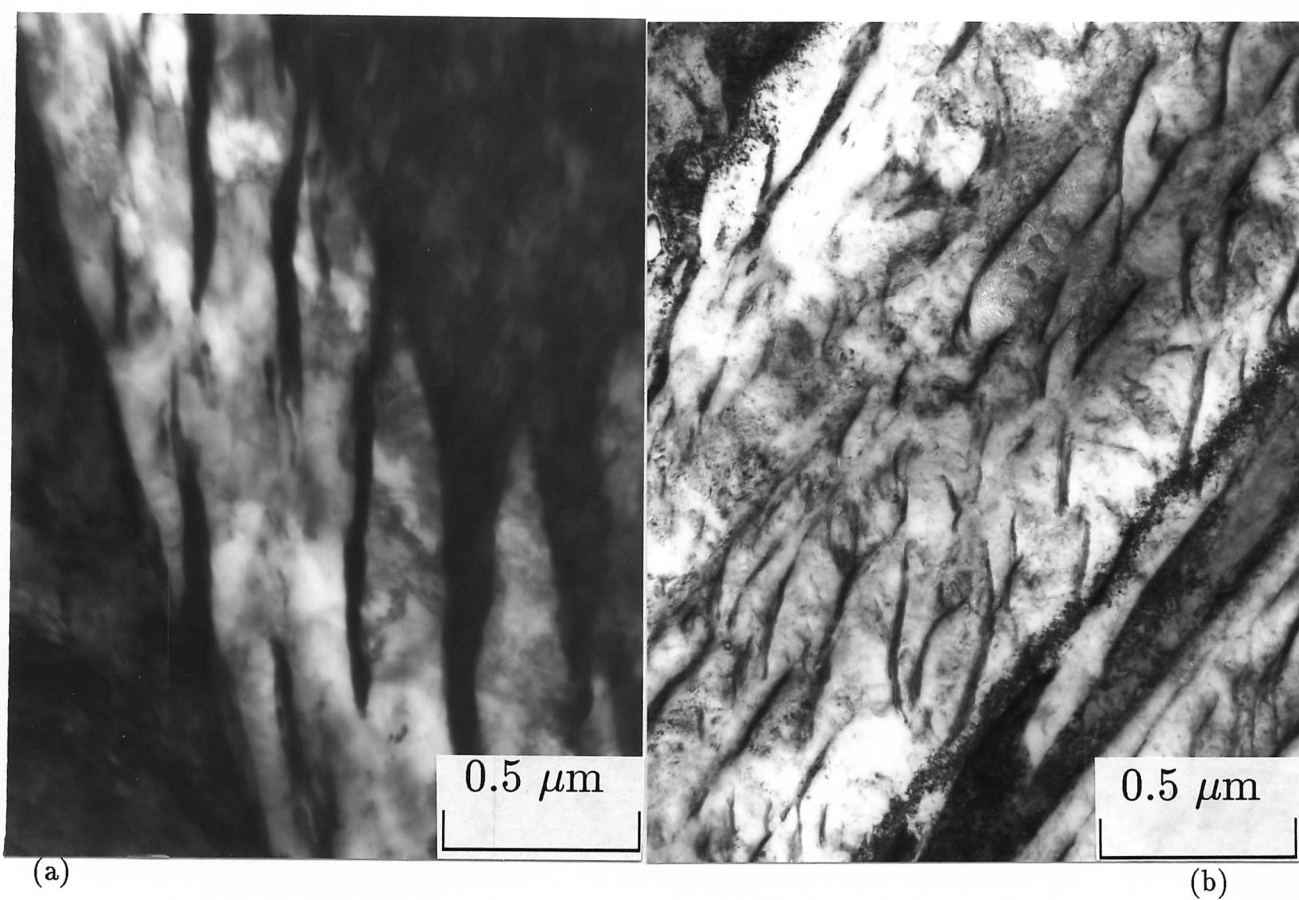
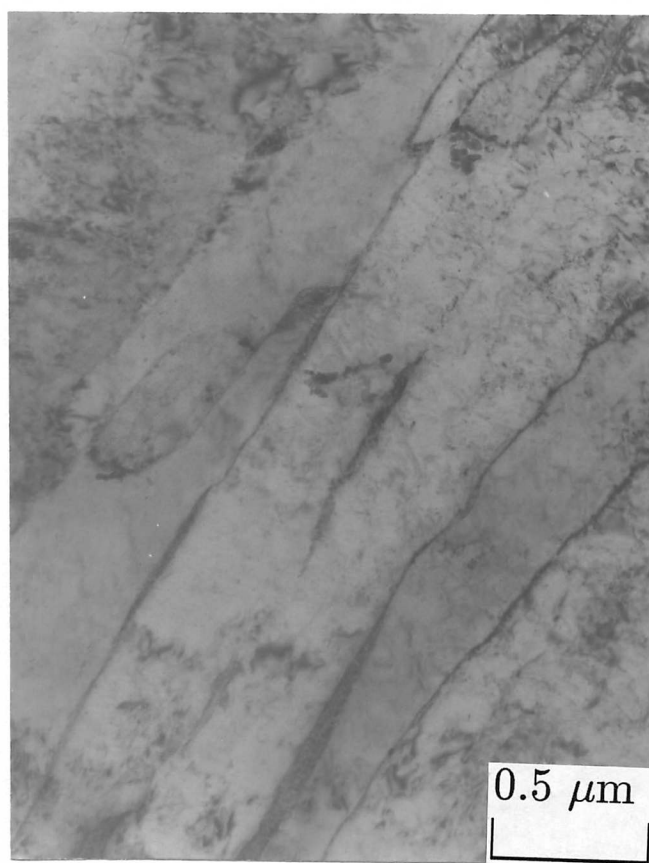


Fig. 4.4: Transmission electron micrographs showing films of austenite. (a) Alloy C: films of austenite between sub-units of bainitic ferrite, in a sample transformed isothermally at 400 °C. (b) As above, but isothermally transformed at 300 °C. (c) Lower carbon alloy E transformed isothermally at 400 °C.



(c)

Fig. 4.4: Transmission electron micrographs showing films of austenite. (a) Alloy C: films of austenite between sub-units of bainitic ferrite, in a sample transformed isothermally at 400 °C. (b) As above, but isothermally transformed at 300 °C. (c) Lower carbon alloy E transformed isothermally at 400 °C.

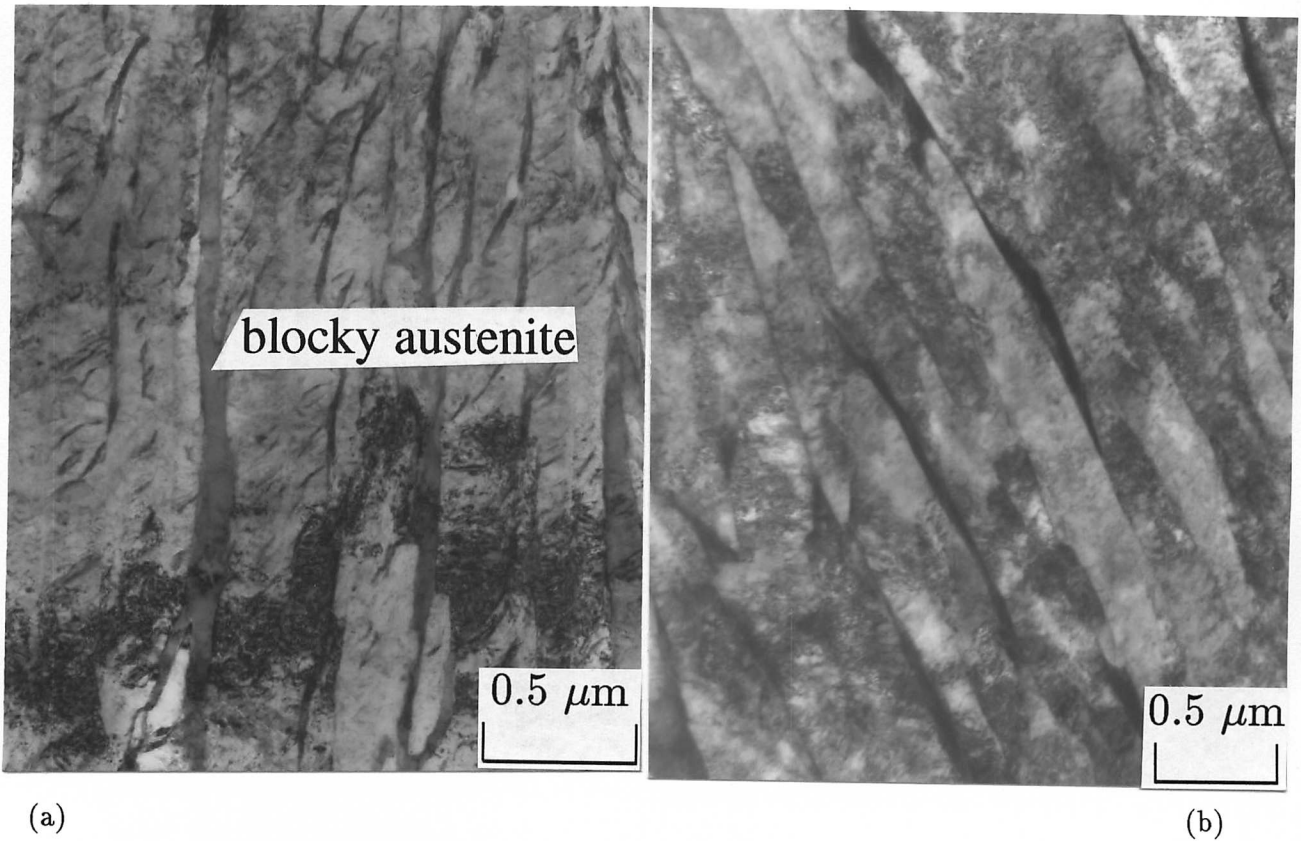
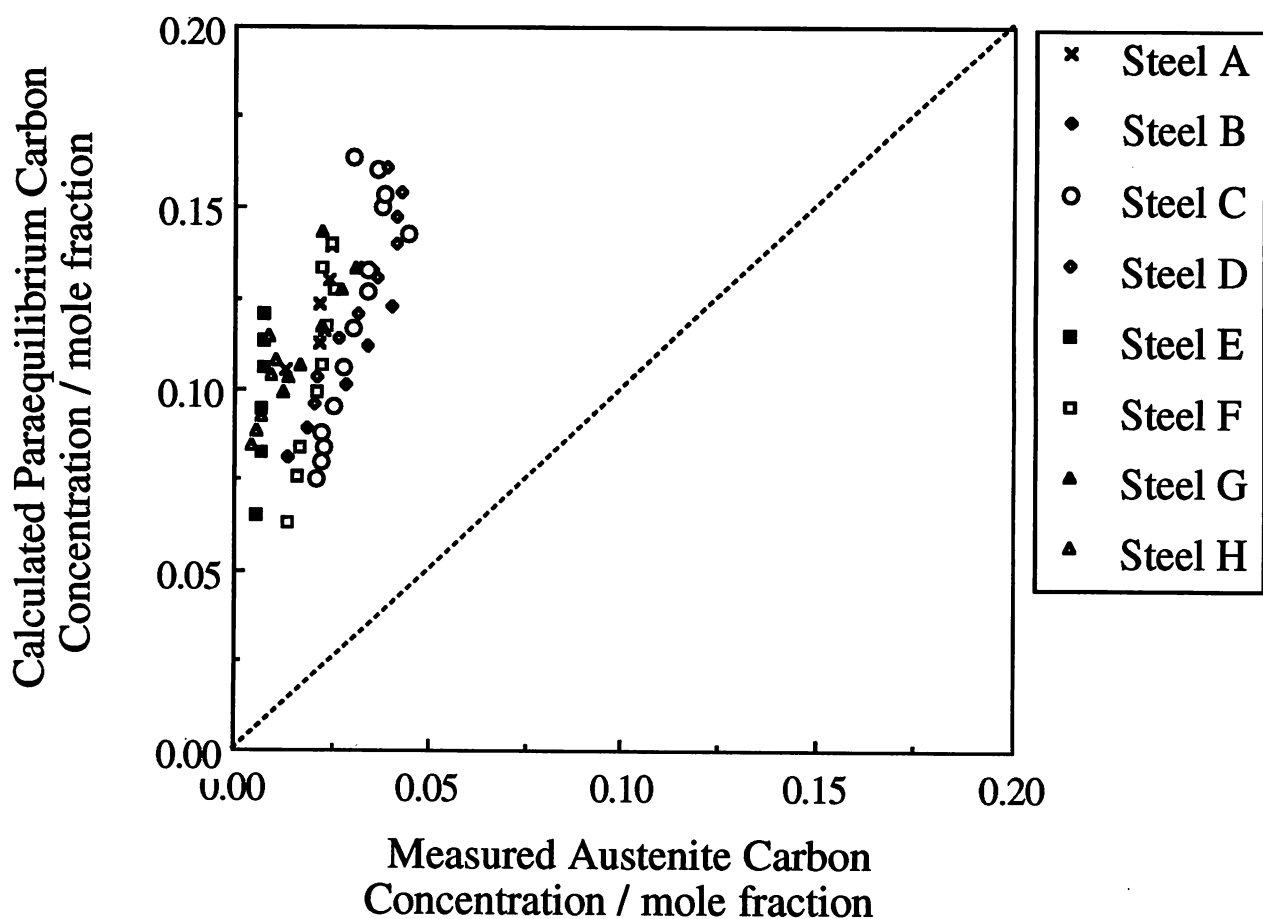
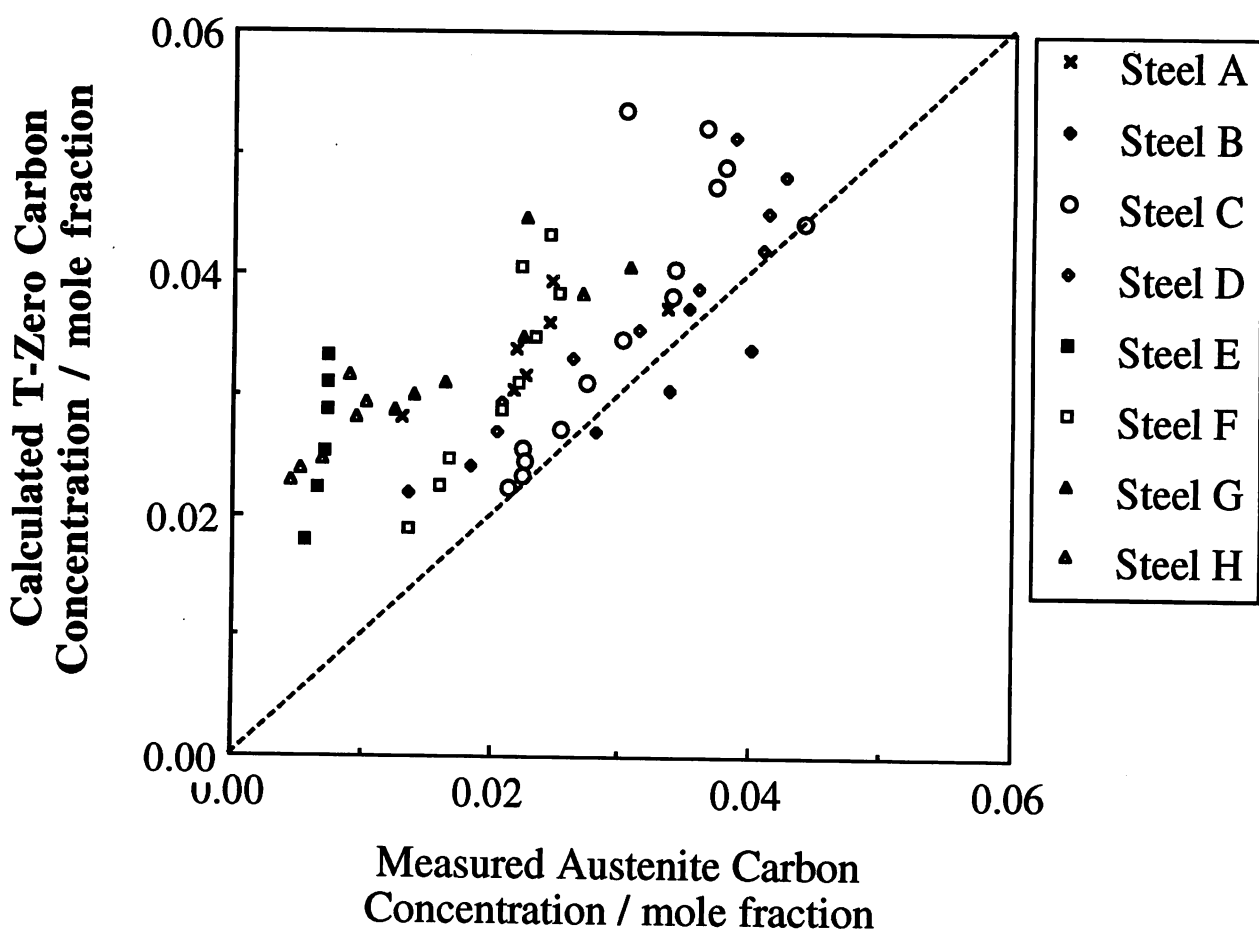


Fig. 4.5: (a) Alloy C isothermally transformed at 300 °C, showing blocks of austenite between parallel sheaves of bainite, the latter also containing films of austenite. (b) Alloy E, isothermally transformed at 380 °C. The distinction of the individual sheaf is unclear.



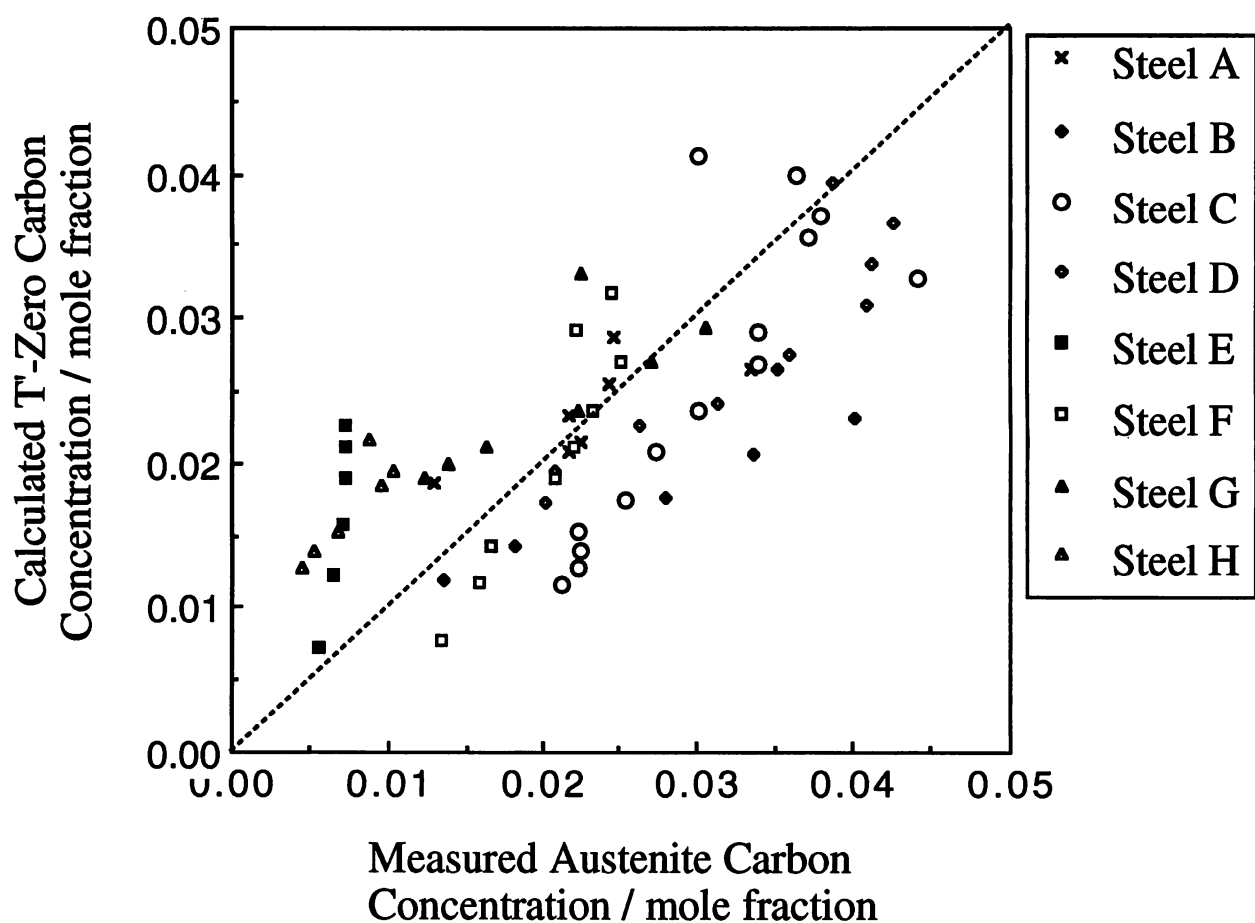
(a)

Fig. 4.6: A comparison of the measured carbon concentration of the austenite at the point where transformation to bainite stops, against a variety of calculated concentrations. (a) Comparison against the Ae'_3 condition. (b) Comparison against the T_0 condition. (c) Comparison against the T'_0 condition (note the magnified scale).



(b)

Fig. 4.6: A comparison of the measured carbon concentration of the austenite at the point where transformation to bainite stops, against a variety of calculated concentrations. (a) Comparison against the Ae'_3 condition. (b) Comparison against the T_0 condition. (c) Comparison against the T'_0 condition (note the magnified scale).



(c)

Fig. 4.6: A comparison of the measured carbon concentration of the austenite at the point where transformation to bainite stops, against a variety of calculated concentrations. (a) Comparison against the Ae'_3 condition. (b) Comparison against the T_0 condition. (c) Comparison against the T'_0 condition (note the magnified scale).

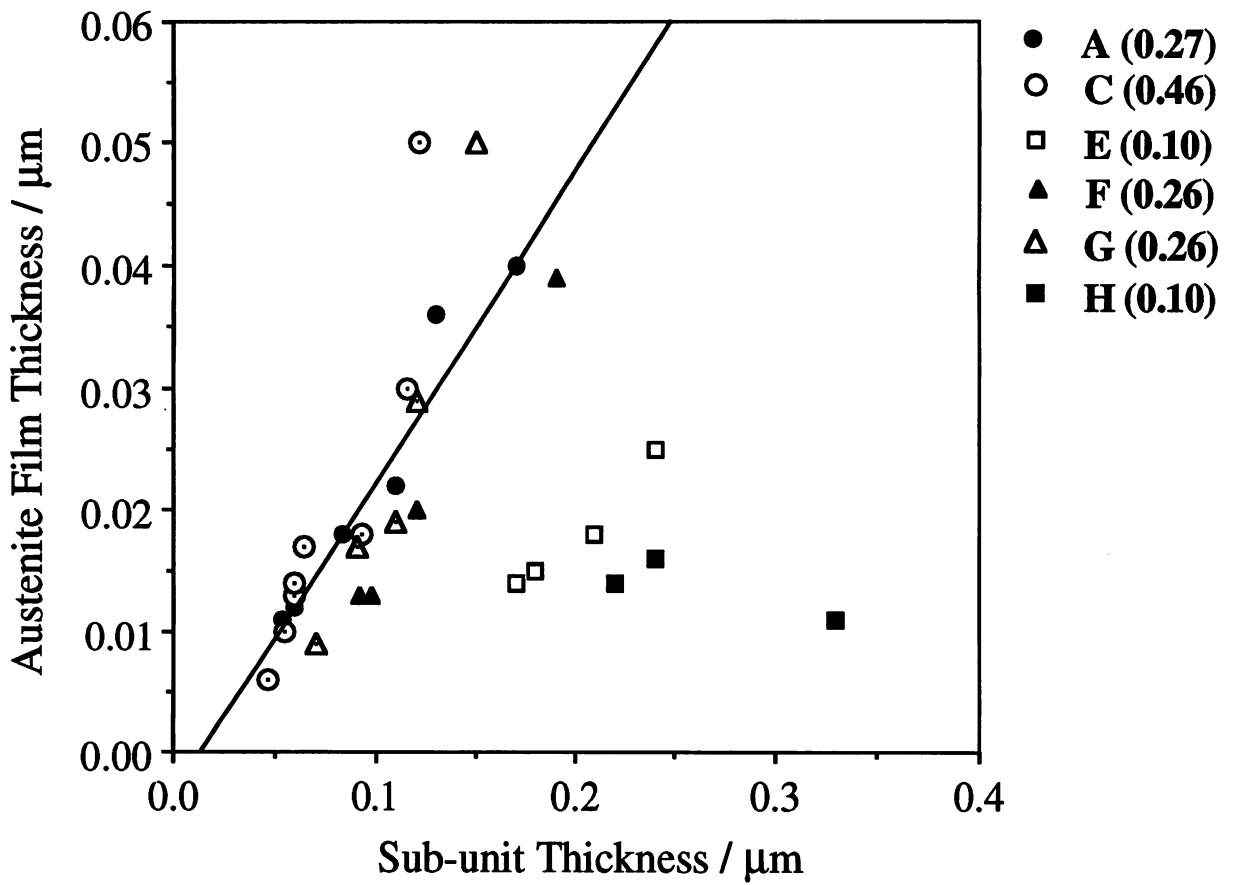


Fig. 4.7: Experimentally determined austenite film thickness as a function of the thickness of the adjacent ferrite plate, for a variety of steels and transformation temperatures. The bracketed numbers represent the carbon concentrations, in wt.%, of the alloys concerned. The best fit line is determined by the data from the steels except steels E and H which both contain 0.1 wt.% carbon.

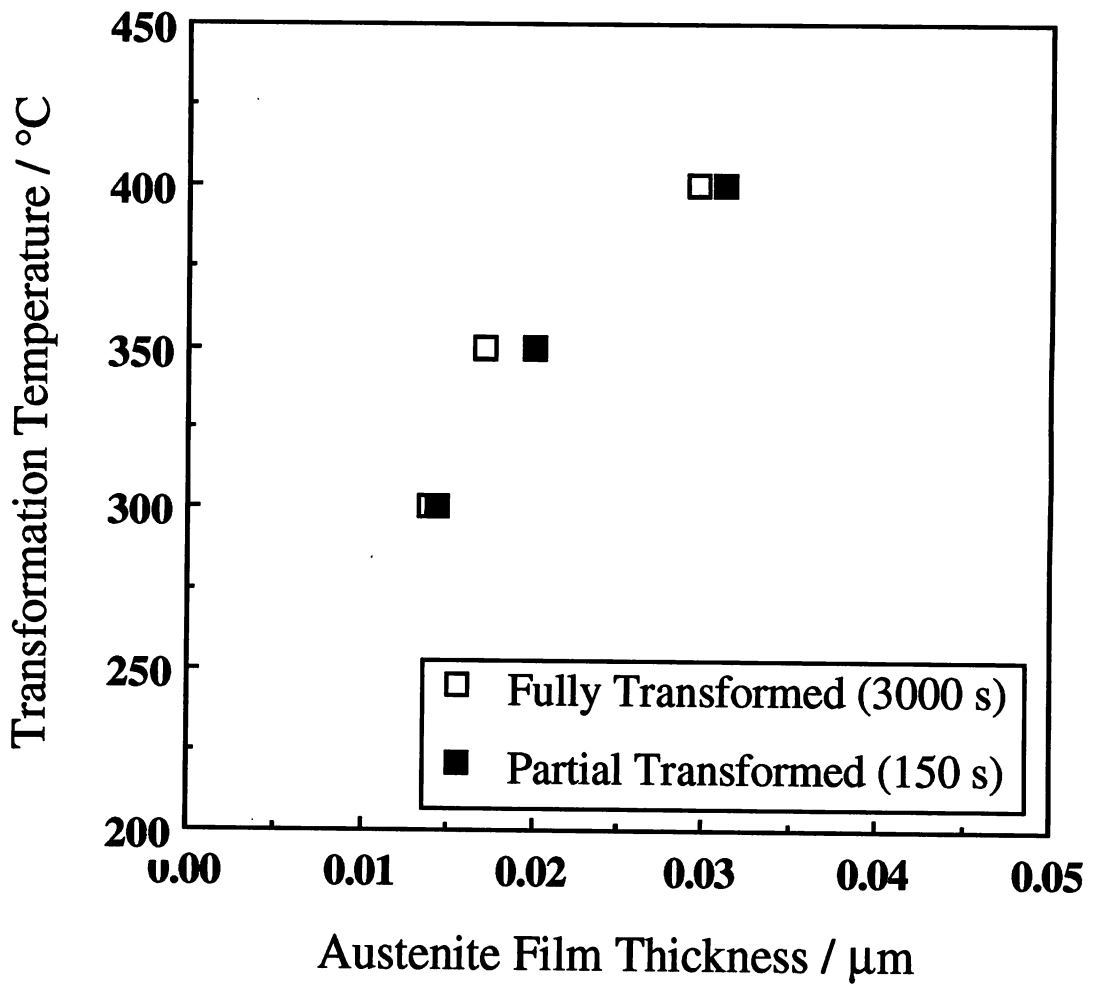


Fig. 4.8: Measured thickness of films of austenite in the partial (150 s) and fully transformed specimens for alloy C at the temperatures of 300 °C, 350 °C and 400 °C. The two sets of data are essentially identical.

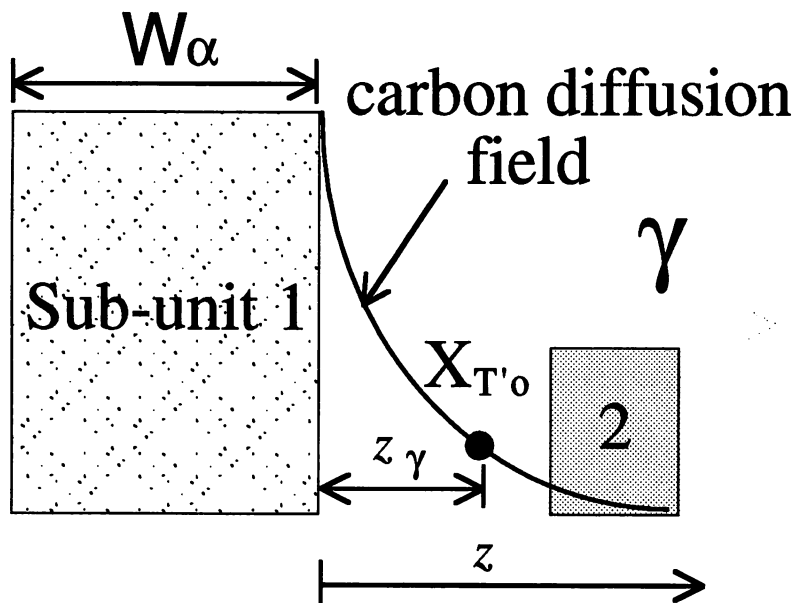
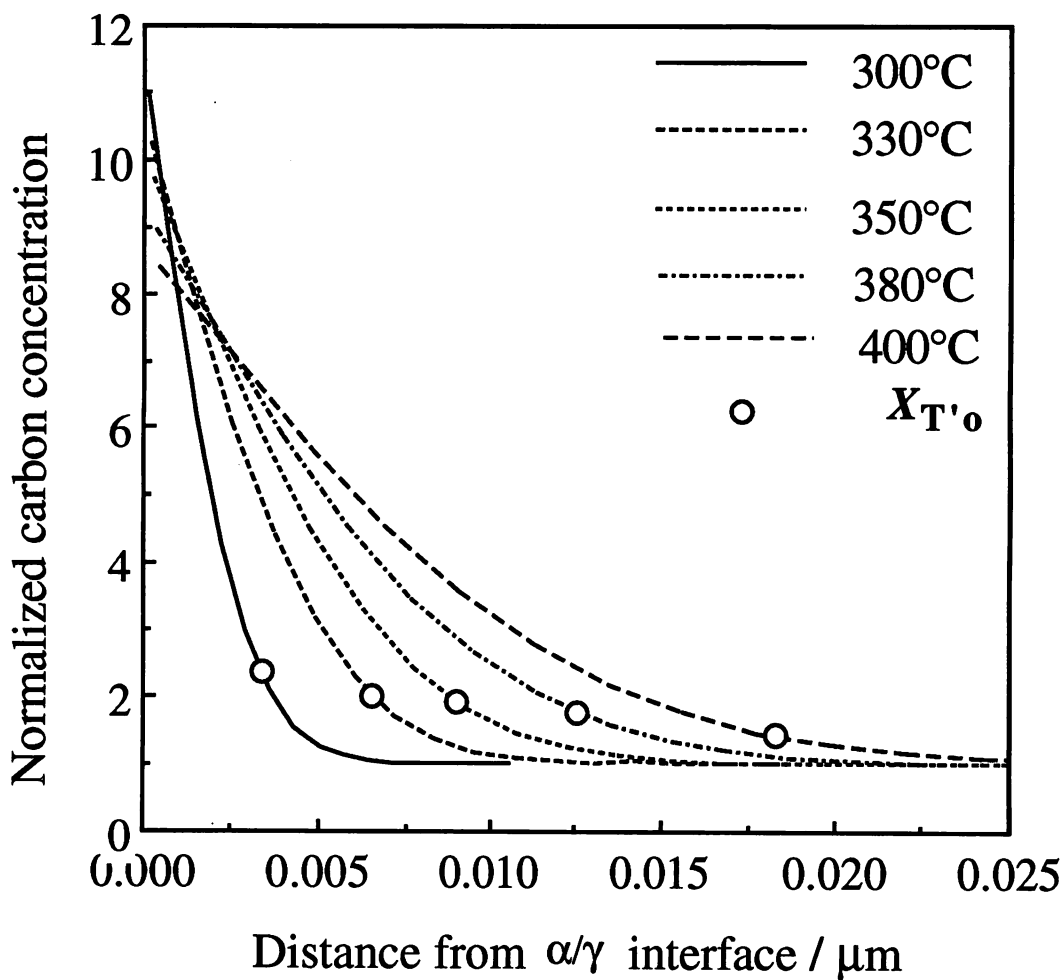
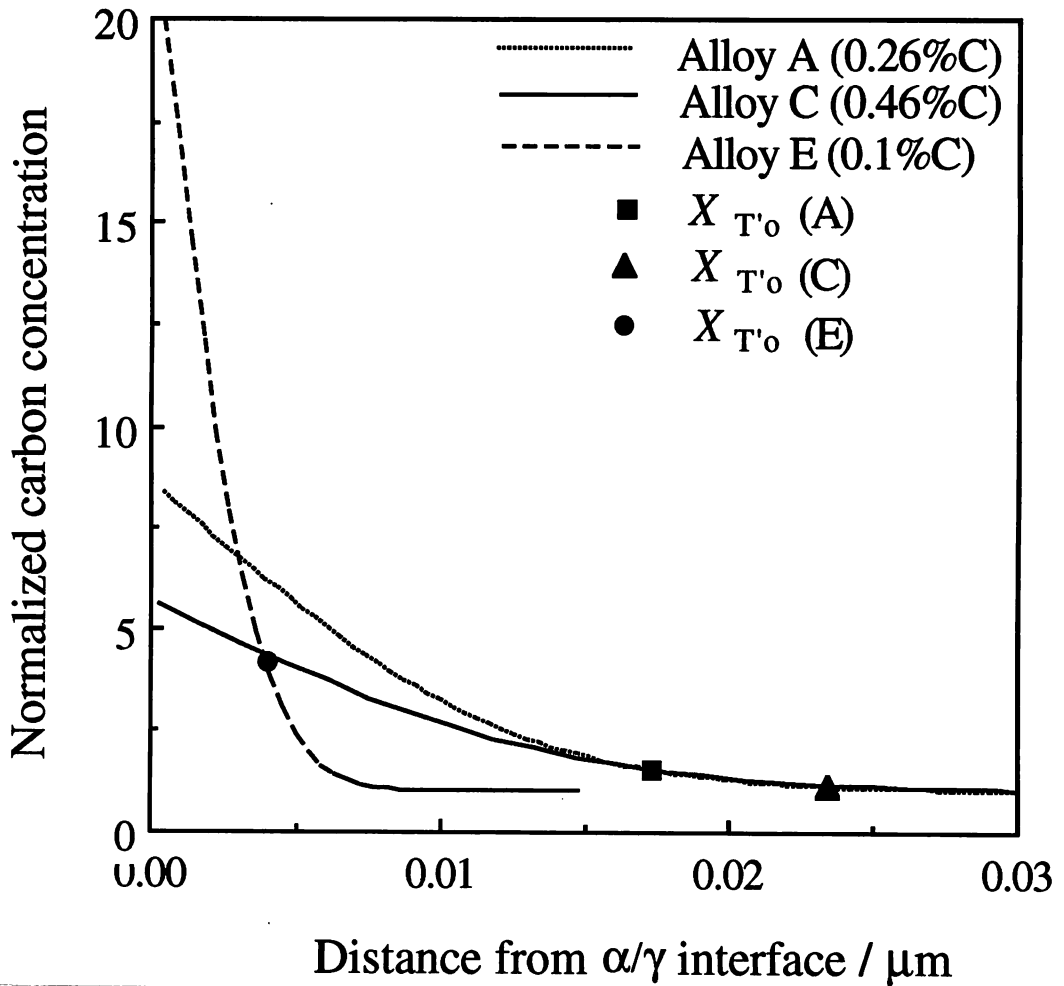


Fig. 4.9: Schematic illustration of the method used in estimating the thickness of austenite films. Sub-unit 1 forms first, and sub-unit 2 is allowed to approach it to the point where $x_\gamma \leq x_{T'_0}$. The distance of this point from sub-unit 1 is denoted z_γ .



(a)

Fig. 4.10: (a) Carbon concentration variation in austenite (Alloy A) as a function of the transformation temperature, together with the corresponding values (circles) of $x_{T'_0}$ for each temperature. (b) Carbon concentration variation in austenite (Alloys A, C and E) as a function of alloy chemistry for particular transformation temperatures (400 °C), together with the corresponding values (points) of $x_{T'_0}$.



(b)

Fig. 4.10: (a) Carbon concentration variation in austenite (Alloy A) as a function of the transformation temperature, together with the corresponding values (circles) of $x_{T'_0}$ for each temperature. (b) Carbon concentration variation in austenite (Alloys A, C and E) as a function of alloy chemistry for particular transformation temperatures (400 °C), together with the corresponding values (points) of $x_{T'_0}$.

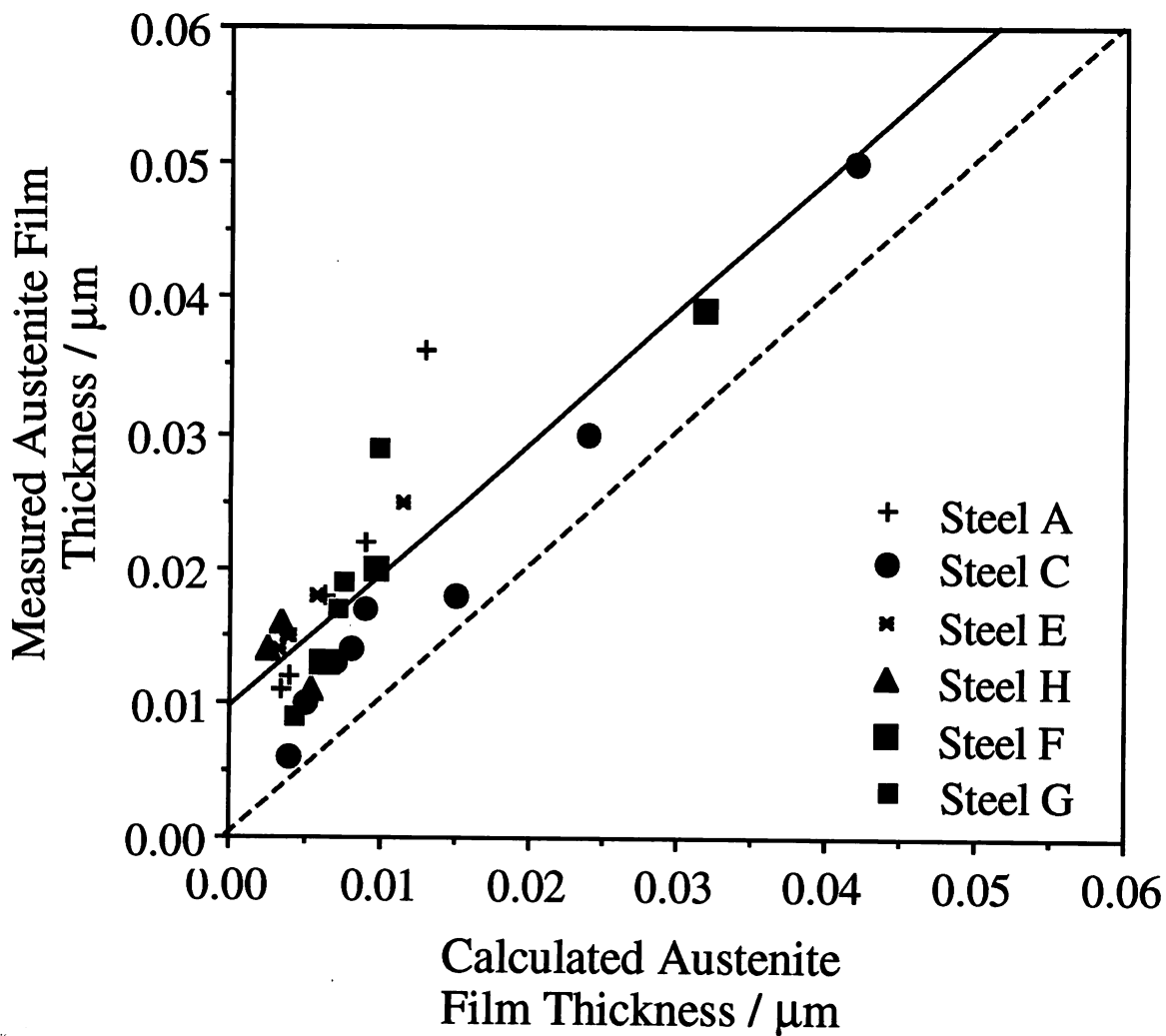
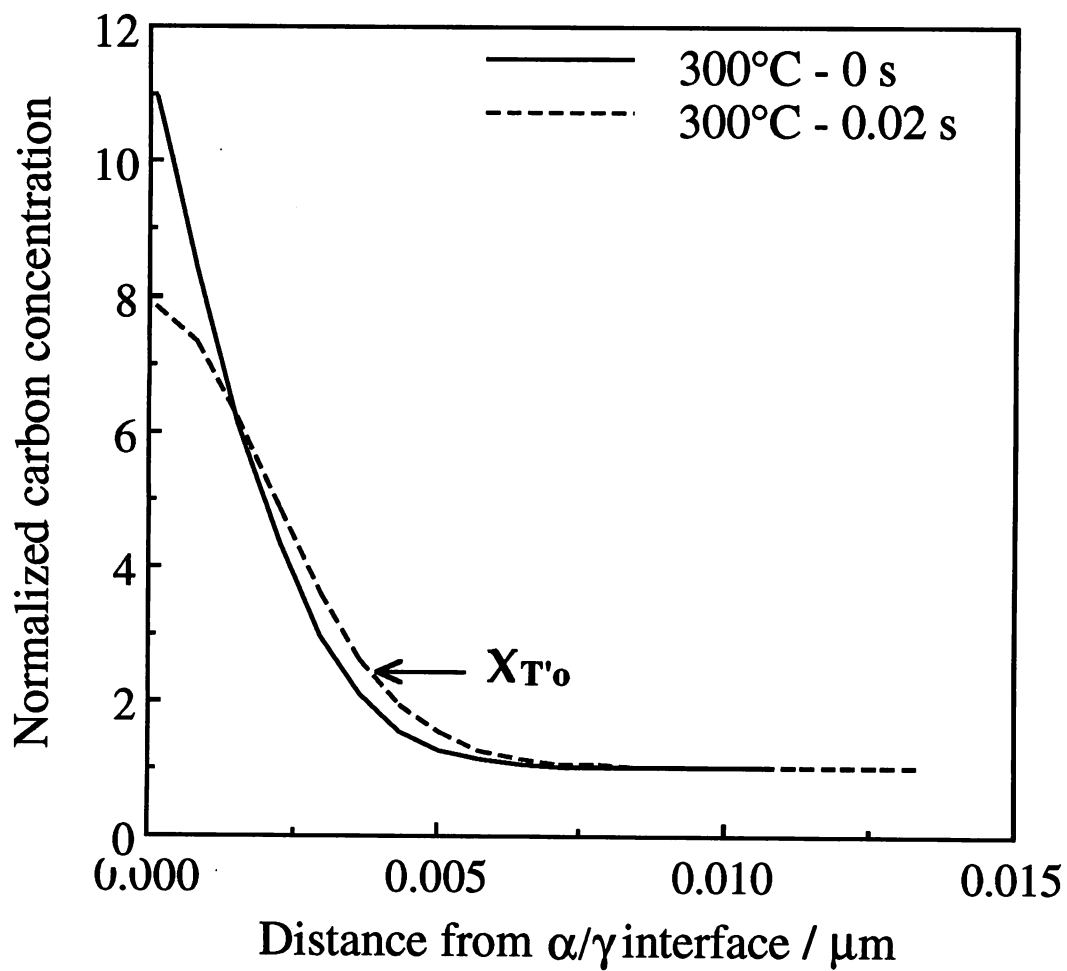
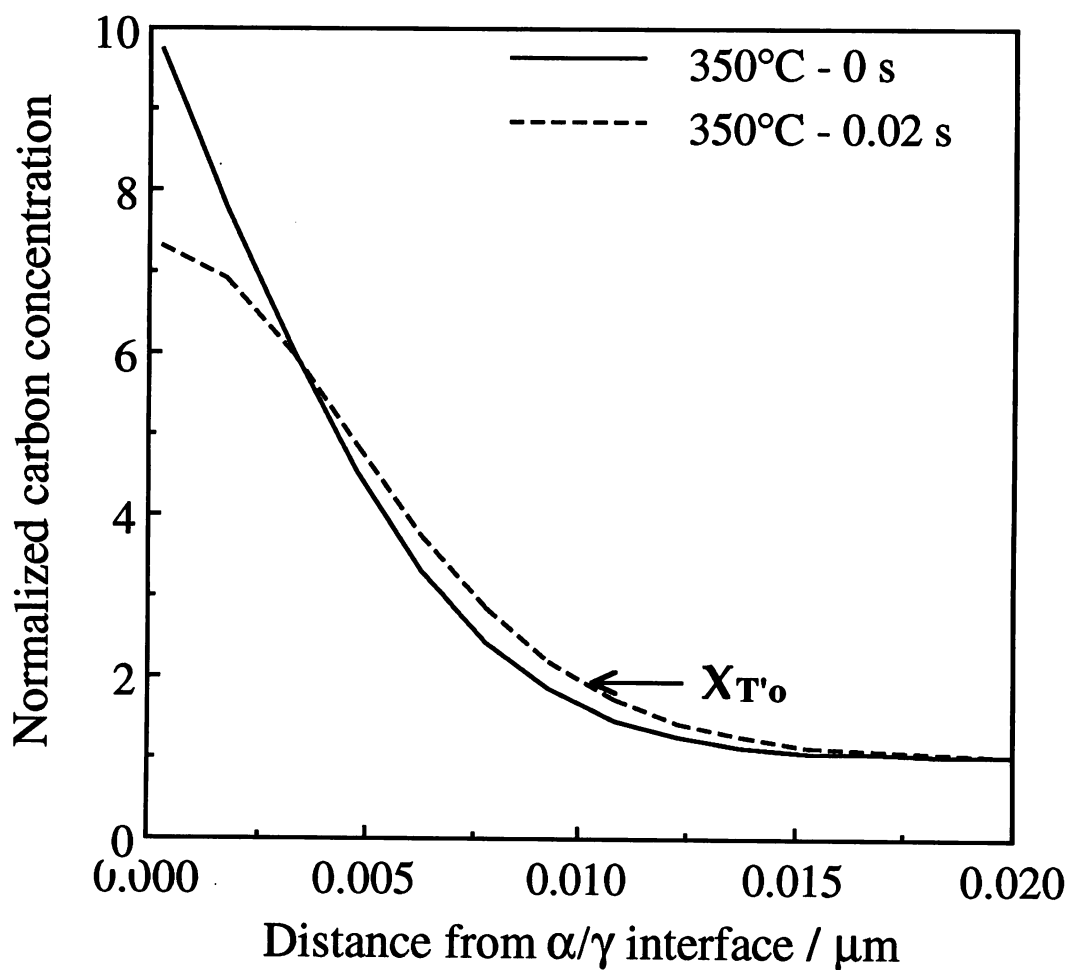


Fig. 4.11: Comparison of the measured and calculated austenite film thicknesses for a variety of alloys.



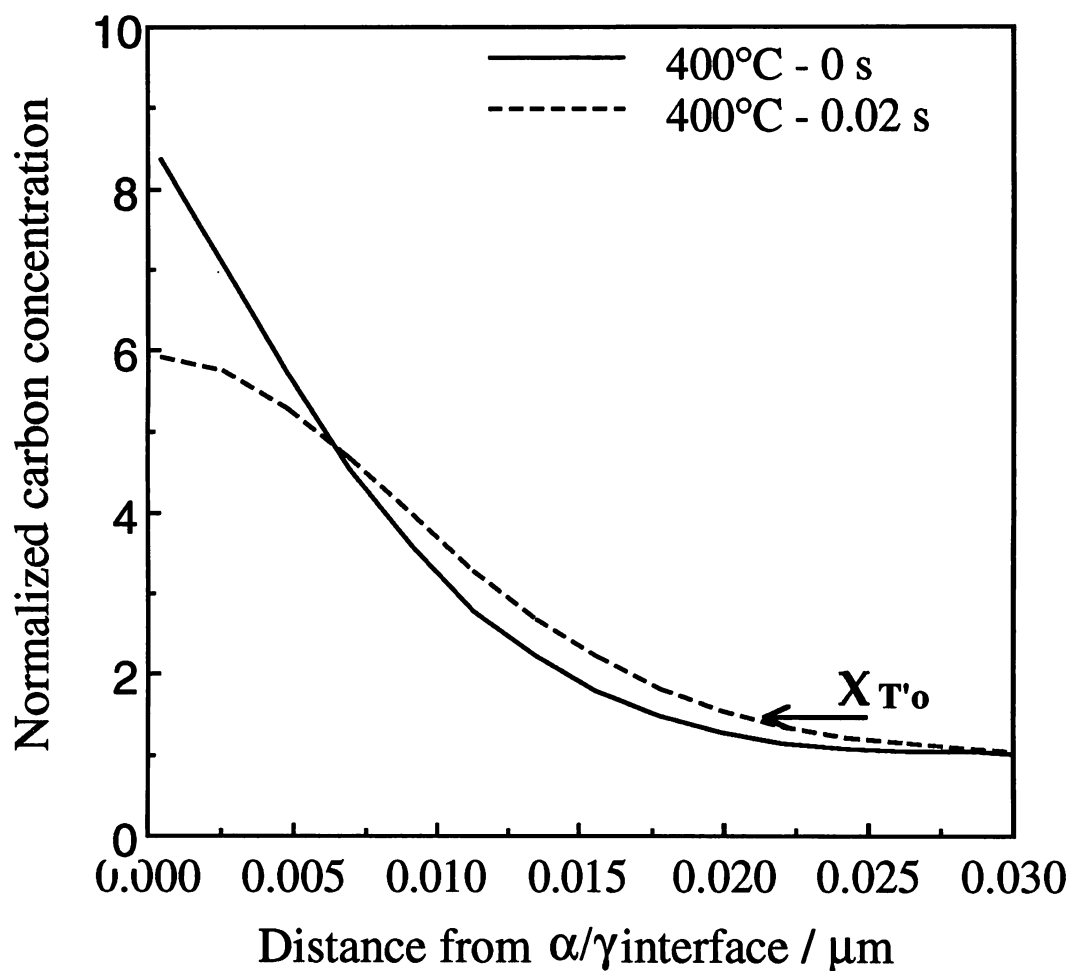
(a)

Fig. 4.12: Finite difference calculations showing the homogenisation of the carbon concentration profiles for Alloy A, as a function of the temperature and time. The $x_{T'_0}$ values are also indicated. (a) At 300 °C. (b) At 350 °C. (c) At 400 °C.



(b)

Fig. 4.12: Finite difference calculations showing the homogenisation of the carbon concentration profiles for Alloy A, as a function of the temperature and time. The $x_{T'o}$ values are also indicated. (a) At 300°C . (b) At 350°C . (c) At 400°C .



(c)

Fig. 4.12: Finite difference calculations showing the homogenisation of the carbon concentration profiles for Alloy A, as a function of the temperature and time. The $x_{T'o}$ values are also indicated. (a) At 300 °C. (b) At 350 °C. (c) At 400 °C.

CHAPTER 5

THE MICROSTRUCTURE OF LOWER BAINITE FORMED AT A LARGE UNDERCOOLING BELOW THE BAINITE-START TEMPERATURE

5.1 INTRODUCTION

It is often observed, though rarely highlighted or reported, that lower bainitic microstructures can contain a strongly bimodal size-distribution of plates. A few coarse plates can be observed on an optical scale, whereas the remaining microstructure consists of much finer plates which can only be resolved using transmission electron microscopy [Bhadeshia, 1979; Bhadeshia *et al.*, 1979a; Padmanabhan and Wood, 1984]. This is also a feature of lath martensitic microstructures, where a few coarse plates can be observed on an optical scale, whereas the remaining microstructure consists of much finer plates which can only be resolved using transmission electron microscopy [Bhadeshia *et al.*, 1979c].

It was necessary during the course of the same experiments on the design of high-strength steels, for us to undertake a detailed characterisation of the bainitic microstructures of a series of alloys. These experiments revealed a mechanism for the generation of the bimodal size distribution; it is these results which are reported in this chapter. In addition, an analysis of the temperature at which lower bainite first forms, (LB_S) temperatures, was conducted to reveal the effect of silicon, which tends to retard the precipitation of cementite.

5.2 EXPERIMENTAL METHODS

The chemical compositions of the experimental alloys are given in Table 2.1. Transformation experiments were performed using the thermomechanical simulator *Thermecmaster-Z*, as described earlier. While for the alloy with only 0.095 wt.% of carbon, the heat treatments could not be conducted in the thermomechanical simulator because of inadequate hardenability. The alloy was therefore heat treated using a salt bath, in order to reach the desired isothermal transformation temperature without spurious transformation at elevated temperatures. After completion of the desired heat treatment in the salt bath, the samples were quenched into water at ambient temperature.

5.3 RESULTS AND DISCUSSION

5.3.1 Transformation Temperatures

Extensive routine metallography, and dilatometric experiments were carried out to determine the upper and lower bainite transformation temperatures and the martensite-start

temperatures (B_S , LB_S and M_S respectively). These studies were conducted at isothermal transformation temperature intervals of 20 °C, which therefore represents the relative accuracy of the bainite–transformation–start temperatures. The results are plotted against only the carbon concentration in Fig. 5.1 and tabulated in Table 5.1. Note that the LB_S temperature reported in Table 5.1 was measured in partially transformed specimens. Otherwise, mixed microstructures of upper and lower bainite are possible in the range $B_S \rightarrow LB_S$. This is because the carbon–enrichment of the austenite caused by upper bainitic transformation can result in the subsequent formation of lower bainite [Takahashi and Bhadeshia, 1990].

It is interesting that in all cases, the lower bainite–start temperature is found to be quite close to that of martensite. The silicon, which is contained in all the steels examined, has the effect of retarding cementite precipitation [Owen, 1954], ^{and} appears to be responsible for depressing the LB_S temperature. It has been suggested [Takahashi *et al.*, 1990] that there is no fundamental difference in the transformation mechanism for these two forms of bainite. The bainitic ferrite grows supersaturated with carbon. The excess carbon may then partition into the residual austenite or precipitate in the ferrite in the form of carbides. If the latter process is dominant, lower bainite is obtained. Upper bainite is obtained only when carbon partitions relatively rapidly into the residual austenite, before the carbides have an opportunity to precipitate. The presence of silicon in steel will therefore prolong the time for the precipitation of cementite, and favour the formation of upper bainite. The present results are consistent with this model.

LB_S temperatures have been reasonably predicted in ^{the} Fe-C system and one high silicon steel by comparing the time needed for ferrite-decarburation and for precipitation in bainitic ferrite sub-units [Takahashi *et al.*, 1990]. If the former is larger, then lower bainite is obtained and *vice versa*. However, the precipitation of cementite in carbon rich ferrite has not been modelled except for Fe-0.43C-2.0Si-3.0Mn (wt.%) alloy. The cementite precipitation parameters published for this alloy are employed in the present work. The details of calculations can be found elsewhere [Takahashi and Bhadeshia, 1990] and are not repeated here. The calculated results (Table 5.2), except alloy C, show the absence of lower bainite. This discrepancy is not surprising since the effect of alloying elements on cementite precipitation could not be properly taken into account and, also, the choice of detectable volume fraction of cementite, 0.01 [Takahashi *et al.*, 1990], is uncertain. Nevertheless, the trend is correct: the addition of silicon effectively shifts the LB_S temperature toward M_S , as observed experimentally.

Table 5.1: The measured transformation–start temperatures (°C).

Alloy	B_S	LB_S	M_S
A	400	325	300
B	460	330	300
C	510	300	260
D	450	280	245
E	540	390	350
F	540	360	315
G	450	340	320
H	460	390	370

Regression analysis confirms the role of silicon. The present data^{and} these from Llopis [1977], Pickering [1967] gave the equation which is illustrated in Fig. 5.2:

$$LB_S (^{\circ}C) = 500 - (155 \pm 40) C - (38 \pm 14) Si - (17 \pm 13) Mn \\ - (4 \pm 11) Ni - (10 \pm 13) Cr - (5 \pm 20) Al - (4 \pm 56) Co \quad (5.1)$$

where the compositions of all the elements are in wt.%. The correlation coefficient (R) of 0.89 indicates rather good correlation. Silicon clearly depresses the LB_S temperatures more effectively than any other element except carbon.

Table 5.2: The calculated results for lower bainite–start temperatures.

Alloy	LB_S
A	No Lower Bainite
B	No Lower Bainite
C	No upper Bainite
D	No Lower Bainite
E	No Lower Bainite
F	No Lower Bainite
G	No Lower Bainite
H	No Lower Bainite

5.3.2 New Metallographic Observations

It is not necessary to record the routine metallography which was used in order to determine the transformation temperatures. However, some particularly interesting observations

were made during the formation of lower bainite at temperatures close to M_S ; these are discussed below.

Considering the lowest carbon alloy (H) first, lower bainite forms during isothermal transformation at temperatures less than 390 °C (Table 5.1), the martensite-start temperature being 370 °C .

Fig. 5.3a is a montage of a sample transformed isothermally at 380 °C, a temperature which is just 10 °C above M_S . The transformation begins with the formation of the usual small sub-units of lower bainite at an austenite grain boundary (illustrated at higher magnification in Fig. 5.3b), but the sub-units then coalesce to form a single larger plate. The coalescence is accompanied by a thinning of the austenite films between the lower bainite sub-units, until they eventually vanish as the sub-units develop into the coarser structure.

This striking change in the form of growth can in fact be understood when transformation happens at a large undercooling below the B_S temperature. There is then a large austenite grain boundary nucleation rate, giving rise to the numerous adjacent sub-units, the collection of sub-units being the classical sheaf of bainite. Given that the adjacent sub-units are all in identical orientation, there is no reason why they should not combine and grow as a single unit, assuming that:

- (a) there is sufficient chemical driving force to sustain the larger amount of strain energy associated with a thicker plate;
- (b) there is nothing to stifle the lengthening of the sub-units.

The first condition is satisfied because the transformation illustrated in Fig. 5.3 has occurred at the largest feasible undercooling below B_S (*i.e.* only 10 °C above M_S). The chemical driving force available for diffusionless transformation at that temperature, for alloy H, is estimated to be:

$$\Delta G^{\gamma\alpha} = -1149 \quad \text{J mol}^{-1}$$

This calculation was carried out using methods described elsewhere [Bhadeshia, 1982b]. The transformation is accompanied by an invariant-plane strain shape deformation with a shear component $s \simeq 0.22$ and a dilatational component directed normal to the habit plane of $\delta \simeq 0.03$.; If this is elastically accommodated then Christian [1958] has shown that the resulting strain energy G_S is the combination of dilatational component, G_{S1} , and shear component, G_{S2} , which were shown, respectively, to be:

$$G_{S1} = \frac{\mu V_m}{1 - \nu} \frac{\pi c}{4a} (\delta^2) \quad (5.2)$$

$$G_{S2} = \frac{\mu V_m}{1 - \nu} \frac{\pi c}{8a} (2 - \nu) s^2 \quad (5.3)$$

Total strain energy, G_S , associated with the formation of bainite plate is therefore given by:

$$G_S = \frac{\mu V_m}{1 - \nu} \frac{\pi c}{4a} (\delta^2 + 0.5(2 - \nu)s^2) \quad (5.4)$$

where c is the plate thickness, a is the plate length, ν is the Poisson's ratio, μ is the shear modulus of austenite, and V_m is the molar volume of the austenite. Temperature dependent elastic constants are obtained from empirical equations [Aaronson *et al.*, 1975], such that:

$$E = -18.8T + 52400 \quad \text{Cal/cm}^3 \quad (5.5)$$

$$\nu = 3.6 \times 10^{-5} + 0.284 \quad (5.6)$$

The temperature ranges valid for E (elastic modulus) and ν above are 20 °C to 540 °C and 260 °C to 595 °C, respectively. It can be demonstrated that for a chemical driving force of $\Delta G^{\gamma\alpha} = -1149 \text{ J mol}^{-1}$, a plate with an aspect ratio of $c/a \simeq 0.05$ can easily be tolerated. Because stereological effects cannot be taken into account, the likely overestimated value of the aspect ratio of the plate illustrated in Fig. 5.3a is found to be about 0.1, consistent with the calculated value.

The second condition (b) stated earlier, that the coalescence of sub-units is only possible if the growth process cannot be stifled, has several implications. It implies that such coalescence can only occur in the early stages of transformation, when the growth cannot be hindered either by hard impingement with other regions of bainite, or by soft impingement processes. For example, the carbon concentration of the austenite increases as transformation progresses. The corresponding decrease in $|\Delta G^{\gamma\alpha}|$ should render coalescence much less likely. It is obvious from Fig. 5.3a, that the coalesced plate formed first, followed by the surrounding bainite sheaves which have retained their sub-unit morphology.

Another reason why coalescence should only occur at relatively low temperatures is that the shape deformation accompanying the growth of bainite is not completely elastically accommodated. This is the reason why sub-units usually tend to reach some limiting length which is less than that of the austenite grains. Lower temperatures favour more elastic accommodation, since the yield strength of all phases increases as the temperature is reduced. Thus, the sub-units can grow to longer lengths, allowing an opportunity for coalescence to occur.

Fig. 5.3a shows that in the region adjacent to the coarse plate, the sub-units are quite long in all cases where impingement has not limited growth.

It is worth noting from Fig. 5.3a, that the films of retained austenite between the sub-units at the austenite grain surface are much thinner than that adjacent to the coalesced thick plate, as would be expected theoretically [Chapter 4].

It was possible to frequently observe coalescence effects in the microstructure, which appeared consequently to contain a bimodal distribution of plates, as illustrated in Fig. 5.4.

Exactly the same observations could be made on all the other alloys. They were really striking in the high carbon alloys, where the carbide precipitation in the bainite emphasized the coalescence, as illustrated in Fig. 5.5 for Alloy C transformed isothermally at 305 °C.

Similar coalescence effects could not be found for upper bainite, presumably because of the lower chemical driving force available at higher transformation temperatures, a greater degree of plastic accommodation of the shape deformation (due to reduced yield strength) and because the carbon would tend to partition more rapidly from supersaturated ferrite at elevated temperatures. Consequently, the distribution of plates was observed to be much more uniform, as illustrated in Fig. 5.6.

Fig. 5.7 shows a different observation, in which a thick plate of lower bainite in alloy A tends to break up in a series of sub-units at its tip. Similar observations have been reported for martensite plates [Bhadeshia *et al.*, 1979c]; such splitting is thought to occur in order to reduce the strain energy at the growing tip of the plate. Another example is illustrate in Fig. 5.8, where the remnants of the sub-unit structure can be seen clearly inside the coarse plate.

5.4 CONCLUSIONS

It is found that the fine platelets of lower bainite that nucleate at austenite grain boundaries during isothermal transformation at large undercoolings below the bainite-start temperature, tend to coalesce into coarser plates. The coalescence process is favoured by large undercoolings, and can only occur if impingement effects do not dominate at the early stages of growth. This explains the frequently observed bimodal distribution of plates found in bainitic microstructures. The effect of silicon in depressing LB_S temperatures is confirmed by theoretical calculations and regression analysis of numerous sources of data.

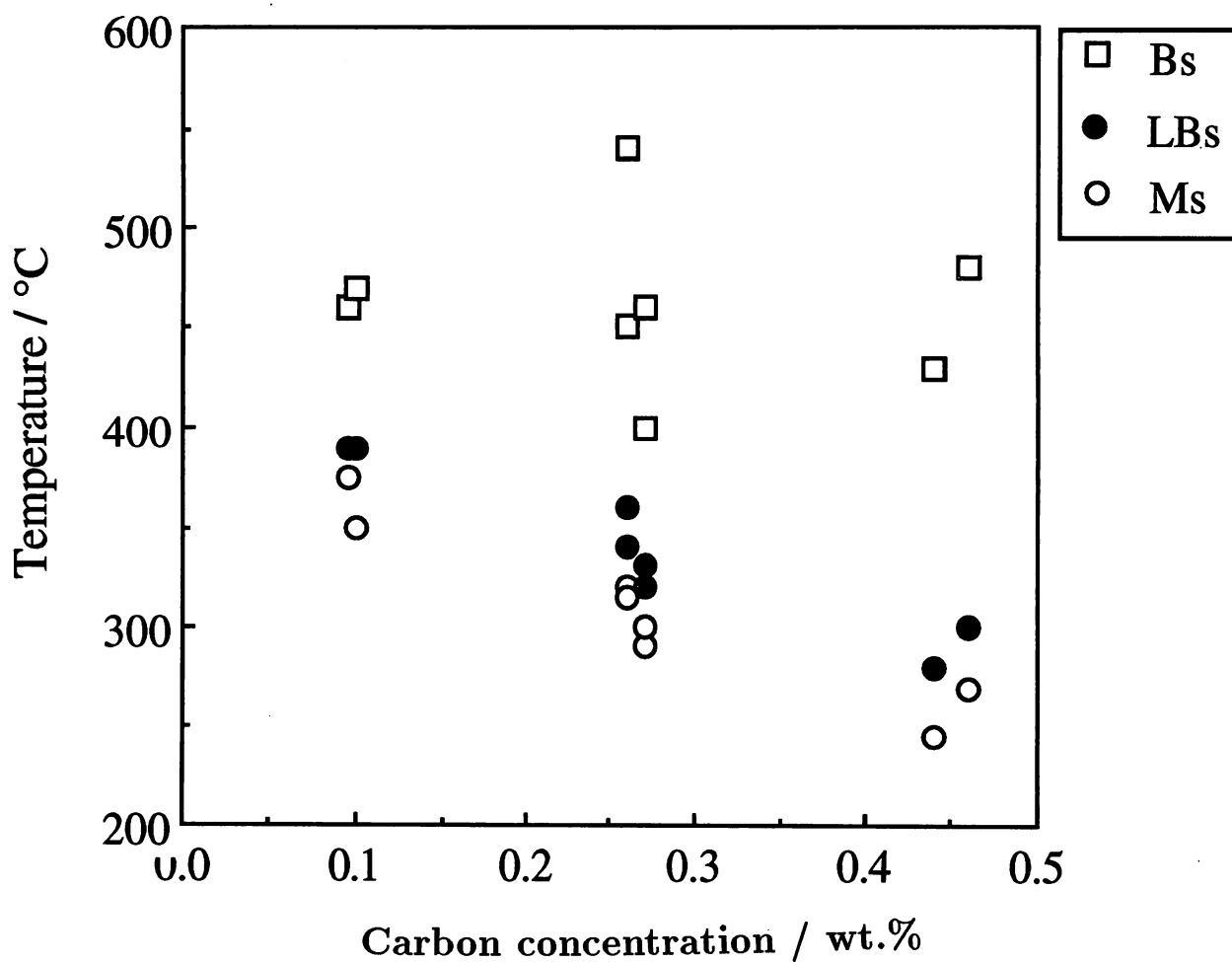


Fig. 5.1: The measured upper and lower bainite-start temperatures, and martensite-start temperatures (listed in Table 5.1), plotted as a function of the steel carbon concentration. Note that the substitutional solute content of the steels within any carbon category are not identical (Table 2.1).

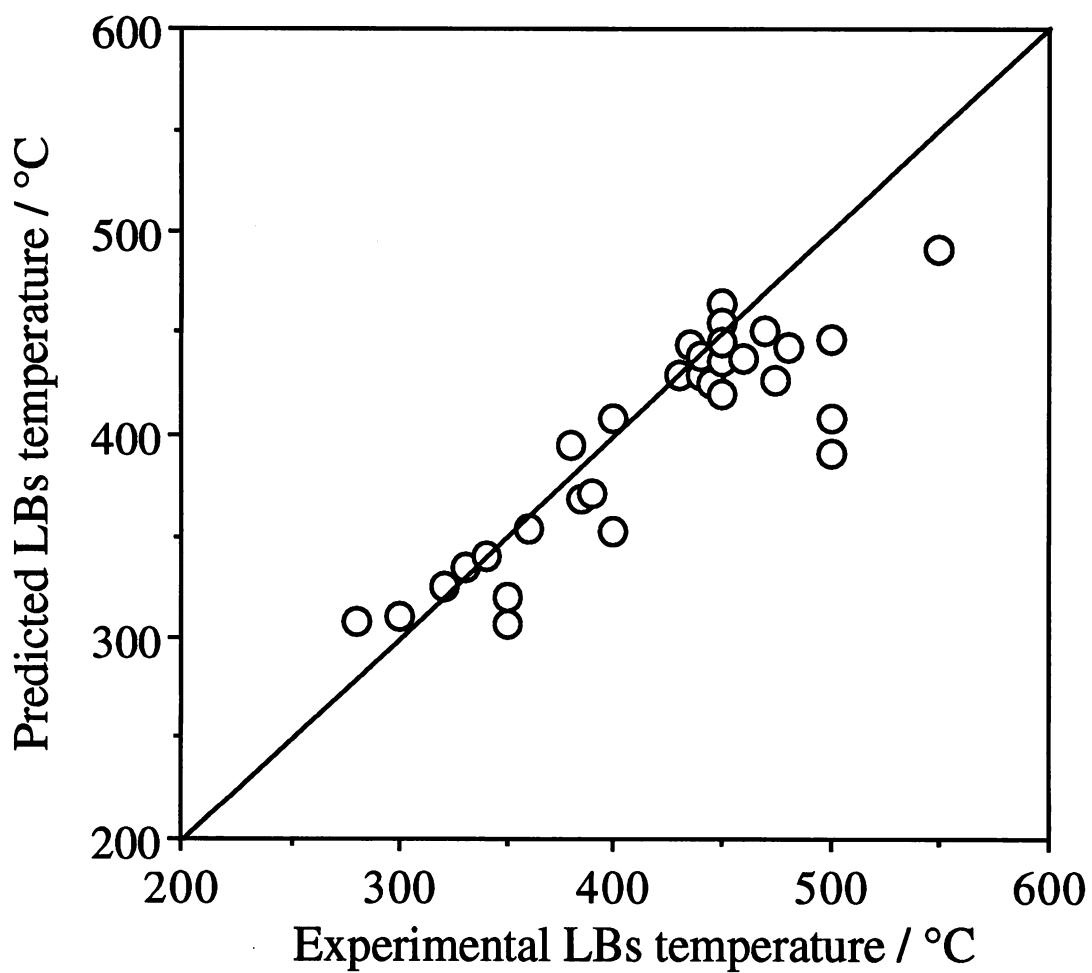
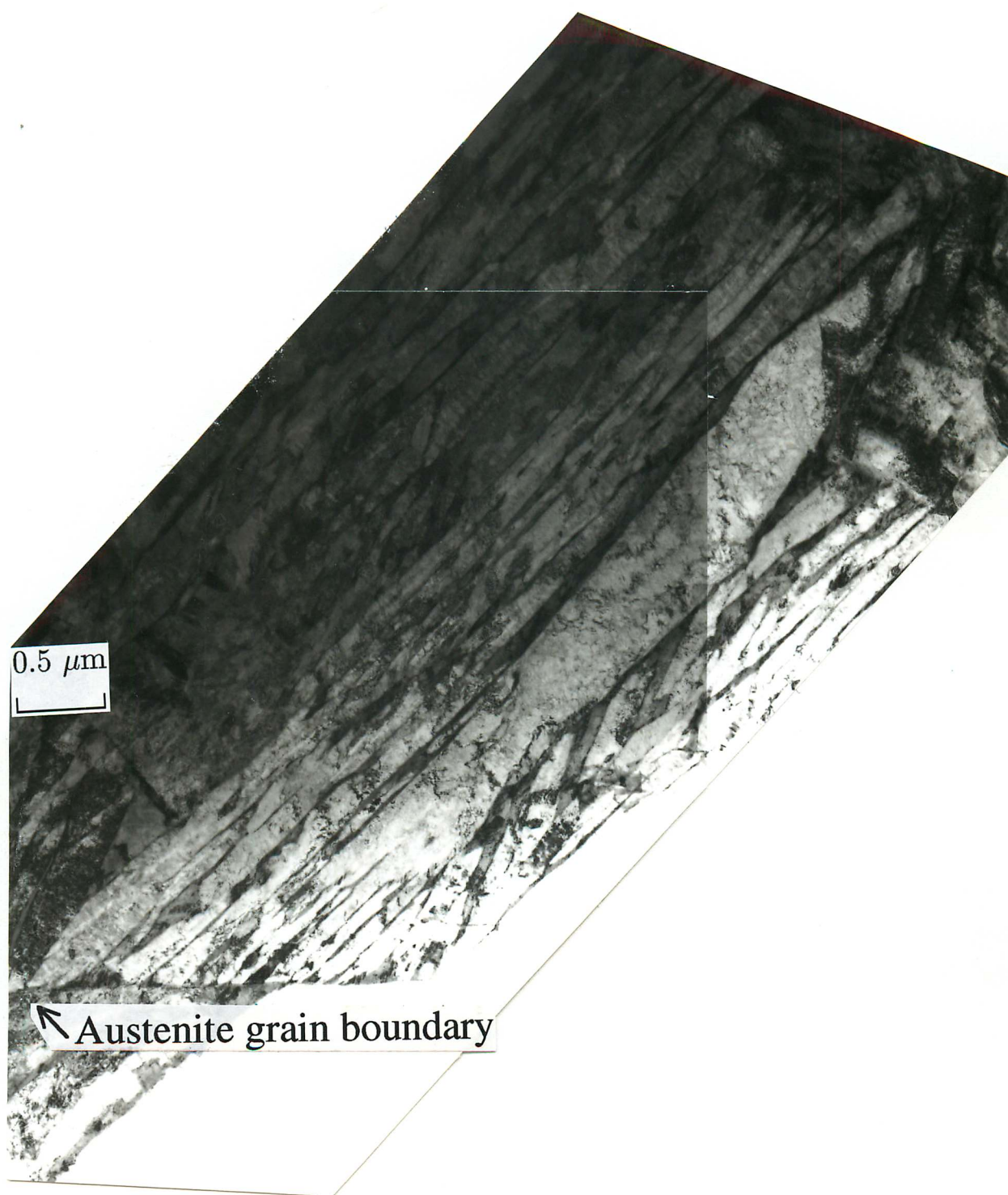
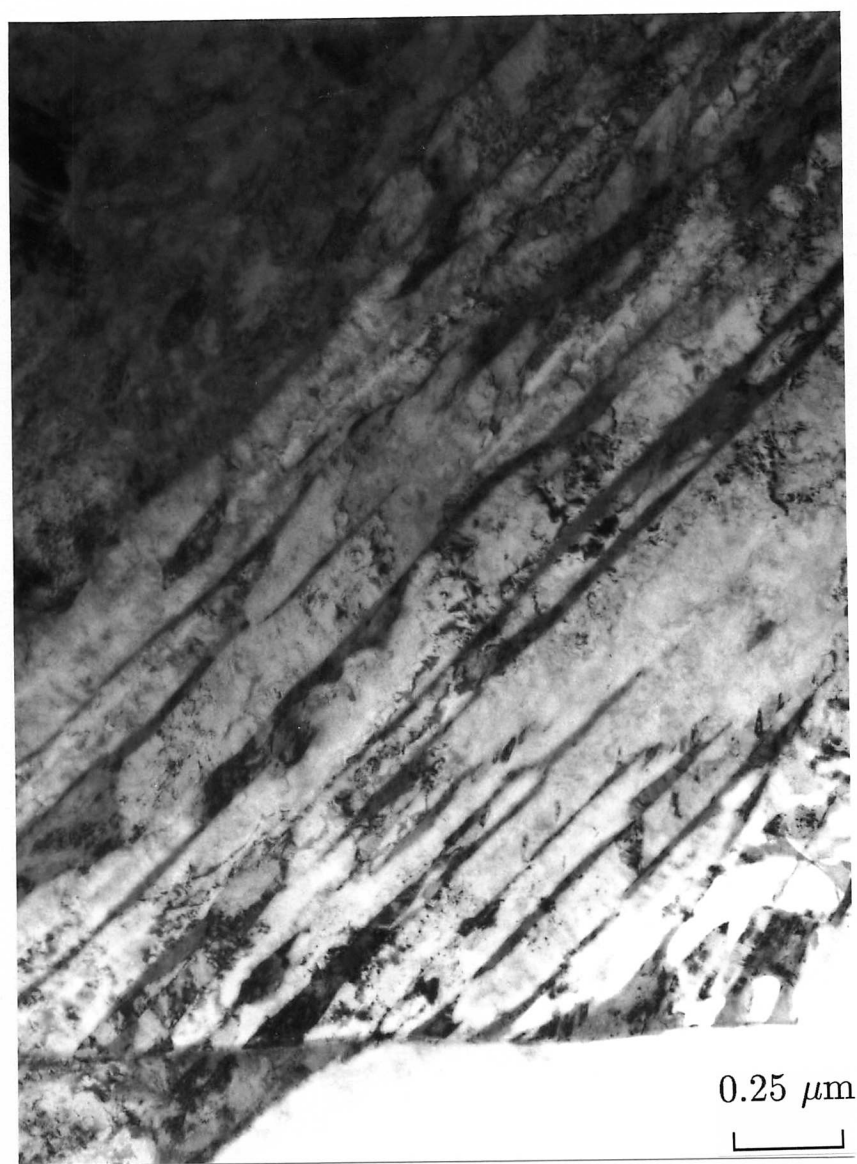


Fig. 5.2: A comparison of the experimental lower bainite-start temperatures against calculated values obtained from linear regression analysis, equation (5.1).



(a)

Fig. 5.3: Alloy H, isothermally transformed at 380 °C for 50 s before water-quenching. (a) Transmission electron micrograph montage showing the coalescence of sub-units nucleated at the austenite grain boundary, into a coarse plate of lower bainite. (b) Higher magnification transmission electron micrograph of the austenite grain boundary region, showing the carbides within the lower bainite.



(b)

Fig. 5.3: Alloy H, isothermally transformed at 380 °C for 50 s before water-quenching. (a) Transmission electron micrograph montage showing the coalescence of sub-units nucleated at the austenite grain boundary, into a coarse plate of lower bainite. (b) Higher magnification transmission electron micrograph of the austenite grain boundary region, showing the carbides within the lower bainite.

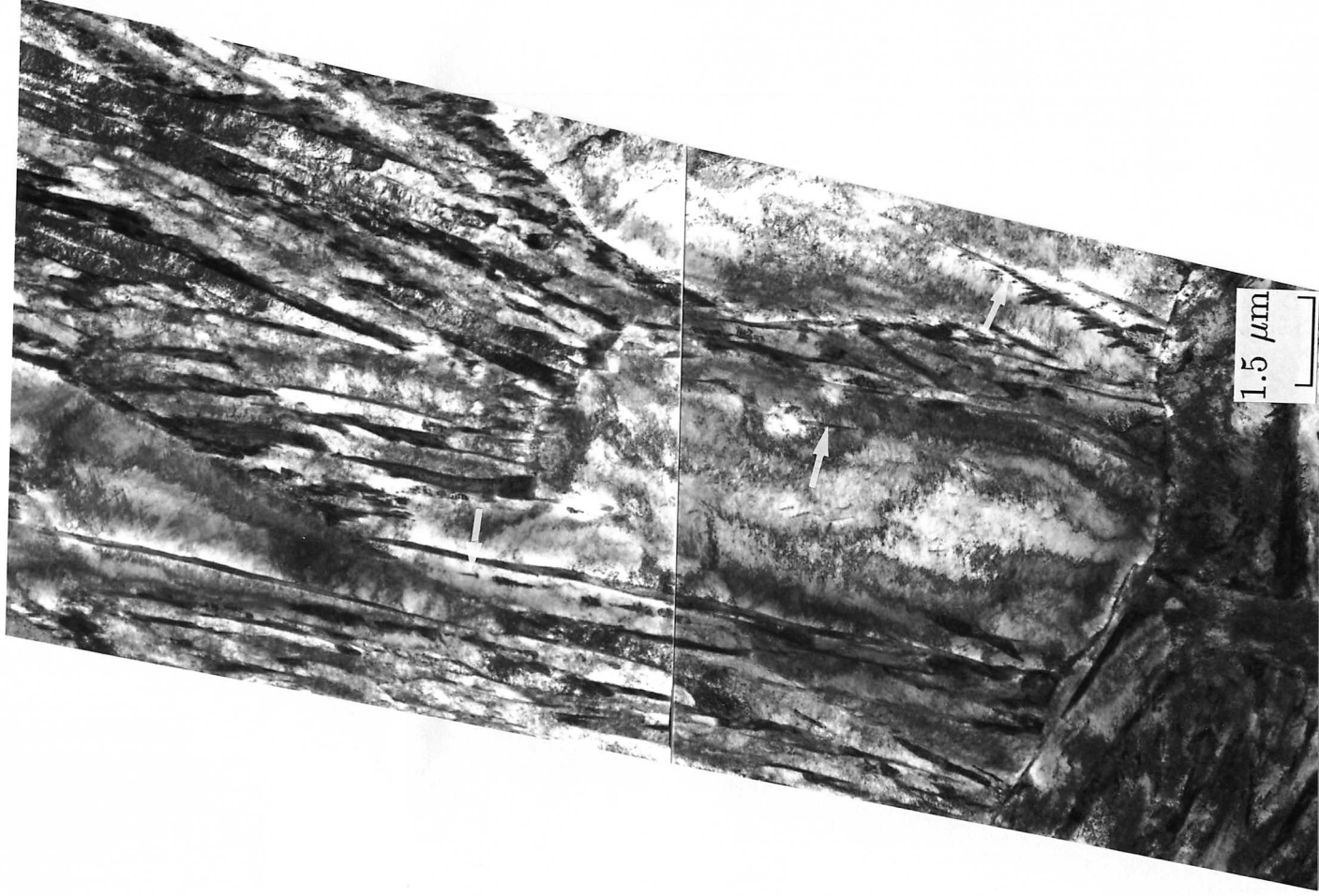


Fig. 5.4: Alloy H, isothermally transformed at 380 °C for 50 s before water-quenching. Transmission electron micrograph showing coalescence events (arrows), and illustrating the bimodal distribution of plate thicknesses.

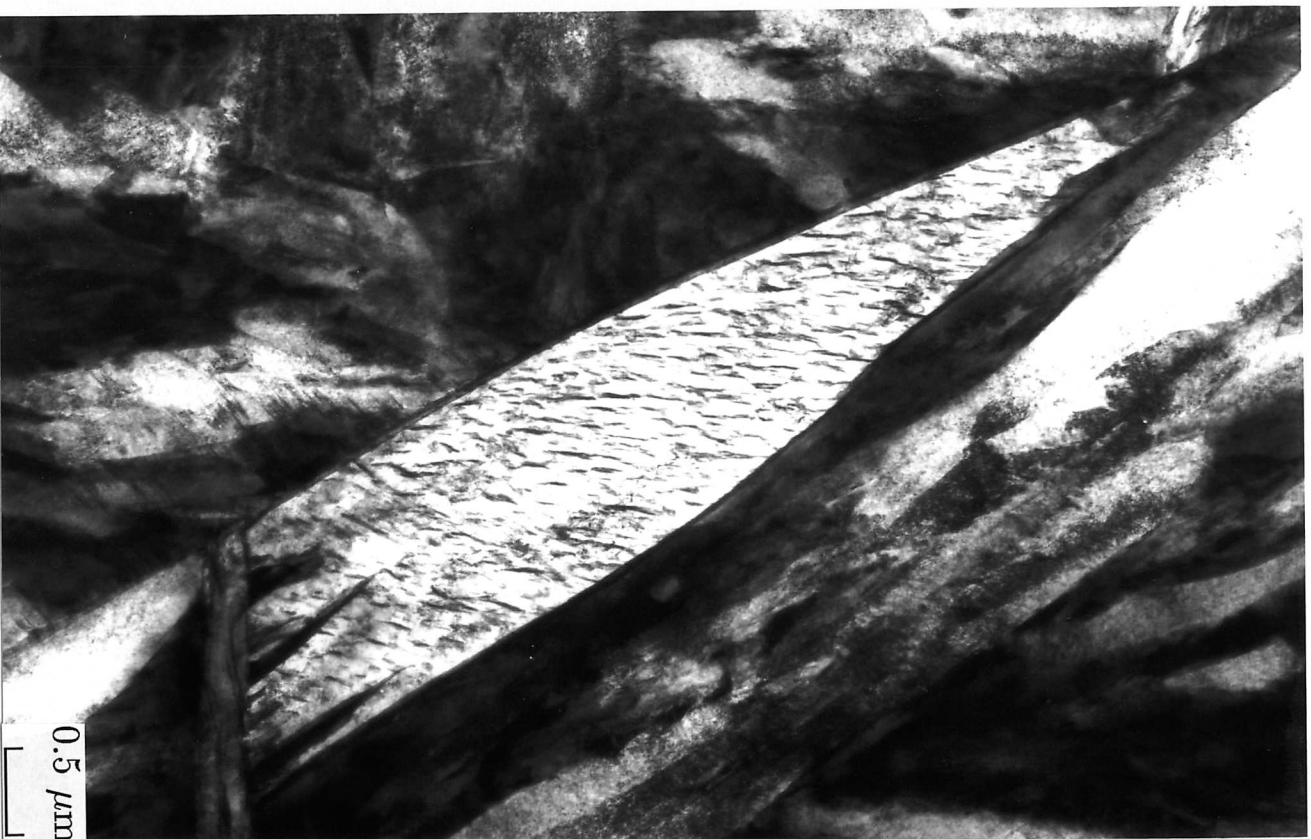


Fig. 5.5: Alloy C, isothermally transformed at 305 °C for 150 s before quenching in the thermomechanical simulator. Transmission electron micrograph showing a coalescence event and the intense carbide precipitation present in all parts of the bainite (*i.e.* the sub-units before and after they coalesce).

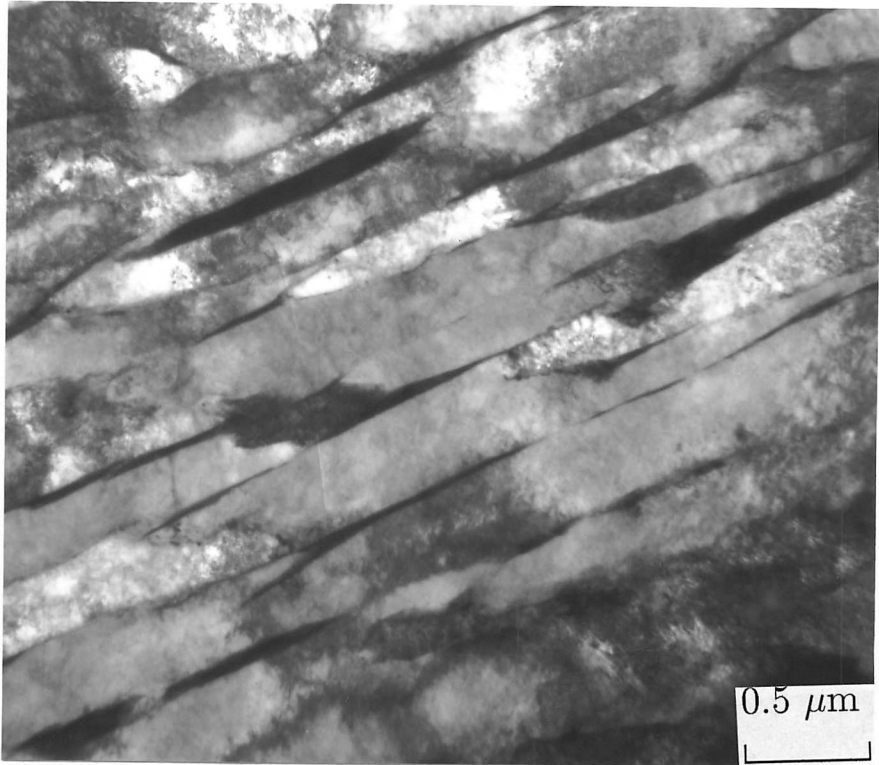


Fig. 5.6: Alloy H, isothermally transformed at 400 °C for 800 s before water-quenching. Transmission electron micrograph of upper bainite with a more uniform distribution of plate thicknesses.

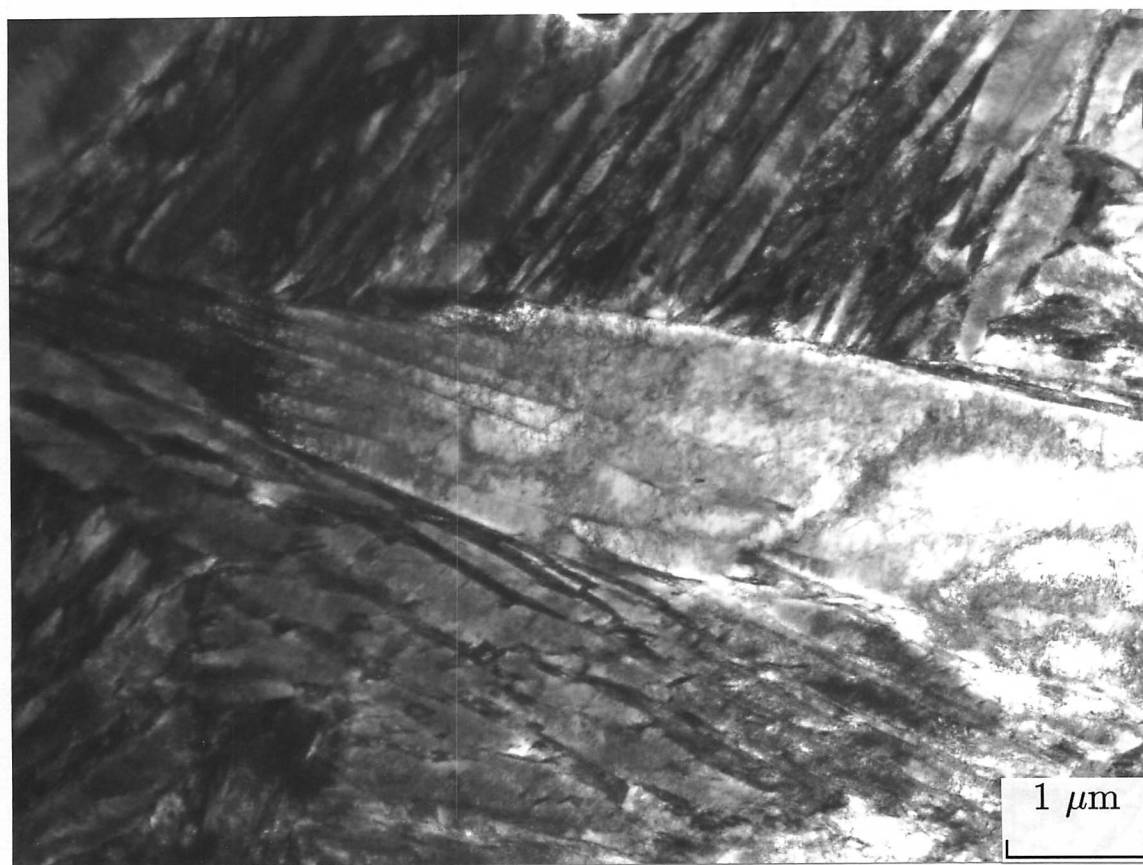


Fig. 5.7: Alloy A, isothermally transformed at 325 °C for 2000 s before water-quenching. Transmission electron micrograph showing sub-units are visible at the tip of a lower bainite plate.

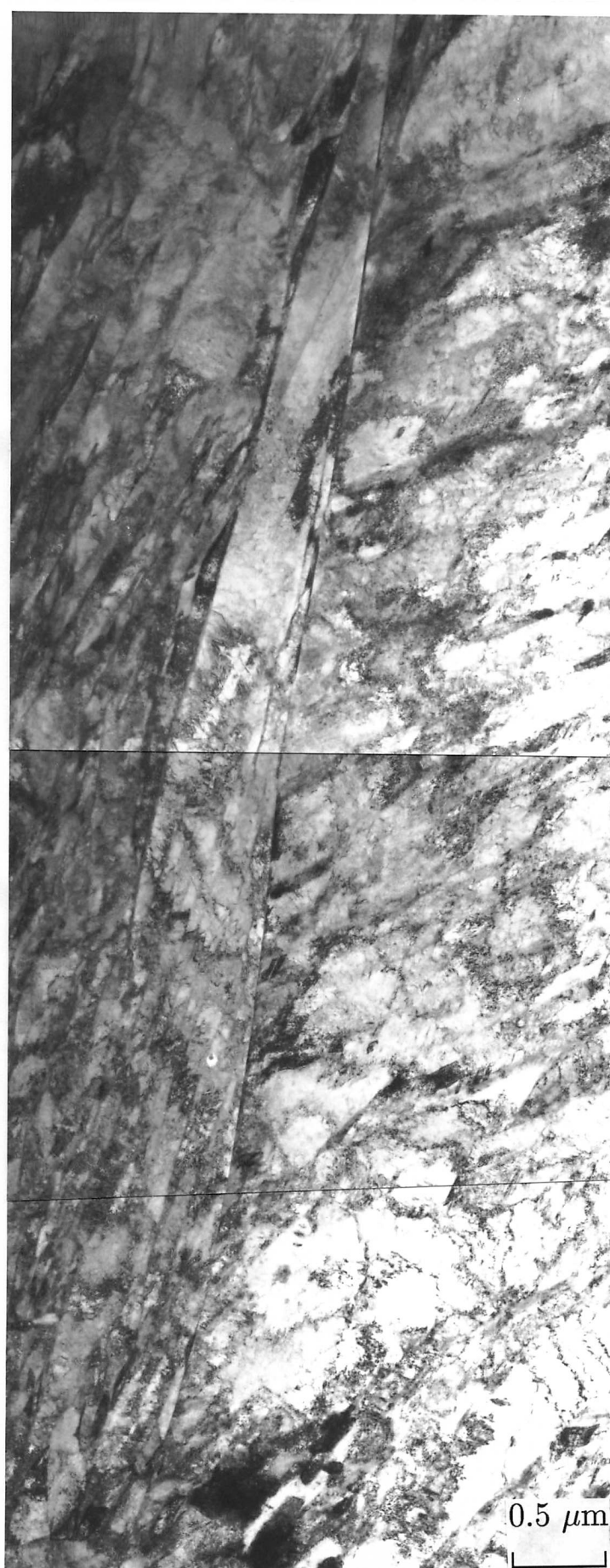


Fig. 5.8: Alloy C, isothermally transformed at 300 °C for 150 s before water-quenching. Transmission electron micrograph showing sub-units along the whole lower bainite plate, with some retention of austenite films between the sub-units.

CHAPTER 6

TWO METALLOGRAPHIC OBSERVATIONS ON THE TRANSFORMATION OF THE BAINITE TRANSFORMATION

6.1 INTRODUCTION

The purpose of the work presented in this chapter is to report some metallographic observations made during the course of the investigations on the design of high strength steels for rail applications. These observations are interesting in that they reveal quite new aspects of the mechanism of bainitic transformation in steels.

6.2 EXPERIMENTAL MATERIALS

The chemical compositions of the alloys studied are shown in Table 6.1.

Table 6.1: Chemical compositions (wt.%) of the alloys studied.

Alloy	C	Si	Mn	Ni	Cr	Mo	V
A	0.27	1.98	2.18	–	1.9	–	–
C	0.46	2.10	2.15	–	–	–	–
I	0.30	–	–	30.1	–	–	–
J	0.44	1.74	0.67	1.85	0.83	0.39	0.15

Alloy I is an experimental steel which transforms only to martensite. It was quenched into liquid nitrogen to generate plate martensite. Alloy J is a commercial high–strength steel (300M) which was austenitised at 1100 °C and quenched in water to generate a martensitic microstructure. Alloys A and C are experimental steels already described in chapter 2.

Transformation experiments for alloys A and C were carried out in the thermomechanical simulator *Thermecmaster Z* (chapter 2). The isothermal transformation conditions were 325 °C (2000 s) and 270 °C (2500 s) for alloys A and C respectively. In the case of alloy C, the sample was under a uniaxial compressive stress of 700 MPa during isothermal transformation. This is to encourage the plates of bainite form close to the planes of maximum shear stress in order to encourage them to form with large relative inclinations for reasons discussed later.

6.3 THERMOELASTIC EQUILIBRIUM

The shape deformation associated with a displacive transformation of austenite in steel can be described as an invariant-plane strain with a relatively large shear component. Christian [1958] demonstrated that when the shape strain is elastically accommodated, the strain energy scales with the plate aspect ratio (thickness/length). This is why all of the displacive transformation products in steel, *e.g.* Widmanstätten ferrite, bainite and martensite, occur in the form of thin plates.

The need to minimize strain energy demands a thin plate, but that also leads to a minimization of the volume of transformation per plate. Therefore, a plate will tend to adopt the largest aspect ratio consistent with the available free energy change driving the transformation. In ideal circumstances, where the transformation interface remains glissile throughout and where there is no friction to the motion of the interface, thermoelastic equilibrium occurs [Kurdjumov and Khandros, 1949; Olson and Cohen, 1977; Christian, 1979; Salzbrenner and Cohen, 1979]. In this, the plate adjusts its aspect ratio so that the strain energy is equal to the driving force (Fig. 6.1). The driving force can be increased by cooling the austenite, which should lead to fatter plates. Alternatively, it can be decreased by the addition of austenite stabilising elements such as manganese or carbon.

The thermoelastic equilibrium illustrated in Fig. 6.1 has been frequently demonstrated for martensite [Kurdjumov and Khandros, 1949; Olson and Cohen, 1977; Christian, 1979; Salzbrenner and Cohen, 1979], but not for bainite. One reason for this could be that bainite grows in the form of sheaves, which are clusters of connected platelets which grow in parallel formations. The spacing between the platelets is to a large extent controlled by the carbon diffusion field associated with each platelet [Chapter 4]. The platelets therefore are restricted in their thickening by the diffusion fields and by the presence of adjacent parallel platelets (*i.e.* soft and hard impingement effects).

A further complication is that the bainite transformation occurs at high temperatures where the austenite is mechanically weak. The shape deformation therefore causes plastic deformation, and the resulting dislocation debris eventually blocks the transformation interface which loses coherency. This is why platelets of bainite are arrested in their growth even when their size is much smaller than the austenite grain size [Bhadeshia and Edmonds, 1979a; Bhadeshia, 1992].

It should nevertheless be possible to observe the thickening of individual bainite platelets if the process is captured at an early enough stage of growth. Some published observations

[Court and Pollard, 1987; Zhang, 1994] can be interpreted to support the idea that bainite plate thickening continues until the chemical driving force is exhausted by the accumulation of strain energy. The bainite is in these cases in a different microstructural form called “acicular ferrite”. Acicular ferrite is bainite which nucleates intragranularly on non-metallic inclusions [Bhadeshia, 1992]. Thus, isolated platelets can be seen to emanate from ‘point’ nucleation sites and are therefore free to thicken even when their lengthening is restricted by other platelets growing from other inclusions. It is found experimentally that the acicular ferrite aspect ratio decreases as the transformation temperature is raised or as the manganese or carbon concentration is increased [Court and Pollard, 1987; Zhang, 1994].

In the present work, bainite platelets were forced to grow in non-parallel formations by transforming the austenite under the influence of an applied compression stress. Fig. 6.2a shows a phenomenon commonly found with martensite. Because the plates lengthen rapidly, impingement occurs and thickening then continues, restricted by pinning points. The interface of plate A is clearly bowed between these points. The corresponding phenomenon for bainite platelets is illustrated in Fig. 6.2b. It is sometimes considered that bainite grows via a superledge mechanism [Aaronson *et al.*, 1970] in which macroscopic ledge propagate as the habit plane. The smooth curved regions of the interface between the pinning points (Fig. 6.2b) provides evidence that the bainite/austenite interface moves continuously rather than by a step mechanism involving the translation of superledges.

6.4 ACCOMMODATION TWINNING

Bainite and martensite can be regarded as mechanisms for deformation which in addition lead to a change in crystal structure. However, the key feature of the deformation is the large shear component ($\simeq 0.22$) of the invariant-plane strain shape change which is much larger than the dilatational strain ($\simeq 0.03$) [Bhadeshia, 1992].

The small volume strain, which is directed normal to the habit plane, cannot induce any significant shear deformation in its vicinity. It is the shear which is directed parallel to the habit plane which has to be accommodated (elastically or plastically) by the surrounding material. This is why a martensite plate tapers to a sharp point, because the magnitude of the shear displacement scales with the plate thickness. The plate need not taper if the strain is plastically accommodated. This plastic deformation can take the form of accommodation twinning, so-called in order to distinguish these mechanical twins from those sometimes found in martensite as transformation twins [Bhadeshia and Edmonds, 1979c].

This is apparent in the collision illustrated in Fig. 6.3, between inclined plates of marten-

site in a low alloy steel. It is noticeable that the resulting mechanical twins are confined to the abutting surface of plate B, and that as expected, the mechanical twins taper away from the collision site. Exactly the same phenomenon is illustrated for bainite in Fig. 6.4, providing unusual visual evidence for the role of the shear strain of bainite, as the bainite forms deep inside the metal. Sandvik [1982a] has previously demonstrated this by noting the displacement of narrow twins in austenite. The shear has of course on many occasions been revealed in experiments where surface displacements are observed [Bhadeshia, 1992].

6.4 CONCLUSIONS

In appropriate circumstances, the austenite/bainite interface is capable of bowing between strong pinning points as the bainite platelet thickens to an extent permitted by the available chemical driving force. The shear caused by the growth of bainite can induce accommodation (mechanical) twinning in adjacent plates.

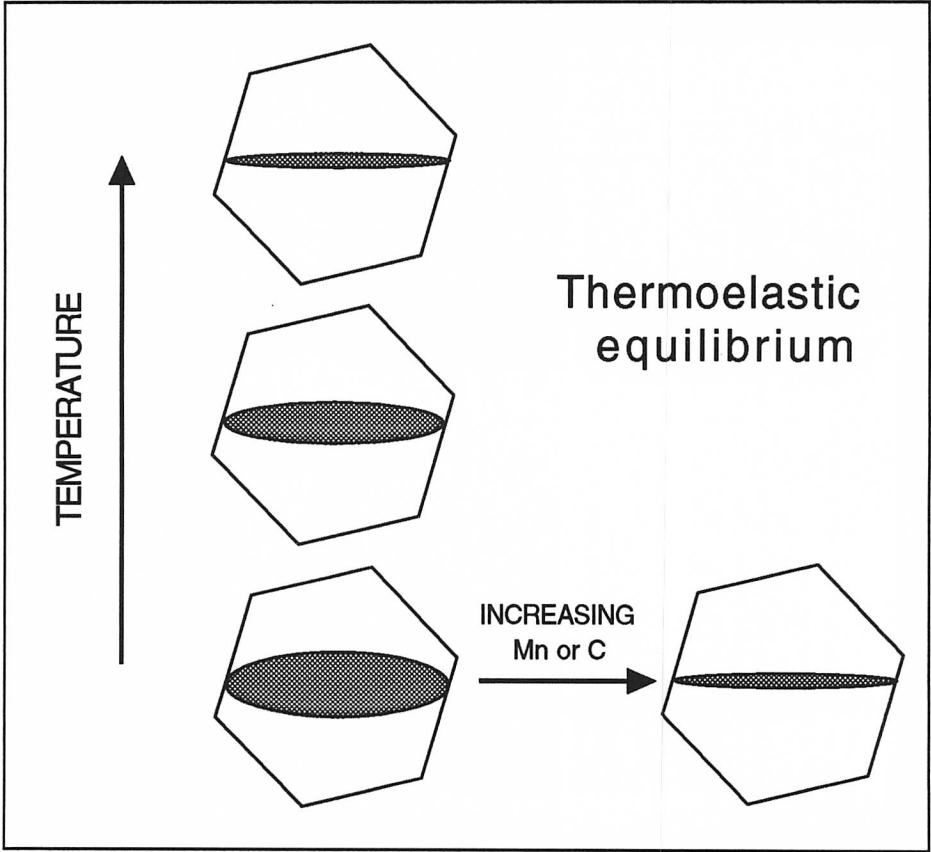


Fig. 6.1: The effect of thermoelastic equilibrium on the aspect ratio of a plate whose length is fixed.

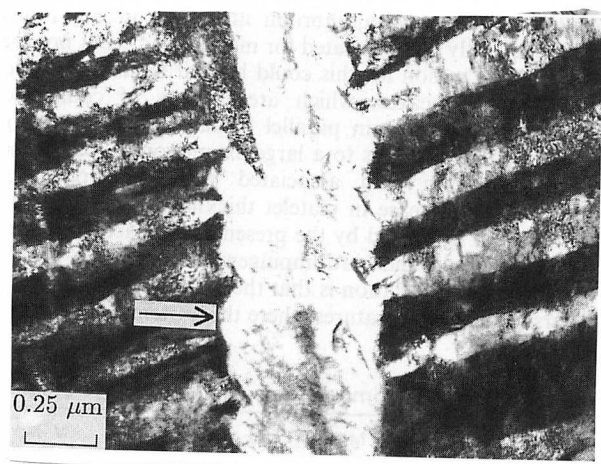
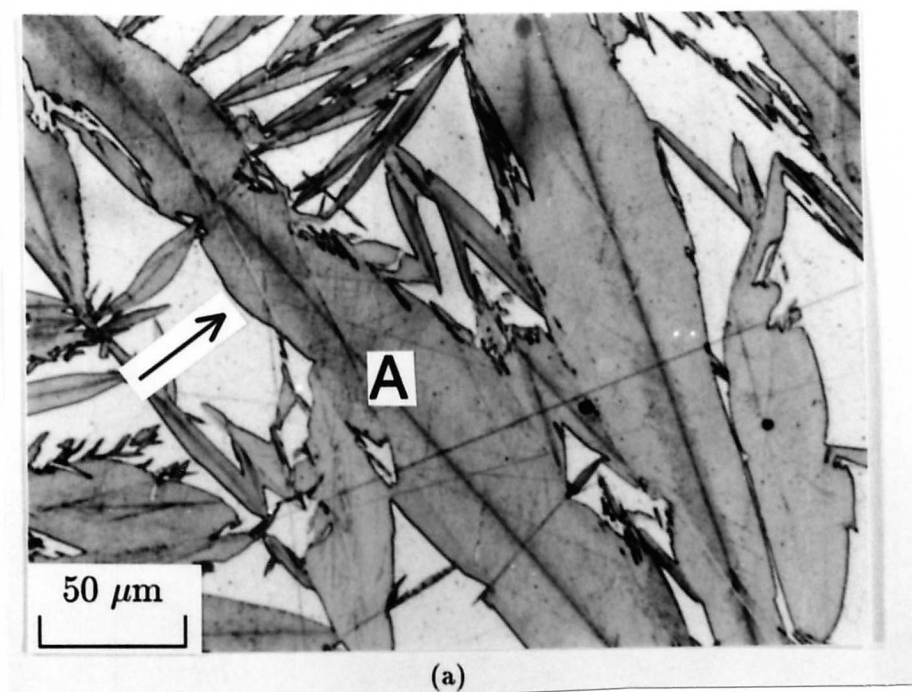
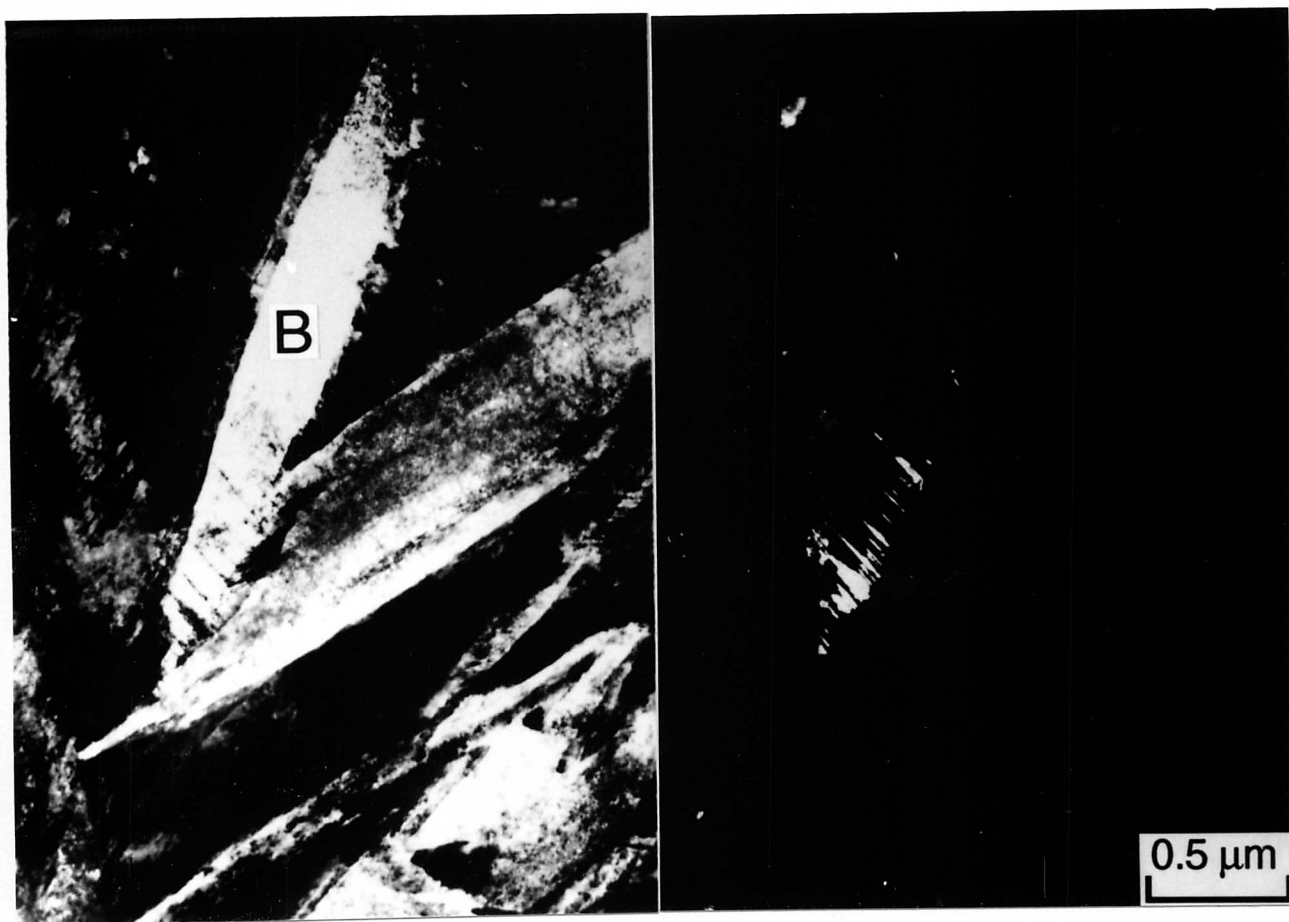


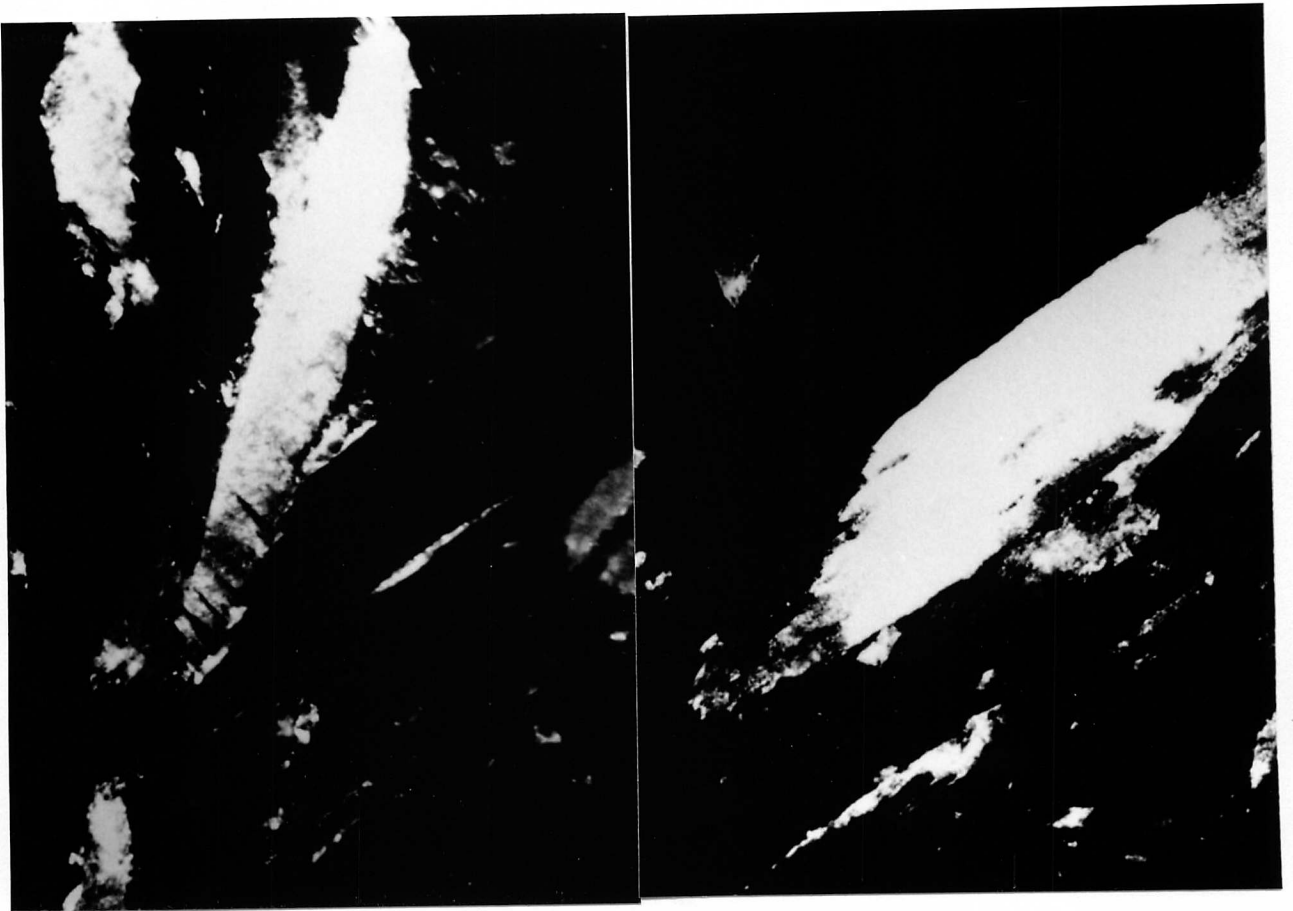
Fig. 6.2: Bowing of the transformation interface at strong pinning points. The bowing is particularly prominent in the regions identified by the arrows. (a) Martensite in Alloy I. (b) Bainite in Alloy C.



(a)

(b)

Fig. 6.3: Martensite in Alloy J showing accommodation twinning at collision sites between inclined plates of martensite. (a) Bright field image. (b) Dark field image of twins in one of the martensite plates. (c) Dark field image of one of the abutting plates. (d) Dark field image of the other abutting plates.



(c)

(d)

Fig. 6.3: Martensite in Alloy J showing accommodation twinning at collision sites between inclined plates of martensite. (a) Bright field image. (b) Dark field image of twins in one of the martensite plates. (c) Dark field image of one of the abutting plates. (d) Dark field image of the other abutting plates.

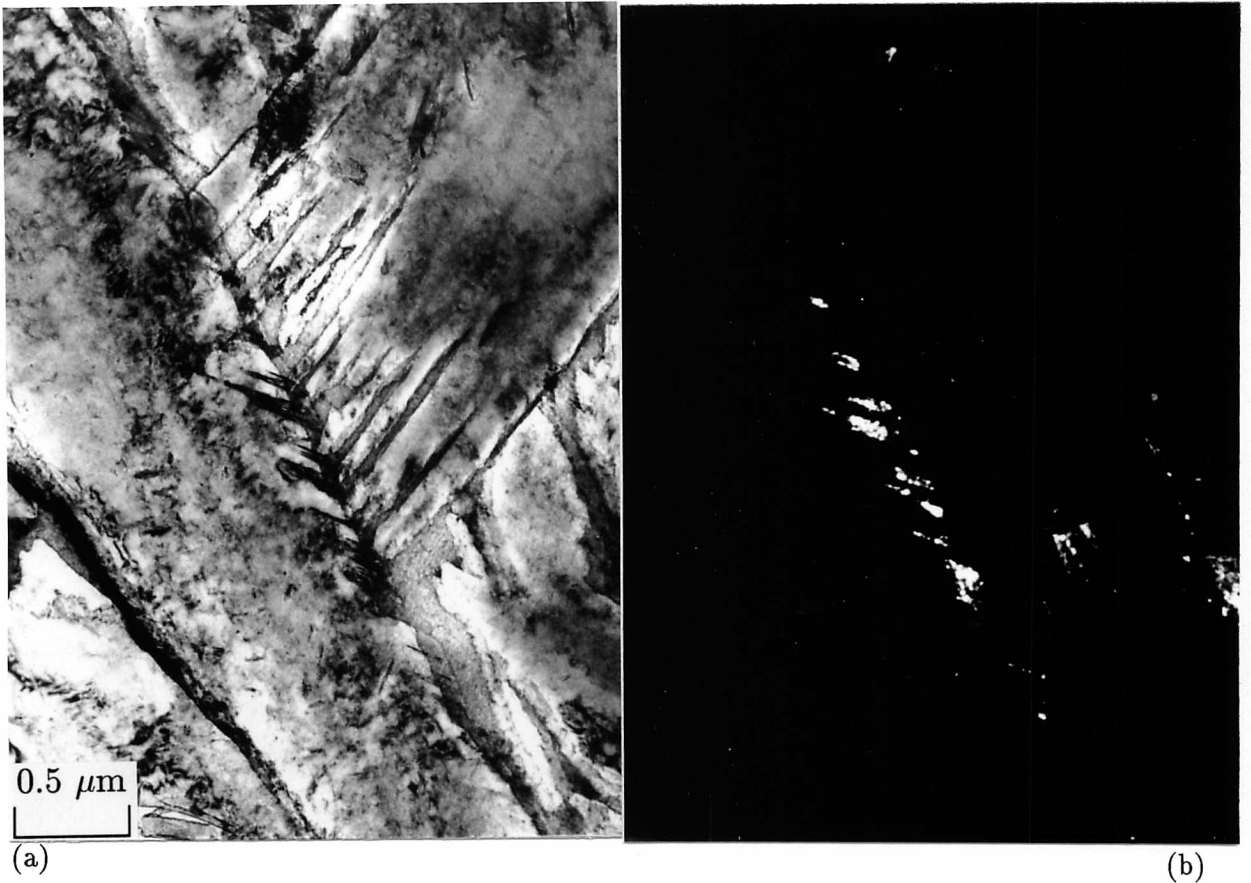
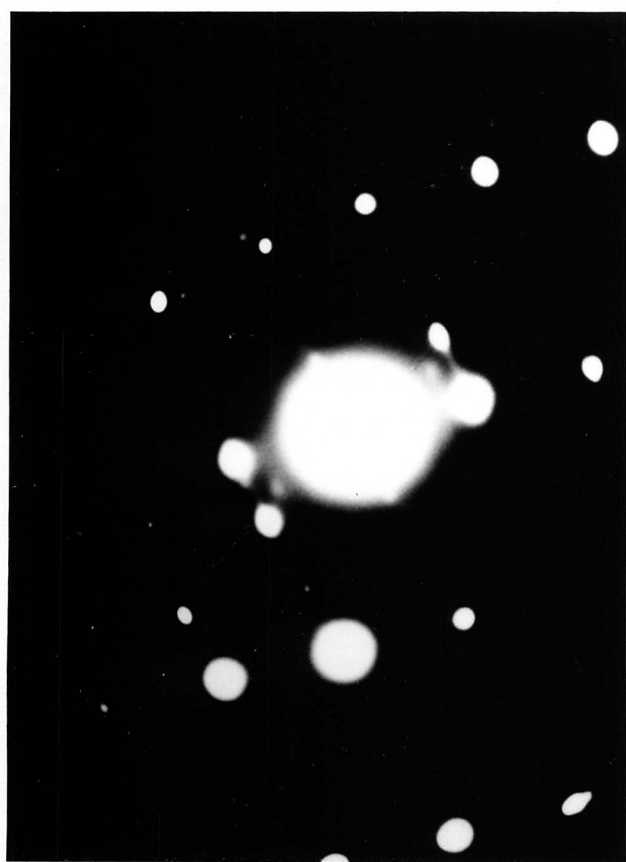
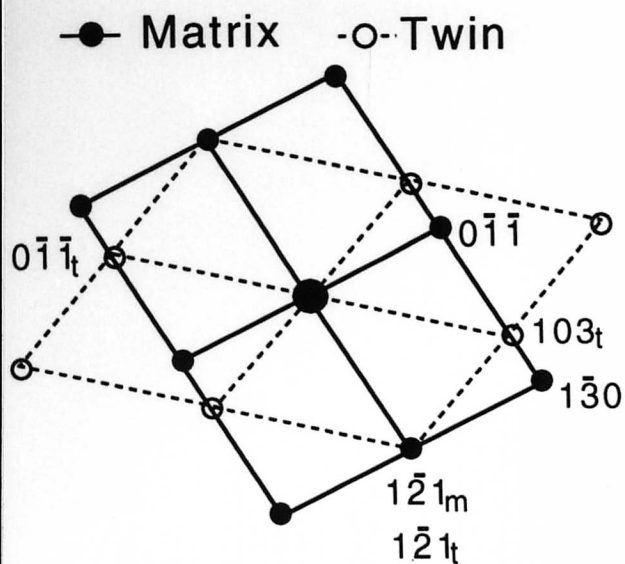


Fig. 6.4: Bainite in alloy A, showing accommodation twinning at collision sites between inclined plates of bainite obtained by isothermal transformation. (a) Bright field image. (b) Dark field image of twins in one of the bainite plates. (c) Diffraction pattern confirming twinning and its interpretation (d).



(c)



(d)

Fig. 6.4: Bainite in alloy A, showing accommodation twinning at collision sites between inclined plates of bainite obtained by isothermal transformation. (a) Bright field image. (b) Dark field image of twins in one of the bainite plates. (c) Diffraction pattern confirming twinning and its interpretation (d).

CHAPTER 7

STRESS AFFECTED TRANSFORMATION TO LOWER BAINITE

7.1 INTRODUCTION

The tempering of martensite in steels leads to the precipitation of carbides, even when the tempering temperature is so low as to prevent the diffusion of iron during the heat treatment. This led to early suggestions that the carbides precipitate by a mechanism in which the iron atoms (and substitutional solutes) are displaced into positions they occupy in the carbide structure, with carbon diffusion enabling the necessary composition change [Bhadeshia, 1989; Tsivinsky *et al.*, 1959; Chance and Ridley, 1981]. This amounts to a displacive, paraequilibrium [Hultgren, 1951; Rudberg, 1952] mechanism of transformation, which has been supported by recent atomic resolution experiments [Babu *et al.*, 1994]. The experiments demonstrate that substitutional solutes do not partition during cementite growth even on the finest conceivable scale.

The cementite particles grow in the form of thin plates, and it is believed that the change in shape, as they grow by a displacive mechanism, can be described as an invariant-plane strain with a large shear component [Olson and Cohen, 1983]. Consequently, the precipitation of cementite becomes sensitive to stress, which favours the formation of those variants which comply with the stress. The mechanical interaction between the stress and the shape change contributes a mechanical driving force [Christian, 1982] which may compliment or oppose the usual chemical driving force for precipitation. If the mechanical driving force dominates then only that crystallographic variant of carbide which complies best with the stress will precipitate [Matsuzaki *et al.*, 1992]; otherwise, even variants which do not comply with the stress will form, although the favoured variant is likely to dominate. Hence, a decrease in stress, or an increase in the carbon concentration (*i.e.* increased chemical driving force) favours the precipitation of multiple variants (refer to the martensite in Fig. 7.1). Notice that the stress need not be externally applied, since each plate of martensite has its own associated stress field. Thus, a single carbide variant is observed in low carbon martensite which is tempered without externally applied stress [Matsuzaki *et al.*, 1992].

Indeed, it may be the case that the classical microstructure of lower bainite can be explained as discussed above (Fig. 7.1). Lower bainite forms above the martensite-start temperature, with a microstructure in which the plates of ferrite usually contain just one crystallographic variant of carbide [Bhadeshia, 1992]. Martensite in the same alloy may temper to give multiple variants of carbides. It is argued that this is because only some of the carbon that is

in lower bainitic ferrite precipitates as carbides, whereas the rest escapes into the surrounding austenite. Thus, the driving force for carbide precipitation is reduced; only the carbide variant which complies with the self-stress of the plate of ferrite then precipitates, giving the classical microstructure of lower bainite.

The purpose of the present work was to show for the first time, that the number of variants of carbide that form in lower bainite can be reduced by the application of stress, in order to confirm the mechanism of transformation. Work like this has already been published for the tempering of martensite [Matsuzaki *et al.*, 1992], but never for lower bainite. In the mean time, the lower bainite response to the external stress will also be investigated.

7.2 EXPERIMENTAL PROCEDURES

The experiments were carried out using alloy C containing a large silicon and carbon concentration:



The silicon suppresses the precipitation of carbides from austenite [Philip, 1983]. The large carbon concentration increases the driving force for the precipitation from supersaturated ferrite [Matsuzaki *et al.*, 1992; Stewart *et al.*, 1994]. This in turn stimulates the precipitation of more than one variant of carbide in any given plate of ferrite, even though the self-stress of the plate favours just one variant. This is because the chemical driving force of carbide precipitation becomes large when compared with the mechanical driving force due to stress, when the carbon concentration is high [Matsuzaki *et al.*, 1992; Stewart *et al.*, 1994]. Hence, from experience, it was expected that the lower bainite would form with multiple variants of cementite. The effect of the applied stress would then be obvious if it reduced the number of variants.

Transformation experiments were performed in a thermomechanical simulator *Thermec-master-Z*. For experiments involving an applied stress, a uniaxial compressive load was applied via silicon nitride discs, at the instant the sample reached the isothermal transformation temperature. The level of stress was chosen to be 700 MPa, in order to ensure a mechanical driving force which is large enough to influence cementite precipitation [Matsuzaki *et al.*, 1992; Stewart *et al.*, 1994]. The stress is certainly larger than the yield strength of the austenite, and this should affect the kinetics of bainite formation; however, this was not the prime purpose of the study and not a matter of concern because the carbides grow from ferrite and not from the austenite. The yielding stress of austenite at the reaction temperature, 270 °C, was calculated to be 200 MPa [Young and Bhadeshia, 1994].

7.3 RESULTS AND DISCUSSION

7.3.1 Aligned Microstructure

Typical electron micrographs, for specimens transformed with and without external applied stress (700 MPa), are shown in Fig. 7.2; the micrographs are longitudinal sections containing the stress axis, in the direction indicated.

These micrographs show the effect of the stress on the development of the bainitic microstructure. As expected [Umemoto *et al.*, 1986; Bhadeshia *et al.*, 1991], the stress has caused a high degree of alignment of the bainite platelets, which tend to form close to the planes of maximum shear stress. These results are not in themselves unusual, because it is well known that the growth of bainite causes a change in the shape of the transformed region. This shape deformation is an invariant-plane strain with a large shear component, so that the transformation is expected to be sensitive to applied stress [Patel and Cohen, 1953].

7.3.2 Carbide Precipitation

The transmission electron micrographs discussed in this section are representative samples of quite extensive studies.

For the steel studied, the upper/lower transition temperature (LB_S) and martensite-start (M_S) were established metallographically to be 295 °C and 260 °C respectively. Fig. 7.3 shows the lower bainitic microstructures obtained at two different transformation temperatures (295, 270 °C).

There are a number of interesting features in Fig. 7.3 and other similar micrographs generated in the studies. Firstly, the carbide precipitates in any given plate of lower bainite could be found to be in a single orientation, or multi-variant. The intensity of precipitation became larger, and the tendency to obtain several variants of carbide greater, as the transformation temperature was reduced. As discussed earlier, many variants are favoured when the carbon concentration is large (Fig. 7.1). The same applies when the transformation temperature is reduced, since less carbon then has an opportunity to partition into the austenite; this also explains the greater intensity of carbide precipitation as the transformation temperature is reduced.

Since the purpose of the work was to cause a change from a multi-variant precipitation morphology to a single variant, the transformation temperature was fixed in subsequent experiments at 270 °C, with identical austenitisation conditions. The two examples illustrated in Fig. 7.4 show clearly that when lower bainite grows under the influence of a large enough stress, the number of variants of cementite to be found in any given plate of ferrite noticeably

decreases.

The results are all consistent with previous work on the proposed mechanism of cementite precipitation at low temperatures [Hume-Rothery *et al.*, 1942; Andress, 1963]. They also support the hypothesis [Bhadeshia, 1980] that the single variant of carbide frequently observed in lower bainite is because the precipitation is influenced by the self-stress of the plate of bainite. This stress favours the growth of a particular variant over other less optimum orientations. It remains to measure directly the shape deformation due to cementite precipitation.

7.4 CONCLUSIONS

It has been demonstrated that it is possible to change a lower bainitic microstructure, in which each plate of bainite contains many orientations of cementite, into a classical microstructure in which the plate contains just one characteristic orientation. This can be achieved by growing the bainite under the influence of a uniaxial stress. The fact that the applied stress can cause such a change, is consistent with a mechanism in which the cementite particles grow by displacive paraequilibrium transformation. It is likely that when, in the absence of an externally applied stress, lower bainite is found with a single variant of cementite, it is the self-stress of the ferrite plate which prevents the precipitation of many cementite variants.

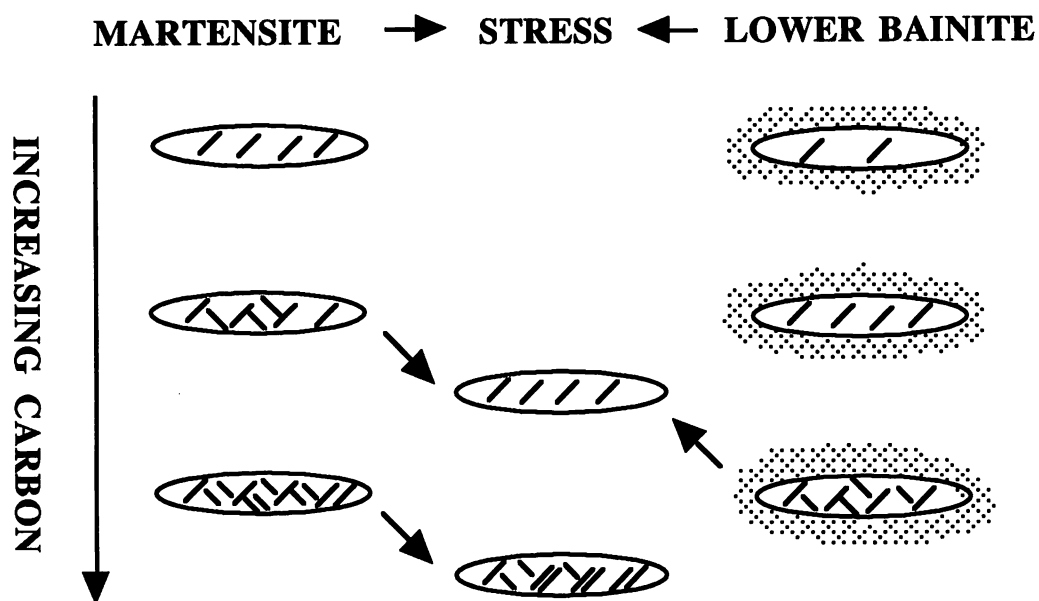


Fig. 7.1: The left and right hand sides represent the tempering of martensite, and formation of lower bainite, respectively, without any applied stress. The central region of the diagram shows how the microstructure might change when the process happens under the influence of a uniaxial applied stress. Note that all the effects observed with martensite are shifted to higher carbon concentrations for lower bainite, because some of the carbon in the lower bainite escapes into the residual austenite, as illustrated by the shading. In general, an increase in the carbon concentration, or a decrease in stress favours the precipitation of multiple variants of cementite during the tempering of martensite [Matsuzaki *et al.*, 1992].

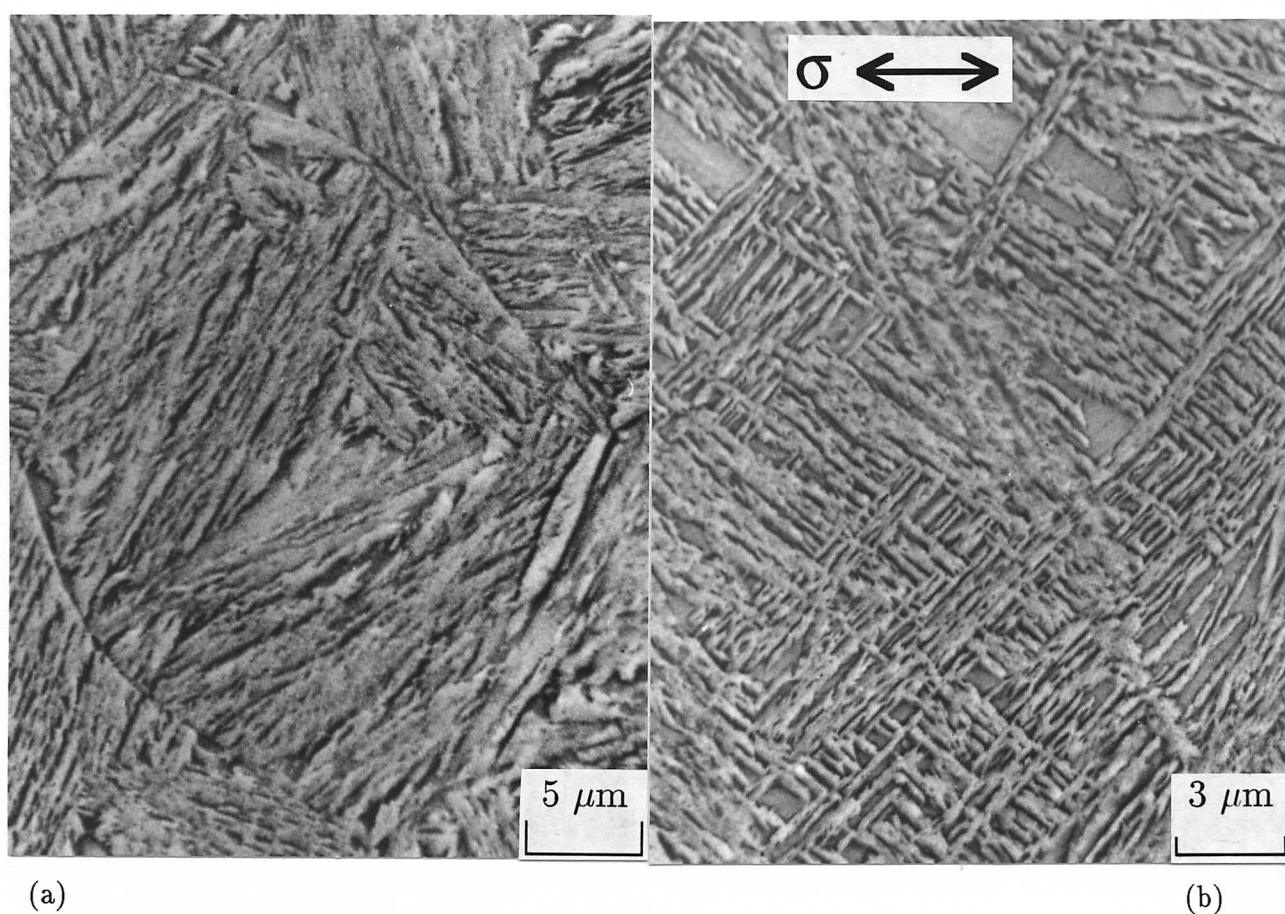


Fig. 7.2: Scanning electron micrographs of samples austenitised at 1000 °C for 600 s, and isothermally transformed at 270 °C for 2500 s before quenching to ambient temperature. (a) Zero applied stress; (b) compressive stress of 700 MPa during transformation.

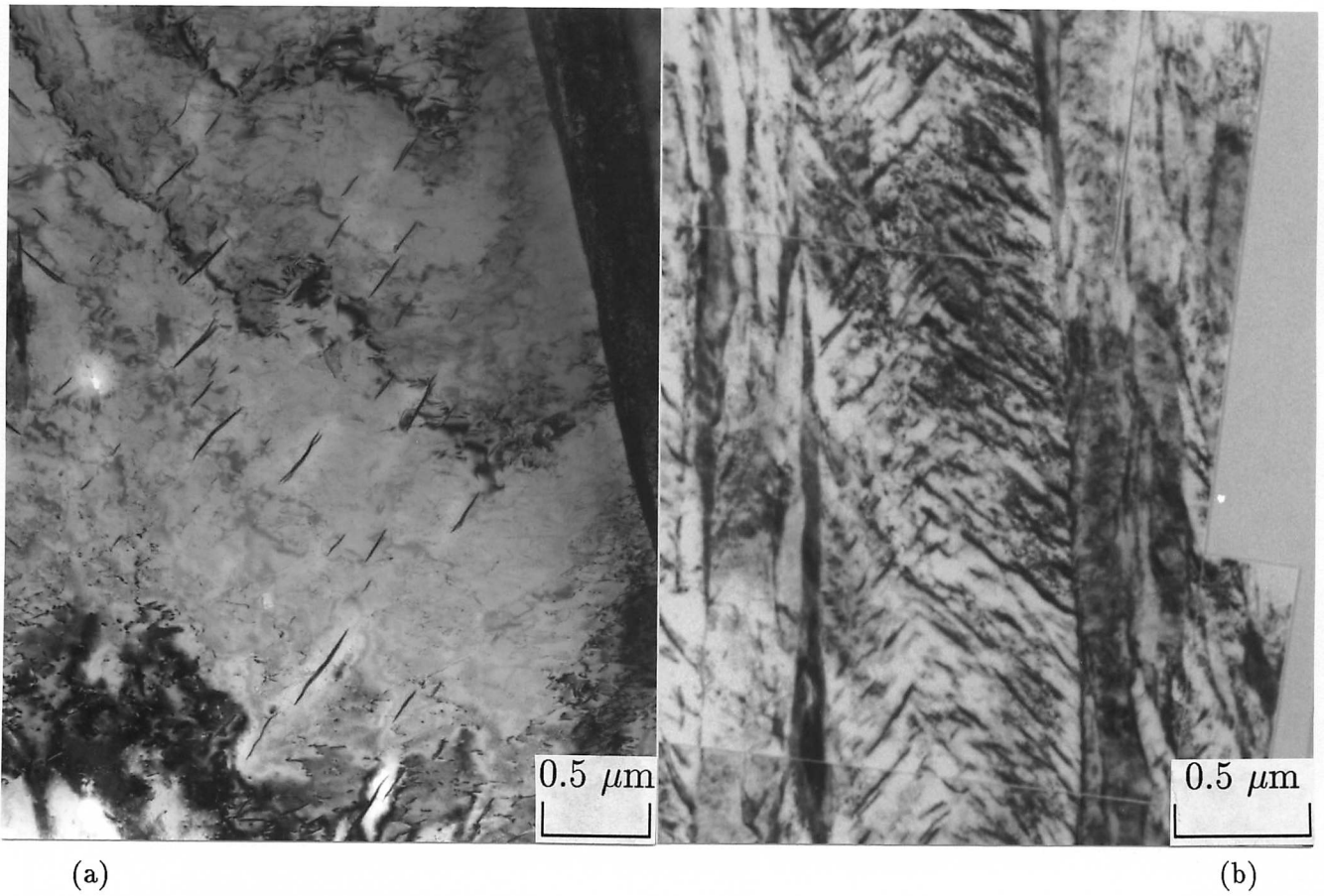


Fig. 7.3: Transmission electron micrographs of lower bainite obtained by austenitisation at 1000 °C for 600 s, followed by isothermal transformation at (a) 295 °C for 2500 s; (b) 270 °C for 2500 s. The samples were quenched to ambient temperature after transformation to bainite.

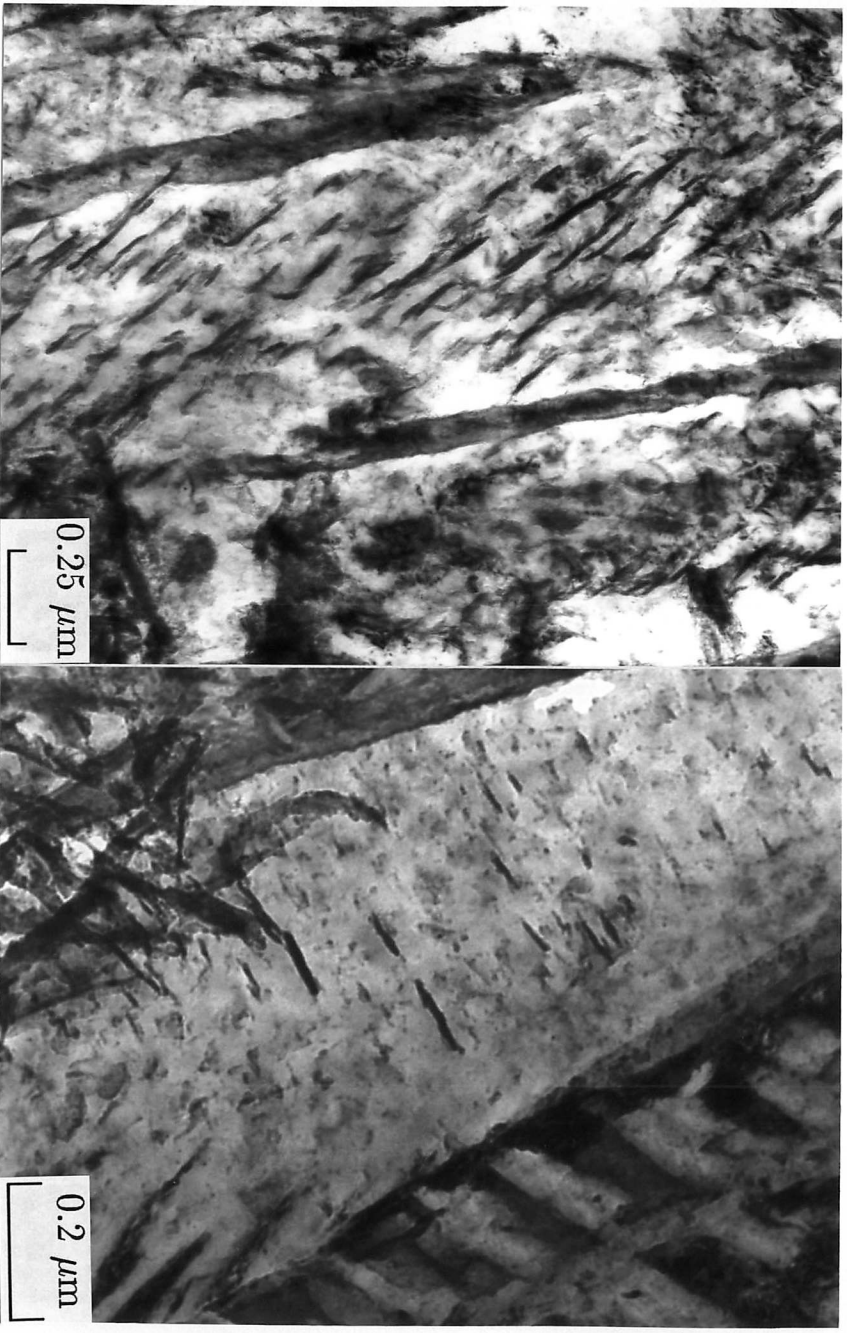


Fig. 7.4: Two examples of lower bainite that has formed under the influence of a compressive stress of 700 MPa. Both cases show a clear tendency for the carbides to precipitate in a single orientation. These micrographs should be compared against Fig. 7. 3b.

CHAPTER 8

THE ROLLING/SLIDING WEAR PERFORMANCE OF HIGH SILICON CARBIDE-FREE BAINITIC STEELS

8.1 INTRODUCTION

Bainitic steels are regarded as candidate materials for heavy duty rails. There have already been successful applications at railway-crossings [Callender, 1983], but there are many results which question their suitability. Some investigations indicate that the wear resistance of bainitic steels is inferior to pearlitic steels, both in service trials and in rolling/sliding laboratory tests [Heller and Schweitzer, 1982; Ichinose *et al.*, 1982; Kalousek *et al.*, 1987; Garnham and Beynom, 1992]. However, Clayton and co-workers [Devanathan and Clayton, 1991; Clayton and Devanathan, 1992; Clayton *et al.*, 1987] showed that bainitic steels may possess better or comparable wear resistance than conventional rail steels, and as a bonus have better toughness, ductility and good weldability (due to their lower carbon concentration). They pointed out that earlier reports of poor wear resistance in bainitic steels may be attributed to mixed microstructures containing other detrimental phases such as allotriomorphic ferrite in addition to bainite [Clayton and Devanathan, 1992].

Lower bainite usually exhibits better strength, toughness and ductility than upper bainite [Johnson and Becker, 1993]. The presence of coarse carbide precipitates in upper bainite gives the microstructure poor ductility and resistance to cleavage fracture. Lower bainite has more refined carbide. The coarsest of carbides in both upper and lower bainite precipitate from the austenite between bainitic ferrite platelets. This precipitation from austenite can be suppressed completely by adding an appropriate concentration of silicon (about 2 wt.%). The resulting carbide-free microstructure consists of bainitic ferrite, retained austenite and martensite only. The stability of the residual austenite is greatly improved by the absence of carbide, since the austenite is then the only sink for carbon, which is a strong austenite stabilizer. Such bainitic microstructures have higher ductility and toughness than comparable coarse carbide containing microstructures [Bhadeshia *et al.*, 1983a, b; Tomita and Okawa, 1993; Sandvik *et al.*, 1981; Mühkinen *et al.*, 1987a, b].

The aim of this study was to investigate the suitability of carbide-free bainite in conditions of rolling/sliding wear, using a number of high silicon bainitic steels. The work includes microstructural and mechanical property evaluations together with a comparison with traditional pearlitic rail steels.

8.2 EXPERIMENTAL MATERIALS

Four alloys were used in this work. The chemical compositions are shown in Table 8.1. For each, a 50 kg vacuum melt was made at by British Steel at Swinden Laboratories, Rotherham. The as-cast ingots, approximately 125 mm × 125 mm in cross section, were then forged into billets with a cross section of 100 mm × 50 mm. The billets, were reheated to 1200 °C and then rolled at this temperature down to 16 mm thick plates in 8 passes, before finally cooling in air.

Table 8.1: Chemical compositions (wt.%) and the calculated M_S , B_S (°C) temperatures [Bhadeshia, 1982b].

Alloy	C	Si	Mn	Ni	Cr	P	S	Al	N	M_S	B_S
A	0.27	1.98	2.18	-	1.9	0.014	0.009	0.01	0.003	306	380
K	0.49	1.53	2.03	-	-	0.015	0.008	<0.007	0.006	250	421
L	0.22	1.39	1.97	-	-	0.015	0.011	0.009	0.004	319	386
P	0.49	1.44	0.51	3.5	-	0.015	0.011	<0.01	0.057	249	360

A number of tensile, Charpy impact and wear test piece blanks, each approximately 125 × 15 × 16 mm in size were cut from each of the as-rolled plates for determination of mechanical properties.

The test samples from alloys K and P were austenitized for 30 minutes at 900 °C. Isothermal transformation was then carried out by quenching from the austenitization temperature into a salt bath at a preset temperatures. The temperature of the salt bath rose about 5 °C during this quenching specimen. Isothermal transformation to bainite was allowed to complete in each case. Alloy L was quenched into boiling water after austenitization. Alloy A was investigated in the air-cooled condition. The isothermal transformation temperatures used are listed in Table 8.2.

8.3 EXPERIMENTAL PROCEDURES

8.3.1 Wear Tests

The laboratory rolling contact machine consists of two counter-rotating discs of 56 mm (rail steel - sample) and 112 mm diameter (tyre steel sample, which is machined from En24 oil quenched and tempered steel, with a hardness of about HV 295). The discs have a contact width of 7 mm and which run together under a contact stress of 750 N mm⁻², equivalent to a

44 ton axle load [Timoshenko and Goodier, 1970]. The 112 mm diameter specimen (run at 135 rev min⁻¹) has a circumferential speed 25% faster than that of the 56 mm diameter specimen; it oscillates laterally by 1 mm throughout the test, thereby ensuring an even wear distribution over both surfaces. The contact load is applied by means of a spring and screw arrangement, which is designed to allow minor modifications to be made during the course of the test. The contact load is monitored continuously during the test.

Table 8.2: Heat treatment of the experimental alloys.

Alloy	Heat Treatment
K1	Isothermal - 370 °C - 7200 s, water quenched
K2	Isothermal - 315 °C - 7200 s, water quenched
K3	Isothermal - 355 °C - 7200 s, water quenched
L	Boiling water quenched
P1	Isothermal - 300 °C - 3600 s, water quenched
P2	Isothermal - 320 °C - 3600 s, water quenched
P3	Isothermal - 342 °C - 3600 s, water quenched
A	Air cooled

Prior to the wear test, the test specimens were thoroughly degreased in acetone and Vickers hardness (HV 30) measurements were made at four positions around the circumference of each specimen. The wear test specimens were then initially run in to a stage where the work hardened machined surface had been removed over the full width of the running surfaces. Both samples were then weighed, degreased and run for an initial 15 m of slip (213 revolutions). Following reweighing and degreasing the samples were run for a further 135 m of slip and the wear rate was expressed as weight loss per metre of slip (mg m⁻¹ of slip). The contact stress was always kept as 750 N mm⁻². Dry compressed air was blown onto the samples to ensure that their temperature remained below 50 °C throughout the duration of the test.

8.3.2 X-ray Determination of Retained Austenite

The amount of retained austenite was determined using X-ray diffraction [Aberbach and Cohen, 1948]. Samples (10 mm × 6 mm × 1 mm) were cut from the wear specimens both from the worn surface and from regions more than 5 mm beneath the worn surface. The subsurface samples were mounted and mechanically ground using silicon carbide abrasive paper down to mesh number 1200, before polishing with 6 μm diamond paste. They were then

chemically polished using a 5 %HF, 50 %H₂O₂ and 45 %H₂O mixture, for 10 minutes to remove any layer damaged by mechanical polishing. The samples cut from the worn surface were submerged in acetone and cleaned in a ultrasonic bath. The samples were examined in a Philips diffractometer with Cu K_α X-radiation. The diffracting angle, 2θ , was scanned from 39° to 82°, to include the three strongest reflections of both austenite and ferrite, namely the diffractions from (111), (002) and (022) for austenite and (011), (112) and (022) from ferrite. The scan rate was 0.5° 2θ min⁻¹. The diffractometer patterns were recorded and the area under each peak was measured, which is proportional to the integrated intensity.

8.3.3 Microhardness Tests

The examination of the effect of transformation hardening during the wear process was carried out with a Leitz-Vickers micro-hardness tester with a load of 100 g. Specimens were nickel plated before mounting, polishing and grinding to protect the worn surface. The hardness measurements were performed on as-polished samples. The location of testing ranged from 20 μ m to 1200 μ m beneath the wear surface, and an average value was obtained from five different points for a specific depth. The spacing between each indentation was at least 3 times the diagonal length to ensure that each measurement was independent of any others [Metal Handbook, 1985]. This subsurface micro-hardness measurement enabled the extent of transformation hardening and the thickness of hardened layer to be determined.

8.4 RESULTS AND DISCUSSION

8.4.1 Microstructural Characterization

Optical metallography confirmed that steels A and K have a fully bainitic microstructure but with a considerable variation in appearance, as shown in Fig. 8.1. Steel L, due to its poor hardenability, contains substantial amounts of grain boundary allotriomorphic ferrite in a martensitic matrix because the sample was quenched from the austenization temperature.

To obtain better resolution, samples were examined in a scanning electron microscope (SEM). The results are shown in Fig. 8.2. Steel P clearly contains some allotriomorphic ferrite formed during the quench to isothermal transformation temperature. However, alloys A and P do not form any grain boundary allotriomorphic ferrite. In steel L the austenite grain boundaries are decorated with allotriomorphic ferrite, with very little bainite sheaves. It appears that bainite only grows from one side of these decorated boundaries, consistent with a report previously [Babu and Bhadeshia, 1991]. Steel A contains a large volume fraction of very fine bainite, formed along grain boundaries.

All the alloys have a banded microstructure since they were not homogenized. An example of banding is shown in Fig. 8.3; the lighter area is rich in alloying elements and, thus, more austenite is retained at room temperature.

Transmission electron microscopy was employed to examine the fine bainitic microstructure. A typical upper bainitic microstructure is illustrated in Fig. 8.4, showing the growth of parallel sheaves with numerous ferrite sub-units in each individual sheaf. The ferrite sub-units within the sheaf are delineated by dark-imaging austenite films. In Fig. 8.5, the austenite films are illuminated in dark field. Alloys A, K and P all exhibited this type of microstructure. Nevertheless, due to the variation, some other morphologies of upper bainite could also be observed as shown in Figs. 8.6a and 8.6b. These upper bainite sheaves contain no or few austenite films between the sub-units and thus, are supposed to form at higher temperatures. Figs. 8.7 and 8.8 show the growth of bainite from grain boundary allotriomorphic ferrite in alloys P and L, respectively, as discussed earlier.

It should be noted that prolonged isothermal heat-treatment will lead to the growth of pearlite at the austenite grain boundaries (Fig. 8.9a) or to the decomposition of austenite films into a degenerate mixture of ferrite and carbides (Fig. 8.9b).

8.4.2 Tensile Properties and Hardness

The tensile and hardness data are given in Table 8.3, which includes a commercial MHT (mill heat-treated) rail steel as well [Jerath *et al.*, 1991].

Table 8.3: Tensile properties and hardness of the experimental alloys.

Alloy	H(HV 30)	TS(MPa)	0.2%PS(MPa)	RA(%)	EL(%)	$\frac{0.2\%PS}{TS}$
K1	446	1444	1067	41	13	0.74
K2	372	1183	862	39	25	0.73
K3	351	1050	842	35	25	0.73
L	374	1245	725	23	10	0.59
P1	442	1440	1074	40	14	0.75
P2	391	1266	934	44	16	0.74
P3	349	1100	866	48	19	0.80
A	543	1732	1191	10	7	0.69
MHT rail steel	379	1210	-	-	10	-

Tensile properties of the higher carbon steels ($\sim 0.5\text{wt.}\%$) coded K and P show a similar trend: the 0.2 % proof and tensile strengths were found to increase with decreasing isothermal transformation temperature. The overall tensile properties of these high carbon steels are found to be significantly better than those of the current British Steel heat treated rail. Steel A (air cooled) shows a extremely high strength, presumably due to its high hardenability. Steel L, although containing a similar level of carbon as steel A has lower concentrations of other alloying elements. It has a reasonable tensile strength but the 0.2 %proof strength is significantly lower than that of the other steels. The trends for hardness are similar to those for strength.

8.4.3 Impact Properties

Charpy V-notch impact data for the steels K and P over a range of temperatures are given in Table 8.4. The nickel based steel P possessed significantly better impact properties than the manganese based steel K. Fig. 8.10 shows the impact energy as a function of temperature for both a British Steel alloy (mill heat-treated plain carbon steel) and steel P. Clearly the impact energy absorbed by the experimental bainitic steel, even at the same tensile strength levels (about 1200 MPa), far exceeds that of the mill heat-treated rail under all conditions tested.

8.4.4 Wear Tests

The results of the rolling contact wear data at a contact stress of 750 N mm^{-2} are given in Table 8.5, along with the measured hardness of wear samples. There are differences in hardness between the tensile (see Table 8.3) and wear samples, especially for steel P, even for identical heat treatments, since the samples differ in size and shape leading to difference in cooling conditions.

Table 8.4: Charpy V-notch impact energy (CVN) for Alloy P and K.

Temperature °C	CVN Impact Energy, J				
	P1	P2	P3	K1	K3
-70	12	13	13	-	-
-40	15	21	22	-	-
-20	21	22	24	-	-
20	26	34	26	10	8
65	32	33	60	15	11
90	31	38	71	36	15

Table 8.5: The relation between hardness (HV 30 kg) and wear rate (mg m^{-1}).

Alloy	K1	K2	K3	L	P1	P2	P3	A
Hardness	399	404	334	444	367	382	407	556
Wear rate	14	11	28	47	38	22	15	0.3

Fig. 8.11 shows the wear rate as a function of hardness for the experimental steels. The wear rate generally decreased with increasing hardness; however, steel L has an anomalously high wear rate. The higher carbon steels ($\sim 0.5\text{wt.}\%$) (K and P) gave relatively low wear rates of 11 and 15 mg/m of slip respectively for the hardness level of ~ 400 HV, *i.e.* toward the top end of the hardness range of current heat treated rail [Jerath *et al.*, 1991]. For the low carbon ($\sim 0.2\text{wt.}\%$) alloys, the wear rate is strongly dependent on the microstructure. Steel L has a mixed microstructure of allotriomorphic ferrite and martensite with a hardness of around 450 HV. Its wear rate of 47 gm m^{-1} of slip was the worst of all the experimental steels. Steel A with a predominantly bainitic microstructure of hardness HV 556, shows a wear rate of only 0.3 mg m^{-1} , which is 155 times less than that of steel K, with only a difference in hardness of about HV 100.

Fig. 8.12 shows typical wear scars from all the samples tested. Thin metallic flakes either are partially attached or totally removed from the surface leaving behind small depressions which can be observed in all cases. This is consistent with the severe Type III wear reported previously by Clayton and Danks [1990], which involves a self-generated mutual abrasion by soft abrasives resulting from the initial break-in of the surface.

Gouging, which is a material removal process normally occurring in pin-on-ring sliding wear [Bolton and Clayton, 1984] was found locally in these specimens. Fig. 8.13 shows an example of heavily deformed partially detached wear debris. The wear scar of Alloy A is smoother than those of the other alloys and the platelets of debris are smaller and less numerous. The other alloys all have wear scars of similar, though rougher appearance, irrespective of their wear rate.

Fig. 8.14, shows the transverse sections perpendicular to the sliding direction for all the experimental steels following wear testing. A lip of material has been “extruded” laterally on all samples except Alloy A. The length of this lip can be used as a measure of deformation resistance. Steel P1 exhibited a large deformation lip, which is consistent with its low hardness and high wear rate. No obvious sign of deformation can be observed for the steel A, again consistent with both hardness and wear rate. The least wear resistant steel, Alloy L, had a lip of similar magnitude to the other medium wear resistant steels, but its hardness is of similar

magnitude to those steels indicating that the size of the deformation lip depends largely on hardness, and that its formation is not a significant mechanism of mass loss during the wear test.

The deformation of the alloys during the wear process response can be more clearly observed in a transverse section parallel to the sliding direction. Fig. 8.15 shows such an example; the near surface microstructure is much finer than that in the bulk, and has suffered large strain with elongation parallel to the sliding direction. However, in spite of the severe deformation, there is no evidence of cracking. The depth of the severely deformed zone is strongly dependent on the hardness (Fig. 8.16). The transverse section of the worn surface of Alloy A (HV 556) shows a deformed zone of about 10 μm , compared with about 30 μm of Alloy P3 (HV 407). A more detailed investigation of the deformed layer using microhardness will ^{be} presented later.

Wear debris attached to the worn surface is found to be made up of several layers (laps) of plastically convoluted material as seen in Fig. 8.17. Cracks are visible between two laps and the top layer appears to be partially detached. Microhardness tests were conducted to investigate the hardness of the deformed layer, and the results (Fig. 8.17) show significant hardening at the surface. This increase might be attributed to the defects caused by plastic deformation, and to the strain-induced martensitic transformation of retained austenite described later. Debris partially attached to the worn surface is shown in Fig. 8.18 where severe cracking is observed parallel to the wear direction. Devanathan and Clayton [1991] have made similar observations and have shown that the layers represent wear debris which has become reattached to the wear surface. In the present study, under similar wear conditions, discrete regions of layers actually transferred from the wheel counterpart in the wear test (Fig. 8.17). The formation of transferred layers is not surprising in rolling/sliding wear processes, since the debris from the wear parts can eventually be mechanically welded together [Sasada, 1984]. The chemical composition of the transfer was measured using energy dispersive X-ray (EDX) analysis, and is compared with that of the base materials in the wear pair (Table 8.6). The transfer contains silicon, manganese and nickel indicating that it is a mixture of both the materials in the wear pair, and thus that it is composed of small particles of wear debris. The chromium content of the transfer layer indicates that it is substantially made up of wheel material, though molybdenum content is anomalous. The anomaly requires further work; but, it is clear that the transfer is a mixture of the two materials involved in the wear.

The microhardness of the transfer layer is in excess of HV 900, much higher than the bulk material (Fig. 8.17). Newcomb and Stobbs [1984] examined a layer of this type formed on a rail steel subjected to predominantly high-load rolling wear and concluded that it was entirely

ferritic with a high density of dislocations supersaturated with carbon, a structure similar to that of martensite.

Table 8.6: The chemical composition (wt.%) of the transfer layer determined using EDX analysis, together with the compositions of the base materials in the wear pair.

	Si	Mn	Ni	Cr	Mo
Wheel	0.30	0.63	1.46	1.07	0.26
Rail steel K	1.53	2.03	-	-	-
Transfer layer*	0.55	0.94	0.91	1.05	0.02

*: average of five measurements

The high sulphur content (about 100 ppm) in the alloys investigated leads to a high fraction of MnS inclusions. These inclusions decohere or crack during wear process. Fig. 8.19 shows a flattened MnS inclusion in the highly deformed region just below the wear surface. In this case no crack can be observed; however material removal is likely to be accelerated by the presence of such inclusions as they come close to the surface and form open cracks. Wear debris associated with this type of inclusion can be observed in Fig. 8.20, where fracture along the inclusion/matrix interface can be seen.

Another source of weakness in the microstructures is the allotriomorphic ferrite which decorates the austenite grain boundaries in some alloys. This mode of weakness is significant for Alloy L which contains a substantial amount of allotriomorphic ferrite. The wear scar (Fig. 8.21) for this alloy shows that allotriomorphic ferrite usually occupies the top layer of the worn surface (Fig. 8.21a), implying that previous material removal has occurred as a result of decohesion along the allotriomorphic ferrite/matrix interphase boundaries. The cracks penetrate from worn surface to the subsurface region, and propagate along allotriomorphic ferrite/matrix boundaries. The micrograph of the unetched structure in Fig. 8.21(b) clearly shows the presence of such cracks.

8.4.5 Retained Austenite Content

Large amounts of retained austenite are detected in these silicon-rich experimental steels (Table 8.7).

In the high carbon steels, K and P, the austenite content is around 17 %, while only 6 % is detected in the lower carbon steels, A and L. This difference in the amount of austenite retained can be rationalized in the following way. Bainitic ferrite grows in a diffusionless manner

from the austenite and then partitions its excess carbon into surrounding residual austenite. Subsequently, bainite grows from the carbon enriched austenite, and the process continues until such a transformation becomes energetically impossible when the carbon content in austenite reaches the T_0 curve, where ferrite and austenite have identical free energy. This critical point is reached at an earlier stage in the transformation as the carbon concentration becomes higher, and thus a larger volume fraction of austenite can be retained after cooling to room temperature.

Table 8.7: The amount of retained austenite (Vol.%) before (underneath the worn surface, ≥ 5 mm) and after wear test (worn surface).

Alloy	K1	K2	K3	L	P1	P2	P3	A
Before wear test(γ_b)	17.0	15.6	17.1	6.2	16.1	16.5	17.1	7.3
After wear test(γ_a)	1.2	1.2	1.5	0.7	1.6	1.2	1.5	1.7

After wear testing, the amount of austenite decreased drastically (Fig. 8.22). The (111) peak of the austenite decreased significantly following wear testing. The truncated peak is the main (110) bainitic ferrite peak, which appeared to widen following wear due to the distortion of the lattice by deformation defects. Most of the retained austenite has been mechanically transformed into martensite regardless of the alloy.

To examine the extent of the hardening due to transformation, microhardness measurements at various depths from the worn surface were performed. The results of these tests are shown in Fig. 8.23. The maximum hardness increment and the thicknesses of the hardened layers are summarized in Table 8.8.

Fig. 8.24 shows that the hardness increment in the worn surface is proportional to the amount of austenite transformed to martensite, and confirms that a greater initial austenite content can result in a greater hardness increase as a result of the wear process. However, the expected increase in dislocation density will also contribute to the hardness increment.

Hardness is a measure of resistance to plastic deformation, and therefore it is not surprising that the depth of deformation (hardening) is closely related to the bulk hardness before the wear test (Fig. 8.25). This is a general trend, but is obviously microstructure sensitive; the data point for Alloy L shows an anomalously small deformed layer for its bulk hardness, but as discussed previously, its microstructure was very different to the others. It can be seen that the higher carbon steels K and P exhibit a higher extent and higher degree of hardening due to the higher amount of austenite transformed to martensite.

Table 8.8: The hardness (HV 100 g) and hardness increment after wear test and the thickness of hardening layer (μm)

Alloy	K1	K2	K3	L	P1	P2	P3	A
Hardness before test	442	470	407	488	468	411	444	673
Hardness of worn surface	664	722	632	599	728	628	688	800
Hardness increment	222	252	225	111	240	217	244	117
Thickness of hardened layer	700	500	700	120	800	500	600	200

The hardness tests performed here with a 100 g indenting load give different values of hardness to those used earlier which had a 30 kg indenting load. Table 8.9 shows the difference in hardness values measured when the bulk areas of the samples were indented with these two loads. Although the microhardness values are consistently higher than the macrohardness values, the trends observed with hardness are still valid.

Table 8.9: The difference of hardness measured by bulk hardness test (HV 30 kg) and microhardness test (HV 100 g).

Alloy	K1	K2	K3	L	P1	P2	P3	A
HV 30 kg	376	404	333	423	381	344	395	543
HV 100 g	442	470	407	488	468	411	444	673
Difference	66	66	74	65	87	67	47	140

The formation of transfer layers from the wear debris is confirmed to be martensite. The results of the retained austenite content and the microhardness measurements of the wear-affected layer are therefore affected. Nevertheless, the general trends as outlined above are still considered to be valid.

8.5 FURTHER DISCUSSION

The material-removal process in the present rolling/sliding wear could involve several mechanisms operating together. The sliding component in the wear process can induce plastic shearing [Kayaba and Kato, 1979], asperity rupture and aggregation [Sasada, 1984] and delamination [Hutchings, 1992]. The first two mechanisms are similar with shearing and cutting materials from surface, and possibly transferred layer can happen. The detection of transferred layer (Fig. 8.17) confirms their operation. For delamination, which involves the nucleation of subsurface cracks and their propagation parallel to the surface, the evidence can be observed

in Fig. 8.18, showing debris with cracks parallel to the surface. The mechanisms are likely to operate in segregation or simultaneously during the wear process, though the exact influence is difficult to know.

The wear rate is generally dependent on hardness, but it is evident that allotriomorphic ferrite leads to a deterioration in wear resistance. In some previous reports, cracks detrimental to wear resistance have been found below the wear track in the steels with bainitic microstructures [Devanathan *et al.*, 1991; Garnham *et al.*, 1992]. Deformation incompatibility is the main cause for crack formation at the martensite/bainite boundaries [Devanathan *et al.*, 1991] or lower/upper bainite boundaries and flattened inclusion interfaces [Garnham *et al.*, 1992]. Inclusion interfaces and allotriomorphic ferrite have been identified to be deleterious in the present work.

Transformation of austenite into martensite during the wear process has long been recognized as an effective way of improving wear resistance [Jost *et al.*, 1985]. Increases in hardness of 50 % have been observed and attributed partly to the mechanically induced austenite transformation. Retained austenite transformation is beneficial in two respects: its ductile nature [Bhadeshia *et al.*, 1983a, b; Tomita *et al.*, 1993; Sandvik *et al.*, 1981] and its transformation to hard martensite.

Fig. 8.26 shows the trend in wear resistance of a wide range of conventional rail steels [Jerath *et al.*, 1991]. The wear resistance of steels K and P is comparable to, if not slightly better than the conventional pearlitic steels or heat-treated rails. To summarize, the good wear resistance of the present bainitic steels can be attributed to the combined effects of high strength, high toughness and retained austenite.

8.6 CONCLUSIONS

A carbide-free microstructure containing of a mixture of just bainitic ferrite, retained austenite and martensite is found to exhibit the required high strength, but also has exceedingly high toughness and wear resistance. This is in comparison to conventional rail steels which are based on pearlitic microstructures. The excellent properties of the present alloys are attributed to the absence of carbides, the ability of the microstructures to tolerate a large degree of plastic strain and the mechanically induced martensitic transformation of the retained austenite.

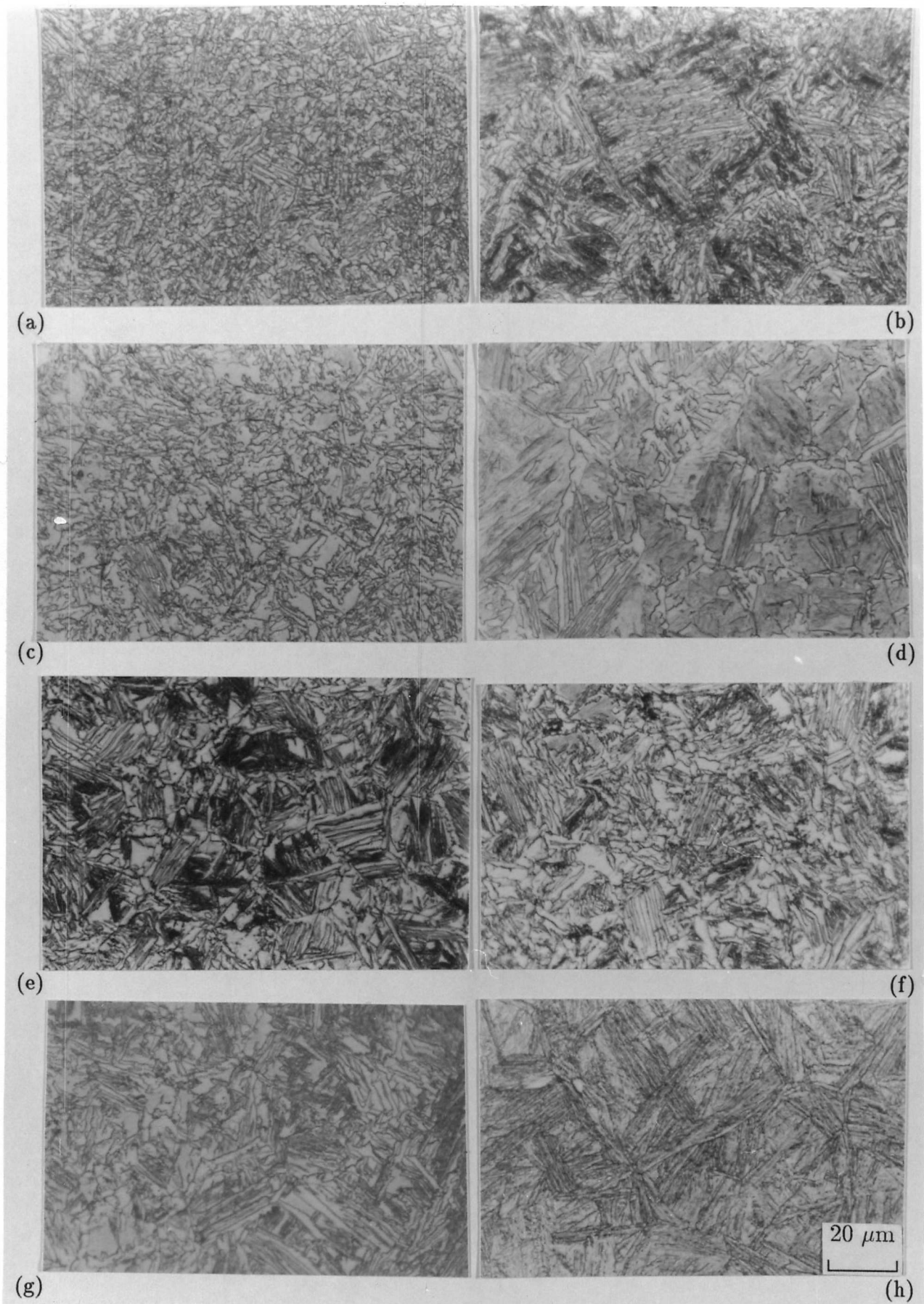


Fig. 8.1: Optical micrographs showing the microstructure of experimental steels. (a) Alloy K1. (b) Alloy K2. (c) Alloy K3. (d) Alloy L. (e) Alloy P1. (f) Alloy P2. (g) Alloy P3. (h) Alloy A.

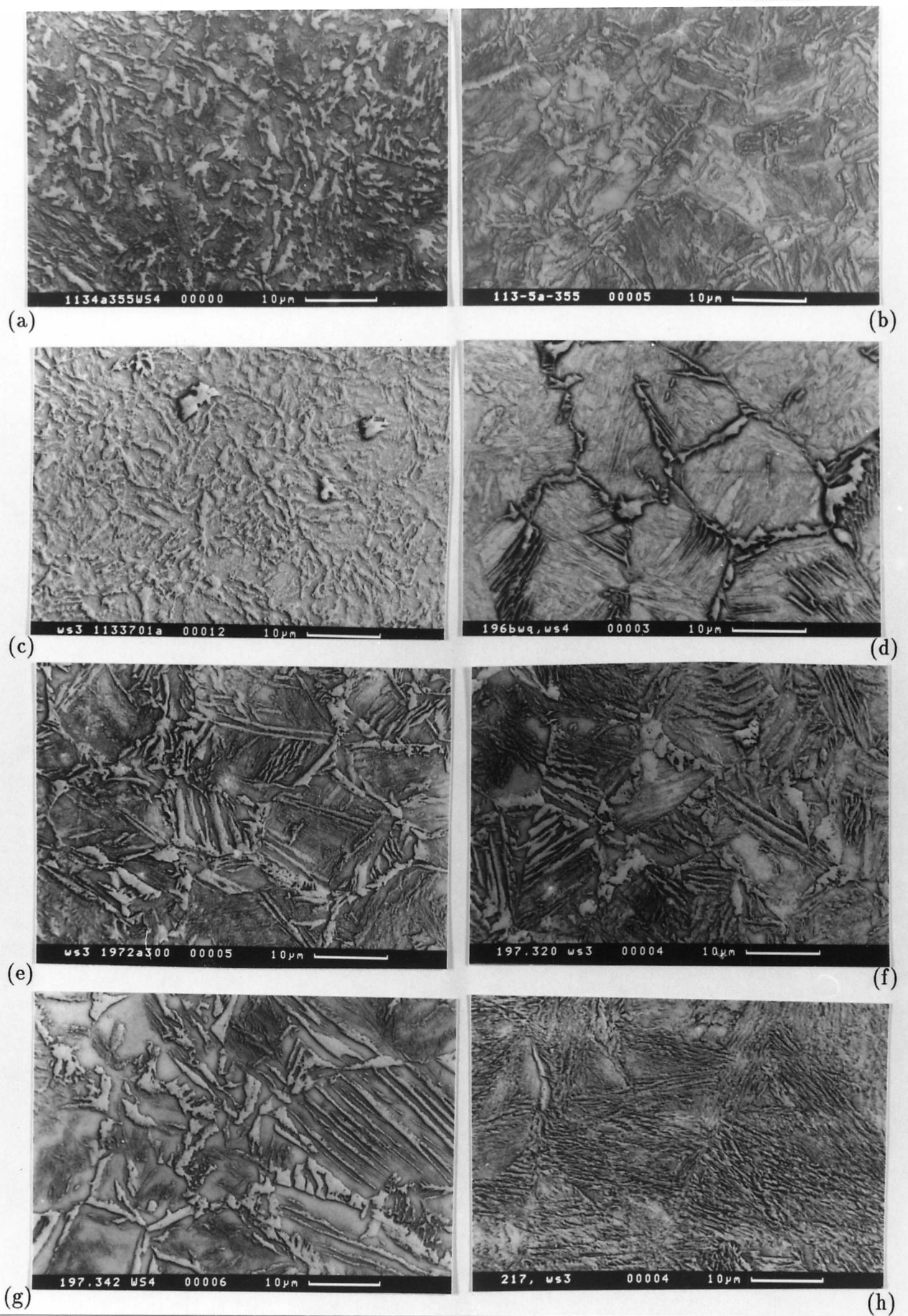


Fig. 8.2: SEM micrographs of the experimental steels. (a) Alloy K1. (b) Alloy K2. (c) Alloy K3. (d) Alloy L. (e) Alloy P1. (f) Alloy P2. (g) Alloy P3. (h) Alloy A.

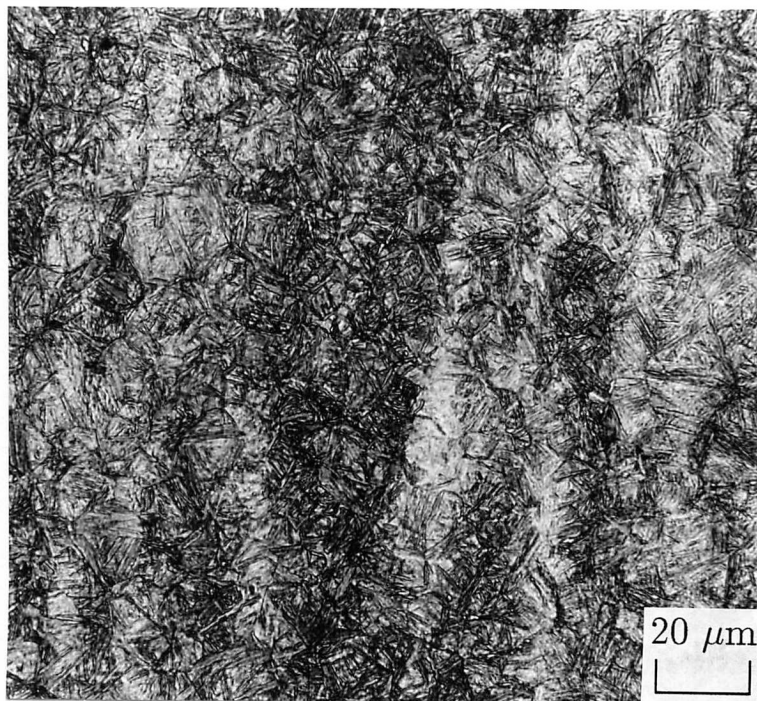


Fig. 8.3: Optical micrograph showing the banded microstructure of steel D.

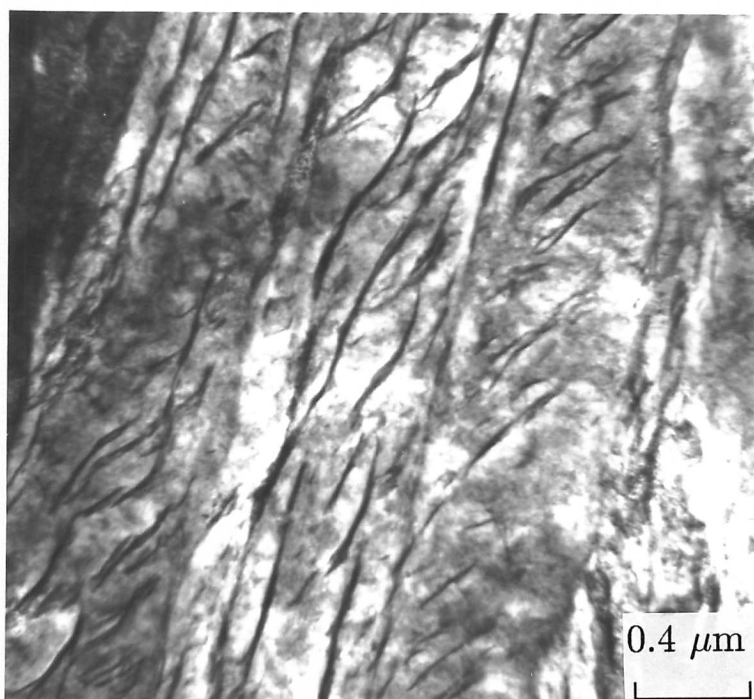
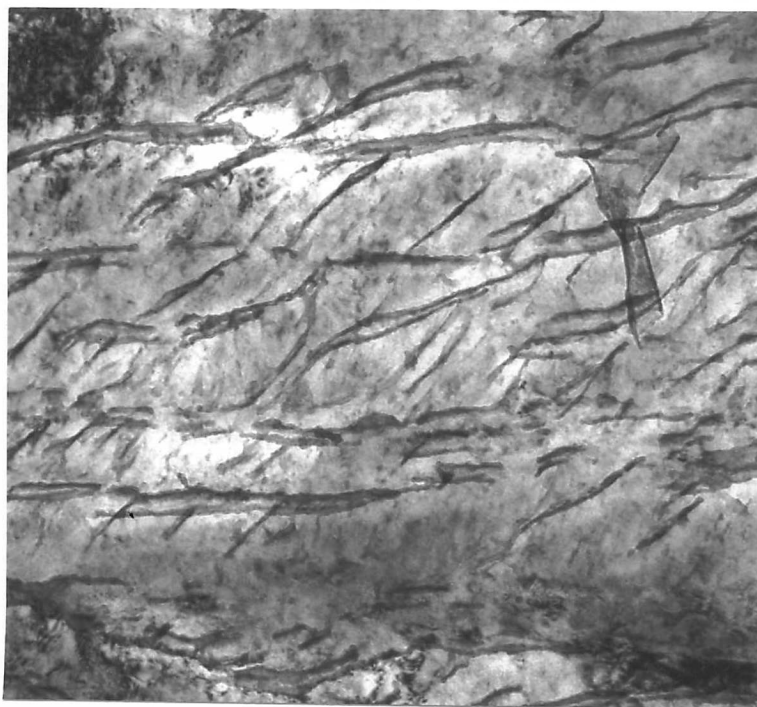
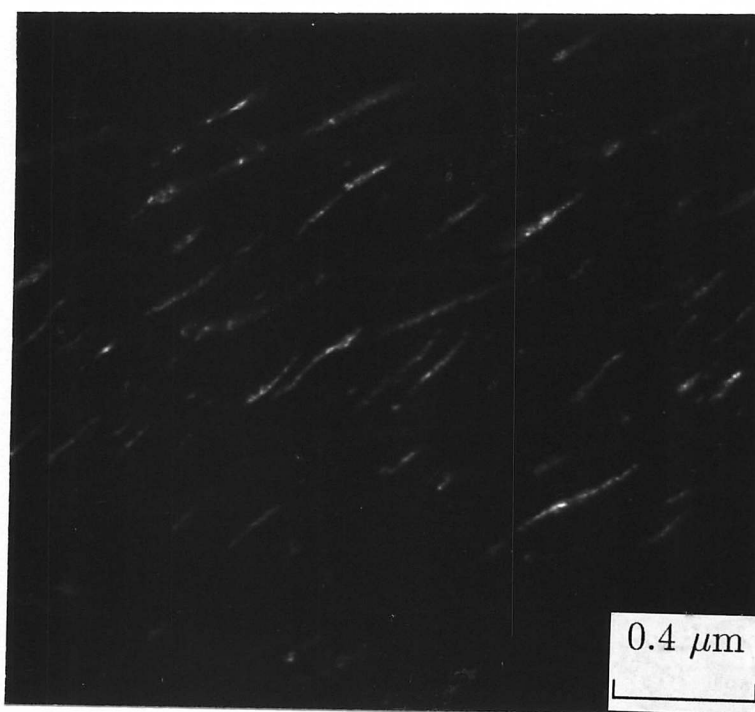


Fig. 8.4: TEM bright-field micrograph shows carbide free upper bainite. Alloy P1, Fe-0.49C-1.44Si-0.51Mn-3.5Ni (wt.%), 900 °C @ 1800 s → 370 °C @ 3600 s → water quenched.



(a)

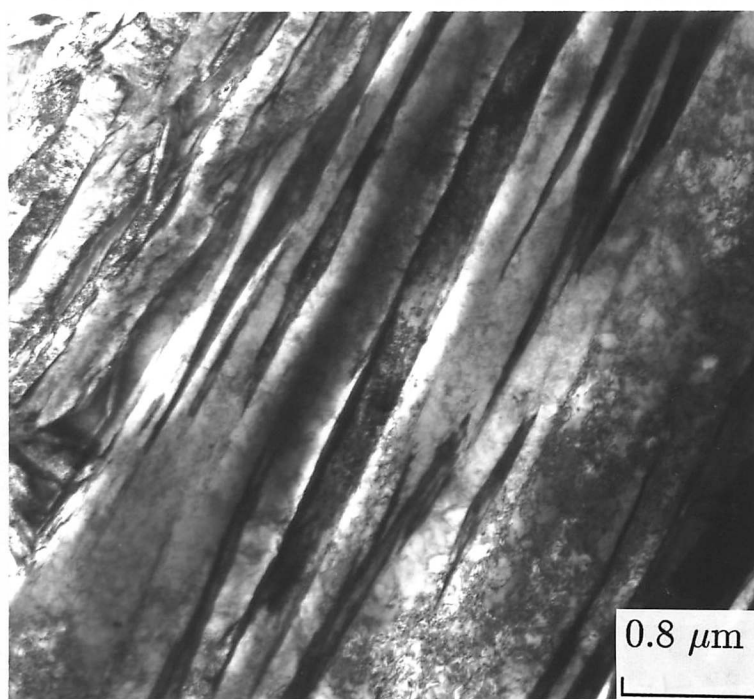


(b)

Fig. 8.5: TEM micrographs show bainite structure and austenite films. Alloy A, Fe-0.27C-1.98Si-2.18Mn-1.9Cr (wt.%). As rolled → air cooled. (a) bright-field image (b) austenite dark-field image



(a)



(b)

Fig. 8.6: TEM bright-field micrograph shows high temperature carbide free upper bainite. (a) Alloy K3, Fe-0.49C-1.53Si-2.03Mn (wt.%), 900 °C @ 1800 s → 370 °C @ 7200 s → water quenched. (b) Alloy P1, Fe-0.49C-1.44Si-0.51Mn-3.5Ni (wt.%), 900 °C @ 1800 s → 370 °C @ 3600 s → water quenched.



Fig. 8.7: TEM bright-field micrograph shows carbide free upper bainite grew from grain boundary ferrite. Alloy P1, Fe-0.49C-1.44Si-0.51Mn-3.5Ni (wt.%), 900 °C @ 1800 s → 370 °C @ 3600 s → water quenched.

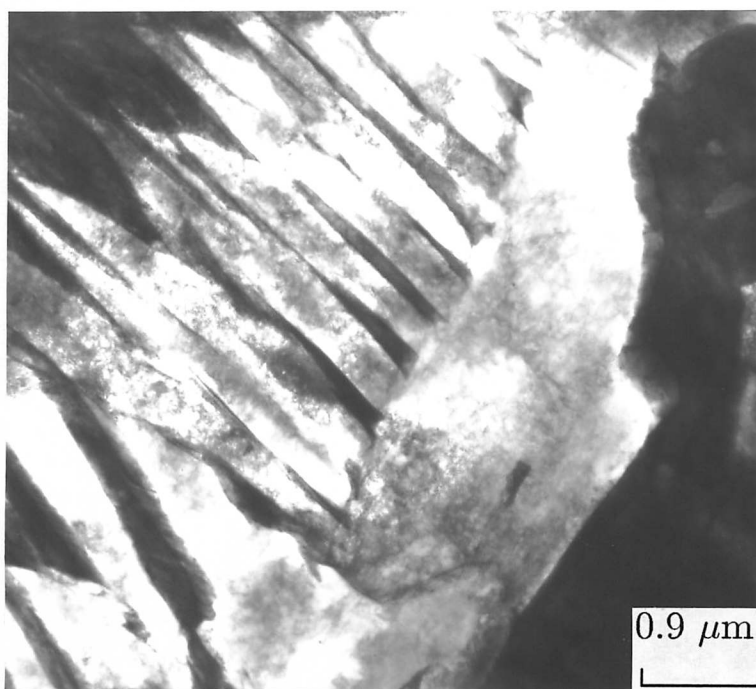
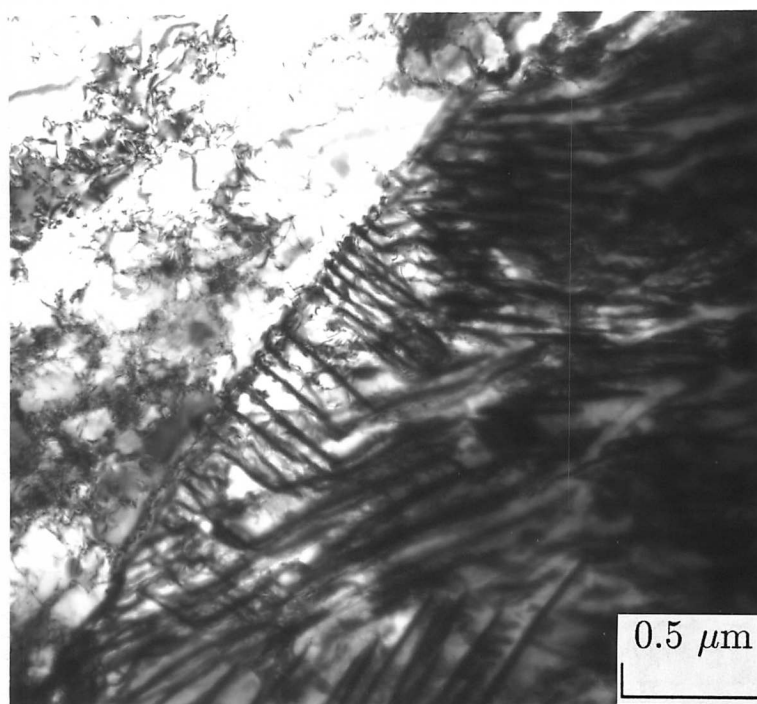
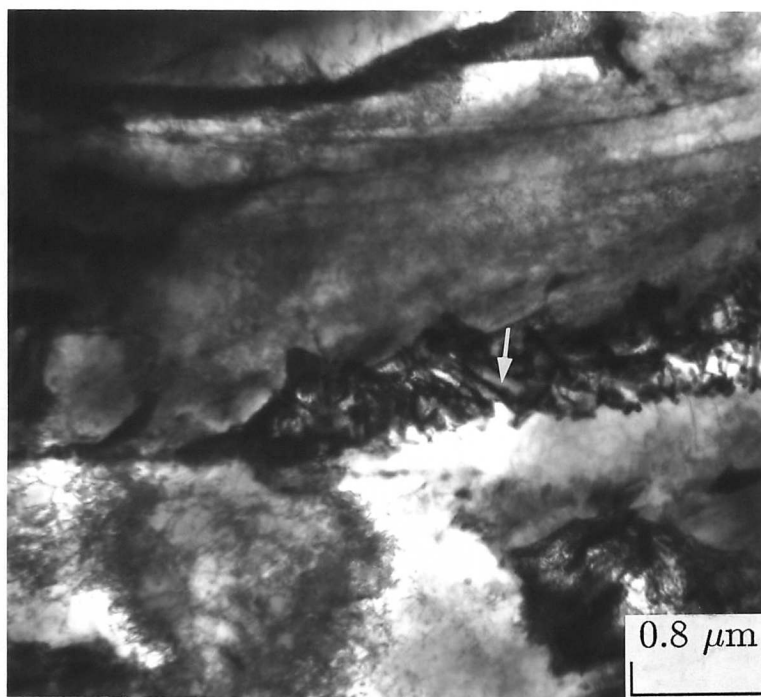


Fig. 8.8: TEM bright-field micrograph shows bainitic ferrite grew from allotriomorphic ferrite. Alloy L, Fe-0.22C-1.39Si-1.97Mn (wt.%), 900 °C @ 1800 s → boiling water quenched.



(a)



(b)

Fig. 8.9: TEM bright-field micrographs showing pearlites (a) growing at an austenite grain boundary, (b) from austenite between parallel bainite sheaves. Alloy K3, Fe-0.49C-1.53Si-2.03Mn (wt.%), 900 °C @ 1800 s → 370 °C @ 7200 s → water quenched.

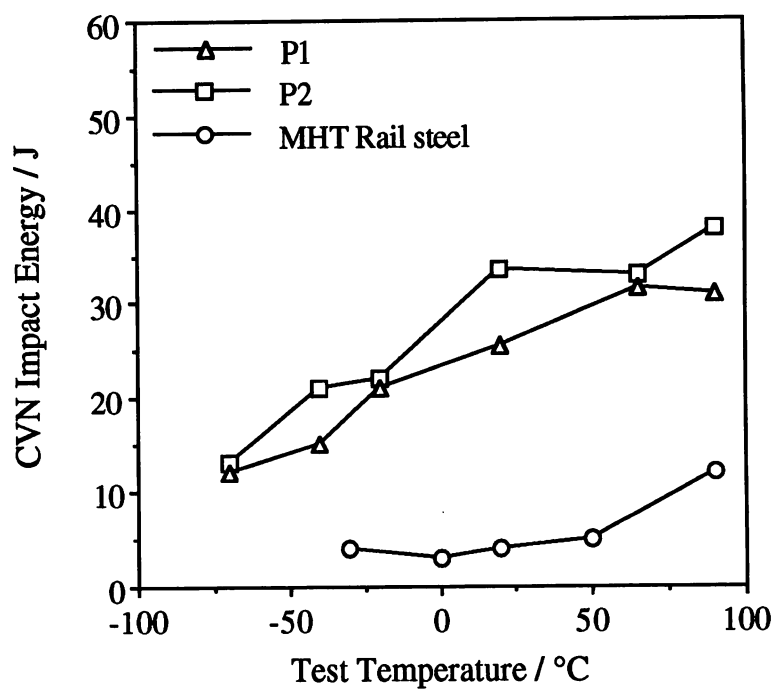


Fig. 8.10: Charpy V-notch impact energy for a plain carbon mill heat-treated rail steel and an experimental steel P.

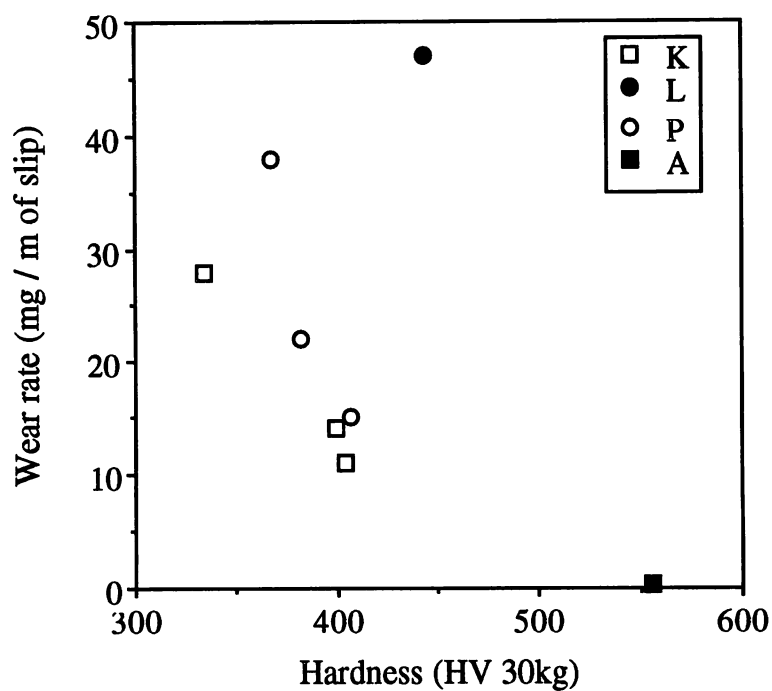


Fig. 8.11: The influence of hardness on rolling contact wear performance of experimental steels.

← wear direction

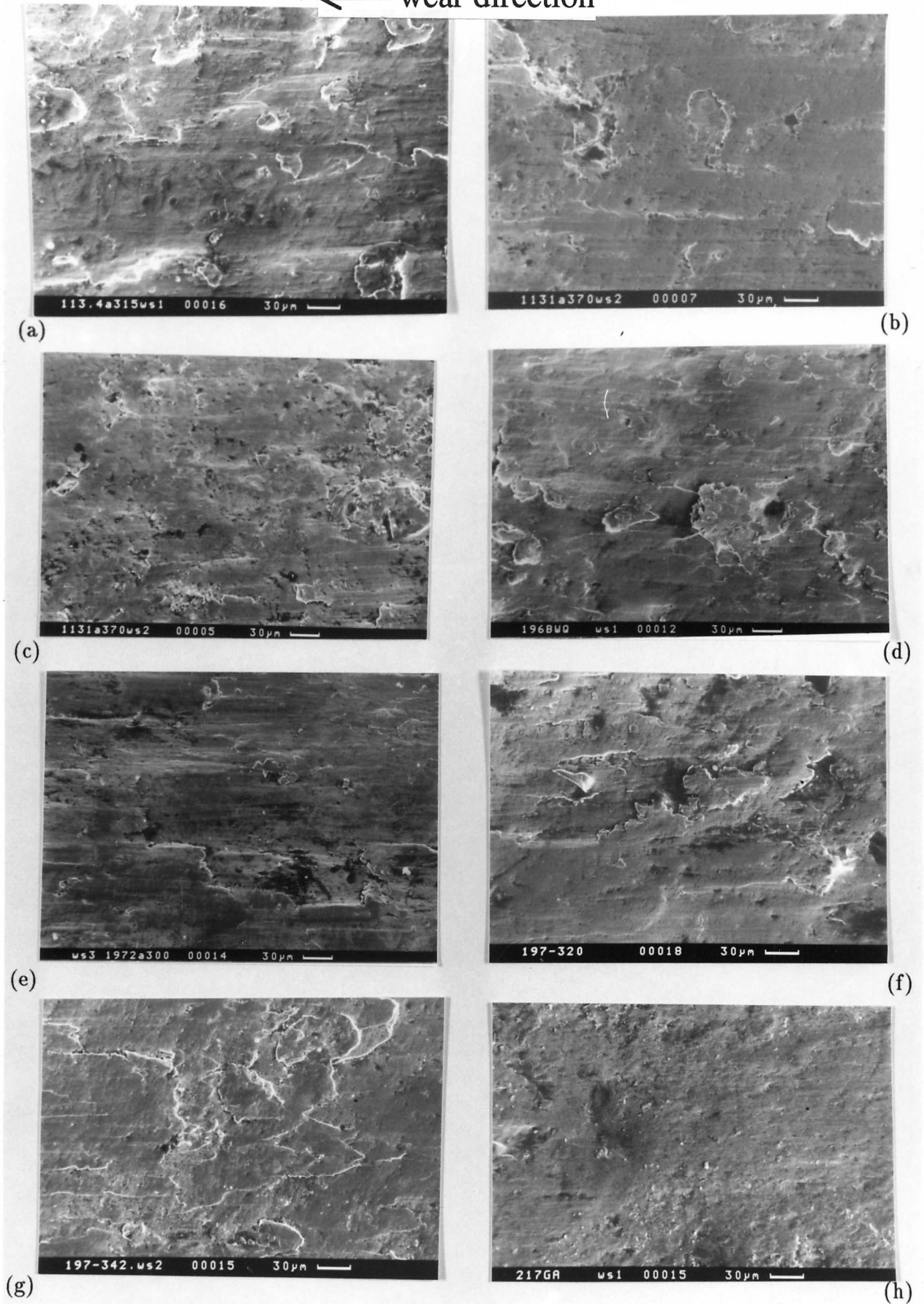


Fig. 8.12: SEM micrographs of worn surfaces. (a) Alloy K1. (b) Alloy K2. (c) Alloy K3. (d) Alloy L. (e) Alloy P1. (f) Alloy P2. (g) Alloy P3. (h) Alloy A.

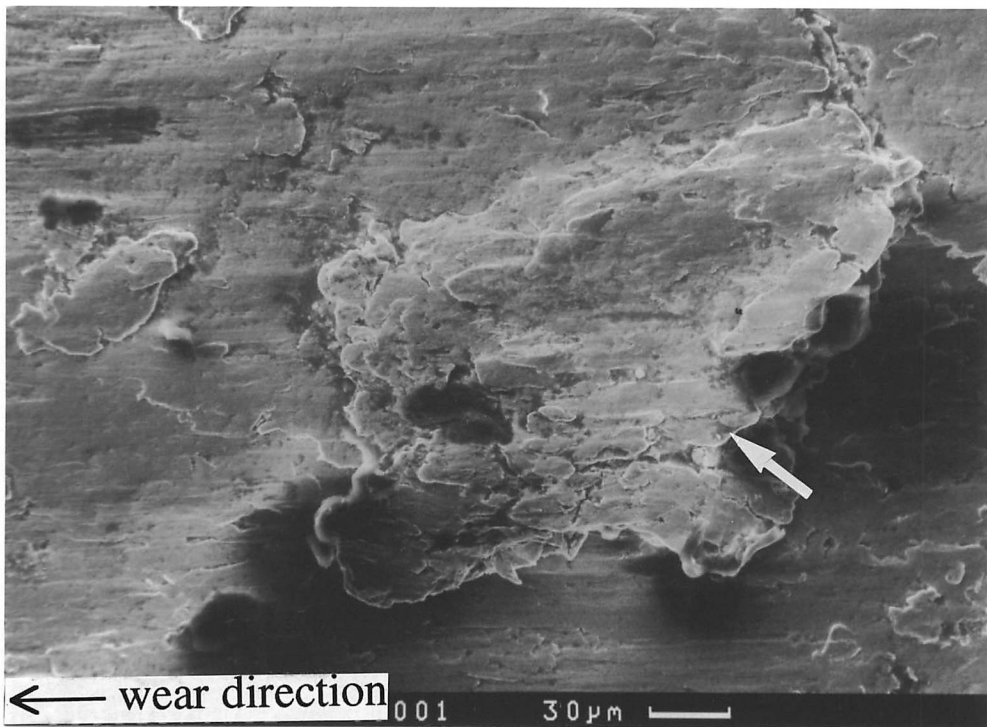


Fig. 8.13: SEM micrograph showing gouging debris (marked by an arrow) partially attached to the worn surface. Alloy K3, Fe-0.49C-1.53Si-2.03Mn (wt.%), 900 °C @ 1800 s → 370 °C @ 7200 s → water quenched.

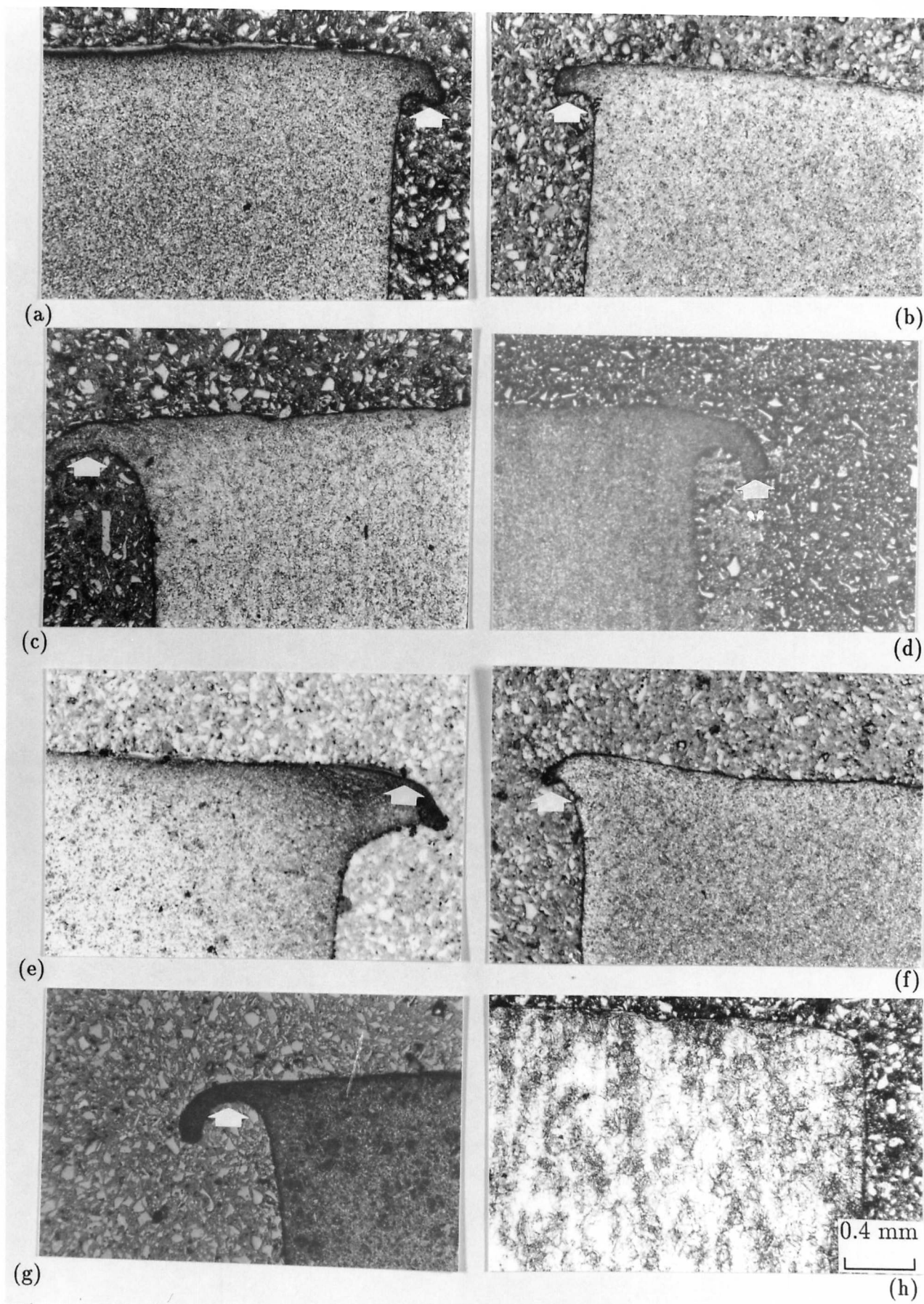


Fig. 8.14: Optical micrographs show the deformation edges form in the cross section perpendicular to the rolling direction from worn samples. (a) Alloy K1. (b) Alloy K2. (c) Alloy K3. (d) Alloy L. (e) Alloy P1. (f) Alloy P2. (g) Alloy P3. (h) Alloy A.

worn surface

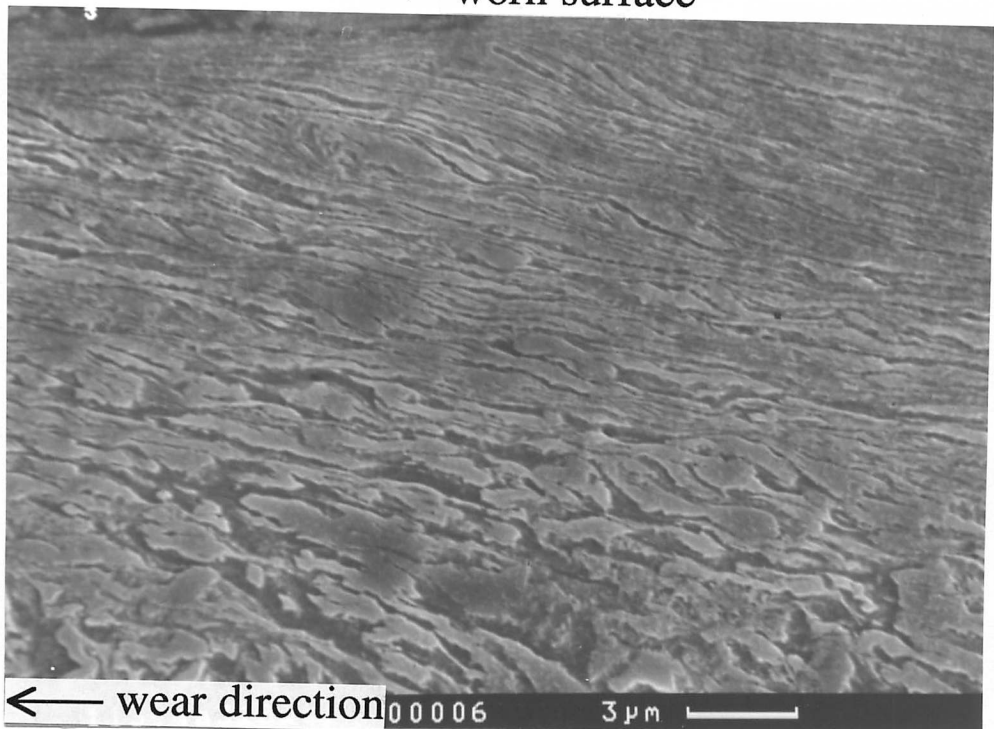
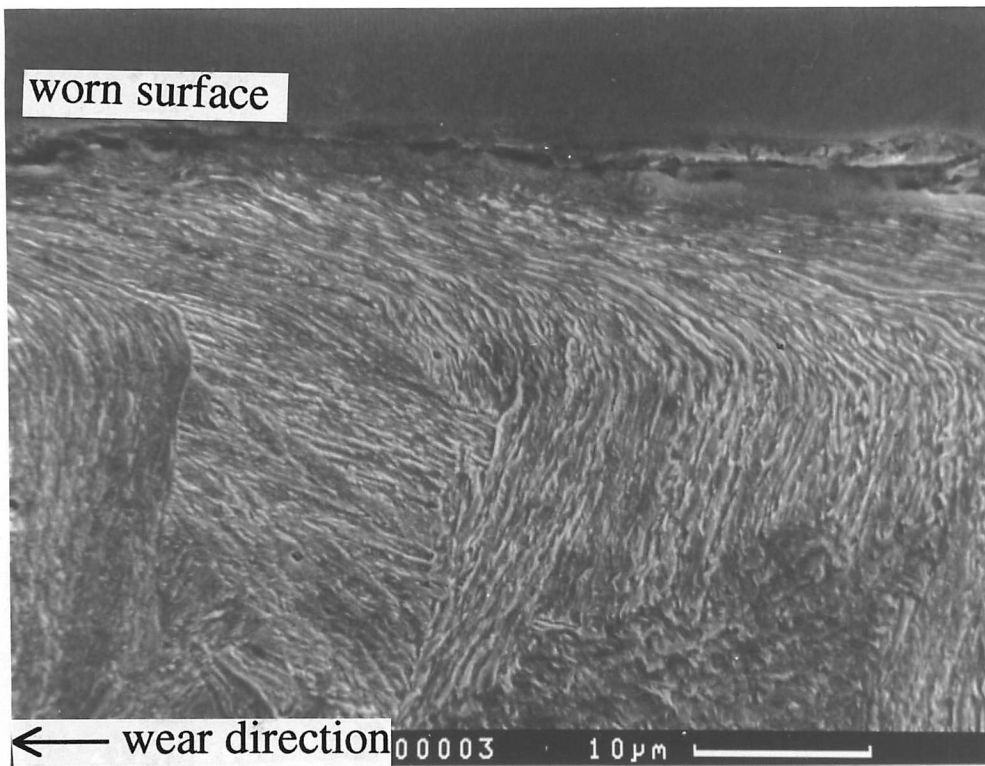
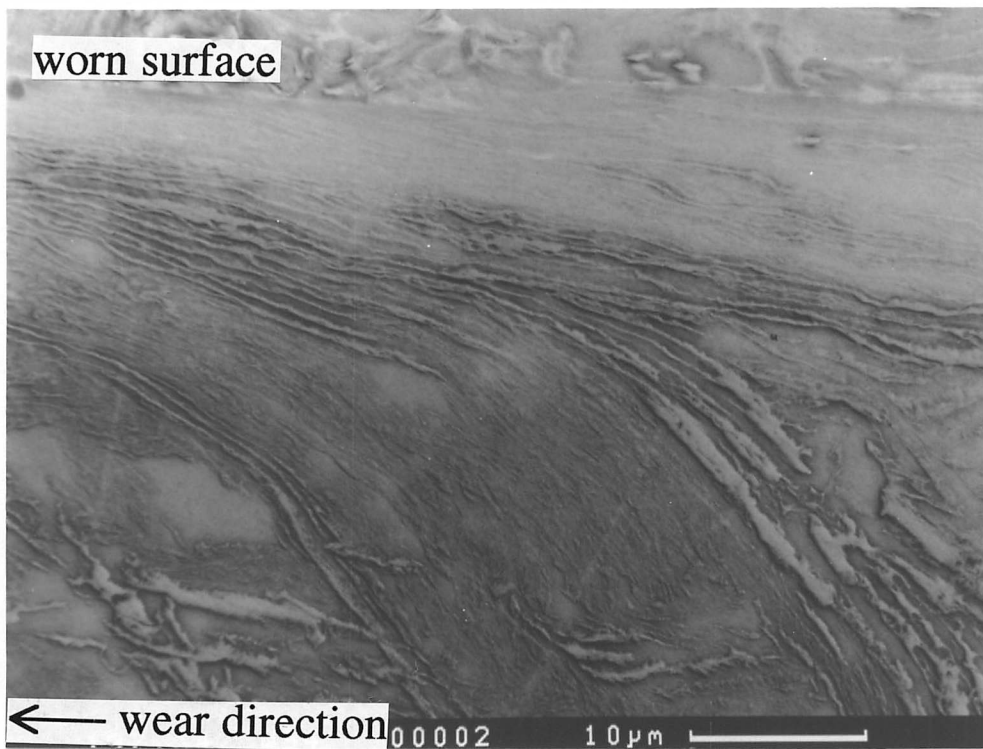


Fig. 8.15: SEM micrograph showing the deformation adjacent to the worn surface. It is noticeable that the microstructure is severely deformed during wear, but nevertheless remains continuity.



(a)



(b)

Fig. 8.16: SEM micrographs showing that the extent of deformation after wear test is dependent on the hardness of the alloy. (a) Alloy A (HV 556). (b) Alloy P3 (HV 407). The deformed layer for Alloy A is about $10\ \mu\text{m}$ thick, whereas it extends to about $30\ \mu\text{m}$ in Alloy P3.

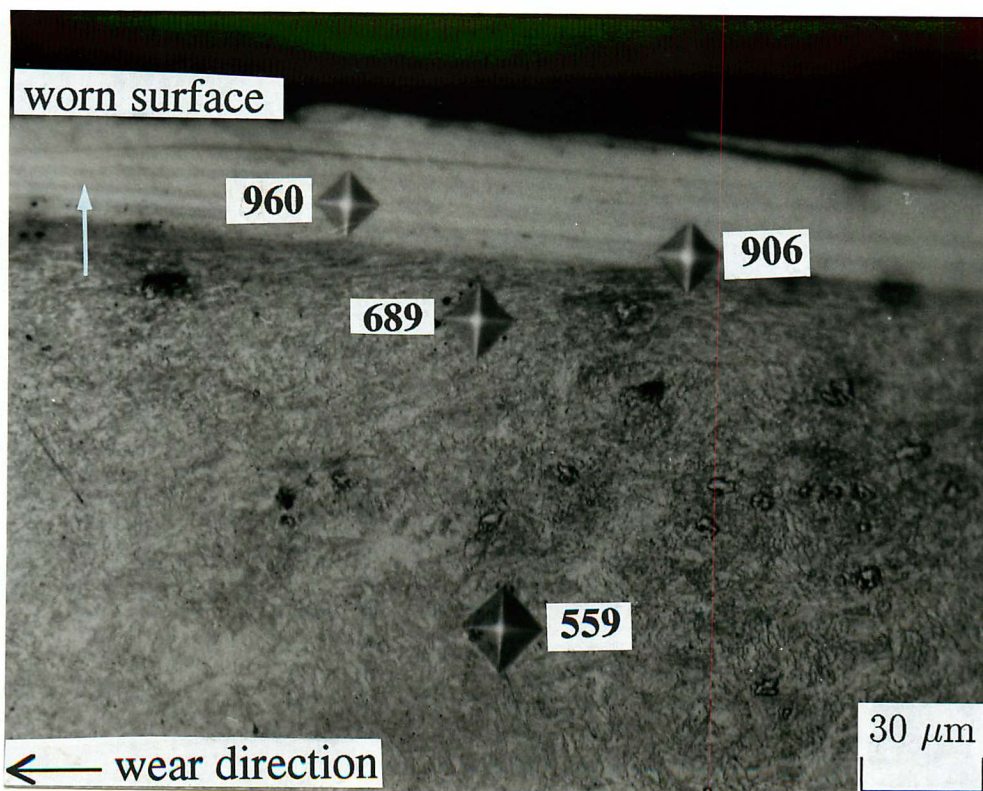


Fig. 8.17: Optical micrograph showing the layered debris (marked by an arrow) at the worn surface. The microhardness of the debris is much higher than the material underneath. Alloy K2, Fe-0.49C-1.53Si-2.03Mn (wt.%), 900 °C @ 1800 s → 355 °C @ 7200 s → water quenched.

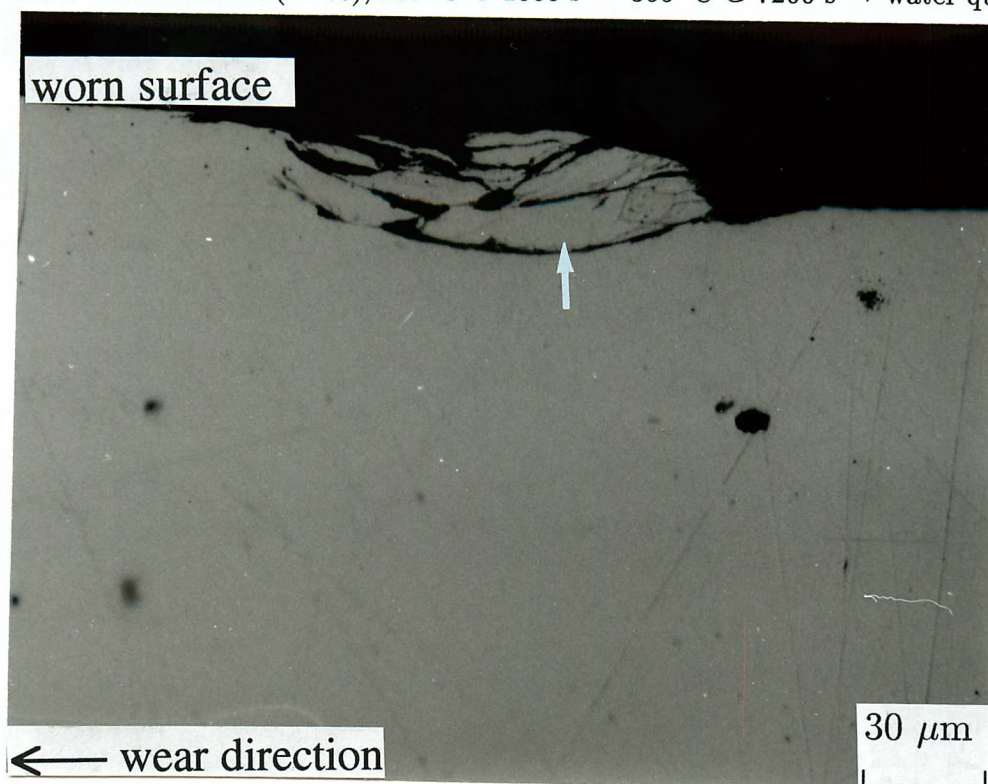


Fig. 8.18: Optical micrograph of partially detached debris (marked by an arrow) with many cracks parallel to the wear direction (unetched). Alloy P3, Fe-0.49C-1.44Si-0.51Mn-3.5Ni (wt.%), 900 °C @ 1800 s → 345 °C @ 3600 s → water quenched.



Fig. 8.19: SEM micrographs of a MnS inclusion situated near the worn surface has been flattened , but no crack can be observed, after wear test. Alloy K2, Fe-0.49C-1.53Si-2.03Mn (wt.%), 900 °C @ 1800 s → 355 °C @ 7200 s → water quenched.

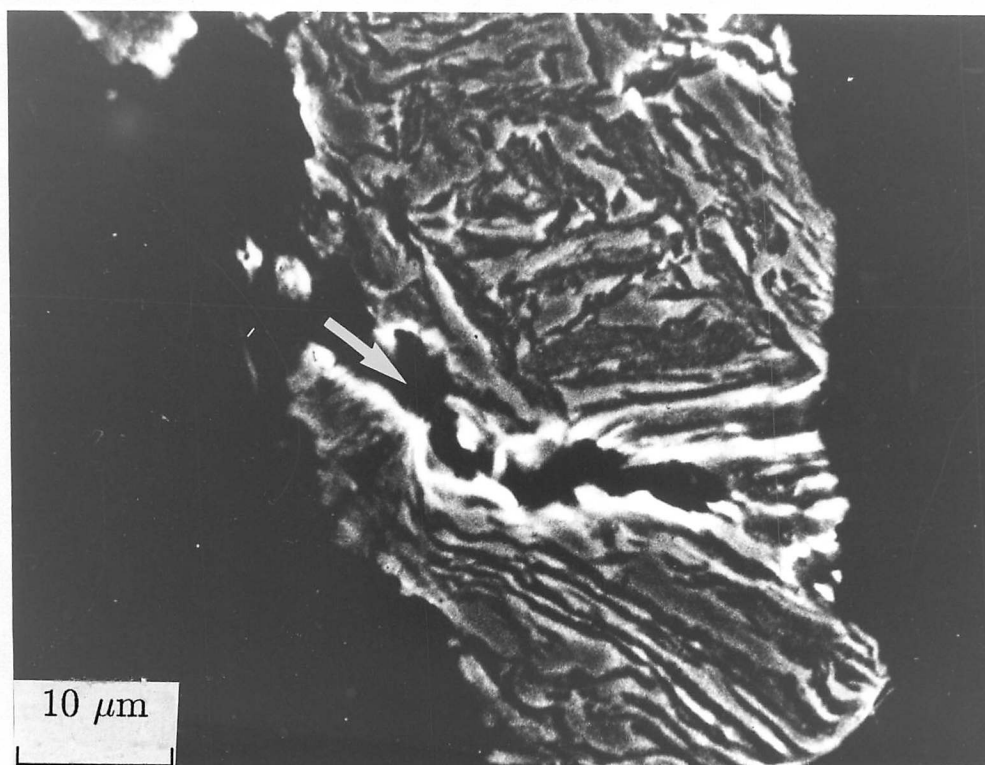


Fig. 8.20: SEM micrograph of a detached debris partially fractured along a MnS inclusion (indicated by an arrow). Alloy L, Fe-0.22C-1.39Si-1.97Mn (wt.%), 900 °C @ 1800 s → boiling water quenched.

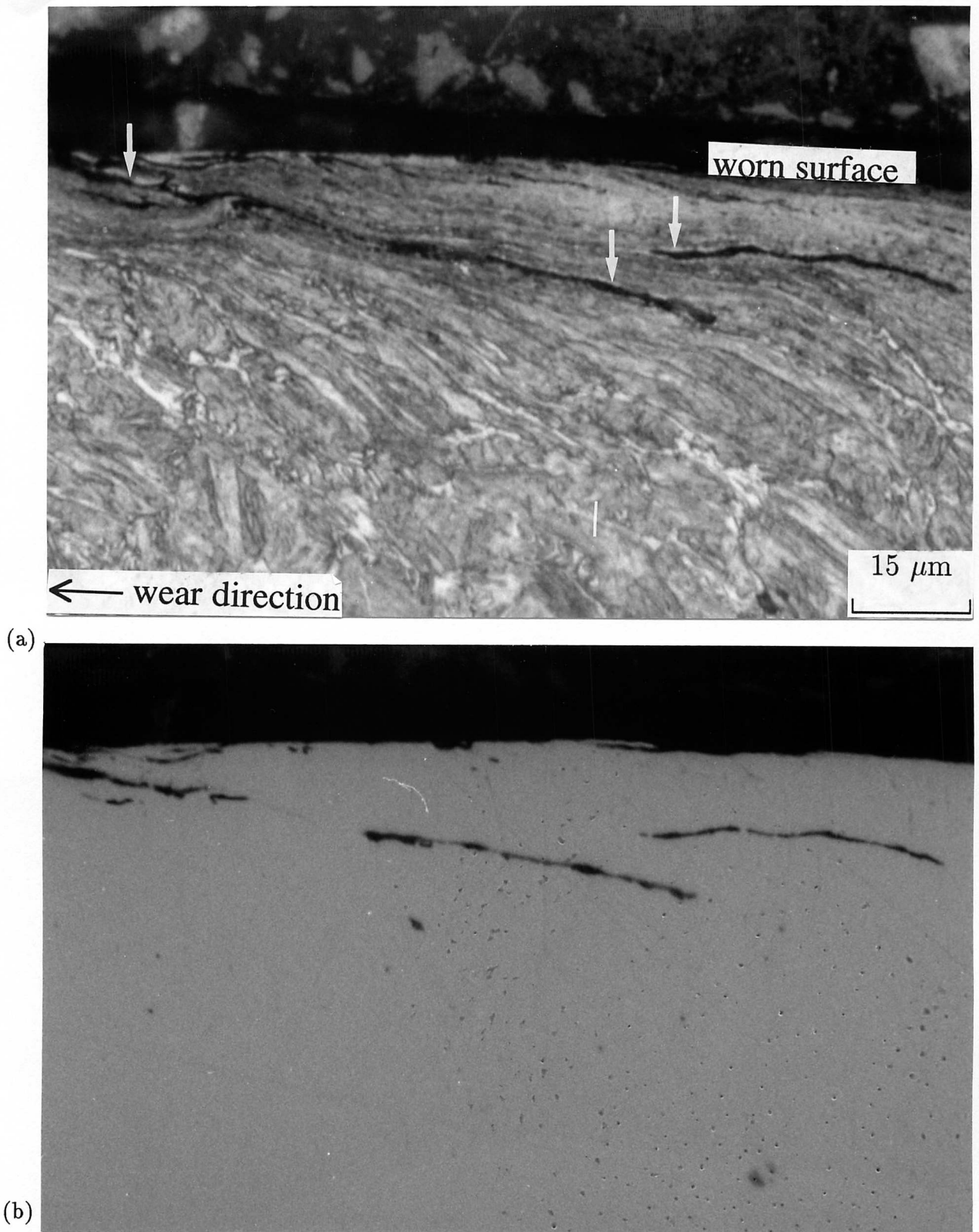
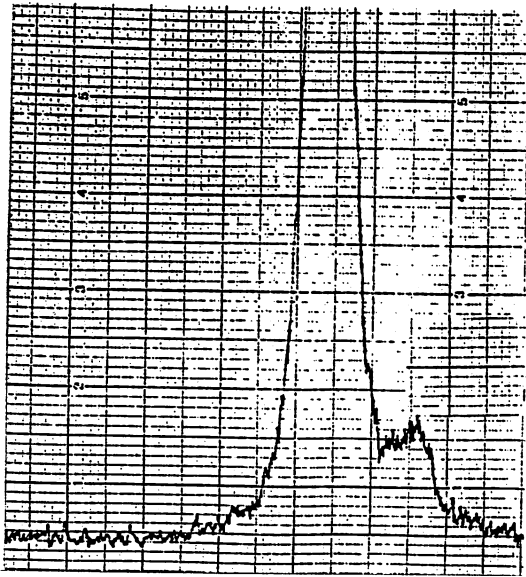
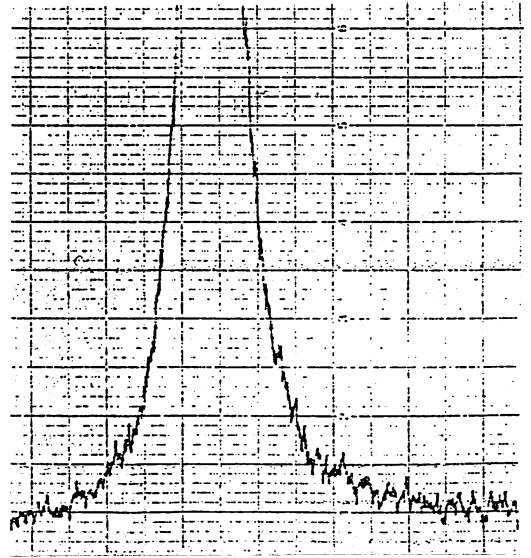


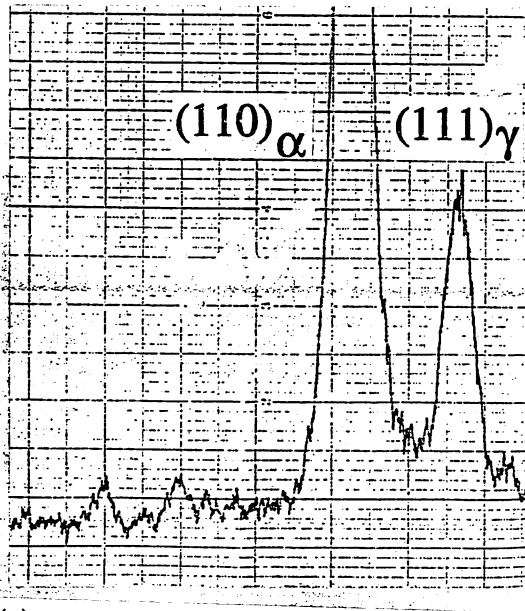
Fig. 8.21: Optical micrograph (a) showing cracks can be found both penetrating from worn surface and in the sub-surface. The cracks clearly grow along the interfaces of allotriomorphic ferrite (white etched phase) and matrix, as indicated by arrows. suggesting the detrimental nature of Allotriomorphic ferrite during wear. Unetched sample can highlight the presence of cracks in (b). Alloy L, Fe-0.22C-1.39Si-1.97Mn (wt.%), 900 °C @ 1800 s \rightarrow boiling water quenched.



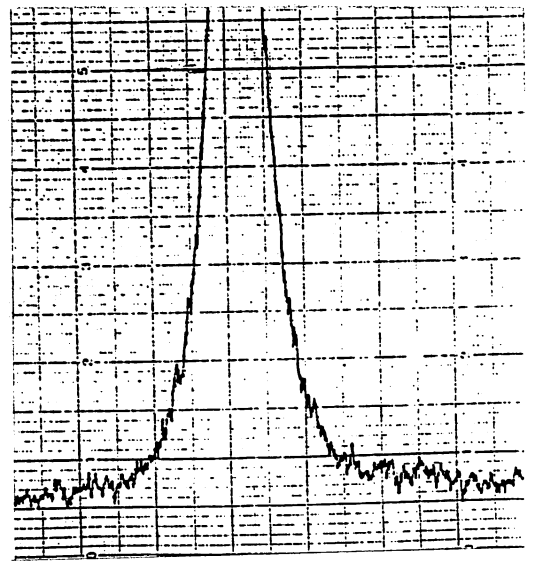
(a)



(b)



(c)



(d)

Fig. 8.22: X-ray analysis of un-worn material and worn surface. (a) Un-deformed material of steel L. (b) Worn surface of steel L. (c) Un-deformed material of steel P3. (d) Worn surface of steel P3.

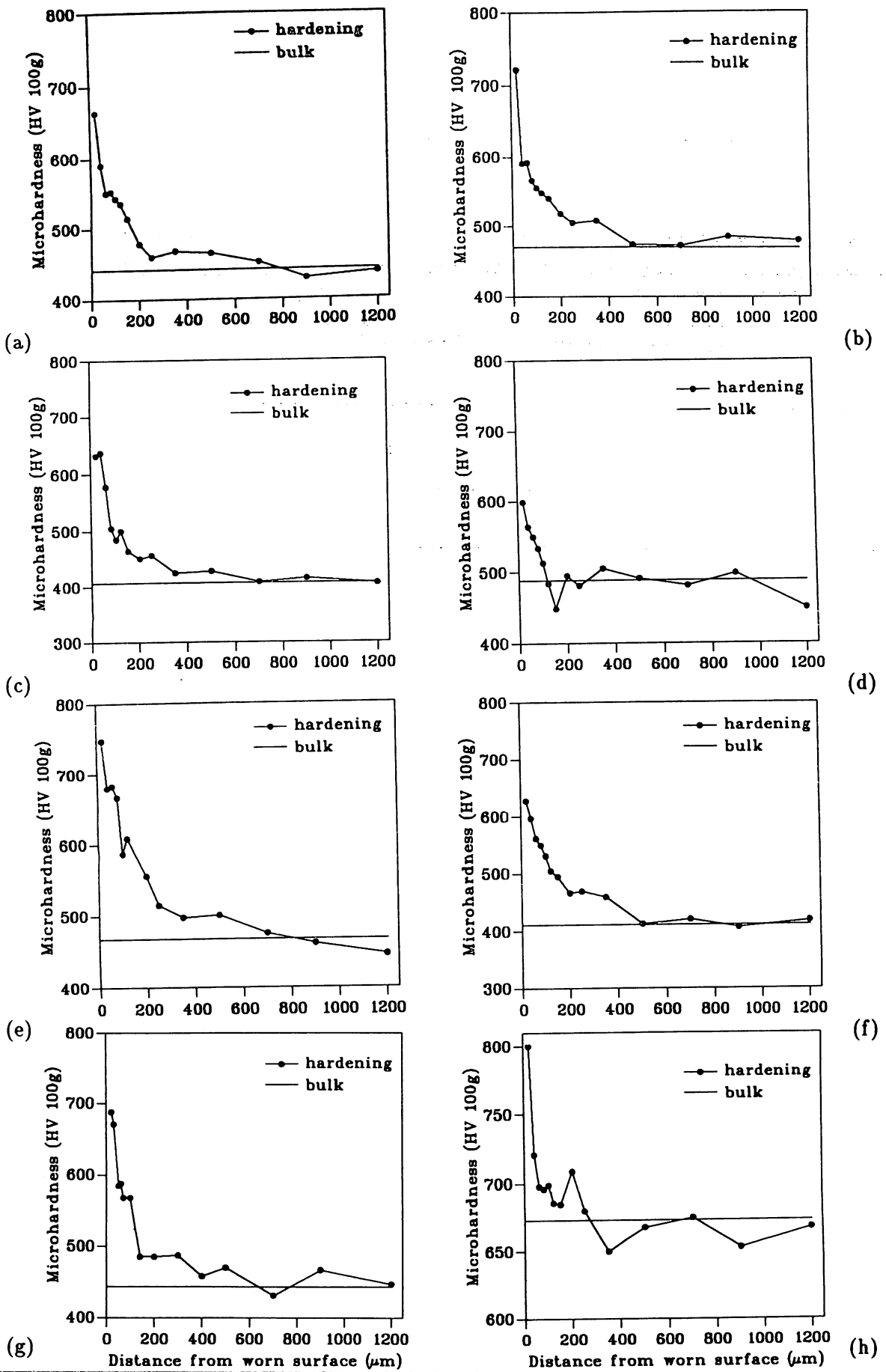


Fig. 8.23: Microhardness (HV 100 g) measurements of worn subsurface. (a) Alloy K1. (b) Alloy K2. (c) Alloy K3. (d) Alloy L. (e) Alloy P1. (f) Alloy P2. (g) Alloy P3. (h) Alloy A.

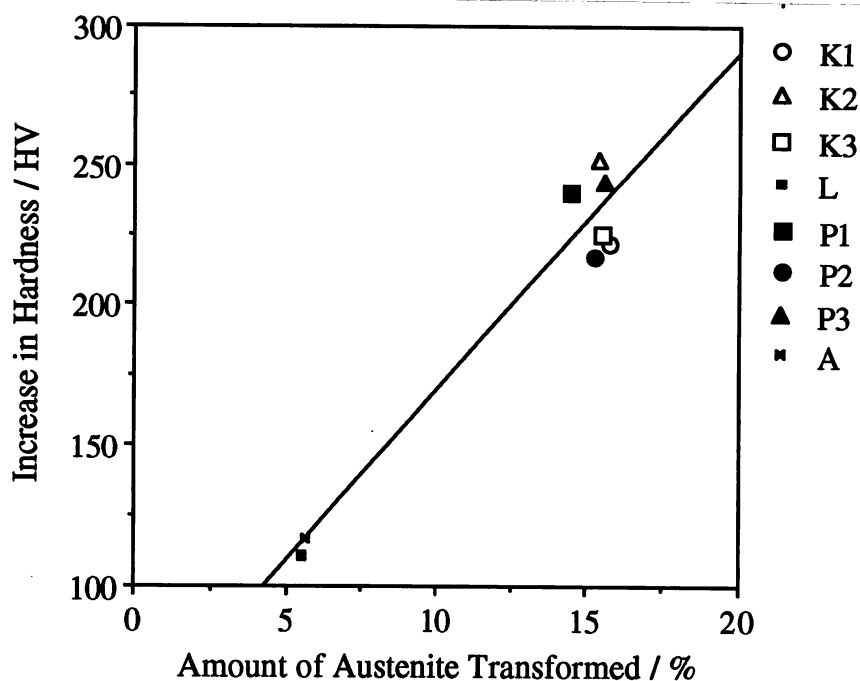


Fig. 8.24: The hardness increment in the worn surface is plotted against the amount of austenite transformed into martensite as a result of wear test.

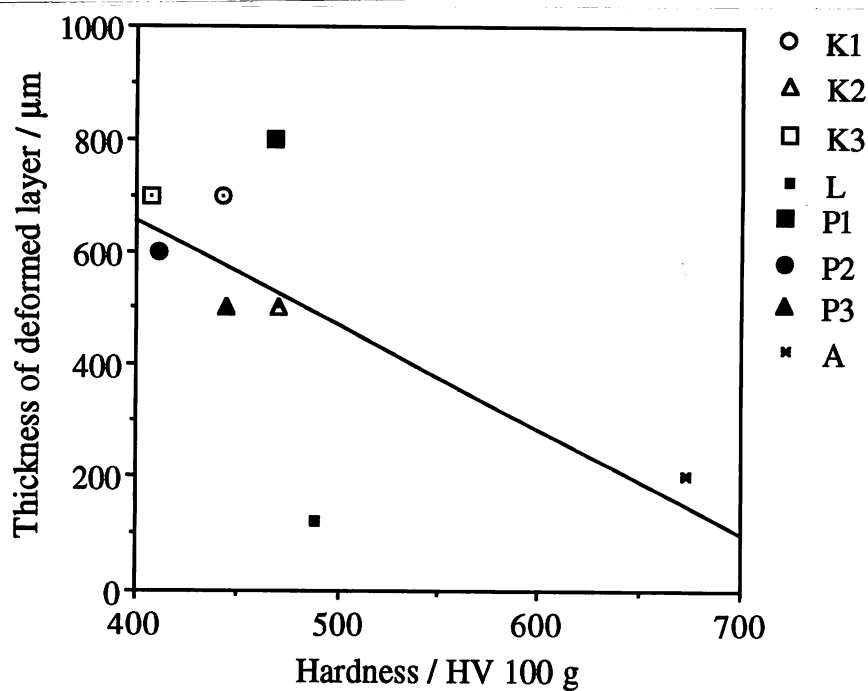
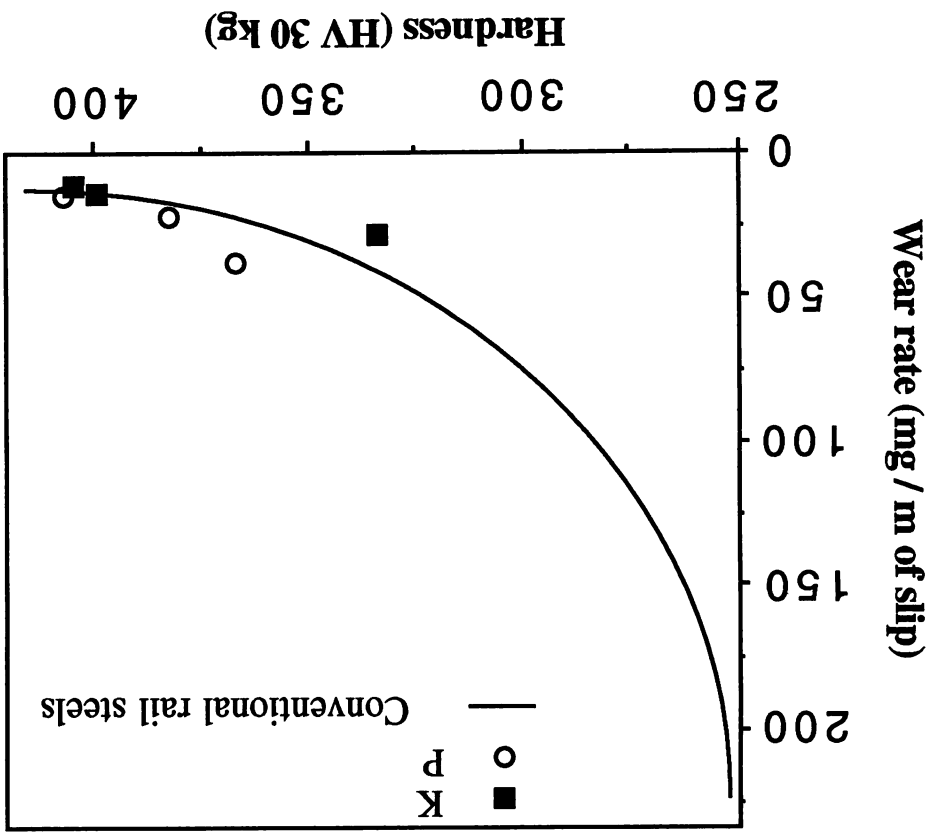


Fig. 8.25: The depth of the deformed layer determined by the microhardness is plotted against the original hardness of the material.

Fig. 8.26: Wear performance of various rail steels and the experimental steels, K and P, under the same test conditions.



CHAPTER 9

IMPURITY-INDUCED TEMPER EMBRITTLEMENT IN CARBIDE-FREE BAINITIC STEELS CONTAINING AUSTENITE AND MARTENSITE

9.1 INTRODUCTION

Bainitic steels have been the subject of intensive studies as potential candidates for rail steels with a better wear resistance (and hence able to tolerate larger loads) than pearlitic alloys [Callender, 1983; Heller and Schweitzer, 1982; Clayton and Devanathan, 1992; Clayton *et al.*, 1987; Devanathan and Clayton, 1991]. It has been shown that carbide-free upper bainite is particularly desirable because the absence of coarse inter-lath carbides makes the nucleation of cracks more difficult [Johnson and Becker, 1993]. The addition of a substantial amount of silicon (up to 2 wt.%) is effective in retarding or preventing cementite precipitation during the formation of bainite [Philip, 1983; Bhadeshia and Edmonds, 1979a]. Another advantage of carbide-free bainitic microstructures is that all the excess carbon which partitions from supersaturated bainitic ferrite then enriches the austenite which is subsequently stabilized and hence, retained to ambient temperature. The benefits of stable austenite on the mechanical properties in bainitic microstructures have been reported elsewhere [Bhadeshia and Edmonds, 1983a; Sandvik and Nevalainen, 1981; Miihkinen and Edmonds, 1987a, b].

One important difference between pearlite and bainite is that the former transformation occurs by a reconstructive mechanism whereas the latter is a displacive transformation. Reconstructive transformation involves the diffusion of all atoms and the transformation product can freely transverse austenite grain boundaries (Chapter 1). Displacive transformation, on the other hand, involves the co-ordinated movement of atoms, and such movements cannot be sustained across grain boundaries. Hence, a vestige of the austenite grain boundary remains when the transformation products are displacive, and in the presence of impurities, can lead to intergranular fracture with respect to the prior austenite grain surfaces [Bhadeshia and Svensson, 1993]. This embrittlement is manifested in the chemical temper embrittlement phenomenon.

Reversible temper embrittlement is normally found in martensitic microstructures, after tempering in the range 350 to 550 °C [Olefjord, 1978]. The segregation of phosphorus, sulphur or other impurities into the prior austenite grain boundaries during tempering, reduces the cohesion [Olefjord, 1978; Briant and Banerji, 1978; Mulford *et al.*, 1977; Joshi *et al.*, 1975], leading to a loss of toughness and, in some cases, ductility [Olefjord, 1978; Joshi *et al.*, 1975;

Viswanathan and Sherlock, 1972]. It is characterised by intergranular fracture along prior austenite grain boundaries [Olefjord, 1978; Briant and Banerji, 1978; Mulford *et al.*, 1977; Joshi *et al.*, 1975]. The addition of about 0.5 wt.% Mo has been shown to be effective in preventing such fracture, perhaps by association of the molybdenum atoms with the impurities, thereby preventing them from segregating to the boundaries [Powers, 1956]. Alternatively, the embrittlement can be avoided by quenching through the sensitive temperature range or by reducing the impurity content [Narayan and Murphy, 1973]. Such embrittlement phenomena have rarely been reported experimentally for bainitic microstructures [Johnson and Becker, 1993; Viswanathan and Sherlock, 1972; Bondar *et al.*, 1989; Ohmori *et al.*, 1974], because most bainitic steels do not require tempering, and perhaps because the toughness of conventional carbide-containing bainite is so bad that any impurity effects are masked [Bhadeshia, 1992].

The aim of the present work was to examine the susceptibility of carbide-free bainitic microstructures to reversible temper embrittlement and to eliminate the embrittlement in some experimental steels.

9.2 EXPERIMENTAL MATERIALS

Materials preparation and rolling procedure have been described in Chapter 2, with final plate thicknesses of 15 mm and 30 mm. Immediately after rolling, the plates were cooled in air and, in some cases, water quenched from finish rolling temperatures ranging from 800 to 1000 °C. The cooling rates of 15 and 30 mm plates were measured, in the temperature range 200 to 500 °C, to be 0.18 and 0.11 °C s⁻¹ respectively. Unless specified, the samples were air cooled after rolling. Molybdenum-containing alloys are denoted starting from M, while N-series represent alloys contain no molybdenum. Alloys described in Chapter 1 are also included and ^{the} original designation is used. The chemical compositions of the experimental alloys in the present chapter are listed in Table 9.1.

9.3 RESULTS AND DISCUSSION

9.3.1 Microstructures Characterization

The microstructures in all cases consisted of a mixture of bainite, martensite and retained austenite, the relative amounts depending on the chemical composition and cooling rate (plate thickness). Typical microstructures of 15 mm and 30 mm plates are shown in Fig. 9.1 (alloy N11). As expected, the thinner plate tends to form more martensite than the thicker one. An individual sheaf actually consists of a number of sub-units, between which retained austenite

Table 9.1: Chemical compositions of the experimental alloys (wt.%).

Alloy	C	Si	Mn	Ni	Cr	Mo	B	P	S	N	Cu
A	0.27	1.98	2.18	-	1.9	-	-	0.015	0.011	0.0054	0.02
B	0.27	2.01	2.16	2.07	-	-	-	0.015	0.011	0.0048	0.2
C	0.46	2.10	2.15	-	-	-	-	0.014	0.013	0.0062	0.2
D	0.44	2.13	2.14	-	0.5	-	-	0.014	0.011	0.0079	0.2
E	0.10	1.77	2.12	2.0	-	-	-	0.015	0.013	0.0053	0.2
F	0.26	1.85	2.10	-	-	-	-	0.015	0.013	0.0086	0.2
G	0.26	1.93	2.04	-	1.02	-	-	0.015	0.010	0.0080	0.2
H	0.095	1.63	1.99	-	1.97	-	-	0.013	0.011	0.0080	0.2
M1	0.26	2.04	2.03	-	2.02	0.22	0.0027	0.017	0.012	0.0085	0.2
M2	0.25	2.09	2.02	-	2.01	0.45	0.0025	0.017	0.012	0.0085	0.2
M3	0.25	2.01	2.03	-	1.05	0.24	0.0028	0.017	0.012	0.0085	0.2
M4	0.24	2.05	2.03	-	1.05	0.49	0.0025	0.017	0.012	0.0085	0.2
M5	0.24	2.03	2.0	-	0.52	0.52	0.0026	0.017	0.012	0.0085	0.2
M6	0.18	2.01	2.03	-	2.02	0.25	0.022	0.017	0.012	0.0085	0.2
M7	0.17	2.05	2.02	-	1.99	0.50	0.0020	0.017	0.012	0.0085	0.2
M8	0.18	2.01	2.04	-	1.04	0.24	0.0020	0.017	0.012	0.0085	0.2
M9	0.17	1.97	2.0	-	1.01	0.49	0.0027	0.017	0.012	0.0085	0.2
M10	0.18	2.0	2.01	-	0.50	0.51	0.0022	0.017	0.012	0.0085	0.2
M11	0.18	1.99	2.04	1.0	1.04	0.48	0.0023	0.017	0.012	0.0085	0.2
M12	0.17	0.99	2.01	1.0	1.04	0.48	0.0023	0.017	0.012	0.0085	0.2
N1	0.21	2.14	2.29	-	2.08	-	-	0.018	0.012	0.0098	0.2
N2	0.22	1.63	2.29	-	2.09	-	-	0.018	0.014	0.0093	0.2
N3	0.20	2.09	1.80	-	2.08	-	-	0.017	0.012	0.0085	0.2
N4	0.26	2.11	2.27	-	1.59	-	-	0.017	0.014	0.0095	0.2
N5	0.24	2.18	2.32	1.05	1.58	-	-	0.017	0.013	0.0090	0.2
N6	0.17	2.09	2.21	-	2.09	-	-	0.015	0.016	0.0097	0.2
N7	0.11	2.16	2.30	1.03	2.03	-	-	0.015	0.016	0.0097	0.2
N8	0.26	1.97	2.03	-	2.0	-	-	0.017	0.012	0.0085	0.2
N9	0.18	2.02	2.01	-	2.01	-	-	0.017	0.012	0.0084	0.2
N10	0.16	1.88	2.15	1.05	2.08	-	-	0.018	0.013	0.0087	0.2
N11	0.18	1.94	2.18	-	2.09	-	-	0.017	0.012	0.0097	0.2
N12	0.13	1.99	2.76	-	2.08	-	-	0.018	0.014	0.0097	0.2
N13	0.15	1.94	2.04	-	1.59	-	-	0.018	0.012	0.0095	0.2
N14	0.14	1.86	2.73	-	1.58	-	-	0.018	0.017	0.0098	0.2

can be seen (Fig. 9.2a). Cementite was not found in any of the microstructures studied. The typical morphology of lath martensite is shown in Fig. 9.2b. No attempt was made to evaluate the volume fraction of each constituent. Instead, a model known to be reliable, was used to estimated the microstructure that evolves during continuous cooling [Takahashi and Bhadeshia, 1991]. The transformation to martensite was modelled according to Koistinen and Marburger [1959]. To illustrate the trend, some results of the calculations are listed in Table 9.2. The data will be used later to calculate the hardness.

Table 9.2: Calculated volume fractions of bainite, martensite and retained austenite for the experimental alloys.

alloy	15 mm thick plate			30 mm thick plate		
	bainite	martensite	austenite	bainite	martensite	austenite
A	50	41	8	53	37	10
C	39	44	17	41	39	20
E	84	14	3	86	11	4
N1	60	33	7	62	29	8
N8	55	36	8	58	32	10

9.3.2 Impact Energy

Fig. 9.3 shows the results of Charpy V-notch impact tests, plotted against hardness for all the experimental alloys. It is clear that the alloys with Mo additions exhibit better toughness and insensitivity to the cooling rate. The two water quenched samples clearly have significantly better toughness in spite of their high hardness. It is interesting to note that the 15 mm plates exhibit somewhat better or comparable impact toughness despite their higher hardness. Larger cooling rates can reduce the extent of segregation of impurities into prior austenite grain boundaries, and hence the degree of embrittlement. The susceptibility to temper embrittlement is also evident from the two 15 mm plates (alloys N10 and N11) which were water quenched after rolling, instead of being air-cooled. They have toughness values comparable to those of the Mo-containing alloys, indicating that both Mo addition and high cooling rates can ameliorate impurity-induced embrittlement.

The fractographic evidence is shown in Fig. 9.4, which reveals grain boundary failure in the embrittled sample, but a more ductile failure in the water quenched sample of the same thickness. This is in spite of the fact that the water-quenched sample contained more

martensite, as indicated by its higher hardness (HV 442 compared with HV 429).

The addition of molybdenum clearly reduces the susceptibility to impurity-induced embrittlement. This is emphasized in Fig. 9.5 where molybdenum additions have been made to the base alloy. The impact energy increases as a result of the molybdenum additions, especially at high temperatures. Fig. 9.6 shows the fracture along the austenite grain boundaries (Alloy N9) is prevented by adding molybdenum (Alloy M7). A further improvement is obtained by reducing the overall hardness (Alloy M9).

The results discussed above are from samples which were cooled continuously through the embrittlement temperature range. To illustrate the effect of isothermal tempering, alloy N4 (30 mm plate) was heat treated at 550 °C for 5 hrs in order to weaken further the grain boundaries. As expected, carbide particles precipitated along lath boundaries and, to a less extent, inside the laths (Fig. 9.7). The CVN energy decreased from 14 J to 5 J. Before tempering, the fracture surface showed some grain boundary embrittlement (Fig. 9.8a), which became exaggerated by tempering (Fig. 9.8b). Fig. 9.8c shows a transverse section of the tempered sample, again emphasizing grain boundary failure. The tempered sample also contained carbide particles along lath boundaries, but this did not affect the fracture path.

9.3.3 Ductility

For the sake of clarity, the data for 15 mm and 30 mm plates are plotted separately in Figs. 9.9a and 9.9b respectively. Unlike the impact toughness data, the ductility appears insensitive to cooling rate or Mo content. This is probably because of the relatively slow strain rate associated with the tensile test conducted here.

The situation can be better illustrated in Fig. 9.10, which shows again that molybdenum addition does not significantly improve ductility. Reasonable ductility is only obtained when the hardness is reduced to below 400 HV by decreasing the concentration of elements such as Cr or Si (Fig. 9.10). Fractography revealed that the fracture path remained along the grain boundaries in alloy N8 which contains no molybdenum (Fig. 9.11a), while a rough fracture surface was observed in the Mo-containing alloy M2 (Fig. 9.11b). The ductility improved significantly as a result of decrease in hardness which is considered to be beneficial to ductility (Fig. 9.11c).

Some alloys, against the overall trend, exhibit improved ductility by employing higher cooling rate (Table 9.3), even though this leads to an increase in hardness. This situation is exactly the same as the case of the impact tests (Fig. 9.3). These consistent findings, among others, illustrate chemical impurity-induced temper embrittlement in the bainitic microstructures.

Table 9.3: Mechanical properties of some experimental alloys.

Alloy	Thickness(mm)	Heat Treat	HV 30 kg	PS(MPa)	TS(MPa)	EL(%)	RA(%)	CVN(kg mm)
A	15	AR	512	1181	1762	8	15	16
	30	AR	504	1068	1470	1	5	14
	15	WQ	442	1008	1488	14	53	29
N6	15	AR	431	863	1393	15	55	9
	30	AR	421	824	1249	3	5	
	30	WQ	450	1149	1511	14	56	
N11	15	AR	408	792	1331	14	45	10
	30	AR	397	770	1293	5	5	10
	15	WQ	441	1027	1461	13	55	33
	30	WQ	432	1019	1465	14	57	

PS: proof strength; TS: tensile strength; EL: elongation; RA: reduction area; CVN: charpy V-notch energy; AR: as-rolled; WQ: water quench.

9.3.4 Regression Analysis

Multi-variable regression analysis was conducted to correlate ductility and toughness against cooling rate and molybdenum content:

$$\begin{aligned}
 CVN \text{ energy } (J) = & 13.495 - 0.04 \pm 0.008 (HV) - 32.5 \pm 20.2 (\text{cooling rate}, ^\circ\text{C } s^{-1}) \\
 & + 46.6 \pm 3.1 (Mo, wt. \%)
 \end{aligned} \tag{9.1}$$

$$\begin{aligned}
 Elongation (\%) = & 36.029 - 0.051 \pm 0.007 (HV) - 36.7 \pm 18.6 (\text{cooling rate}, ^\circ\text{C } s^{-1}) \\
 & + 0.439 \pm 3.1 (Mo, wt. \%)
 \end{aligned} \tag{9.2}$$

Mo clearly has a large effect on impact energy, and on elongation. It is not surprising that increased hardness is detrimental to both properties. The results are illustrated in Fig. 9.12. The hardness data were compared against a model developed by Bhadeshia and Edmonds [1983a], which assumes a rule of mixtures:

$$H = V_\gamma H_\gamma + V_b H_b + V_{\alpha'} H_{\alpha'} \tag{9.3}$$

V_γ , V_b , $V_{\alpha'}$ are the volume fractions of austenite, bainitic ferrite and martensite, respectively. Similarly, H_γ , H_b and $H_{\alpha'}$ denote the hardnesses of the three components, austenite, bainitic

ferrite and martensite respectively. These phases fractions (Table 9.2) were calculated as described elsewhere [Takahashi and Bhadeshia, 1991]. The martensite hardness ($H_{\alpha'}$) is a function of the carbon concentration of the residual austenite, such that

$$H_{\alpha'} = QV_b(\bar{x} - s)/(1 - V_b) + H_0 \quad (9.4)$$

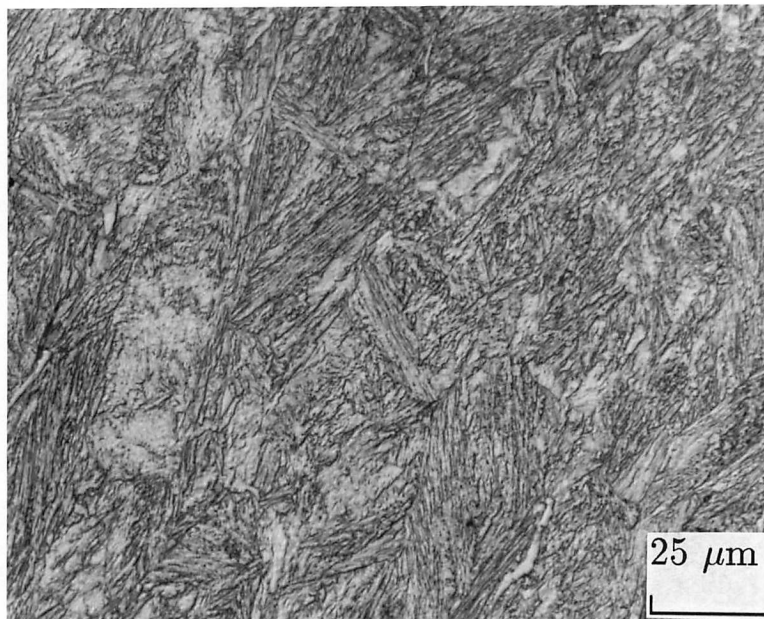
Q is the dependence of martensite hardness on carbon content, found to be HV 1020 wt.%⁻¹ of carbon in solid solution [Bhadeshia and Edmonds, 1983a]. s is the amount of carbon trapped in the bainitic ferrite in solid solution (0.03 wt.%). H_0 the hardness of martensite at the carbon content of \bar{x} , the mean carbon concentration, estimated from the work of Jaffe and Gordon [1957]. There is an upper limit to the hardness of martensite at HV 900 [Bhadeshia and Edmonds, 1983a].

It has been found that for a series of low carbon (0.08 wt.%) Fe-Cr-C alloys the hardness of bainite is insensitive to the isothermal transformation temperature [Lyman and Troiano, 1946]. The low carbon concentration ensures that the microstructure is almost fully bainitic for all of the temperatures studied. Therefore a value of HV 266 is chosen to represent the hardness of bainite (H_b). Austenite is very soft, and its hardness (H_γ) is estimated to be about HV 120 [Young and Bhadeshia, 1994]. The results are illustrated in Fig. 9.13. Although the agreement between experiment and theory is not very good, the general trend is observed to be reasonable.

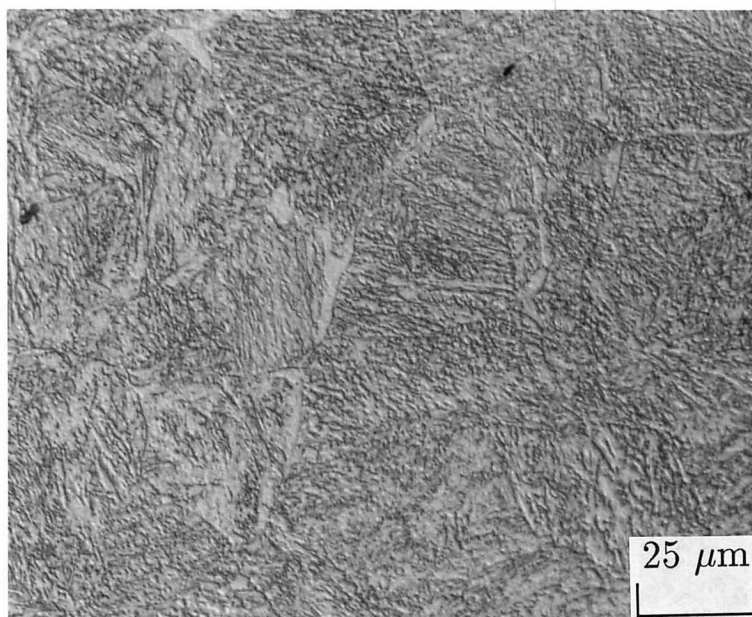
9.4 CONCLUSIONS

Microstructures consisting of mixtures of bainitic ferrite, martensite and retained austenite have been found to be susceptible to impurity-induced temper embrittlement of the kind which leads to failure at the prior austenite grain boundaries. In circumstances where it is impossible to reduce the impurity content, it is found that in the predominantly bainitic microstructures, embrittlement can be reduced by adding molybdenum or by increasing the rate at which the sample cools through the embrittlement temperature range.

The effect of embrittlement is pronounced for impact toughness, but not for ductility. Reasonable levels of ductility could only be achieved in samples with hardness values below about 400 HV.

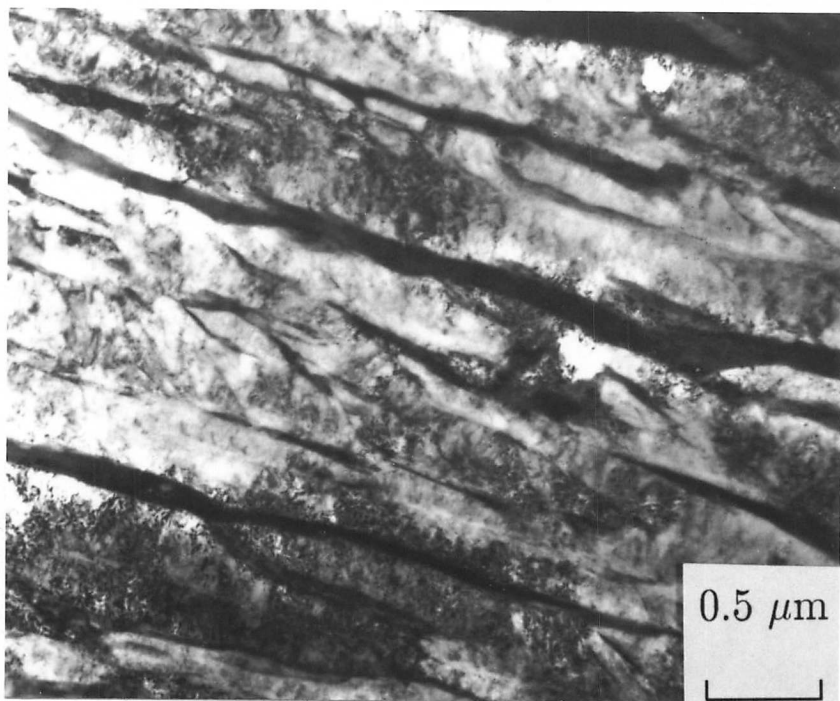


(a)

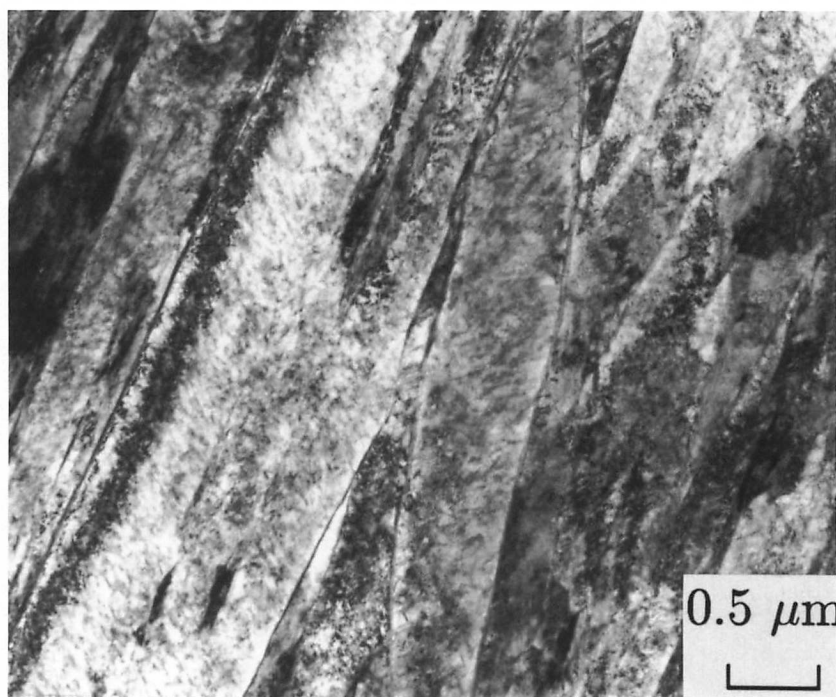


(b)

Fig. 9.1: Optical micrographs showing the typical microstructures of (a) 15 mm (b) 30 mm plates in as-rolled condition. Light etched area is martensite, while the dark region is bainite. Alloy N11: Fe-0.18C-1.94Si-2.18Mn-2.09Cr wt.%.



(a)



(b)

Fig. 9.2: TEM bright field micrographs showing the typical (a) bainite and (b) martensite morphologies. Alloy N4: Fe-0.26C-2.11Si-2.27Mn-1.59Cr wt.%.

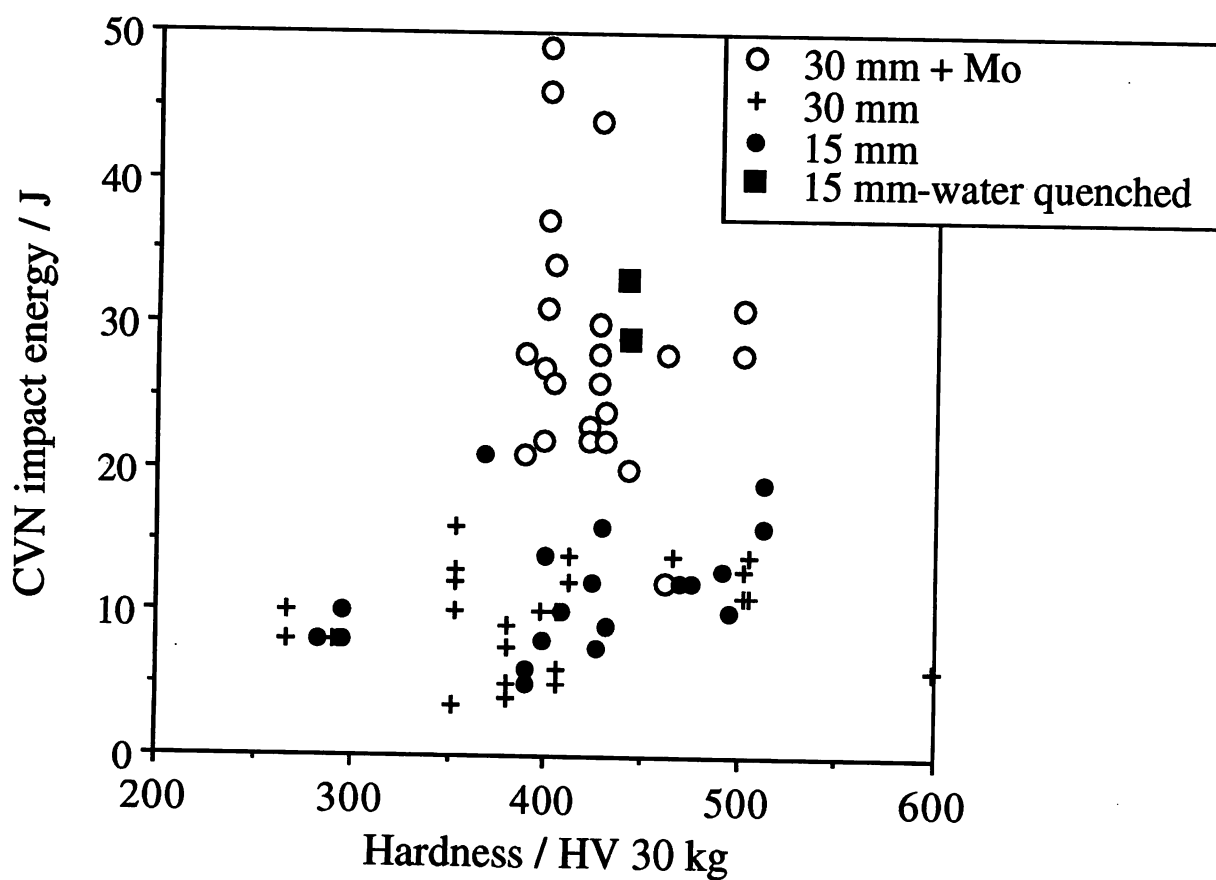
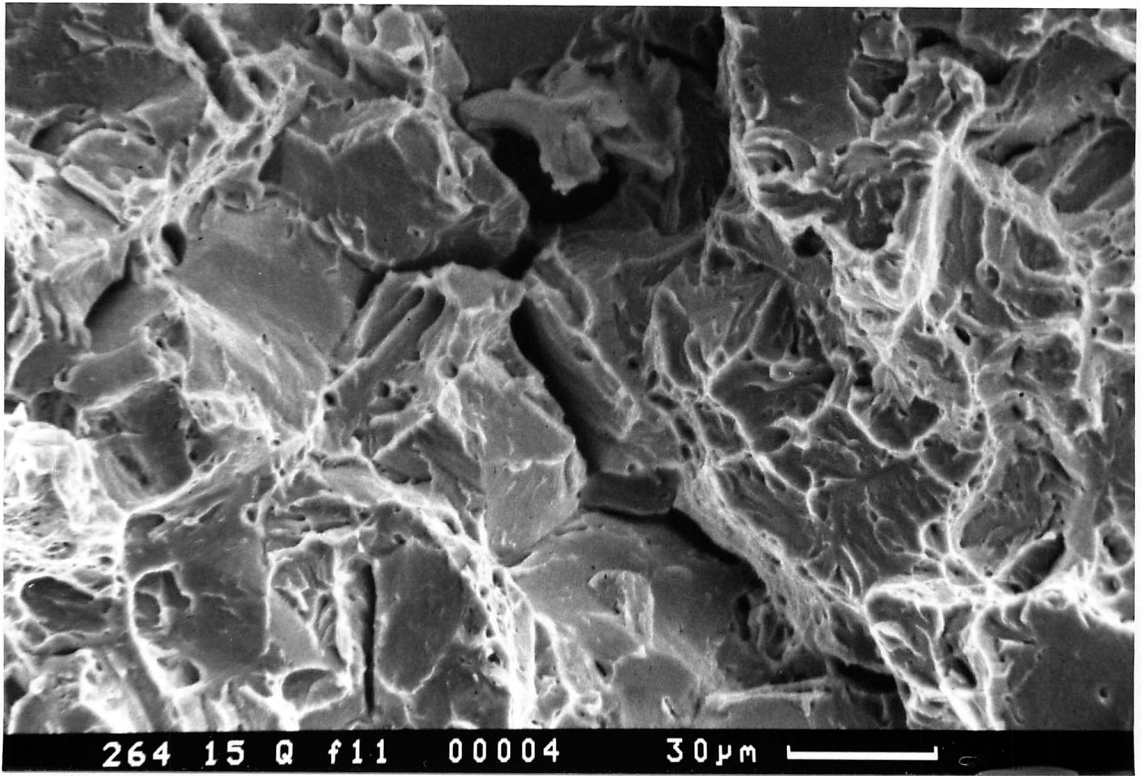
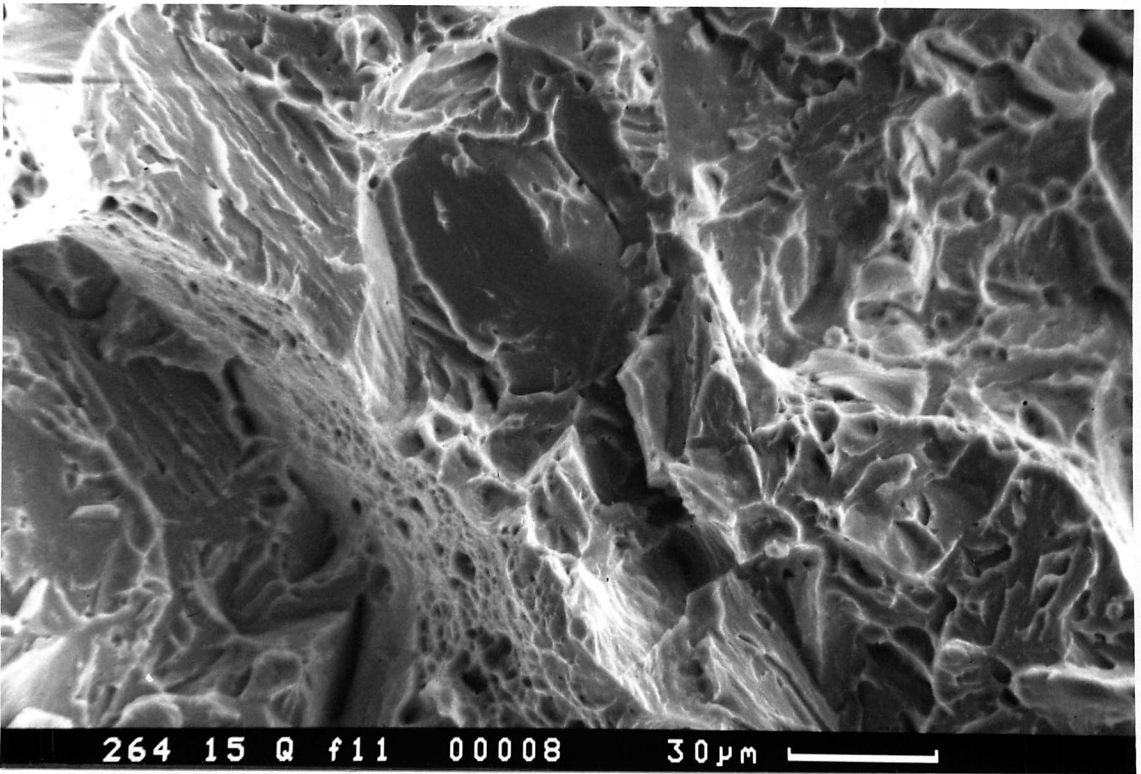


Fig. 9.3: The measured CVN energy data are plotted against hardness. The results indicate that Mo-alloys exhibit far better impact properties than Mo-free alloys, while 15 mm plates show comparable or slightly higher impact energies than 30 mm plates. It is notable that the two water-quenched 15 mm plates have CVN energies comparable to those of the Mo-containing alloys.



(a)



(b)

Fig. 9.4: SEM fractographs of impact test specimens. (a) Grain boundary fracture in 15 mm as-rolled plate. (b) More ductile fracture in water-quenched plate of the same thickness. Alloy N10: Fe-0.16C-1.88Si-2.15Mn-1.05Ni-2.08Cr wt.%.

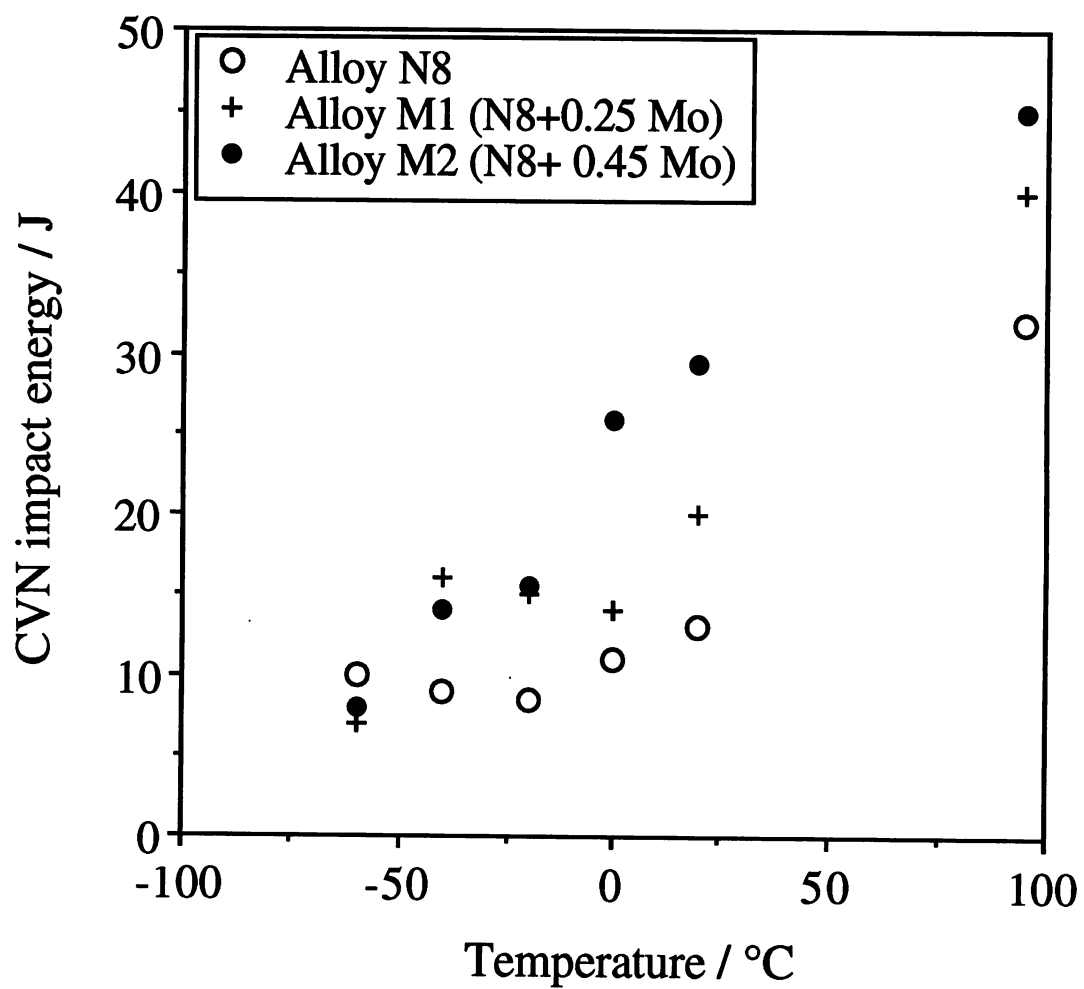
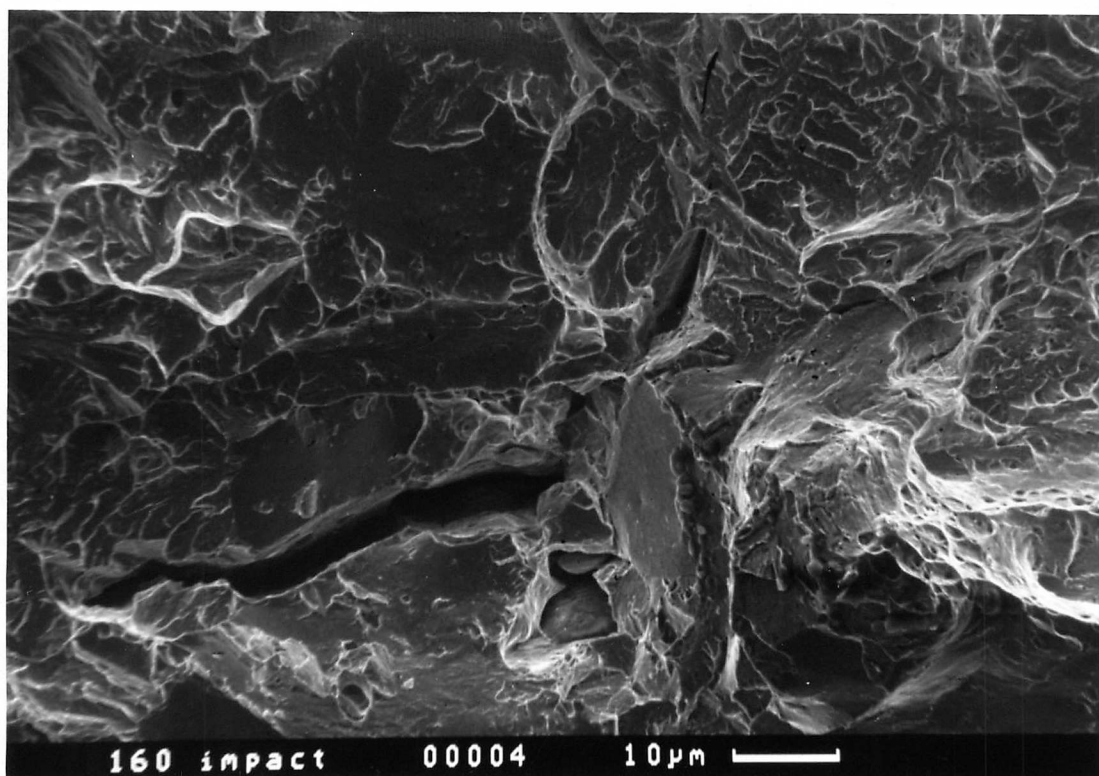
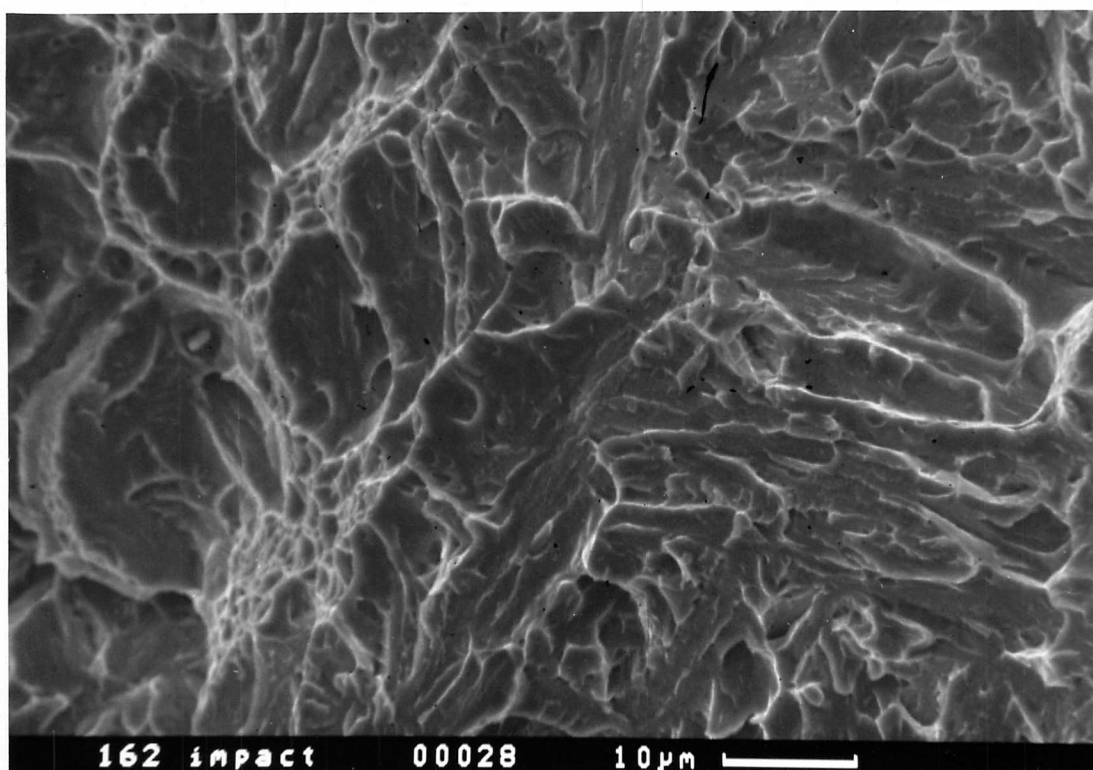


Fig. 9.5: The results of impact energy for a wide range of test temperatures, showing how a molybdenum addition leads to an improvement in toughness.

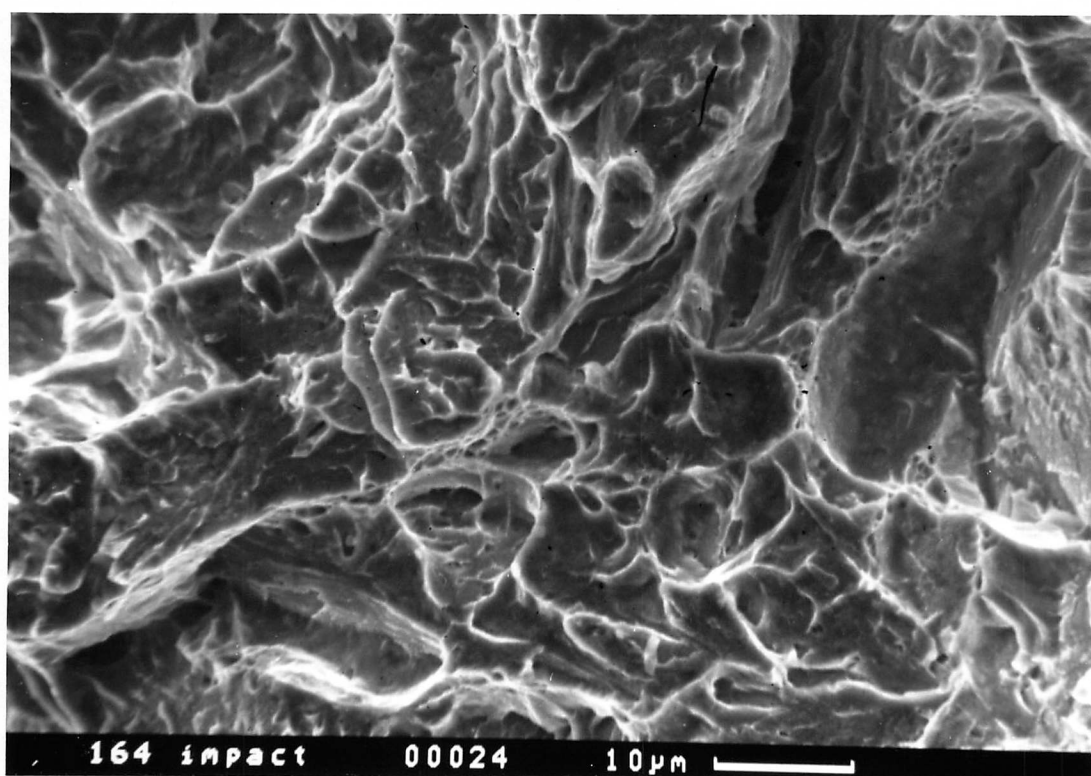


(a)



(b)

Fig. 9.6: SEM fractographs of impact test specimens (30 mm plates). (a) Mo-free alloy (Alloy N9) with toughness 12 J and hardness HV 412. (b) Molybdenum-containing Alloy M7 exhibiting better toughness (20 J) along with higher hardness (HV 443). (c) Alloy M9 shows even better toughness (31 J) by reducing hardness (HV 400). Alloy N9: Fe-0.18C-2.02Si-2.01Mn-2.01Cr. Alloy M7 : Fe-0.17C-2.05Si-2.02Mn-1.99Cr-0.5Mo-0.0020B wt.%. Alloy M9: Fe-0.17C-1.97Si-2.0Mn-1.01Cr-0.49Mo-0.0027B wt.%.



(c)

Fig. 9.6c: SEM fractographs of impact test specimens (30 mm plates). Alloy M9: Fe-0.17C-1.97Si-2.0Mn-1.01Cr-0.49Mo-0.0027B wt.%.

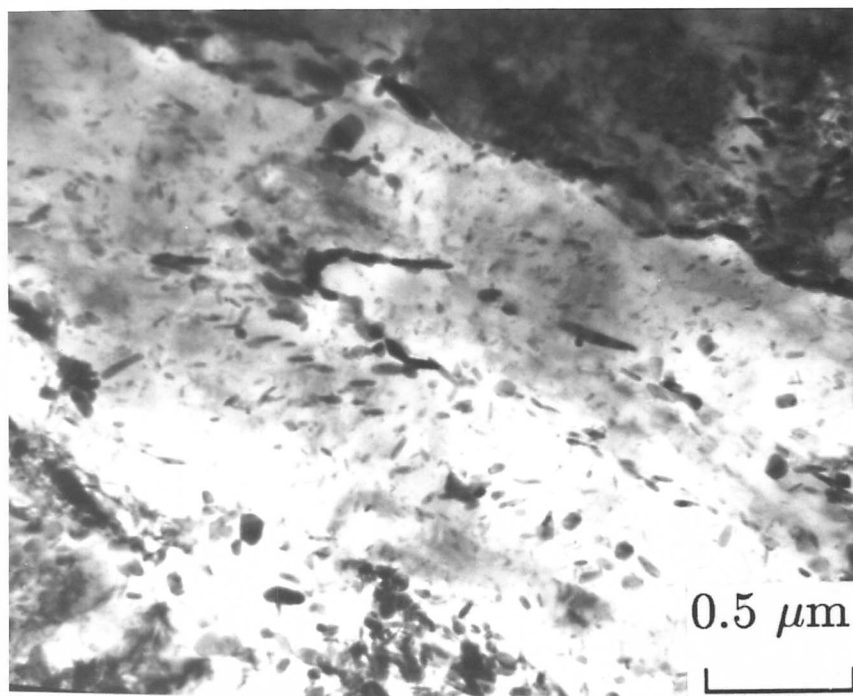
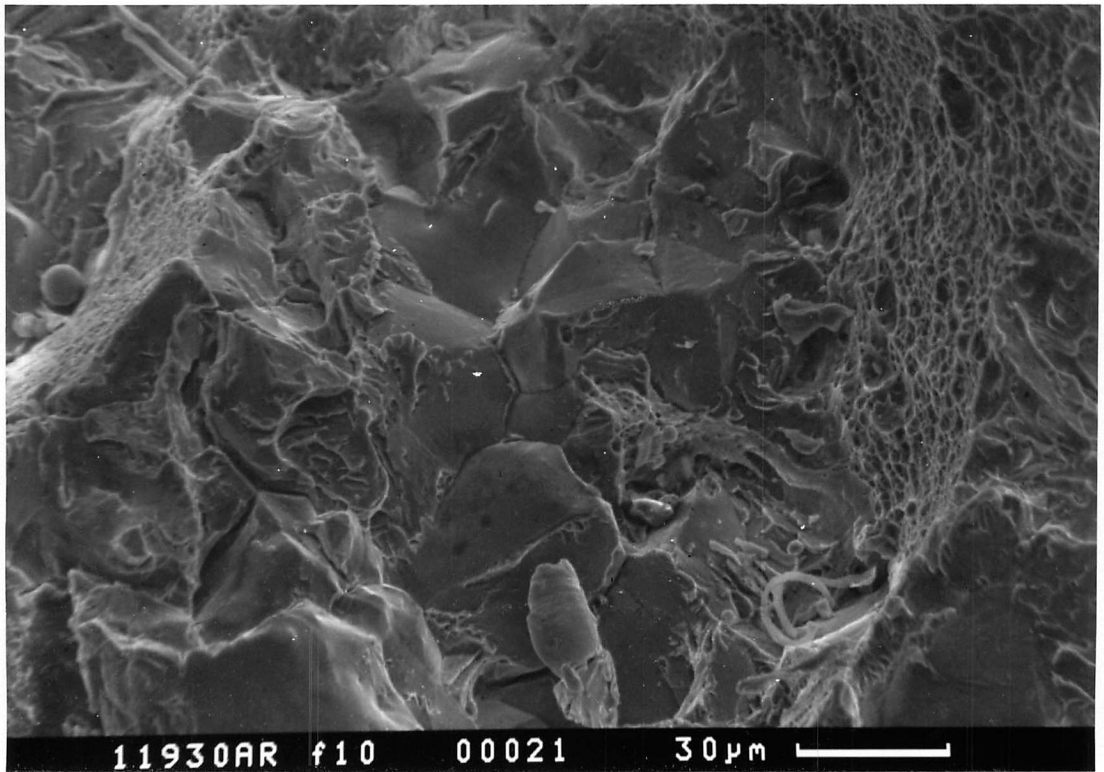
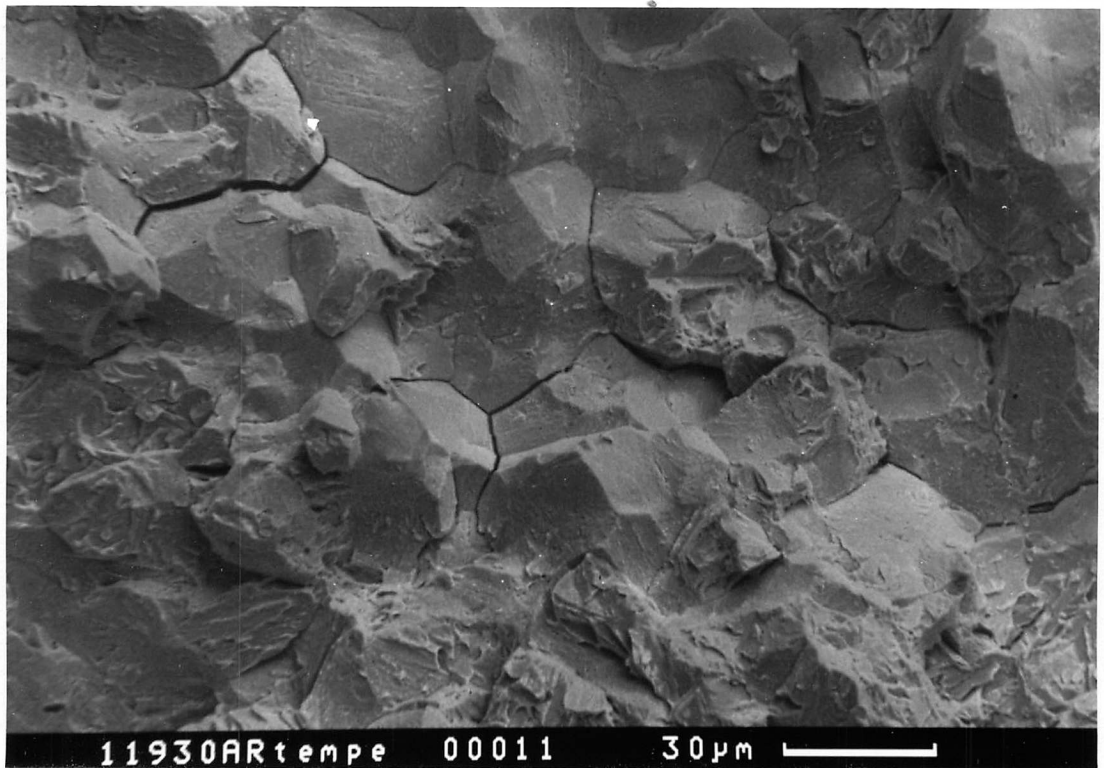


Fig. 9.7: TEM bright field micrograph showing bainite microstructure after tempering at 500 °C for 5 hrs. Alloy N4: Fe-0.26C-2.11Si-2.27Mn-1.59Cr wt.%.

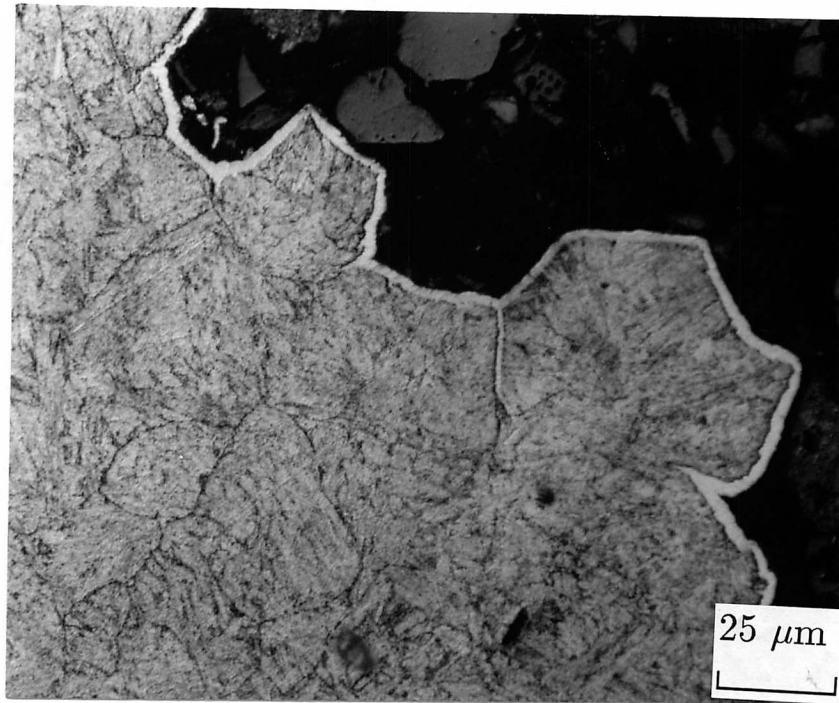


(a)



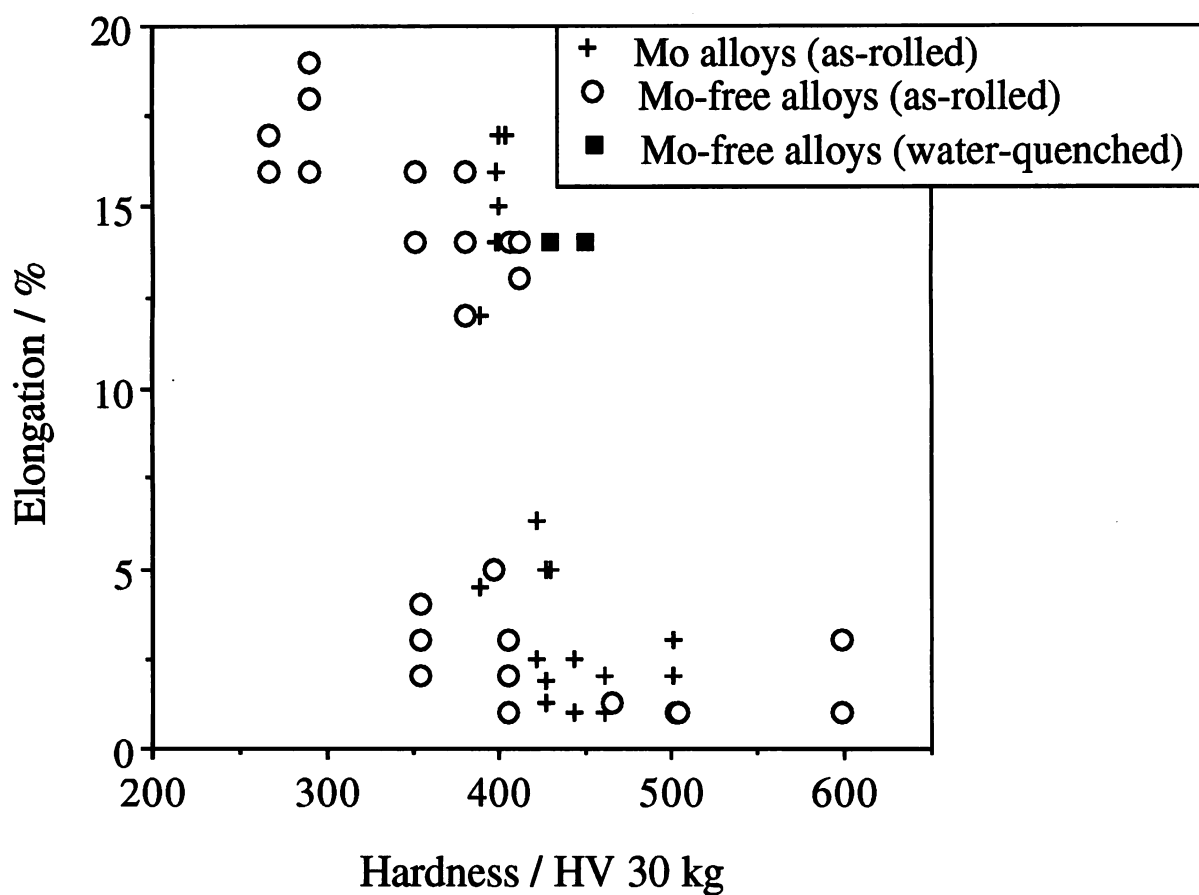
(b)

Fig. 9.8: SEM and optical micrographs showing how isothermal tempering at 550 °C for 5 hrs can enhance grain boundary fracture. (a) Before tempering, 14 J (b) after tempering, 5 J. (c) Transverse section of the isothermal tempered sample. Alloy N4 (30 mm): Fe-0.26C-2.11Si-2.27Mn-1.59Cr wt.%.



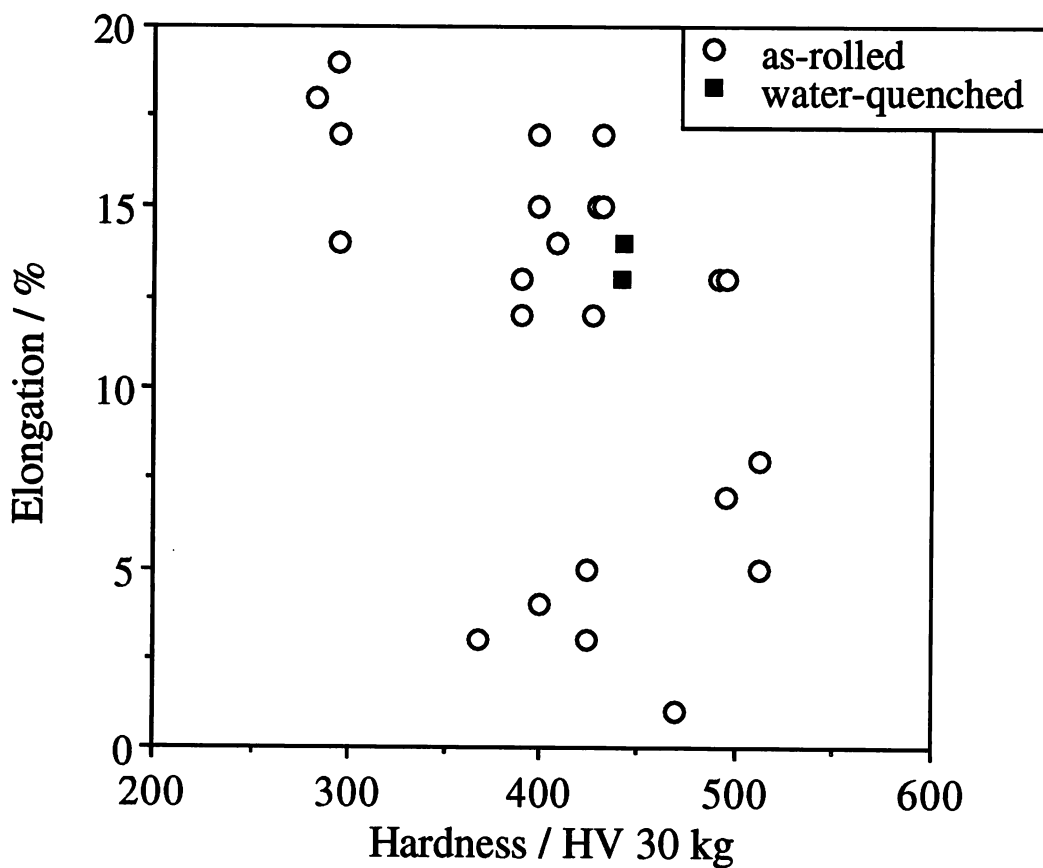
(c)

Fig. 9.8: SEM and optical micrographs showing how isothermal tempering at 550 °C for 5 hrs can enhance grain boundary fracture. (a) Before tempering, 14 J (b) after tempering, 5 J. (c) Transverse section of the isothermal tempered sample. Alloy N4 (30 mm): Fe-0.26C-2.11Si-2.27Mn-1.59Cr wt.%.



(a)

Fig. 9.9: Elongation as a function of hardness, (a) 30 mm plates, (b) 15 mm plates. Molybdenum additions do not necessarily increase ductility. Nevertheless, the ductility is somewhat larger for 15 mm plates than the 30 mm plates, and the water-quenched samples exhibit good ductility.



(b)

Fig. 9.9: Elongation as a hardness hardness, (a) 30 mm plates, (b) 15 mm plates. Molybdenum additions do not necessarily increase ductility. Nevertheless, the ductility is somewhat larger for 15 mm plates than the 30 mm plates, and the water-quenched samples exhibit good ductility.

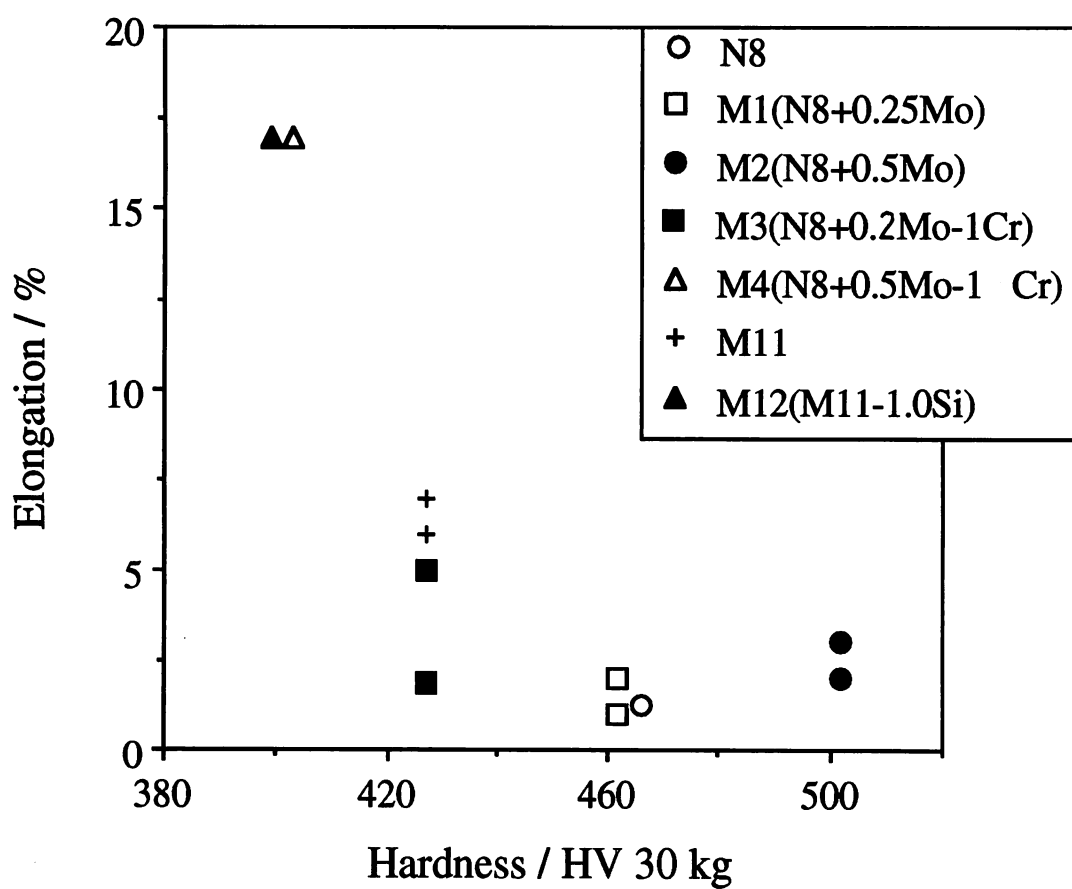
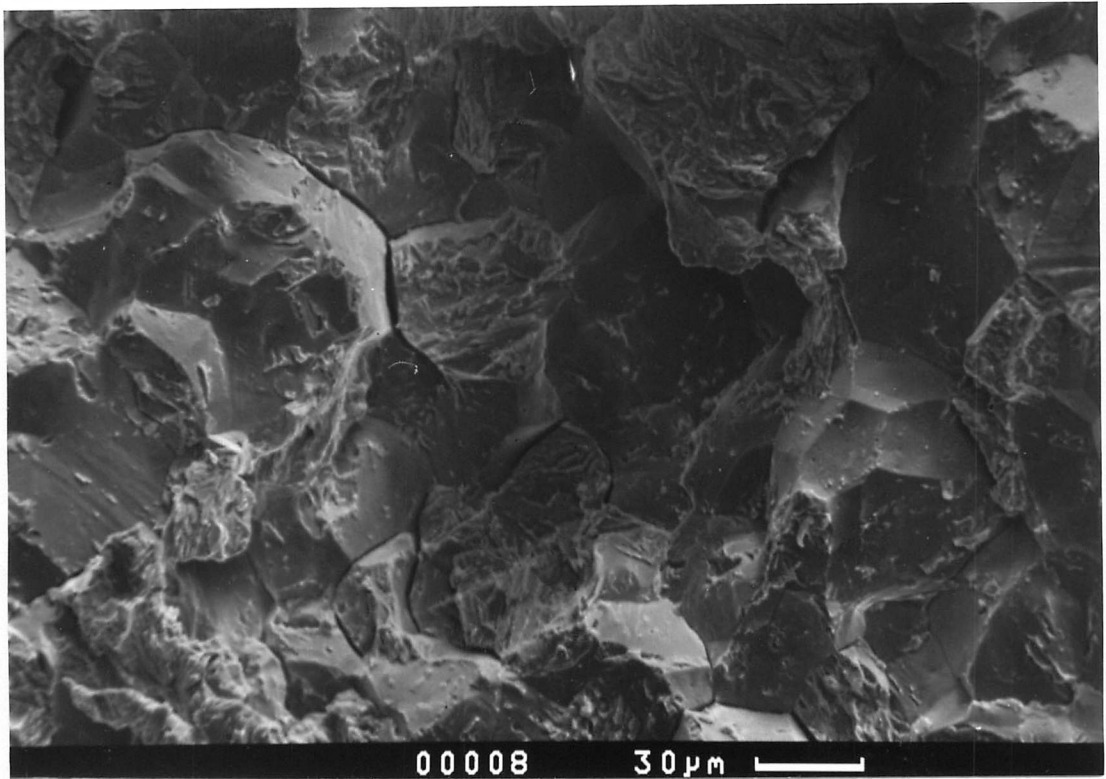
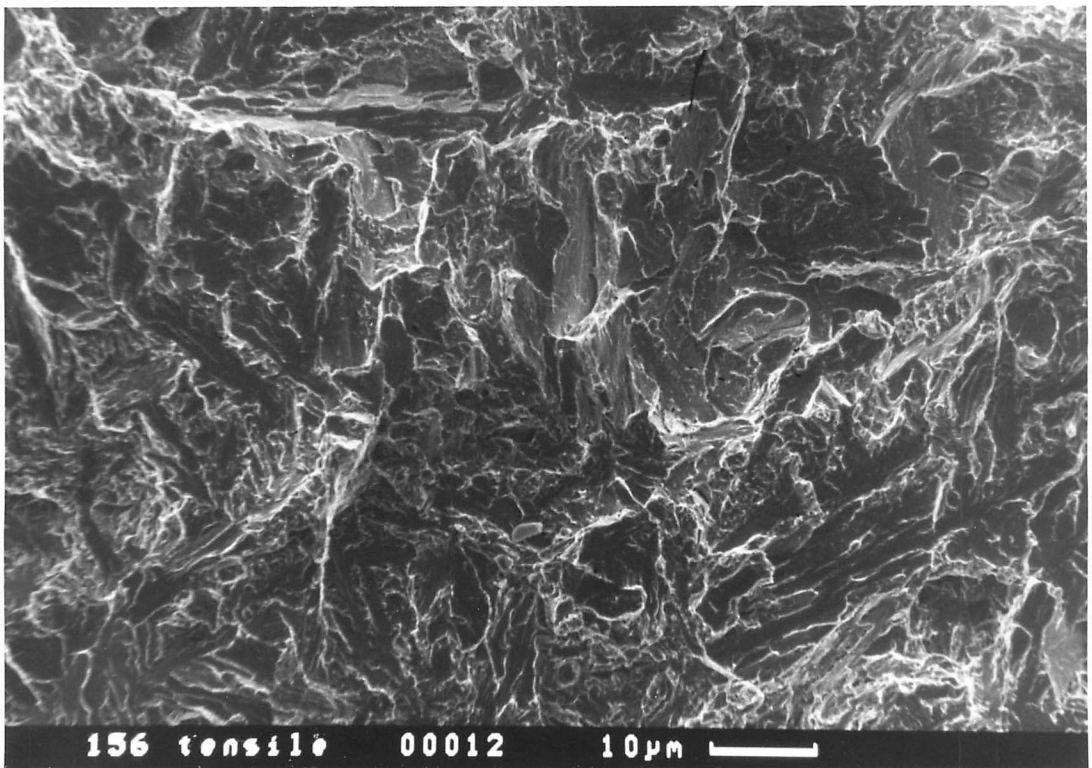


Fig. 9.10: Elongation data plotted against hardness, for alloys with different Mo and Cr or Mo and Si contents.

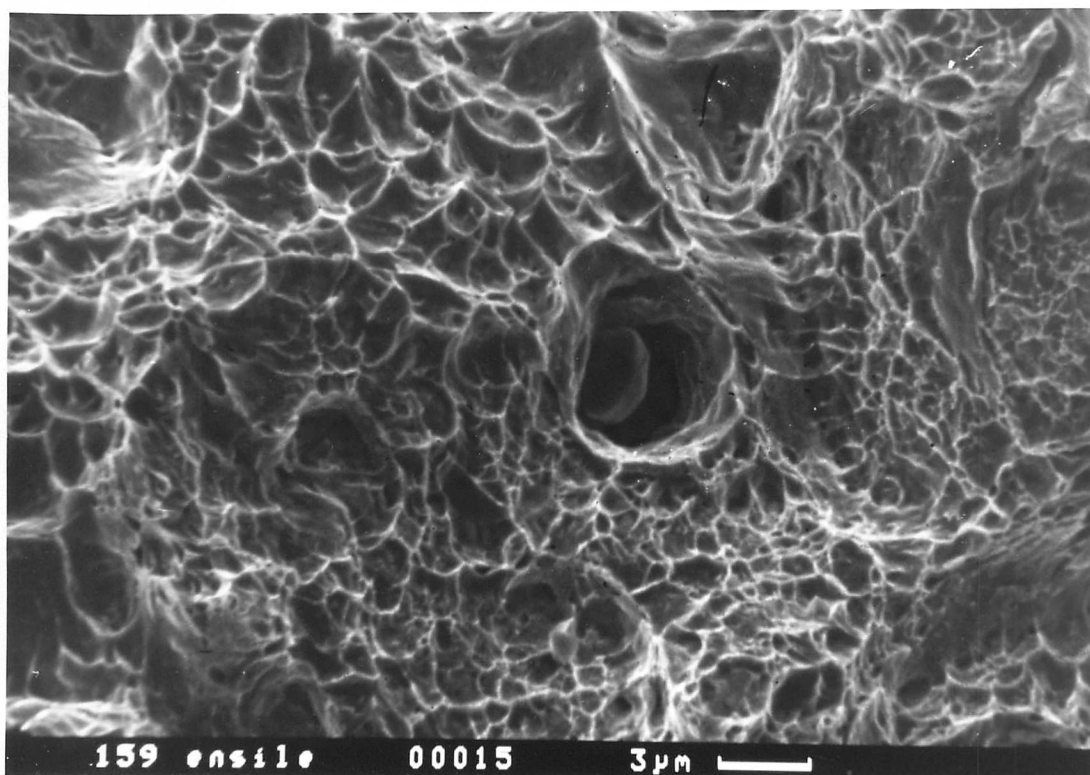


(a)



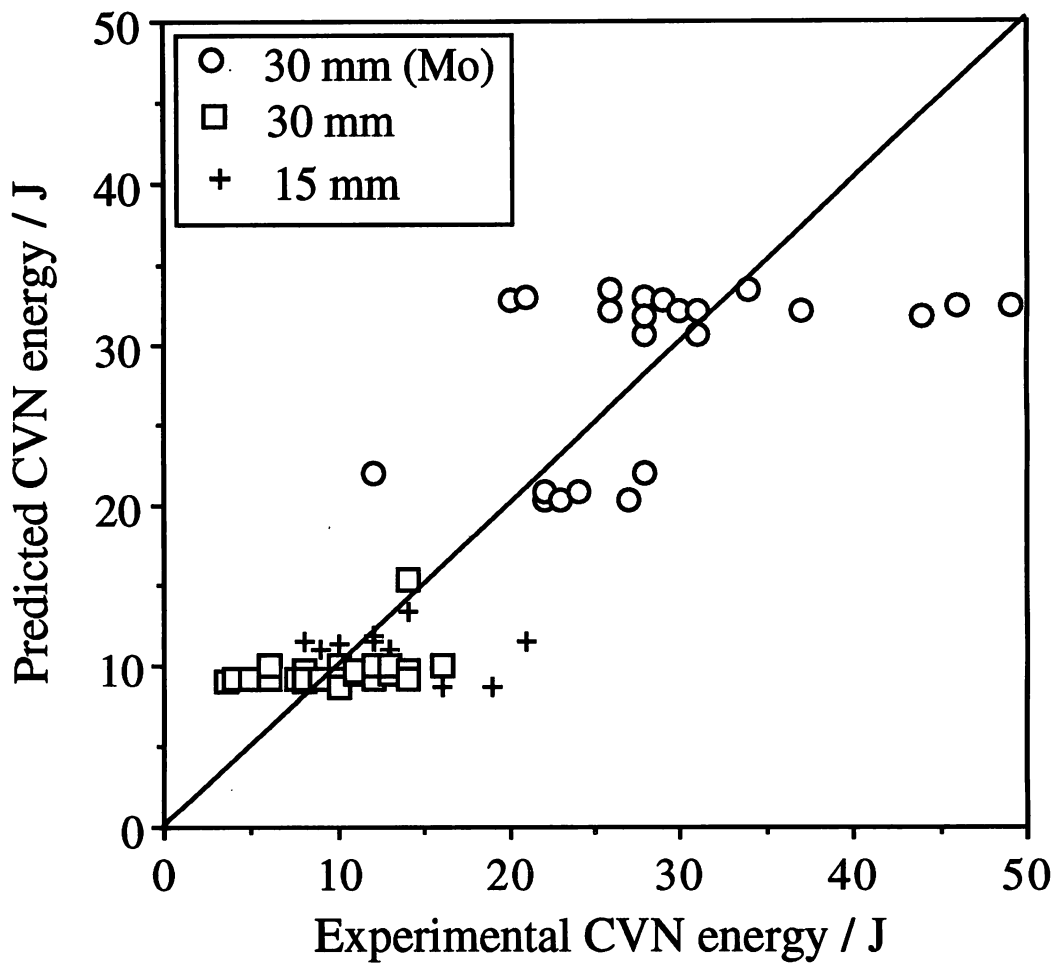
(b)

Fig. 9.11: SEM fractographs of tensile test samples. (a) Alloy N8 contains no molybdenum (4% elongation with HV 466). (b) Molybdenum-containing Alloy M2 shows no better ductility (5% elongation with HV 502). (c) Alloy M5 exhibits much improved toughness(17% with HV 403). Alloy N8: Fe-0.26C-1.97Si-2.03Mn-2.0Cr wt.%. Alloy M2: Fe-0.25C-2.09Si-2.02Mn-2.01Cr-0.45Mo-0.0027B wt.%.



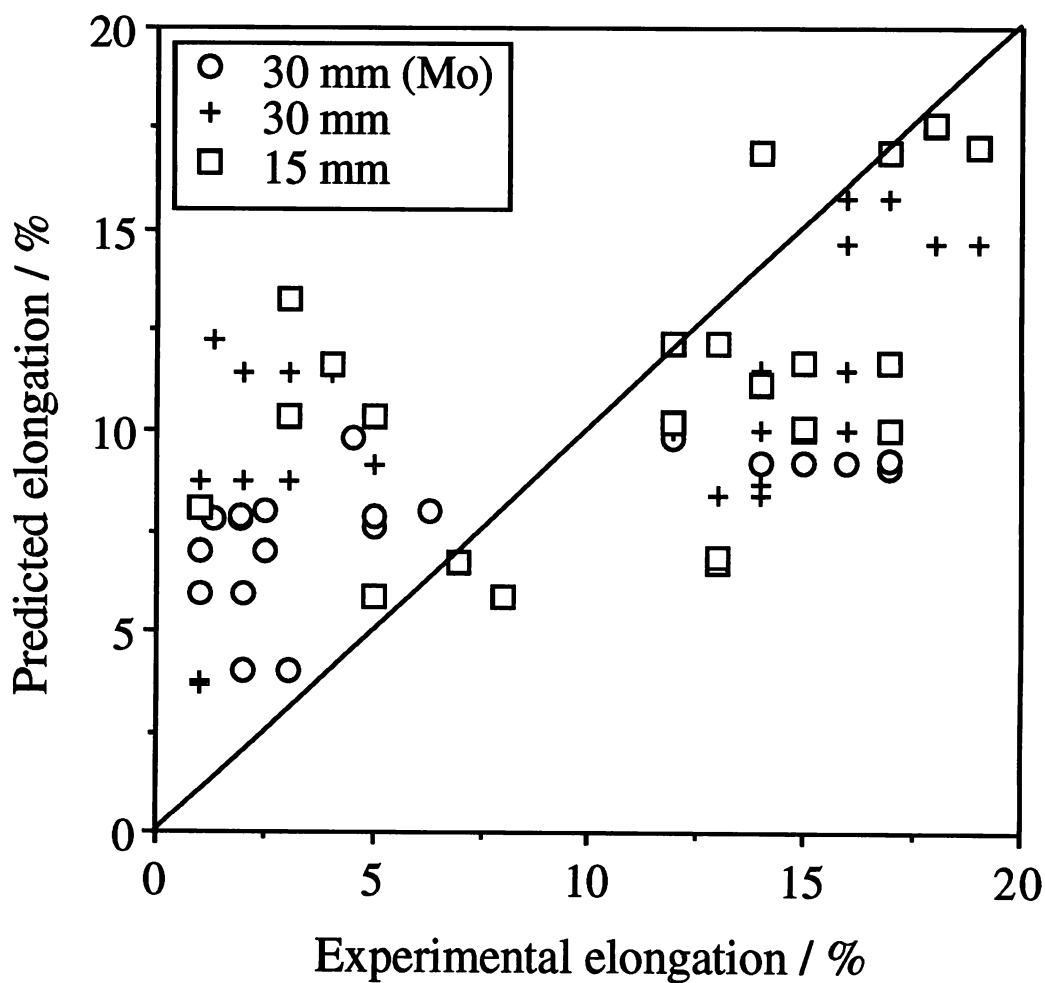
(c)

Fig. 9.11: SEM fractographs showing tensile test samples. Alloy M5: Fe-0.24C-2.03Si-2.0Mn-0.52Cr-0.52Mo-0.0026B wt.%.



(a)

Fig. 9.12: Comparison of predicted values using regression analysis against the experimental data. (a) CVN impact energy. (b) Elongation. The line represents the locus of perfect fit between experiment and regression analysis.



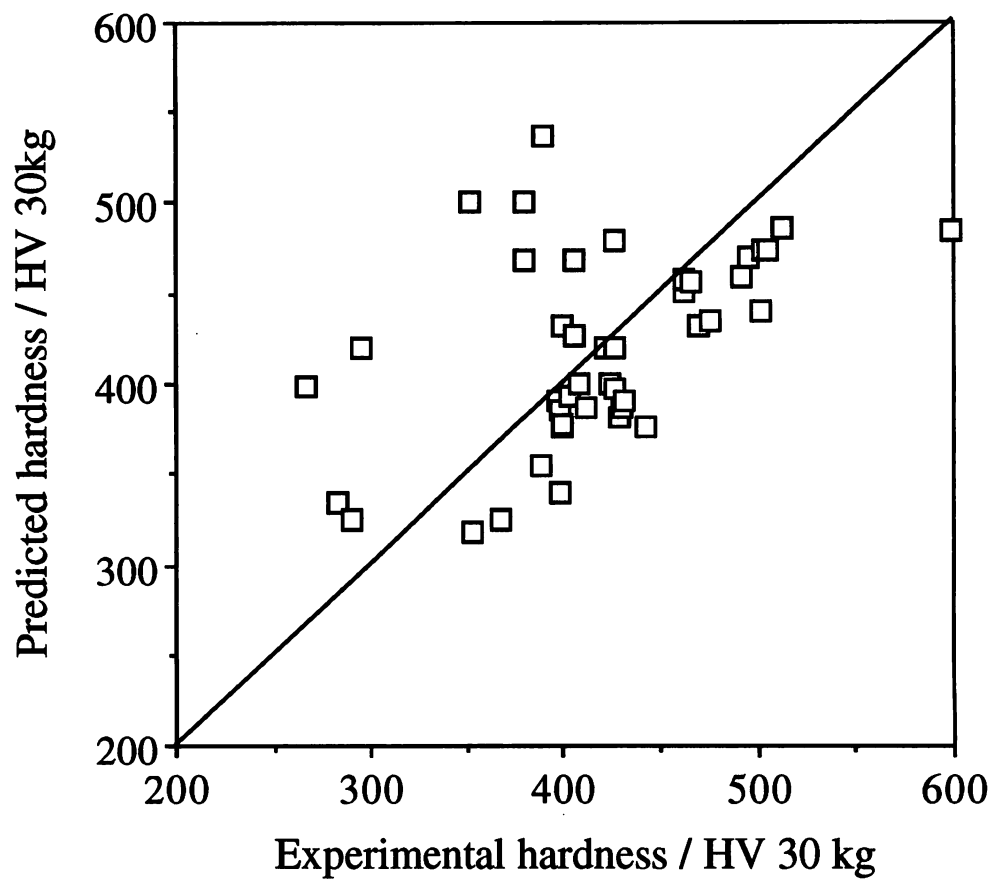


Fig. 9.13: The experimental hardness data plotted against predictions using equation (9.4).

CHAPTER 10

SUMMARY AND FUTURE WORK

The mechanism of the bainite transformation in steels has been investigated during the course of work on the design of rail steels. The work therefore involved fundamental research as well as a technological goal. The studies focussed on a special class of carbide-free bainitic steels, because carbides are known to be detrimental to toughness especially when present at large volume fractions as in pearlitic alloy (used for conventional rails). The microstructure of the silicon-rich steels was designed to consist of a mixture of bainitic ferrite, retained austenite and martensite. The steels were also designed to have a high hardness, since they were destined for applications in the railway industry; resistance to mechanical wear is then an important selection criterion.

For commercial production it is necessary for any steel or thermomechanical treatment to be cheap and practicable. It is particularly important for the kinetics of transformation to be such that the alloys can be manufactured on a large scale using continuous cooling transformation. A considerable effort was therefore devoted to the mechanism and kinetics of transformation.

Results from experiments on the isothermal transformation kinetics for the bainite reaction have been demonstrated to be reasonably consistent with a mechanism in which bainitic ferrite grows without diffusion. This particular mechanism has also been demonstrated to be consistent with a new theory which has allowed the factors responsible for the thickness of austenite films found in bainitic microstructures to be identified quantitatively. Such films have in the past been shown to be of the utmost importance in controlling toughness.

Some new information of fundamental importance was revealed during the course of routine metallographic investigations. It is found that when the driving force for transformation is large, it is possible for separately nucleated platelets of bainite to coalesce into coarse plates. Other observations have proved that the bainitic ferrite/austenite interface behaves like that of martensite, in that it bows between obstacles. In addition, there is clear evidence that the shear associated with bainite growth can be accommodated by mechanical twinning when differently oriented plates collide.

An exciting result is that the number of carbide variants that form in lower bainite can be influenced by the application of an external stress. This reinforces a published hypothesis that the frequently observed single variant of carbide in lower bainite is a consequence of stress-affected precipitation.

The wear properties of the bainitic alloys have been measured and found in many cases to be excellent. Problems with impurity-induced embrittlement have been effectively overcome by the addition of a controlled quantities of molybdenum to the steels.

There are two aspects of the work which are really worth investigating further. The fact that the lower bainitic cementite particles respond to external stress in a manner similar to classical behaviour of stress-affected martensite indicates that the cementite grows by a displacive paraequilibrium mechanism. If this is true then the resultant surface relief could be investigated using the atomic force microscope, which has a high enough resolution for the fine particles.

The second aspect is more difficult. There is a clear need to understand the factors controlling the size of bainite sub-units. It is likely that this kind of work requires a detailed finite element model in which the stress field of a perfect invariant-plane strain can be relaxed dynamically as the platelet grows.

REFERENCES

- Aaronson, H.I. and Wells, C., (1956)
Trans. AIMME **256**, 1216
- Aaronson, H.I., Domian, H.A. and Pound, G.M., (1966a)
Trans. Metall. Soc. AIMME **236**, 753.
- Aaronson, H.I., Domian, H.A. and Pound, G.M., (1966b)
Trans. Metall. Soc. AIMME **236**, 768.
- Aaronson, H.I., Laird, C. and Kinsman K. R., (1970)
Phase Transformations, ASM, Metals Park, Ohio, 313-396.
- Aaronson, H.I., Hall, M.G.; Barnett, D.M. and Kinsman, K.R., (1975)
Script Metall. **9**, 705.
- Aberbach, B.L. and Cohen, M., (1948)
Trans. AIMME **176**, 401.
- Ali, A. and Bhadeshia, H. K. D. H., (1989)
Mater. Sci. Technol. **5**, 398.
- Anderson, J. C., Leaver, K. D., Rawlings, R. D. and Alexander, J. M., (1985)
Materials Sciences, 3rd. ed. Van Nostrand Reinhold, Workingham England, 268.
- Andress, K. W., (1963)
Acta Metall. **11**, 939.
- Austin, A.E. and Schwartz, C.M., (1952)
Proc. ASTM **52**, 623.
- Babu, S. S. and Bhadeshia, H. K. D. H., (1991)
Mater. Sci. Technol. **A142**, 209.
- Babu, S. S., Hono, K. and Sakurai, T., (1994)
Metall. Trans. **25A**, 499.
- Bhadeshia, H.K.D.H., (1979)
Ph.D. Thesis, Cambridge Univ.
- Bhadeshia, H.K.D.H., (1980)
Acta Metall. **28**, 1103.
- Bhadeshia, H.K.D.H., (1981a)
Acta Metall. **29**, 1117.
- Bhadeshia, H.K.D.H., (1981b)
Metal Sci. **15**, 477.
- Bhadeshia, H.K.D.H., (1982a)
J. de Physique **43**, C4-437.
- Bhadeshia, H.K.D.H., (1982b)
Metal Sci. **16**, 159.
- Bhadeshia, H.K.D.H., (1982c)
J. de Physique **43**, C4-443.
- Bhadeshia, H.K.D.H., (1985a)
Mater. Sci. Technol. **1**, 497.

- Bhadeshia, H.K.D.H., (1985b)
Progress in Materials Science **29**, 321.
- Bhadeshia, H. K. D. H., (1989)
Mater. Sci. and Technol. **5**, 131.
- Bhadeshia, H. K. D. H., (1992)
Bainite in Steels, Institute of Materials, London.
- Bhadeshia, H.K.D.H., and Edmonds, D.V. (1979a)
Metall. Trans. **10A**, 895.
- Bhadeshia, H.K.D.H., and Edmonds, D.V. (1979b)
Metal Sci. **13**, 325.
- Bhadeshia, H. K. D. H. and Edmonds, D. V., (1979c)
Phase Transformations, Institution of Metallurgists, London IV.4.
- Bhadeshia, H.K.D.H. and Edmonds, D.V. (1980)
Acta Metall. **28**, 1265.
- Bhadeshia, H.K.D.H. and Waugh, A.R., (1982)
Acta Metall. **30**, 775.
- Bhadeshia, H.K.D.H. and Edmonds, D.V., (1983a)
Metal Sci. **17**, 411.
- Bhadeshia, H.K.D.H. and Edmonds, D.V., (1983b)
Metal Sci. **17**, 420.
- Bhadeshia, H. K. D. H., (1987)
Worked Examples in the Geometry of Crystals, The Institute of Metals, London.
- Bhadeshia, H.K.D.H. and Christian, J.W., (1990)
Metall. Trans. **7A**, 767.
- Bhadeshia, H. K. D. H., David, S. A., Vitek, J. M. and Reed, R. W., (1991)
Mater. Sci. Technol. **7**, 686.
- Bhadeshia, H. K. D. H. and Svensson, L. -E., (1993)
Mathematical Modelling of Weld Phenomena, eds. by H. Cerjak and K. E. Easterling, The Institute of Materials, London, 123.
- Bolton, P. J. and Clayton, P., (1984)
Wear **93**, 145.
- Briant, C.L. and Banerji, S.K., (1978)
Int. Metals Rev. **4**, 164.
- Callender, W.R., (1983)
Ph.D. Thesis, Univ. of Sheffield.
- Chance J. and Ridley, N., (1981)
Metall. Trans. **21A**, 1205.
- Chang, L. C. and Bhadeshia, H. K. D. H., (1994)
Mater. Sci. Technol. **A184**, L17.
- Christian, J. W., (1958)
Acta Metall. **6**, 377.

- Christian, J. W., (1965)
Theory of Transformations in Metals and Alloys, Pergamon Press, Oxford.
- Christian, J. W., (1975)
Theory of Transformations in Metals and Alloys, Part 1, 2nd. edn., Pergamon Press, Oxford.
- Christian, J. W., (1979)
Proc. Int. Conf. on Martensitic Transformations, ICOMAT '79, MIT Press, Massachusetts, USA, 220.
- Christian, J. W., (1982)
Metall. Trans. **13A**, 509.
- Clayton, P., Sawley, K.Y., Bolton, P.J. and Pell, G.M., (1987)
Wear **120**, 120.
- Clayton, P. and Danks, D., (1990)
Wear **135**, 369.
- Clayton, P. and Devanathan, R., (1992)
Wear **156**, 121.
- Coates, D.E., (1973)
Metall. Trans. **4**, 2313.
- Court, S. A. and Pollard, G., (1987)
Welding Metallurgy of Structural Steels, ed. by J. Y. Koo, TMS-AIME, Warrendale, Pennsylvania, USA, 335.
- Crank, J., (1975)
The Mathematics of Diffusion, 2nd edn., Clarendon Press, Oxford.
- Dehoff, R. T. and Rhines, F. N., (1968)
Quantitative Microscopy, McGraw-Hill, New York, USA.
- Devanathan, R. and Clayton, P., (1991)
Wear **151**, 91.
- Dubensky, W. J. and Rundman, K. B., (1985)
AFS Transaction **93**, 389.
- Dyson, D.J. and Holmes, B., (1970)
J. Iron Steel Inst. **277**, 469.
- Ericsson, C. E., Bhat, M. S., Parker, E. R. and Zackay, V. F., (1976)
Metall. Trans. **7A**, 1800.
- Garnham, J.E. and Beynom, J.H., (1992)
Wear **157**, 81.
- Goodenow, R.H., Matas, S.J. and Hehemann, R.F., (1963)
Trans. Metall. Soc. of AIME **227**, 651.
- Gruzin, P.L. and Vashchilo, T.P., (1969)
Metall. i Term. Obrabot. Metallov. **4**, 1969, 66. Quoted as Goritskii *et al.*, 1992.
- Hehemann, R.H., (1970)
Phase Transformation, Chap. 9, ASM, Metal Park, OH, 399.
- Hehemann, R.F., Kinsman, K.R. and Aaronson, H.I., (1972)
Metall. Trans. **3**, 1077.

- Heller, W. and Schweitzer, R., (1982)
Proc. 2nd Int. Heavy Haul Railway Con., Colorado, USA, 282.
- Honeycombe, R.W.K. and Pickering, F.B., (1972)
Metall. Trans. **3**, 1099.
- Huang, Hung-Der and Thomas, G., (1977)
Metall. Trans. **8A**, 1661.
- Hultgren, A., (1951)
Jernkontorets Ann. **135**, 403.
- Hume-Rothery, W., Raynor, G. V. and Little, A. T., (1942)
Arch. Eisenhüttenwes **145**, 143.
- Hutchings, I. M., (1992)
Tribology, Friction and Wear of Engineering Materials, London, Edward Arnold.
- Ichinose, H., Takehara, J. and Ueda, M., (1982)
Proc. 2nd Int. Heavy Haul Railway Con., Colorado, USA, 178.
- Jaffe, L. D. and Gordon, E., (1957)
Trans. ASM **49**, 359.
- Jerath, V., Mistry, K., Bird, P. and Preston, R.R., (1991)
British Steel Report, Report SL/RS/R/S/1975/1/91A.
- Johnson, D.R. and Becker, W.T., (1993)
J. of Mater. Eng. Performance **2(2)** April, 255.
- Josefsson, B. and Andrén, H.O., (1991)
Mater. Sci. Technol., **7**, 849.
- Joshi, A., Plamberg, P.W. and Stein, D.F., (1975)
Metall. Trans. **6A**, 2160.
- Jost, N. and Schmidt, I., (1985)
Wear of Material, 5th Int. Con., ASME, Vancouver, Canada, 205.
- Kalish, D., Kulin, S. A. and Cohen, M. (1965)
J. Met. Feb., 157.
- Kalish, D. and Cohen, M., (1970)
Mater. Sci. Eng. **6**, 156.
- Kalousek, J., Fegredo, D.M. and Laufer, E.E., (1987)
Wear of Material, 6th Int. Con., ed. by Ludema, K.C., ASME, USA, 212.
- Kaneko, H., Nishizawa, T., Tamaki, K. and Tanifuji, A., (1965)
J. Japan Inst. Metal **29**, 166.
- Kayaba, T. and Kato, K., (1979)
Wear of Materials, ASME, eds. by Ludemak, C., Glaeser, W. A. and Rhee, S. K., 45
- Koistinen, D. P. and Marburger, R. E., (1959)
Acta Metall. **7**, 60.
- Kriesement O. and Wever F., (1956)
The Mechanism of Phase Transformations in Metal, Monograph and Report ser. No. 18, Inst. of Metal, London, 253.

- Kunitake, T., Terasaki, F., Ohmori, Y. and Ohtani, H., (1972)
Iron and Steel Dec., 647.
- Kurdjumov, G. V. and Khandros, L. G., (1949)
Dok. Akad. Nauk SSSR **66**, 221.
- Lai, G.Y., (1975)
Metall. Trans. **6A**, 1469.
- Lai, G.Y., Wood, W.E., Clark, R.A., Zackay, V.F. and Parker, E.R., (1974)
Metall. Trans. **5**, 1663.
- Leslie, W.C., (1982)
The Physical Metallurgy of Steels, New York/Tokyo, McGraw-Hill.
- Llopis, A. M., (1977)
Ph.D. Thesis, Univ. of California, Berkeley.
- Lyman, T. and Troiano, A. R., (1946)
Trans. ASM **37**, 402-448.
- Mack, C., (1956)
Proc. Cambridge Philosophical Society **52**, 246.
- Matas, S.J. and Hehemann, R.F., (1961)
Trans. TMS-AIME **221**, 179.
- Matsuzaki, A., Bhadeshia, H. K. D. H. and Harada, H., (1992)
Proc. of The Fundamentals of Aging and Tempering in Bainitic and Martensitic Steel Products, Montreal, Canada, Oct., eds. by G. Krauss and P. E. Repas (The Iron and Steel Society), 47.
- Metal Handbook, (1985)
Metal Handbook **8**, 9th edn., ASM, Metals Park, Ohio, 85.
- McLellan, R. B., Rudee, M. L. and Ishibachi, T., (1965)
Trans. Metall. Soc. AIME **233**, 1938.
- Mehl, R.F., (1939)
Hardenability of Alloy Steels, ASM, Cleveland, OH, 1.
- Miihkinen, V.T.T. and Edmonds, D.V., (1987a)
Mater. Sci. Technol. **3**, 422.
- Miihkinen, V.T.T. and Edmonds, D.V., (1987b)
Mater. Sci. Technol. **3**, 432.
- Mujahid, S.A. and Bhadeshia, H.K.D.H., (1992)
Acta Metall. **40**, 389.
- Mujahid, S.A. and Bhadeshia, H.K.D.H., (1993)
Acta Metall. **41**, 967.
- Mulford, R.A., McMahon, C.J., Pope, D.P. and Feng, H.C., (1977)
Metall. Trans. **7A**, 1269.
- Narayan, R. and Murphy, M.C., (1973)
JISI July, 493.
- Newcomb, S. B. and Stobbs, W. M., (1984)
Mater. Sci. Eng. **66**, 195.

- Oblak, J.M., Goodenow, R.H. and Hehemann, R.H., (1964)
Trans. AIMME **230**, 258.
- Oblak, J.M. and Hehemann, R.F., (1967)
Transformation and Hardenability in Steel, Climax Molybdenum Co., Ann Arbor, 15.
- Ohmori, Y., (1971)
Trans. ISIJ **11**, 339.
- Ohmori, Y. and Honeycombe, R. W. K., (1971)
Proc. ICSTIS, Suppl. Trans. Iron Steel Inst. Jpn. **11**, 1160.
- Ohmori, Y., Ohtani, H. and Kunitake, T., (1971)
Trans. ISIJ **11**, 250.
- Ohmori, Y., Ohtani, H. and Kunitake, T., (1974)
Metal Sci. **8**, 357.
- Ohmori, Y. and Maki, T., (1991)
Mater. Trans. JIM **32**, 631.
- Ohtani, H., Feng, H.C. and McMahon C.J., (1976)
Metall. Trans. **7A**, 1123.
- Ohtani, H., Okaguchi, S., Fujishiro, Y. and Ohmori, Y., (1990)
Metall. Trans. **21A**, 877.
- Oka, M. and Okamoto, H., (1986)
Proc. Int. Conf. on Martensitic Transformations, ICOMAT '86, Japan Institute Metal, 271.
- Olefjord, I., (1978)
Int. Metals Rev. **4**, 149.
- Olson G. B. and Cohen M., (1977)
Scripta Metall. **11**, 345-347.
- Olson G. B. and Cohen, M., (1983)
Metall. Trans. **14A**, 1057.
- Owen, W.S., (1954)
Trans. ASM **46**, 812.
- Padmanabhan, R. and Wood, W.E., (1984)
Mater. Sci. Eng. **66**, 1.
- Patel, J. R. and Cohen, M., (1953)
Acta Metall. **1**, 531.
- Philip, T. V., (1983)
Materials Handbook, 9th edn., ASM, Metals Park, Ohio, 421-443.
- Pickering, F.B., (1967)
Symposium of Transformation and Hardenability in Steel, Climax Molybdenum Co., Ann Arbor, 109.
- Power, A.E., (1956)
Trans. ASM **48**, 149.
- Power, A.E., (1967)
JISI **186**, 323.

- Purdy, G.R., Weichert, D.H. and Kirkaldy, J.S., (1964)
TMS-AIME **230**, 1025.
- Rao, M. M. and Winchell, P. G., (1967)
Trans. Met. Soc. AIME **239**, 956.
- Rao, B. V. N. and Thomas, G., (1979)
Proc. Int. Conf. on Martensitic Transformations, ICOMAT '79, Massachusetts Inst. technol., 12.
- Rees, G. and Bhadeshia, H.K.D.H., (1993a)
Mater. Sci. Technol. **8**, 985.
- Rees, G. and Bhadeshia, H.K.D.H., (1993b)
Mater. Sci. Technol. **8**, 954.
- Rudberg, E., (1952)
Jernkontorets Ann. **136**, 91.
- Salzbrenner, R. J. and Cohen, M., (1979)
Acta Metall. **27**, 739-748.
- Sandvik, B.P.J. and Nevalainen, H.P., (1981)
Metal Technol. **15**, 213.
- Sandvik, B.P.J., (1982a)
Metall. Trans. **13A**, 777.
- Sandvik, B.P.J., (1982b)
Metall. Trans. **13A**, 789.
- Sasada, T., (1984)
Tribology in the 80s, NASA Conf. Pub. 2300, **1**, 197.
- Shipway, P. H. and Bhadeshia, H. K. D. H., (1995)
Mater. Sci. Technol. *in press*.
- Siller, R. H. and Mclellan, R. B., (1970)
Metall. Trans. **1**, 985.
- Simonen, E. P., Aaronson, H. I. and Trivedi, R., (1973)
Metall. Trans. **4**, 1239.
- Smith, R. P., (1953)
Acta Metall. **1**, 578.
- Smith, M. F., Speich, G. R. and Cohen, M., (1959)
Trans. Met. Soc. AIME **215**, 528.
- Speich, G. R. and Cohen, M., (1960)
Trans. Met. Soc. AIME **218**, 1050.
- Speich, G.R., (1962)
The Decomposition of Austenite by Diffusional Processes, eds. by Zackay, V.F. and Aaronson, H.I., Interscience, New York, 353.
- Srinivasan G.R. and Wayman, C.M., (1968)
Acta Metall. A **16**, 609.
- Stewart, J. W., Thomson, R. C. and Bhadeshia, H. K. D. H., (1994)
J. Mater. Sci. **29**, 6079.

- Takahashi, M. and Bhadeshia, H.K.D.H., (1990)
Mater. Sci. Technol. **6**, 592.
- Takahashi, M. and Bhadeshia, H.K.D.H., (1991)
Mater. Trans. JIM **32**, 689.
- Timoshenko, S. P. and Goodier, J. M., (1970)
Theory of Elasticity, McGraw-Hill, New York, 419.
- Tomita, Y. and Okawa, T., (1993)
Mater. Sci. Eng. A **172**, 145.
- Thomas, G., (1978)
Metall. Trans. **9**, 439.
- Trivedi, R., (1970)
Metall. Trans. **1**, April, 921.
- Trivedi, R. and Pound, G. M., (1967)
J. Appl. Phys. **38**, 3569.
- Tsvinsky, S. V., Kogan, L. I. and Entin, R. I., (1959)
"Problems of Metallography and the Physics of Metals, ed. by B. Ya Lybubov, State Scientific Press, Moscow, 1955, (Translation published by the Consultants Bureau Inc., New York), 185.
- Underwood, E. E., (1968)
Quantitative Microscopy, eds. by R. T. Dehoff and F. N. Rhines, McGraw-Hill, New York, 78.
- Umemoto, M., Bando, S. and Tamura, I., (1986)
Int. Con. on Martensitic Transformation, The Japan Inst. of Metal, 595.
- Viswanathan, R. and Sherlock, T.P., (1972)
Metall. Trans. **3**, 459.
- Watson, J.D. and McDougall, P.G., (1973)
Acta Metall. **21**, 961.
- Woodfine, C.L., (1953)
Iron Steel Institute **173**, 1953, 229.
- X-Ray Power Data File, (1955)
US National Bureau of Standards.
- Young, C. H. and Bhadeshia, H. K. D. H., (1994)
unpublished research.
- Zener, C., (1946)
Trans. AIMME **167**, 550.
- Zhang, Z. Y., (1994)
Ph.D. Thesis, Univ. of Southampton.